Title
Computational Material Synthesis and Electromagnetic Wave Scattering in Particle Aggregates and Mesoporous Monoliths and Films

Author
Galy, Tiphaine

Publication Date
2020

Peer reviewed|Thesis/dissertation

UNIVERSITY OF CALIFORNIA

Los Angeles

Computational Material Synthesis and Electromagnetic Wave Scattering in Particle Aggregates and Mesoporous Monoliths and Films

A dissertation submitted in partial satisfaction
of the requirements for the degree
Doctor of Philosophy in Mechanical Engineering

by

Tiphaine Galy

2020

ABSTRACT OF THE DISSERTATION

Computational Material Synthesis and Electromagnetic Wave Scattering in Particle Aggregates and Mesoporous Monoliths and Films

by

Tiphaine Galy
Doctor of Philosophy in Mechanical Engineering
University of California, Los Angeles, 2020
Professor Laurent G. Pilon, Chair

Mesoporous materials could serve as promising thermally insulating materials for window applications due to their low thermal conductivity at ambient conditions. However, they tend to be translucent and hazy due to their nanoscale porous architecture controlling their optical and radiative properties. This dissertation aims to (i) computationally generate and characterize realistic mesoporous materials, (ii) explore how their nanoscale structure affect their light scattering characteristics, and (iii) apply the knowledge gained to understand light transfer through drying mesoporous monoliths and optical characterization of thin films.

First, three-dimensional mesoporous materials consisting of a network of touching or overlapping spheres were computationally generated using the diffusion-limited cluster-cluster aggregation (DLCCA) method. A new algorithm was developed to reproduce nitrogen adsorption porosimetry and retrieve their pore size distributions. The numerically computed specific surface areas and pore size distributions were in good agreement with experimental data reported for mesoporous silica. Second, unpolarized electromagnetic wave scattering by the computer-generated mesoporous structures, described as porous fractal aggregates, were investigated using the T-matrix and discrete-dipole approximation (DDA) methods. The transition between the independent and dependent scattering regimes

was studied in systems with up to 8 particles. Independent scattering refers to situations when particles are sufficiently distant that some radiation characteristics of the ensemble can be determined by adding the contributions of each particle. When particles are in close proximity, however, dependent scattering prevails and is affected by near-field interactions and far-field interferences among scattered waves from nearby particles. Here, the dimensionless parameters governing the scattering cross-section and asymmetry factor of non-absorbing particle suspensions and aggregates were found to be (i) the particle size parameter, (ii) the relative index of refraction, (iii) the interparticle distance-to-wavelength ratio, and (iv) the number of particles. Different transition criteria were derived for the scattering cross-section and the asymmetry factor. Dependent scattering effects prevailed in all aggregates and increased with decreasing particle size parameter. In addition, particle overlapping had a negligible effect on the scattering cross-section and asymmetry factor. Furthermore, predictions of the integral scattering characteristics of non-absorbing aggregates with relatively small particle size parameter were found to be accurately predicted by the equivalent effective property (EEP) approximation treating the aggregates as homogeneous spheres with the same volume and an effective refractive index. The EEP approximation was then combined with the Monte Carlo method to predict the transmittance and haze of ambiently drying mesoporous monoliths. The temporary decrease in transmittance and increase in haze observed experimentally during drying of the monoliths could be explained by light scattering by growing dry domains forming within the monolith. Finally, optical interferometry was demonstrated as a robust and simple alternative to ellipsometry for measuring the film thickness, effective refractive index, and total porosity of non-absorbing multicomponent mesoporous thin films.

The dissertation of Tiphaine Galy is approved.

Yongjie Hu

Pei-Yu Chiou

Bruce S. Dunn

Laurent G. Pilon, Committee Chair

University of California, Los Angeles

2020

TABLE OF CONTENT

LIST OF SYMBOLS

A_g	specific surface area, m^2/g
A_i	interfacial area concentration, m^{-1}
A, B, C	coefficients in Cauchy dispersion law, Equation (E.1)
B_λ	baseline, %
C_{N_2}	cross-sectional area of a nitrogen molecule, m^2
C_{abs}	absorption cross-section, nm^2
C_{sca}	scattering cross-section, nm^2
c	clearance distance, nm
$\bar{c}$	average clearance distance, nm
c^*	clearance-to-wavelength ratio, $c^* = c/\lambda$
$\bar{c}^*$	average clearance-to-wavelength ratio, $\bar{c}^* = \bar{c}/\lambda$
D	coefficient, $D = (n_{eff,\lambda}^2 - 1)/(n_{eff,\lambda}^2 + 2)$
D_λ	dark signal, %
d	interparticle distance, nm
$\bar{d}$	average interparticle distance, nm
d_{min}	minimum interparticle distance, nm
d^*	interparticle distance-to-wavelength ratio, $d^* = d/\lambda$
$\bar{d}^*$	average interparticle distance-to-wavelength ratio, $\bar{d}^* = \bar{d}/\lambda$ or dimensionless average interparticle distance, $\bar{d}^* = \bar{d}/2r_s$
d_{min}^*	minimum interparticle distance-to-wavelength ratio, $d_{min}^* = d_{min}/\lambda$
$\bar{d}_i$	average diameter of empty space in pores, nm
d_p	pore diameter, nm
$\bar{d}_p$	average pore diameter, nm
f_v	particle volume fraction
g	asymmetry factor
h_λ	haze, %

h_{vis}	visible haze, %
k_λ	absorption index
L	thickness of monoliths/films or dimensions of the simulation domains, nm
l_o	overlapping distance, nm
$\bar{l}_o^*$	dimensionless average overlapping distance, $\bar{l}_o^*$=$\bar{l}_o/2r_s$
l_s	traveling distance of particles during structure generation, nm
M	polymer to inorganic components mass ratio, g/g
M_w	molecular weight, Da
m	relative complex index of refraction, $m = m_s/n_m$
m_s	complex index of refraction of particles, $m_s = n_s + ik_s$
N_A	Avogadro constant, $N_A = 6.02\text{x}10^{23}$ mol^{-1}
N_c	number of elementary cubes in simulation domain
N_d	number of dipoles
N_m	monolayer capacity, mol/g
N_s	number of particles
n_c	final number of clusters
N_T	number of drained regions per unit volume, #/ μm^3
N_t	initial number of spheres for aggregate generation
$N_{d,\lambda}$	number of scattered photons
$N_{i,\lambda}$	number of incident photons
$N_{nh,\lambda}$	number of photons transmitted through the monolith
n_{eff}	effective refractive index of the aggregate
n_λ	refractive index
n_m	index of refraction of the non-absorbing surrounding medium
n_s	index of refraction of particles
k_λ	absorption index
k	thermal conductivity, W/m.K
P	adsorbate pressure, Pa

P_0	adsorbate saturation pressure, Pa
Q_{sca}	scattering efficiency factor
$R_{pred,\lambda}$	predicted film reflectance, %
R_s	aggregate radius, nm
r_a	volume adsorbed ratio
r_{eq}	equivalent radius, nm
r_{eff}	effective radius of the aggregate, nm
r_D	radius of dry regions, μm
$\bar{r}_D$	average radius of dry regions, μm
r_s	particle radius, nm
$\bar{r}_s$	mean radius of polydisperse particles, nm
r_λ	amplitude of the reflected wave
$r_{ij,\lambda}$	Fresnel's coefficient at the interface of media i and j
S	standard deviation, μm
S_a	specific surface area, m^2/g
$S_{d,\lambda}$	diffuse transmitted signal, %
S_i	apparent surface area at iteration i, m^2
$S_{nh,\lambda}$	normal-hemispherical transmitted signal, %
S_0	total surface area, m^2
s	standard deviation of a particle radius distribution, nm
T_c	condensation temperature, °C
$T_{d,\lambda}$	diffuse transmittance, %
$T_{nh,\lambda}$	normal-hemispherical transmittance, %
T_{vis}	visible transmittance, %
t	time, day
t_i	"adsorbate" layer thickness at iteration i, nm
V_λ	photopic spectral luminous efficiency function
V_i	apparent pore volume at iteration i, m^3

V_m	molecular volume of the adsorbate, cm^3
V_p	pore volume, m^3
$V_{p,cu}$	cumulative pore volume, m^3
$V_{p,tot}$	total pore volume, m^3
v_p	specific pore volume, cm^3/g
$v_{p,cu}$	specific cumulative pore volume, cm^3/g
$v_{p,tot}$	specific total pore volume, cm^3/g
V_s	volume occupied by the particles, nm^3
V_t	total volume occupied by the aggregate, nm^3
V_{tot}	volume embedding the suspension or aggregate, nm^3
x_w	water mass fraction in the monolith

Greek symbols

α_a	molecular polarizability of the adsorbate, cm^3
β_λ	phase difference, rad
β	phase shift, $\beta = 2\chi_s\|m-1\|$
χ_s	particle size parameter
Δd	dipole size, nm
Δ_λ	phase difference between $r_\perp$ and $r_\parallel$, rad
Δt	change in adsorption layer thickness, nm
Δx	cube size, nm
ϵ	emissivity
λ	wavelength of radiation, nm
μ	resistivity of the silicon substrate, Ω.cm
Φ	phase function
ϕ	total porosity, %
ϕ_o	open porosity, %
ψ	dry domain size distribution, $\#/\mu m^4$

ρ	density of the solid phase, g/cm^3
ρ_{eff}	effective density, g/cm^3
ρ_s	silica density, $\rho_s = 2.2$ g/cm^3
$\sigma_{s,\lambda}$	scattering coefficient, mm^{-1}
$\tan \Psi_\lambda$	amplitude ratio of $r_\parallel / r_\perp$
Ω	solid angle, sr
Θ	scattering angle, rad
θ	angle of incidence or transmission, rad
τ_λ	optical thickness

Subscripts and superscripts

1	refers to the surrounding medium, i.e., air
2	refers to the thin film
3	refers to the silicon substrate
a	as a superscript: refers to scattering characteristics of aggregates
a	as a subscript: refers to the air
b	refers to bispheres
BET	refers to the Brunauer-Emmett-Teller (BET) method
c	refers to the continuous phase
cr	refers to critical values delimiting the scattering regimes
D	refers to the dry/drained domains
d	refers to the dispersed phase
EEP	refers to the equivalent effective properties approximation
EV	refers to the equivalent volume approximation
eff	refers to effective properties
F	refers to the falling rate period
M	refers to Lorenz-Mie theory
m	refers to properties of the monolith

$pane$	refers to a glass pane
PC	refers to point-contact structure
$\perp$	refers to the perpendicular polarization
$\parallel$	refers to the parallel polarization
PSD	refers to the pore size distribution algorithm
R	refers to Rayleigh scattering
SC	refers to surface-contact structure
s	as a superscript: refers to particle systems
s	as a subscript: refers to silica
TB	refers to properties of a thermal barrier
W	refers to the wet domains
w	refers to water

LIST OF FIGURES

LIST OF TABLES

ACKNOWLEDGMENTS

I would like to thank my advisor, Professor Laurent Pilon, for his guidance and encouragement throughout the duration of my doctoral work. Moreover, I would like to thank Professor Bruce Dunn, Professor Pei-Yu Chiou, and Professor Yongjie Hu for serving on my thesis committee. Furthermore, I would like to express my appreciation to my collaborators Dr. Michal Marszewski, Sophia King, Yan Yan, Patricia McNeil, and Maggie Fox for their help with the experimental work and Mu Du and Daniel Huang for their help with the numerical simulations.

I would also like to acknowledge all my lab members Bing-Ang Mei, Obaidallah Mohammad Munteshari, Benjamin Young, Ampol Likitchatchawankun, Eylul Simsek, Ali Dashti, Sara Vallejo, Matevž Frajnkovič, Jack Hoeniges, and Sun Woong Baek. I am also grateful to all my friends who have made my life enjoyable during my study at UCLA, especially Gabriel Fernandez. Finally, I would like to thank my family for their love and support.

VITA

2016–2020 Graduate Student, Mechanical and Aerospace Engineering Department, UCLA.

PUBLICATIONS

T. Galy, D. Huang, and L. Pilon, Revisiting Independent versus Dependent Scattering Regimes in Suspensions or Aggregates of Spherical Particles, *Journal of Quantitative Spectroscopy and Radiative Transfer*, 246, 106924 (2020)

T. Galy, M. Marszewski, S. C. King, Y. Yan, S. H. Tolbert, and L. Pilon, Comparing Methods for Measuring Thickness, Refractive Index, and Porosity of Mesoporous Thin Films, *Microporous and Mesoporous Materials*, 291, 109677 (2020)

T. Galy, M. Du, M. Marszewski, and L. Pilon, Computer-Generated Mesoporous Materials and Associated Structural Characterization, *Computational Materials Science*, 157, 156-167 (2019)

T. Galy, S. C. King, M. Marszewski, P. E. McNeil, M. Fox, A. Dashti, G. Bar, V. Wall, B. S. Dunn, S. H. Tolbert, and L. Pilon, Drying of Mesoporous Monoliths: from Transparent to White to Transparent Again, in preparation

T. Galy and L. Pilon, Scattering Characteristic Approximations for Non-Absorbing Aggregates, in preparation

Y. Yan, M. Li, S. C. King, **T. Galy**, M. Marszewski, J. S. Kang, Y. Hu, L. Pilon, and S. H. Tolbert, Controlling Thermal Conductivity in Mesoporous Silica Films Using Pore Size and Nanoscale Architecture, *The Journal of Physical Chemistry Letters*, 2020

X. Quian, Y. Zhao, Y. Alsaid, X. Wang, M. Hua, **T. Galy**, H. Gopalakrishna, Y. Yang, J. Cui, N. Liu, M. Marszewski, L. Pilon, H. Jiang, and X. He, Artificial Phototropism for Omnidirectional Tracking and Harvesting of Light, *Nature Nanotechnology*, 14, 1048-1055 (2019)

Y. Yan, S. C. King, M. Li, **T. Galy**, M. Marszewski, J. S. Kang, L. Pilon, Y. Hu, and S. H. Tolbert, Exploring the Effect of Porous Structure on Thermal Conductivity in Templated Mesoporous Silica Films, *Journal of Physical Chemistry C*, 123, 35, 21721-21730 (2019)

M. Marszewski, S. C. King, Y. Yan, **T. Galy**, M. Li, A. Dashti, D. M. Butts, J. S. Kang, P.E. McNeil, E. Lan, B.S. Dunn, Y. Hu, S. H. Tolbert, and L. Pilon, Thick Transparent Nanoparticle-Based Mesoporous Silica Monolithic Slabs for Thermally Insulating Window Materials, *ACS Applied Nanomaterials*, 2, 7, 4547-4555 (2019)

M. Marszewski, D. Butts, E. Lan, Y. Yan, S. King, P.E. McNeil, **T. Galy**, B. Dunn, S.H. Tolbert, Y. Hu and L. Pilon, Effect of Surface Hydroxyl Groups on Heat Capacity of Mesoporous Silica, *Applied Physics Letters*, 112(20), 201903 (2018)

CHAPTER 1

Introduction

1.1 Heat losses through windows

Heating, ventilation, and air conditioning (HVAC) of commercial and residential buildings consume about 14% of the total amount of primary energy consumed every year in the United States [27]. In 2013, direct greenhouse gas (GHG) emissions from buildings accounted for approximately 12% of the total GHG emissions in the U.S., mainly due to combustion of fossil fuels for heating in the winter months. One way to reduce building energy consumption and the associated GHG emissions is to reduce heat losses through the building envelope. Windows are arguably the weakest constituent of the building envelope. In fact, heat losses through windows in cold weather across the U.S. consumes about 4% of the primary energy [27]. While double-pane windows have excellent thermal, optical, and acoustic performance, their adoption has been relatively slow. In fact, between 30 and 40% of single-pane windows remain in use in the Northeastern/Midwestern and Southern regions of the US, respectively [27]. This relatively small percentage of single-pane windows contributes significantly to building heat losses since single-pane windows conduct heat approximately twice as much as multi-pane windows. Therefore, the realization of single-pane windows with a thermal barrier leading to a reduction in U-value under 0.4 BTU/ft^2.h.°F (from 1.1 BTU/ft^2.h.°F) without a significant change in appearance may create a simplified alternative for retrofitting single-pane systems and improve the energy efficiency of residential and commercial buildings.

1.2 Mesoporous materials

Porous materials feature interconnected or dispersed pores of different morphologies such as cylindrical and spherical pores. Depending on their average pore diameter $\bar{d}_p$, these materials can be divided into three categories including (i) microporous ($\bar{d}_p < 2$ nm), (ii) mesoporous (2 nm $\leq \bar{d}_p \leq 50$ nm) or (iii) macroporous ($\bar{d}_p > 50$ nm) [28, 29]. In particular, mesoporous materials exhibit several defined nanostructures (ordered or disordered), numerous morphologies (film, powder, monolith), and various frameworks (silica, metal-oxides, etc.). Since the discovery of this class of materials in the early 1990's [30], researchers have focused on varying their composition and structure [31–33] and on expanding the range of applications including catalysis [34], medicine [35, 36], electrochemistry [37], electronics [38], optics [39], and thermal insulation [40, 41]. Indeed, mesoporous materials provide excellent opportunities for tunable functionality. First, the inorganic framework of the host system can be chosen for its suitable properties (e.g., optical transparency in the visible and near UV range) for a specific advanced applications (e.g., window insulation). Second, additional functionality can be developed by tuning the porosity and pore size distribution of the materials. The porous nanostructure controls the physical properties of the materials such as thermal and electric conductivity [42].

One of the most common methods for synthesizing mesoporous materials with pore diameters in the 2-50 nm range includes the diffusion-limited aggregation as commonly found in aerogel or aerogel-like synthesis [43]. In this case, reactive inorganic building blocks in solution aggregate in a diffusion-limited manner to form a fractal network of overlapping particles. Figure 1.1 shows scanning (SEM) and transmission (TEM) electron microscopy images of typical silica aerogels [1–3]. It illustrates how silica aerogels consist of distinct overlapping nanoparticles.

An alternative to aerogel synthesis is to use templating to create nanoporous

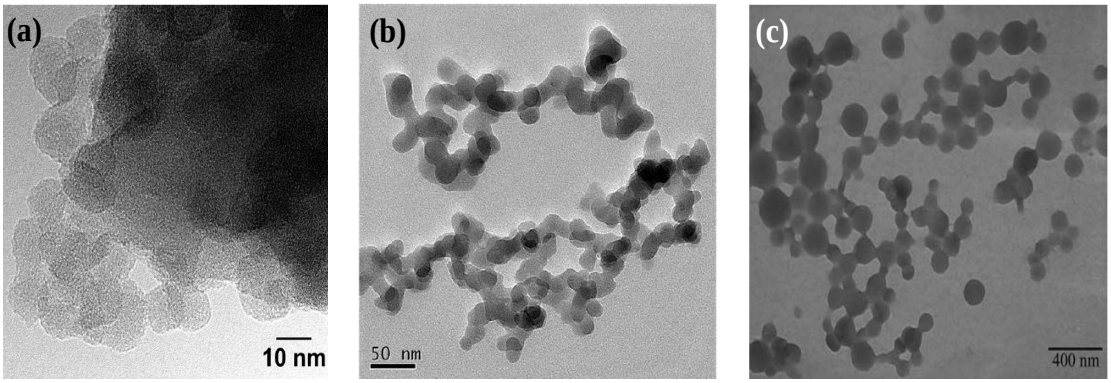

Figure 1.1: TEM images of (a),(b) silica aerogels (reprinted with permission from Ref. [1] and Ref. [2] Copyright Springer International Publishing A.G. 2007 and Copyright Elsevier B.V. 2013, respectively), and (c) silica solution during gelation (reprinted with permission from Ref. [3] Copyright Springer International Publishing A.G. 2007).

materials [44–46]. A range of materials, from block copolymers, to surfactants, to polymer colloids can be used to create mesoporous materials with both ordered and disordered porosity from a wide range of crystalline and amorphous oxide and non-oxide materials [45, 47].

1.2.1 Aerogels, ambigels, and xerogels

Synthesis of aerogels can be divided into four successive stages namely (1) sol phase, (2) gelation, (3) aging, and (4) drying [48]. During the sol phase, the gel precursor reacts and forms nanoparticles. The gelation occurs when the nanoparticles start aggregating and forming a network. Nanoparticles clusters form and grow by aggregation of individual particles and by collision with other clusters. The process progressively leads to a continuous network [49]. Aging results in the growth of necks between particles which strengthens the network [50]. During drying, the solvent contained in the pores is removed. The drying method

strongly affects the porosity and pore size distribution of the final mesoporous structure [43, 49]. The capillary pressure imposed by the solvent on the network during drying results in shrinkage of the gel structure. Gels dried quickly in the open air have typical porosity less than 50% due to significant shrinkage and are referred to as xerogels [51]. By contrast, aerogels reach porosity above 80% thanks to supercritical CO_2 drying at high pressure so as to minimize capillary forces. Alternatively, capillary forces can also be minimized by exchanging the pore liquid with a non-polar solvent featuring low surface tension (e.g., hexane or cyclohexane) and by slow drying at ambient temperature and pressure [51]. Gels dried via non-polar solvent exchange at ambient temperature and pressure are referred to as ambigels [43]. Aerogels have larger porosity and pore size than ambigels and xerogels [49] while ambigels typically feature porosity and pore size between those of xerogels and aerogels [43].

1.2.2 Templated mesoporous thin films

Mesoporous thin films are usually prepared using templating methods by evaporation-induced self-assembly (EISA) processes [45, 47]. The most common deposition techniques are dip-coating and spin-coating [45, 47, 52]. For dip-coating deposition, the substrate is vertically immersed in the solution before being withdrawn at a constant speed. For spin-coating, the liquid flows radially outward onto the substrate driven by centrifugal force. Here, solvent evaporation is the main parameter that governs the film-formation process. The film deposition is typically followed by a heat treatment aiming to stabilize and stiffen the network, and to increase the porosity through template calcination [47].

1.3 Windows energy performance

Energy performances of windows are usually estimated based on three characteristics namely (1) the U-value, (2) the solar heat gain coefficient (SHGC), and (3) the condensation temperature. The U-value or U-factor, expressed in Btu/ft^2.h.°F, is a measure of the heat loss across the window. The lower the U-value, the more thermally insulating the window is. The SHGC is the fraction of the incident solar radiation that enters the building through the window and includes transmitted radiation and absorbed radiation eventually released inside the building. The lower the SHGC, the smaller the amount of solar heat the window admits. The condensation temperature is defined as the exterior temperature at which condensation appears on the inside surface.

In this study, the U-value, SHGC, and condensation temperature, were predicted using the software WINDOW 7.6 developed by LBNL [53]. The U-value and SHGC were calculated using the National Fenestration Research Council (NFRC) 100-2010 environmental conditions [54] corresponding to (i) an interior ambient temperature of 21°C, (ii) an exterior ambient temperature of -18°C, (iii) an exterior windspeed of 5.5 m/s, and (iv) without solar illumination. Moreover, the U-value and SHGC calculated were the "center-of-glass" values, i.e., they did not include the effects of the window frame and sash. For the condensation temperature, the relative humidity was assumed to be 30% and the exterior ambient temperature was progressively changed until the temperature of the inside surface of the window pane featured condensation. The other environmental conditions were also taken as those of the NFRC 100-2010.

In addition, reducing the emissivity of one or more of the window surfaces, so that it reflects long-wave infrared energy (or thermal radiation), improves a window's insulating properties. Uncoated glass has an emissivity of 0.84 [53]. It can be significantly reduced by adding a low-e coating featuring low emissivity

at room temperature. For example, the Low-E^3 366 coating by Cardinal Glass Industry (Eden Prairie, MN) has an emissivity of 0.022 and is, to the best of our knowledge, one of the lowest emissivity achieved for a low-e coating. Finally, energy efficiency of basic single windows can be improved by adding a thermal barrier layer consisting of an insulating material such as a monolith of mesoporous silica.

1.3.1 Enhanced single-pane windows

Low-e coating location

For single-pane windows, the location of the low-e coating and the key design parameters to be optimized depend on the geographical zone for which the product is developed. In northern states, where energy is mainly used for heating, the low-e coating is placed on the inside surface to reflect the thermal radiation emitted by the dwelling walls, as illustrated in Figure 1.2(a). In this climate zone, the key parameters controlling the performance of the windows are the U-value and the condensation temperature. By contrast, in southern states with warm climates, a low solar heat gain coefficient (SHGC) is the most important property to achieve. Therefore, the low-e coating is placed on the exterior surface to reflect sunlight [Figure 1.2(b)] and reduce solar heat gain.

Since thermal barrier layers of mesoporous silica are transparent and non-absorbing, they have little impact on the solar heat gain. They are more effective and useful in improving the performances of single-pane windows for the northern states zone. Therefore, the preferred enhanced single-pane window is that illustrated in Figure 1.2(a) for northern states and consists of a 3 mm glass pane coated with a 3 mm mesoporous thermal barrier coated with a low-e coating facing the interior of the dwelling.

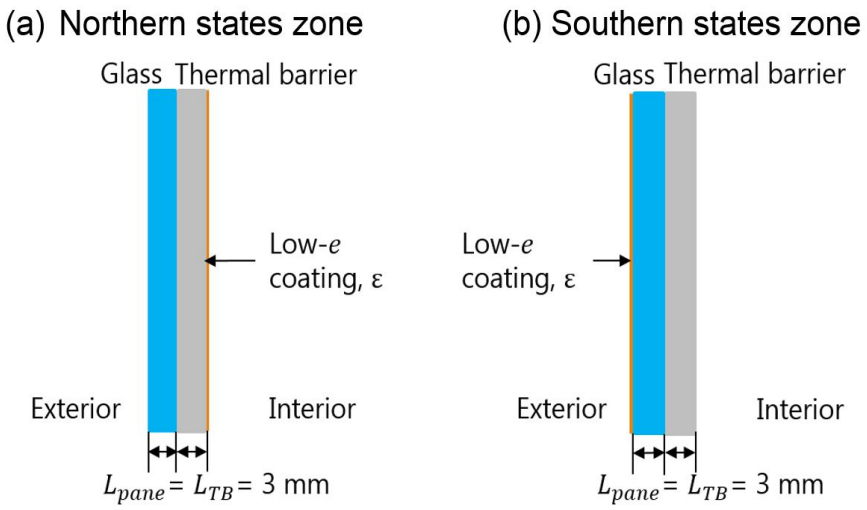

Figure 1.2: Single-pane window with a thermal barrier and a low-e coating on the (a) inside and (b) outside surface.

U-value and condensation temperature

Figure 1.3 plots the condensation temperature as a function of the U-value at the center of a 3 mm thick single-pane window (k_{pane} = 1 W/mK) for two configurations (1) with a low-e coating with emissivity ϵ varying between 0.84 (glass) and 0.1 and (2) with a thermal barrier or insulating coating with thermal conductivity k_{TB} varying between 0.17 W/m.K and 0.014 W/m.K and a low-e coating $\epsilon = 0.1$ (enhanced single-pane). Figure 1.3 indicates that the low-e coating alone cannot achieve a U-value lower than 0.6 Btu/ft^2.h.°F. However, when combined with a thermal barrier, the U-value decreased with decreasing thermal conductivity k_{TB} and reached 0.34 Btu/ft^2.h.°F when k_{TB} = 0.014 W/m.K. Moreover, in the case of a single-pane with a low-e coating, the condensation temperature was higher than -3°C and increased with decreasing emissivity ϵ. On the other hand, for enhanced single-pane windows, the condensation temperature decreased with decreasing thermal conductivity and reached values as low as -15.5°C when k_{TB} = 0.014 W/m.K.

Table 1.1 presents the U-value and condensation temperature T_c of enhanced

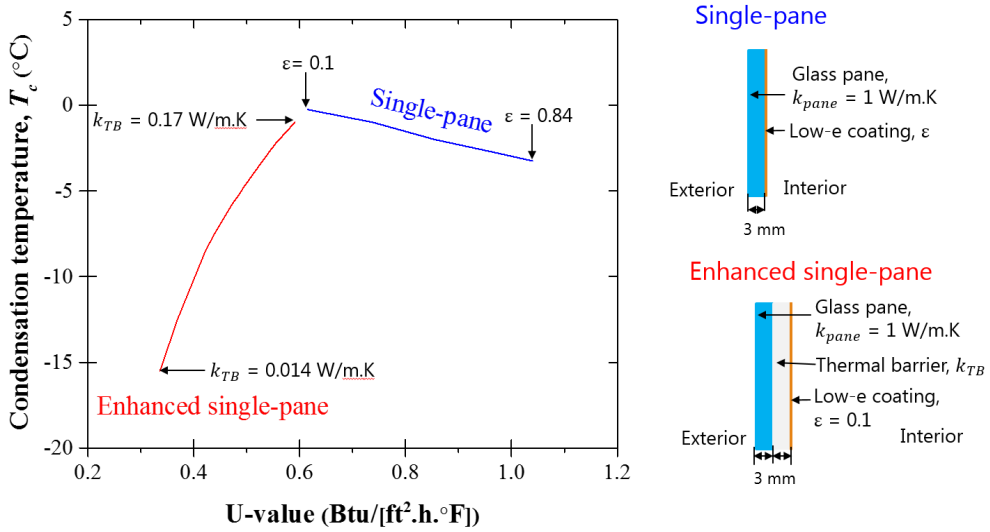

Figure 1.3: Condensation temperature as a function of U-value for a single-pane window (blue line) and an enhanced single-pane window (red line).

single-pane windows depicted in Figure 1.2(a). The thermal conductivity of the glass pane was k_{pane}= 1 W/m.K and its emissivity was ϵ_{pane}= 0.84. The thermal conductivity k_{TB} of the thermal barrier was varied from 0.07 W/m.K to 0.025 W/m.K. A thermal conductivity k_{TB}= 0.07 W/m.K is representative of the thermal conductivity of silica nanoparticle-based monoliths and a thermal conductivity k_{TB}= 0.025 W/m.K is representative of that of silica ambigel. The emissivity ϵ of the low-e coating was varied between 0.3 to 0.022. Performances of a basic 3 mm single-pane are also presented for comparison.

Table 1.1: Performances of an enhanced single-pane window with a mesoporous silica insulating coating on the inside surface [Figure 1.2(a)].

ϵ	**Single-pane**	k_{TB} **= 0.07 W/m.K**	**0.025 W/m.K**
0.3	U=0.74 Btu/ft².h.°F T_c=0°C	U=0.62 Btu/ft².h.°F T_c=-4°C	U=0.48 Btu/ft².h.°F T_c=-10.5°C
0.1	U=0.62 Btu/ft².h.°F T_c=0.5°C	U=0.52 Btu/ft².h.°F T_c=-2.5°C	U=0.42 Btu/ft².h.°F T_c=-7.5°C
0.022	U=0.57 Btu/ft².h.°F T_c=1°C	U=0.49 Btu/ft².h.°F T_c=-1.75°C	U=0.39 Btu/ft².h.°F T_c=-6°C

Table 1.1 shows that the U-value and condensation temperature T_c decreased with decreasing k_{TB}, as previously mentioned. On the other hand, decreasing the

emissivity ϵ decreased the U-value, but increased condensation temperature, as more heat is reflected back into the room resulting in a lower interior window surface temperature. However, all cases of enhanced single-pane windows considered still achieved a lower condensation temperature than a simple single-pane. Especially, enhanced windows with a thermal barrier with thermal conductivity of k_{TB}= 0.025 W/m.K achieved the lowest condensation temperatures for any emissivity ϵ considered. Therefore, the preferred configuration will be that of an enhanced single-pane window with k_{TB}= 0.025 W/m.K and ϵ = 0.022. In addition, the SHGC of this configuration was 0.86. As mentioned previously, the SHGC is not a key parameter for Northern state zones. However, in these regions, a high SHGC is preferred so that solar energy will contribute to heating the building.

1.3.2 Insulating Glass Units (IGUs) or double-pane windows

Another advantage of enhanced single-pane windows is that they can be added to existing single-pane windows to form an IGU or double-pane window. Figure 1.4 displays this possibility. In this case, the two panes are separated by an air gap and the glazing system can feature a low-e coating on the 2^{nd} and/or 4^{th} surfaces. To calculate the performances of this system, the thickness of the air gap was taken as L_{gap}= 12 mm and the emissivity of the low-e coating as ϵ = 0.1.

Table 1.2 presents the U-value and condensation temperature of enhanced single-pane window added to an existing single-pane window to form an IGU as illustrated in Figure 1.4. Table 1.2 demonstrates that the performances of the double-pane window with a thermal barrier were improved when compared to enhanced single-pane windows [Table 1.1 and Figure 1.2(a)]. In particular, U-values lower than 0.28 Btu/ft^2.h.°F and condensation temperatures lower or equal to -20°C were achieved whereas the lowest U-value and condensation temperature achieved for enhanced single-pane windows were 0.389 Btu/ft^2.h.°F and

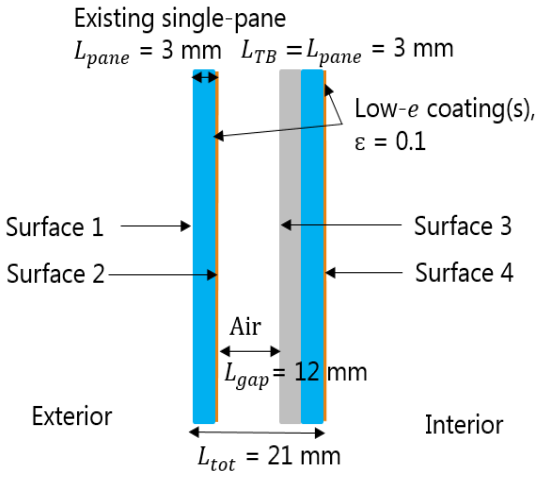

Figure 1.4: Single-pane window with a thermal barrier added to an existing single-pane.

-6°C (when k_{TB} = 0.025 W/m.K), respectively.

Furthermore, Table 1.2 shows that the lowest U-value was achieved for a system with two low-e coatings on the 2^{nd} and 4^{th} surfaces. Therefore, the preferred double-pane window is that with two low-e coatings. Finally, Table 1.2 also indicates that this product outperformed basic double-pane windows with two glass panes separated by a 12 mm air gap.

Table 1.2: Performances of an enhanced single-pane window added to an existing window and incorporating a mesoporous thermal barrier as illustrated in Figure 1.4.

Low-e	**Double-pane**	k_{TB} **= 0.025 W/m.K**
2^{nd} surface	U=0.32 Btu/ft^2.h.°F	U=0.26 Btu/ft^2.h.°F
	T_c=-44.5°C	T_c=-60.5°C
4^{th} surface	U=0.35 Btu/ft^2.h.°F	U=0.27 Btu/ft^2.h.°F
	T_c=-12°C	T_c=-20°C
2^{nd} and 4^{th} surfaces	U=0.24 Btu/ft^2.h.°F	U=0.21 Btu/ft^2.h.°F
	T_c=-24°C	T_c=-32°C

Enhanced double-pane windows consisting of two glass panes each coated with a thermal barrier are another alternative (Figure 1.5). The gap was assumed to be 12 mm in thickness and filled with a mixture of air (10%) and argon (90%),

commonly used for double-pane windows.

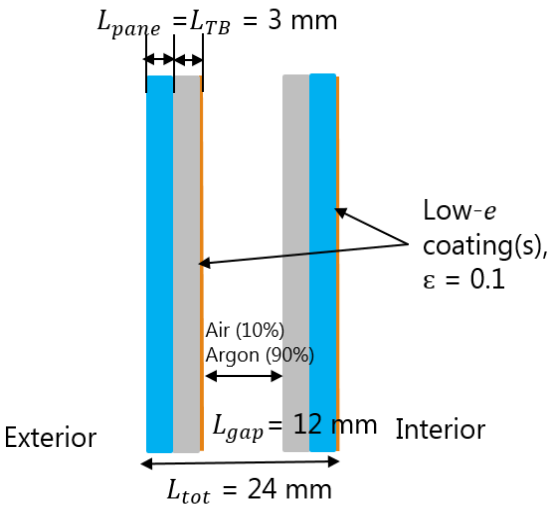

Figure 1.5: Enhanced double-pane window with two thermal barriers.

Table 1.3 shows the U-value and condensation temperature of enhanced double-pane windows. Comparing Tables 1.1, 1.2, and 1.3 indicates that enhanced double-pane windows were more insulating than enhanced single-pane windows and IGUs with one thermal barrier. They also featured lower condensation temperatures. Similarly to what was observed for double-pane windows with one thermal barrier, Table 1.3 indicates that the enhanced double-pane windows with two thermal barriers and low-e coatings featured the best performances. An enhanced double-pane window with low-e coatings on the 2^{nd} and 4^{th} surfaces enabled to achieve a U-value of 0.16 Btu/ft^2.h.°F and a condensation temperature of -44.5°C.

Table 1.3: Performances of an enhanced double-pane window incorporating mesoporous thermal barriers as illustrated in Figure 1.5.

Low-e	**Double-pane**	k_{TB} **= 0.025 W/m.K**
2^{nd} surface	U=0.27 Btu/ft^2.h.°F	U=0.19 Btu/ft^2.h.°F
	T_c=-53.5°C	T_c=-84°C
4^{th} surface	U=0.33 Btu/ft^2.h.°F	U=0.22 Btu/ft^2.h.°F
	T_c=-13.5°C	T_c=-30°C
2^{nd} and 4^{th} surfaces	U=0.21 Btu/ft^2.h.°F	U=0.16 Btu/ft^2.h.°F
	T_c=-29°C	T_c=-44.5°C

1.4 Light scattering by a single spherical particle

Scattering by a single spherical particle depends on its (i) size parameter χ_s and (ii) relative complex index of refraction m [55]. The particle size parameter χ_s is defined as $\chi_s = 2\pi r_s/\lambda$ where r_s is the particle radius and λ is the wavelength of the incident light. The relative complex index of refraction m is defined as $m = m_s/n_m$ where n_m is the index of refraction of the non-absorbing surrounding medium and m_s is the complex index of refraction of the particle defined as $m_s = n_s + ik_s$ where n_s and k_s are the refractive and absorption indices of the particle, respectively.

The scattering cross-section $C_{sca}(\chi_s, m, r_s)$ and asymmetry factor $g(\chi_s, m)$ of a single spherical particle in a non-absorbing medium can be predicted by the Lorenz-Mie theory [56]. Notably, in the Rayleigh scattering regime, corresponding to $\chi_s \ll 1$ and $\chi_s|m-1| \ll 1$, the scattering cross-section of a particle with size parameter χ_s and relative complex index of refraction m can be expressed as [57]

$$C_{sca}^{R}(\chi_s, m, r_s) = \frac{24\pi^3 V_s^2}{\lambda^4}\left|\frac{m^2-1}{m^2+2}\right|^2 = \frac{8\pi r_s^2 \chi_s^4}{3}\left|\frac{m^2-1}{m^2+2}\right|^2 \tag{1.1}$$

where V_s is the volume of the particle. On the other hand, the asymmetry factor g can be defined as [55]

$$g(\chi_s, m) = \frac{1}{4\pi}\int_{4\pi} \Phi(\chi_s, m, \Theta)\cos\Theta \mathrm{d}\Omega \tag{1.2}$$

where $\Phi(\chi_s,m,\Theta)$ is the scattering phase function representing the probability that a wave be scattered from the incident direction $\hat{s}_i$ into direction $\hat{s}$. Here, Θ is the scattering angle between unit vectors $\hat{s}_i$ and $\hat{s}$ and Ω is the associated solid angle. Particles in the Rayleigh scattering regime feature a negligible phase shift $\beta = 2\chi_s|m-1|$ between the incident electromagnetic wave and that traveling through them [57, 58]. Thus, their scattering phase function is isotropic, i.e., $\Phi(\chi_s, m, \Theta)$

$\simeq 1$ and $g(\chi_s,m) \simeq 0$.

Moreover, predicting the transparency of mesoporous materials with respect to their nanostructure is challenging. Scattering characteristics of systems with distant particles are usually determined by assuming that the particles scatter independently from one another so their individual contributions can be added, based on superposition principles. In situations when the particles are spherical, the Lorenz-Mie theory can be used to predict the scattering characteristics of each individual particle. However, this approximation, sometimes called "independent scattering approximation" depends on some measure of the proximity of the constitutive particles. In the case of mesoporous materials, particles overlap and form a connected network. When particles are in close proximity, light scattering is affected by near-field interactions and far-field interferences resulting in so-called "dependent scattering effects" [59]. In the dependent scattering regime, scattering characteristic of particle systems cannot be determined by merely adding up the contributions of individual particles.

1.5 Motivation of the study

Mesoporous silica materials, particularly silica aerogels, are known to have some of the lowest reported thermal conductivities (< 20 mW/m.K) at room temperature and atmospheric pressure [60]. Thanks to their low thermal conductivity, a number of studies used silica aerogels sandwiched between two glass panes to create a thermally insulating windows [40, 61]. Unfortunately, light scattering by aerogel is significant despite the ability to adjust porosity by tuning the pH in the gelation process and/or through heat treatment. As a result, the windows are only translucent and not transparent. Optical transparency could be achieved by controlling the aerogels' pore size and pore size distribution. However, it is difficult to synthesize aerogels with large porosity and small pores [62]. In fact,

xerogels, although featuring smaller porosity (∼50%) compared to aerogels, can achieve better transparency thanks to their smaller and narrower pore size distribution [8].

1.6 Objectives of the present study

The structural characterization of mesoporous materials is of great practical interest and critical to correctly determine the relationships between their nanoscale architecture and their thermal and optical properties. Experimental optimization of mesoporous materials by trial and error to achieve the desired thermophysical properties can be challenging and time consuming. Alternatively, computer simulations can quickly generate various representative mesoporous structures with a wide range of structural parameters. Then, nanostructure-property relationship can be derived and used to identify the optimum nanostructure for the desired properties. First, this study aims to numerically generate and characterize a wide variety of three-dimensional mesoporous structures featuring aggregated spherical nanoparticles with either point-contact or surface-contact. Whenever possible, the results were compared with experimental data reported in the literature. The developed computational tools and methods can accelerate the discovery and optimization of mesoporous materials for a wide range of applications.

Furthermore, in the perspective of the application of mesoporous materials as a transparent and thermally insulating layers in window solutions, it would be insightful to know the effect of their porous nanostructure on their scattering characteristics. This study also aims (1) to identify the parameters controlling the scattering cross-section and asymmetry factor of aggregates and mesoporous materials consisting of non-absorbing monodisperse spherical particles; (2) to determine the conditions under which independent and dependent scattering regimes prevail for particle ensemble; and (3) to assess the effects of dependent scattering

on the scattering cross-section and asymmetry factor of non-absorbing aggregates with touching or overlapping particles. The radiative characteristics of aggregates are usually computed using algorithms solving Maxwell's equations. However, it would be computationally far more efficient to quickly estimate the radiation characteristics of aggregates using simple approximations. Therefore, this study also aims to identify approximations capable of rapidly predicting the scattering cross-section and asymmetry factor of non-absorbing aggregates.

Moreover, questions aroused from our experimental observations and from anecdotal reports in the literature of transparent gels turning white and milky during drying before becoming transparent again when fully dried. No clear understanding of the reasons for such observations was given in the literature. However, such understanding could provide insight into light scattering by the dry ambigel and final product. In addition, the apparent changes in haze could be used for continuous monitoring of the drying process. Thus, this dissertation also aims to identify the physical phenomena responsible for the temporary haziness observed in the sol-gel synthesis of mesoporous monoliths during drying. The objectives of the study were (1) to experimentally measure changes in transmittance and haze as functions of time during the drying process and (2) to predict the observed changes by modelling light transfer through the drying gel.

Finally, templated mesoporous thin films are also of interest for a wide range of applications from optical waveguides to interlayer dielectrics for microprocessor-based integrated circuits. Moreover, their synthesis is relatively fast and their study can provide insights into the effect of the porous nanoscale architecture on their thermal and optical properties. In all their applications, accurately and reliably measuring their thickness, refractive index, porosity, and pore size distribution is essential to ensure proper performance of the materials and to correctly assess their nanostructure-property relationships. Contrary to mesoporous monoliths, the transmittance and reflectance of mesoporous thin films feature in-

terference patterns which depend on the thickness and optical properties of the film and its substrate. This study aims (1) to determine how accurately optical interferometry can retrieve thickness, refractive index, and porosity of multicomponent mesoporous thin films and (2) to investigate if the porosity and pore size distribution of thin films can be estimated from their equivalent powders, as commonly done in the literature. This method was used to investigate the effects of pore size and nanoscale architecture on the thermal conductivity of mesoporous silica films [63, 64] as well as the role of atomic scale heterogeneities [65].

1.7 Organization of the document

Chapter 2 presents computational tools and methods to generate realistic three-dimensional mesoporous materials and perform numerical porosimetry characterization. Chapter 3 investigates the parameters controlling the transition between dependent and independent scattering regimes and derives transition criteria for bispheres, ordered and disordered suspensions and aggregates with up to 8 spherical particles. Chapter 4 studies the effect of dependent scattering on aggregates with up to 30,000 spherical touching or overlapping particles and investigates the validity of the equivalent effective property approximation to rapidly estimate the integral scattering characteristics of aggregates. Chapter 5 elucidates the scattering phenomena responsible for the significant temporary drop in transmittance and increase in haze of mesoporous monoliths during their drying. This chapter reports for the first time quantitative measurements of solvent mass fraction, transmittance and haze as functions of time. Chapter 6 compares different methods to measure the thickness, refractive index, porosity, and/or pore size distribution of silica and silica-titania mesoporous thin films with a particular interest in optical interferometry. Finally, Chapter 7 summarizes the finding of this PhD thesis and provides recommendations for future research.

CHAPTER 2

Computer Generated Mesoporous Silica and Associated Structural Characterization

This chapter demonstrates how to computationally generate and fully characterize realistic three-dimensional mesoporous materials. Notably, a new algorithm reproducing gas adsorption porosimetry was developed to calculate the specific surface area and pore size distribution of computer-generated structures. The diffusion-limited cluster-cluster aggregation (DLCCA) method was used to generate point-contact or surface-contact mesoporous structures made of monodisperse or polydisperse spherical particles. The generated structures were characterized in terms of particle overlapping distance, porosity, specific surface area, interfacial area concentration, pore size distribution, and average pore diameter. The different structures generated featured particle radius ranging from 2.5 to 40 nm, porosity between 35 and 95%, specific surface area varying from 35 to 550 m^2/g, and average pore diameter between 3.5 and 125 nm. The specific surface area and pore size distribution of computer-generated mesoporous materials were in good agreement with experimental data reported for silica aerogels. The specific surface area and pore size distribution of computer-generated mesoporous materials were in good agreement with experimental data reported for silica aerogels. Finally, widening the particle size distribution and increasing the particle overlapping were shown to strongly decrease the specific surface area and increase the average pore size of the mesoporous structures.

2.1 Background

2.1.1 Numerically-generated mesoporous structures

Several particle aggregation models have been developed to numerically simulate the gelation process [66]. They differ mainly in the way the particle clusters grow and diffuse. For example, the monomer-cluster aggregation method consists of clusters formed from particles added one-by-one throughout the process [66]. Alternatively, the cluster-cluster aggregation method consists of a given initial number of particles moving, colliding, and forming clusters which themselves diffuse, collide, and grow [49]. The cluster-cluster aggregation method generates less compact structures (i.e., with lower fractal dimension) than the monomer-cluster method and has been reported to be more representative of the aerogel gelation process [49].

Moreover, one can distinguish diffusion-limited aggregation from reaction-limited aggregation [49]. Under diffusion-limited aggregation, the colliding clusters aggregate immediately and irreversibly upon contact [49]. By contrast, under reaction-limited aggregation, particles or clusters can collide several times before aggregating and the connection between clusters is reversible, i.e., clusters can break apart [49]. Reaction-limited aggregation is more representative of the gelation process of structures in which chemical bonds are formed after several collisions [49]. On the other hand, diffusion-limited aggregation corresponds better to the gelation of reactive specimens forming bonds after few collisions [49,67]. For example, for silica aerogel synthesis, the occurrence of bonds formation depends on the pH and solution composition [68]. At high pH, silica is very reactive and nanoparticles form bonds only after few collisions [67]. Finally, the diffusion-limited cluster-cluster aggregation (DLCCA) method has been shown to reproduce the gelation growth process and the cluster size distribution of gels [49, 67, 69].

2.1.2 Numerically-generated silica aerogels

Silica aerogels have been generated numerically as fractal structures using aggregation models to predict their morphology [70–72], physical characteristics [73,74], and thermophysical properties [75–77]. Numerically-generated silica aerogels by DLCCA method have considered point-contact structures [73,75–77] and surface-contact structures with overlapping particles [72, 74]. For example, Primera et al. [71] numerically generated 3D silica aerogel structures by the DLCCA method. The generated structures consisted either of monodisperse cubic particles less than 4 nm in size or of bimodal mixture of cubic particles of size $r_{s_1} \leq 4$ nm and $r_{s_2} = 7r_{s_1}$ nm with porosity ranging from 80 to 95%. The authors also characterized them in terms of specific surface area, average pore size, and pore size distribution.

Morales et al. [72] developed a diffusion-limited monomer-cluster aggregation algorithm to generate surface-contact silica structure with monodisperse spherical particles. The particle radius was 1.1 or 1.2 nm and the porosity ranged from 80 to 90%. The authors showed that the mechanical strength of computer-generated surface-contact silica aerogel structures agreed well with experimental measurements [74]. Similarly, Ma et al. [73] used DLCCA method to generate mesoporous silica structures and model their elastic properties using finite element method (FEM). The structures consisted of monodisperse spherical silica particles with arbitrary diameter and porosity ranging from 92 to 99%. The authors showed that increasing the aerogel density reinforced its mechanical stiffness. They also derived a scaling relation between the elastic bulk modulus and the effective density of the DLCCA silica aerogel structures.

Lallich et al. [76] used computer-generated DLCCA aggregates with point-contact spherical monodisperse particles with radius of 3.5, 4.5, and 7.25 nm and porosity around 90% to predict the extinction coefficient and scattering albedo of silica powders. Hasmy et al. [75] used computer-generated DLCCA structures with

monodisperse and polydisperse nanoparticles to characterize the X-ray scattered intensity by silica aerogels. They compared their results with experimental small-angle X-ray scattering (SAXS) measurements for structures with porosity around 95% and particle radius around 2.3 nm. They showed that the scattered X-ray intensity calculated from the DLCCA structures was in qualitative agreement with experimental measurements.

Furthermore, Zhao et al. [77] used DLCCA-generated structures with point-contact monodisperse silica nanoparticles of radius less than 2.5 nm and with porosity ranging from 85 to 98% to predict the effective thermal conductivity of silica aerogels. They used finite volume method (FVM) to solve the combined two-flux radiative transfer equation and the energy equation through the generated structures.

Finally, pore size distribution (PSD) has been previously determined numerically either from simulated nitrogen adsorption isotherms calculated by Grand Canonical Monte Carlo (GCMC) simulations [78, 79] or by a 2D triangulation method applied to 3D structures [70–72]. Unfortunately, the GCMC method is time consuming and computationally complex [78]. On the other hand, the 2D triangulation method calculates pore sizes from cross-sections of the pores. Unfortunately, the extension of the triangulation method to 3D pore volumes is far from trivial [80].

2.1.3 Experimental characterization methods

Nitrogen adsorption porosimetry is commonly used experimentally to characterize the specific surface area $A_{g,BET}$ (in m^2/g), pore size distribution (PSD), and open porosity ϕ of mesoporous materials [28, 81]. The specific surface area can be obtained by the Brunauer-Emmett-Teller (BET) method based on the expression

[81, 82]

$$A_{g,BET} = N_m N_A C_{N_2} \tag{2.1}$$

where N_A is the Avogadro constant (in mol^{-1}) and C_{N_2} is the cross-sectional area of a N_2 molecule adsorbed in a monolayer (in m^2) while N_m is the measured monolayer capacity (in mol/g), defined as the number of moles of N_2 needed to cover the surface of the pores in 1 g of porous material with a monolayer of N_2.

Moreover, the Barrett-Joyner-Halenda (BJH) method [83] is usually used to obtain the pore size distribution (PSD) of mesoporous materials. The BJH method assumes that the pores are cylindrical with diameter d_p and relies on the Kelvin equation relating the pore filling pressure to the radius of curvature of the adsorbate [84]. This estimate is then corrected for the layer of adsorbate present on the pore walls, using the measured statistical film thickness curve [85]. The BJH analysis provides (i) the incremental PSDs, i.e., the volume $V_{p,i}$ of pores having diameter between d_p and $d_p + \Delta d_p$ as a function of pore diameter d_p, and (ii) the differential PSDs, i.e., $\text{d}V_{p,cu}/\text{d}d_p$ as a function of d_p, where $V_{p,cu}$ is the cumulative pore volume of pores with diameter smaller than d_p.

The open porosity ϕ can be determined from the material bulk density ρ_s (in g/cm^3) and the measured specific pore volume v_p (in cm^3/g) as [28]

$$\phi = \frac{v_p}{\frac{1}{\rho_s} + v_p}. \tag{2.2}$$

Here, the specific pore volume v_p is the volume occupied by the pores per unit mass of mesoporous material and can be expressed as [49, 71]

$$v_p = \frac{1}{\rho_{eff}} - \frac{1}{\rho_s} \tag{2.3}$$

where ρ_{eff} is the effective density of the mesoporous material. Note that Equations (2.2) and (2.3) were obtained by ignoring the mass of air contained in the pores

($\rho_{air} \ll \rho_s$). Then, the effective density ρ_{eff} can be estimated as

$$\rho_{eff} = \rho_s(1 - \phi). \tag{2.4}$$

Experimentally, the specific pore volume v_p is estimated from the amount of nitrogen adsorbed at relative pressure $P/P_0 = 0.95$ close to saturation, i.e., when all pores are filled with N_2, where P_0 is the saturation pressure of N_2 [28]. Then, the measured v_p is used to calculate ϕ [Equation (2.2)] and ρ_{eff} [Equation (2.3)]. However, note that Equations (2.3) and (2.4) are valid when all pores are open. Finally, the average pore diameter $\bar{d}_p$ of mesoporous materials can be estimated by treating the pores as cylindrical such that [71, 86]

$$\bar{d}_p = \frac{4v_p}{A_g}. \tag{2.5}$$

Overall, although point-contact structures are easier to characterize in terms of porosity, specific surface, and average pore size, the degree of overlapping among constituent particles should be considered as an important parameter in computer-generated mesoporous structures. Unfortunately, several studies considering computer-generated surface-contact structures did not quantify the effect of particle overlapping on the specific surface area and pore size distribution of the generated structures [71–74]. In addition, the range of porosity (80-99 %) investigated was relatively limited. This study aims to numerically generate realistic mesoporous structures similar to ambigels and aerogels using the DLCCA method for a wide range of particle radius between 2.5 and 40 nm and porosity between 35 and 95%. It also aims to characterize these structures in terms of specific surface area A_g, total porosity ϕ, average pore diameter $\bar{d}_p$, and incremental, cumulative, and differential PSDs. A new algorithm reproducing experimental gas adsorption porosimetry measurements and BJH analysis is proposed to obtain the PSD of the computer-generated mesoporous materials. Particular attention was paid to

the effect of particle overlapping and polydispersity on the structural properties.

2.2 Analysis

2.2.1 Aerogel and ambigel structure generation

The DLCCA method was used to generate aerogel and ambigel structures represented as fractal aggregates of monodisperse or polydisperse nanoparticles. This method was chosen because it can reproduce the gelation growth process and the geometry of the gel structure [49, 67, 69], as previously discussed. The input parameters of the DLCCA method were (i) the initial number of monodisperse nanoparticles N_t, (ii) their radius r_s, (iii) the final number of clusters n_c, and (iv) the dimension L of the cubic simulation domain. The DLCCA algorithm created the structures in four steps: (1) the N_t particles were randomly dispersed in a LxLxL cubic simulation domain. (2) Randomly selected particles or clusters were set in motion in random directions by an incremental and arbitrary traveling distance l_s until they collided with another particle or cluster. (3) If the interparticle distance d, defined as the distance between the centers of two adjacents particles, was equal or smaller than the particle diameter, the particles merged into one cluster that continued moving as a whole in subsequent iterations. (4) The above process was repeated until the number of clusters decreased to a predefined final number of clusters n_c. Periodic boundary conditions were adopted to prevent particles or clusters from exiting the simulation domain.

Two types of nanostructures with monodisperse nanoparticles were generated namely (i) point-contact structures where particles touched at a point but did not overlap and (ii) surface-contact structures consisting of overlapping spherical particles. These two types of structures were denoted by the subscript "PC" and "SC", respectively. To generate point-contact structures, the interparticle distance d was calculated after each collision. If the interparticle distance d was

smaller than $2r_s$, the moving particle or cluster was stepped back in the opposite direction to a new position such that $d = 2r_s$. The distance between adjacent particles was calculated again and if two adjacent particles were still overlapping, they were removed. The fraction of particles removed over the initial number of particles N_t increased with decreasing porosity ϕ and ranged from 11 to 71% as the porosity ϕ decreased from 95 to 50%. Therefore, in point-contact structures, the final total number of particles N_s was less than the initial number of particles N_t while $N_s = N_t$ for surface-contact structures. The porosity ϕ of the final structure was varied between 35 and 95% by decreasing the number of particles N_t. The final number of clusters n_c was set to be less than 2% of the total number of particles N_t. The length L of the simulated cubic domain was set to $L = 40r_s$ to ensure that the computational domain was sufficiently large to be considered a representative elementary volume of mesoporous material. Here, the particle radius r_s ranged from 2.5 to 40 nm and N_s between 750 and 15,000.

Mesoporous structures with surface-contact consisting of polydisperse nanoparticles were also generated and characterized. To do so, the DLCCA algorithm was first used to generate surface-contact structures with monodisperse particles. Then, the radius of randomly selected particles was modified so as to follow a Gaussian distribution $f(r_s)$ given by

$$f(r_s) = \frac{1}{s\sqrt{2\pi}} \exp\left[-\frac{(r_s - \bar{r}_s)^2}{2s^2}\right] \tag{2.6}$$

where $\bar{r}_s$ is the mean particle radius (in nm), and s is the associated standard deviation (in nm). The particle radius was limited to the range $\bar{r}_s - 2s \leq r_s \leq \bar{r}_s + 2s$. Finally, to facilitate comparison with structures consisting of monodisperse spheres, the average radius $\bar{r}_s$ was taken as 2.5, 5, and 10 nm while the standard deviation was taken as either $s = \bar{r}_s/2.5$ or $\bar{r}_s/5$. Here, porosity ϕ varied between 60 and 95% for N_s ranging from 6900 to 800, respectively.

2.2.2 Structural characterization - monodisperse nanoparticles

Overlapping distance

Let us define the interparticle distance d in computer-generated mesoporous structures with monodisperse nanoparticles as the distance between the center of two adjacent particles. Then, the overlapping distance can be expressed as $l_o = 2r_s - d$, as illustrated in Figure 2.1(a). The average interparticle distance among all overlapping particles in the aggregate is denoted by $\bar{d}$ and the dimensionless average interparticle distance can be defined as $\bar{d}^* = \bar{d}/2r_s$. For point-contact structures, d^* is such that $\bar{d}^* = \bar{d}/2r_s = 1$ while that of surface-contact structures is such that $\bar{d}^* < 1$. Similarly, the dimensionless average overlapping distance of surface-contact structures can be defined as $\bar{l}_o^* = \bar{l}_o/2r_s = 1 - \bar{d}/2r_s$ and ranged between 0 and 1. For surface-contact structures, the distance l_s traveled incrementally by particles or clusters during DLCCA structure generation may affect $\bar{d}$ and $\bar{l}_o$. Specifically, $\bar{d}$ was found to increase with decreasing l_s but remained unchanged for $l_s \leq r_s/2.5$ for $r_s = 2.5$ nm and $\phi = 50$ and 95%. Thus, the traveling distance was set to $l_s = r_s/2.5$ to obtain a structure independent of the numerical parameter l_s, i.e., to achieve a numerically-converged structure. The dimensionless average overlapping distance $\bar{l}_o^*$ and the fraction of overlapping particles among the N_s particles in the structure were computed for the generated surface-contact structures. Here, the porosity ranged between 35 and 95% and the particle radius was taken as $r_s = 2.5$, 5, and 10 nm.

Porosity, specific surface area, and interfacial area concentration

For point-contact structures with monodisperse spherical particles of radius r_s, porosity ϕ, specific surface area $A_{g,PC}$ (in m^2/g), and interfacial area concentration

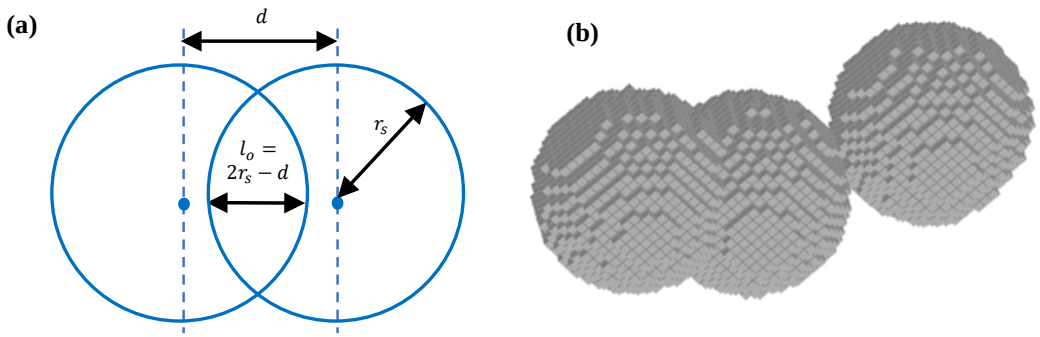

Figure 2.1: (a) Illustration of the overlapping distance $l_o = 2r_s - d$ and (b) example of cube discretization of a surface-contact cluster numerically generated by DLCCA for porosity ϕ and specific surface area A_g calculations.

or surface area per unit volume $A_{i,PC}$ (in m^{-1}) can be expressed as [49, 68]

$$\phi = \frac{V_0}{L^3} = 1 - f_v = 1 - \frac{4\pi N_s r_s^3}{3L^3}, \quad A_{g,PC} = \frac{3}{\rho_s r_s}, \quad \text{and} \quad A_{i,PC} = A_{g,PC}\rho_s f_v. \tag{2.7}$$

Here, V_0 is the total pore volume of the structure, f_v is the volume fraction of the simulation cell occupied by the particles, and ρ_s is the density of the spherical particles. For the purpose of illustration and comparison with experimental data, ρ_s was taken as the density of bulk silica, i.e., $\rho_s = 2.2$ g/cm^3 [68].

For surface-contact structures with monodisperse particles, f_v, ϕ, $A_{g,SC}$, and $A_{i,SC}$ were calculated numerically by discretizing the particles into small cubes of side Δx, as illustrated in Figure 2.1(b). The particle volume fraction f_v was calculated by adding the volume Δx^3 of all cubes located inside the N_s particles. Note that when two adjacent particles overlapped, the cubes contained in both particles were not double-counted. Moreover, the specific surface area $A_{g,SC}$ was estimated by adding up surface areas of the cubes' faces S_{ij} located at the surface of the particles according to

$$A_{g,SC} = \frac{S_0}{\rho_s V_c} = \frac{\sum_{i=1}^{N_s}\sum_{j=1}^{6N_{c,i}} S_{ij}}{\rho_s V_c}. \tag{2.8}$$

Here, S_0 is the total internal surface area of the porous structure, $N_{c,i}$ is the number of cubes of volume Δx^3 inside particle i, V_c is the volume occupied by all cubes (i.e., $V_c = f_v L^3$), and j denotes the surfaces of cubes located in particle i. If the surface next to surface j in particle i was in contact with another cube then $S_{ij} = 0$, otherwise surface j was located at the surface of the particle i so that $S_{ij} = \Delta x^2$. Finally, the expression for interfacial area concentration $A_{i,PC}$ for point-contact structures given by Equation (2.7) was also valid for surface-contact structures with either monodisperse or polydisperse particles.

The algorithm for computing particle volume fraction, porosity, and specific surface area by numerical discretization was first validated with one particle of radius $r_s = 4$ nm set in a cubic simulation domain of length $L = 10$ nm corresponding to porosity $\phi = 73.2\%$ and specific surface area $A_g = 340.9$ m^2/g. The method was further validated with a structure consisting of two overlapping particles with $r_s = 2$ nm, $L = 6$ nm, and $d = 2$ nm corresponding to porosity $\phi = 73.8\%$ and specific surface area $A_g = 597.3$ m^2/g (see Table A.1 in Supporting Information). The volume fraction f_v, porosity ϕ, and specific surface area A_g were found to be independent of the discretization Δx for $\Delta x/r_s \leq 0.04$ when the results were numerically converged. In addition, the porosity ϕ and specific surface area $A_{g,PC}$ for point-contact structures generated by DLCCA method were also computed numerically with the above-described discretization method. Results for f_v and $A_{g,PC}$ calculated by numerical discretization fell within 5% of predictions by exact analytical expressions [Equation (2.7)] further confirming the validity of the algorithm.

Finally, dimensionless average overlapping distance $\bar{l}_o^*$, porosity ϕ, specific surface area A_g, and interfacial area concentration A_i reported in the present study correspond to the average of at least three computer-generated structures. The associated relative standard deviations were shown in the plots only when they were larger than the symbols. Similarly, error bars were represented for experimental

data retrieved from the literature (Refs. [4–8]) whenever they were reported.

Pore size distributions

The pore size distribution was calculated in three steps. First, the computer-generated mesoporous structure was iteratively filled with "adsorbate" layers of thickness Δt to mimic N_2-adsorption porosimetry measurements. At each iteration i, the total volume V_i of unfilled space in the pores and the total surface area S_i of the interface between the "adsorbate" layer and the unfilled space were computed. Second, the data for the volumes $(V_i)_{0\leq i\leq N}$ and surface areas $(S_i)_{0\leq i\leq N}$ were analyzed with an algorithm based on the BJH method [83] to calculate the volumes $(V_{p,i})_{0\leq i\leq N-1}$ of pores with diameter $\bar{d}_{p,i}$. Third, the incremental $V_{p,i}$, cumulative $V_{p,cu}$, and differential $\mathrm{d}V_{p,cu}/\mathrm{d}d_p$ pore size distributions were calculated.

The initial pore volume $V_0 = \phi L^3$ (in m^3) and interfacial surface area $S_0 = A_g \rho_s V_c$ (in m^2) of the as-generated structure (i.e., without "adsorbate") were calculated using the discretization method discussed previously. Then, at iteration $i = 1$, the particle radius was enlarged by a thickness Δt representing the thickness of a monolayer of "adsorbate". The total volume of unfilled space in the pores V_1 (in m^3) and the total surface area of the interface between the "adsorbate" layer and the unfilled space S_1 (in m^2) were calculated using the same discretization method. This procedure was repeated iteratively for $i > 1$ to yield $(V_i)_{1\leq i\leq N}$ and $(S_i)_{1\leq i\leq N}$ corresponding to an "adsorbate" layer thickness $t_i = i\Delta t$. After the last iteration $i = N$, all pores were filled with "adsorbate", i.e., $V_N = 0$ m^3 and $S_N = 0$ m^2.

Once the dataset for $(V_i)_{0\leq i\leq N}$ and $(S_i)_{0\leq i\leq N}$ was generated, it was analyzed based on the BJH method [83]. Between steps $N-1$ and N, the "adsorbate" layer thickness was increased from t_{N-1} to t_N, thus completely filling the largest pores. Therefore, the largest pores had diameter between $d_{p,N-1} = 2t_{N-1}$ and $d_{p,N} = 2t_N$

(see Figure 2.2) and the average pore diameter $\bar{d}_{p,N-1}$ of the largest pores can be approximated as

$$\bar{d}_{p,N-1} = \frac{d_{p,N-1} + d_{p,N}}{2}. \tag{2.9}$$

The volume V_{N-1} and surface area S_{N-1} corresponded to the total volume and surface area of the unfilled space in the largest pores, i.e., the pores with diameter between $d_{p,N-1}$ and $d_{p,N}$. Assuming that this unfilled space in the largest pores at iteration $N-1$ had cylindrical geometry, its average diameter $\bar{d}_{N-1}$ can be expressed as

$$\bar{d}_{N-1} = \frac{4V_{N-1}}{S_{N-1}}. \tag{2.10}$$

Then, from geometric considerations (see Figure 2.2), the volume $V_{p,N-1}$ and the surface area $S_{p,N-1}$ of the largest pores with average pore diameter $\bar{d}_{p,N-1}$ can be related to the dimensions of the unfilled space according to

$$\frac{V_{p,N-1}}{V_{N-1}} = \left(\frac{\bar{d}_{p,N-1}}{\bar{d}_{N-1}}\right)^2 \quad \text{and} \quad \frac{S_{p,N-1}}{S_{N-1}} = \frac{\bar{d}_{p,N-1}}{\bar{d}_{N-1}}. \tag{2.11}$$

Subsequent volume $V_{p,i}$ and surface area $S_{p,i}$ of smaller pores filled between iterations i and $i+1$ were calculated using the same method. However, the unfilled space volume V_i and surface area S_i at iteration i had to be corrected for the contribution of larger pores whose average diameter $\bar{d}_{p,i+1}$ has already been estimated, as illustrated in Figure 2.2. Specifically, the volume V_i was corrected for the volume of unfilled space in pores contained in the pores with diameter larger than $d_{p,i+1}$ already accounted for to yield

$$V_i^* = V_i - V_{i+1} - \Delta t \sum_{j=i+1}^{N-1} S_{p,j} \left(\frac{\bar{d}_{p,j} - 2\bar{t}_i}{\bar{d}_{p,j}}\right) \tag{2.12}$$

where $\bar{t}_i = (t_i + t_{i+1})/2 = i\Delta t + \Delta t/2$ is the average "adsorbate" layer thickness between steps i and $i+1$. Here, V_{i+1} represents the total volume of unfilled space in the pores with diameter larger than $d_{p,i+1}$ when the "adsorbate" layer thickness

was t_{i+1}. The third term on the right hand side of Equation (2.12) represents the volume of unfilled space created in these pores when the "adsorbate" layer thickness was reduced from t_{i+1} to t_i. Similarly, the corrected surface area S_i^* can be expressed as

$$S_i^* = S_i - \sum_{j=i+1}^{N-1} S_{p,j} \left(\frac{\bar{d}_{p,j} - 2t_i}{\bar{d}_{p,j}} \right). \tag{2.13}$$

The general expressions for $\bar{d}_i$, $V_{p,i}$, and $S_{p,i}$ assuming cylindrical geometry of the unfilled spaces and pores were

$$\bar{d}_i = 4\frac{V_i^*}{S_i^*}, \quad \frac{V_{p,i}}{V_i^*} = \left(\frac{\bar{d}_{p,i}}{\bar{d}_i} \right)^2, \quad \text{and} \quad \frac{S_{p,i}}{S_i^*} = \frac{\bar{d}_{p,i}}{\bar{d}_i} \tag{2.14}$$

where $\bar{d}_{p,i} = (2i{+}1)\Delta t$. Note that $V_{p,i}$, and $S_{p,i}$ were constrained to non-negative values.

Then, the cumulative $V_{p,cu}(\bar{d}_{p,i})$ and total $V_{p,tot}$ pore volumes were calculated according to

$$V_{p,cu}(\bar{d}_{p,i}) = \sum_{j=0}^{i} V_{p,j} \quad \text{and} \quad V_{p,tot} = \sum_{j=0}^{N-1} V_{p,j}. \tag{2.15}$$

The differential pore size distribution was then calculated by interpolating the cumulative pore volume $V_{p,cu}(\bar{d}_{p,i})$ as a function of the average pore diameter $\bar{d}_{p,i}$ with a cubic spline to obtain a continuous function $V_{p,cu}(d_p)$ and its derivative $\mathrm{d}V_{p,cu}/\mathrm{d}d_p$. Finally, the normalized pore size distribution was calculated by dividing the differential PSD by $V_{p,tot}$ to obtain the probability distribution expressed as

$$f(d_p) = \frac{1}{V_{p,tot}} \frac{\mathrm{d}V_{p,cu}}{\mathrm{d}d_p}. \tag{2.16}$$

The PSD calculation algorithm was validated with ideal structures made with one to several pores with cylindrical, cubic, or spherical shapes (see Figures A.2 and A.3 in Supporting Information). In addition, the effect of numerical uncer-

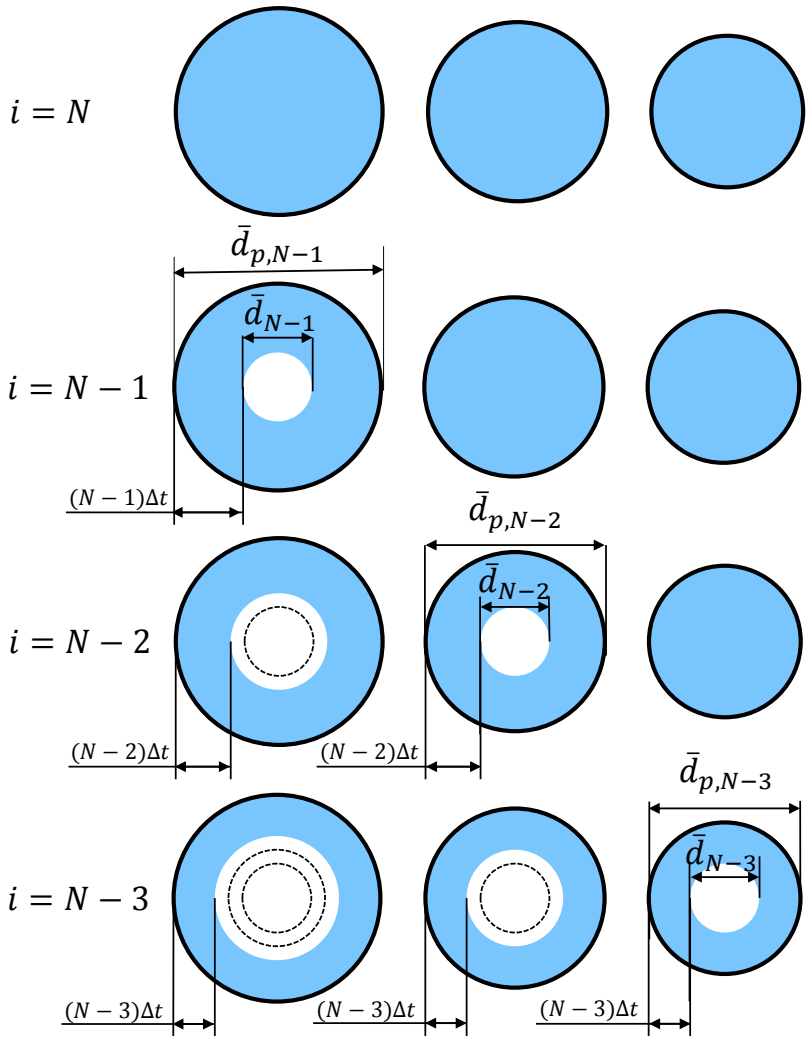

Figure 2.2: Schematic representation of the adsorption process and change in "adsorbate" layer thickness between steps $N-3$ and N (relative dimensions not to scale).

tainties on the apparent pore volume V_i and apparent surface area S_i was studied. Random errors within 3% of the exact values of V_i and S_i did not significantly affect the predicted PSDs. This PSD algorithm was applied to the numerically generated structures of particle radius $r_s = 2.5$ nm and porosity ranging from 40 to 80%. Note that when the porosity increased, large pores located at the surface of the simulation domain were more likely to be cut and considered smaller than they really were. Here, numerical convergence also depended on the ratio $\Delta t/\Delta x$ and this ratio was increased with increasing porosity. Table 2.1 summarizes the

increment of the "adsorbate" layer thickness Δt and the discretization cube size Δx used for each porosity. Table 2.1 also features the relative error $\delta V_{p,tot}$ in calculations of the total pore volume obtained either from porosity calculations or from pore size distribution defined as

$$\delta V_{p,tot} = \frac{\phi L^3 - V_{p,tot}}{\phi L^3}. \tag{2.17}$$

The relative error $\delta V_{p,tot}$ was less than 6% for porosity $\phi = 39.6$, 50.1, and 60.5%, and reached up to 15.2% for $\phi = 79.1\%$. The relative error $\delta V_{p,tot}$ of the computer-generated structures was comparable to the relative error $\delta V_{p,tot}$ calculated for the ideal structures used for validation. In addition, experimental measurements feature uncertainty within 5%, thus confirming the validity of the algorithm. The relative error was mainly due to the assumption of cylindrical pores which is not satisfied by actual silica aerogels and ambigels nor by computer-generated structures.

Finally, the average diameter $\bar{d}_{p,PSD}$ of the PSDs was calculated from the PSD according to

$$\bar{d}_{p,PSD} = \int_0^\infty d_p f(d_p) \mathrm{d}d_p. \tag{2.18}$$

The results could be compared with the average pore diameter $\bar{d}_{p,PC}$ for point-contact structures with monodisperse particles of radius r_s derived by combining Equations (2.3), (2.5), and (2.7) to yield [49]

$$\bar{d}_{p,PC} = \frac{4r_s}{3}\frac{\phi}{1-\phi}. \tag{2.19}$$

2.2.3 Structural characterization - polydisperse nanoparticles

The fraction of overlapping particles and the dimensionless average overlapping distance $\bar{l}_o^*$ were also computed for surface-contact structures with polydisperse

Table 2.1: "Adsorbate" layer thickness Δt, cube size Δx, relative total pore volume error $\delta V_{p,tot}$, specific surface area $A_{g,SC}$, pore diameter range, and average pore diameters $\bar{d}_p$ [Equation (2.5)] and $\bar{d}_{p,PSD}$ [Equation (2.18)] of the PSDs of surface-contact structures with monodisperse particles of radius $r_s = 2.5$ nm.

	$\phi = 39.6\%$	$\phi = 50.1\%$	$\phi = 60.5\%$	$\phi = 79.1\%$
$\boldsymbol{\Delta t}$ **(nm)**	0.1	0.2	0.25	0.5
$\boldsymbol{\Delta x}$ **(nm)**	0.10	0.09	0.09	0.09
$\boldsymbol{\Delta t/\Delta x}$	1.0	2.22	2.78	5.55
$\boldsymbol{\delta V_{p,tot}}$	0.90%	2.57%	5.04%	15.20%
$\boldsymbol{A_{g,SC}}$ **(m²/g)**	330	362	406	479
Pore diameter range (nm)	1.5 - 9.3	2.2 -11.8	2.8 - 19.3	5.5 - 27.5
$\boldsymbol{\bar{d}_p}$ **(nm)**	3.6	5.0	6.9	14.4
$\boldsymbol{\bar{d}_{p,PSD}}$ **(nm)**	3.8	4.8	6.0	9.5

nanoparticles. The dimensionless overlapping distance between two adjacent overlapping particles "j" and "k" in surface-contact structures was defined as $l_o^* = 1 - d_{jk}/(r_{s,j} + r_{s,k})$ where $r_{s,j}$ and $r_{s,k}$ are the radius of the particles and $d_{jk}/(r_{s,j} + r_{s,k})$ is the dimensionless interparticle distance between the particles. The dimensionless average overlapping distance $\bar{l}_o^*$ was then obtained by averaging all computed values of l_o^*. The porosity ϕ of surface-contact structures with polydisperse nanoparticles was calculated using the discretization method detailed previously. Similarly, their specific surface area $A_{g,SC}$ can be calculated in the same manner as for monodisperse structures using Equation (2.8). In addition, Equations (2.5) and (2.7) are still valid for surface-contact structures with polydisperse nanoparticles and can be used to determine A_i and $\bar{d}_p$, respectively.

2.3 Results and discussion

2.3.1 Aerogel and ambigel structures

Figure 2.3 shows examples of surface-contact structures numerically generated by the DLCCA method consisting of monodisperse particles and featuring porosity ϕ of (a) 50.5, (b) 70.4, and (c) 90.5%. For the three illustrated structures, the

final number of clusters was $n_c = 10$, and the total particle number N_s varied from 11,800 to 1,549. Figure 2.3(d) shows details of a computer-generated high-porosity surface-contact structure with overlapping particles. It resembles the structure of actual silica aerogels observed in the TEM image of Figure 1.1(a).

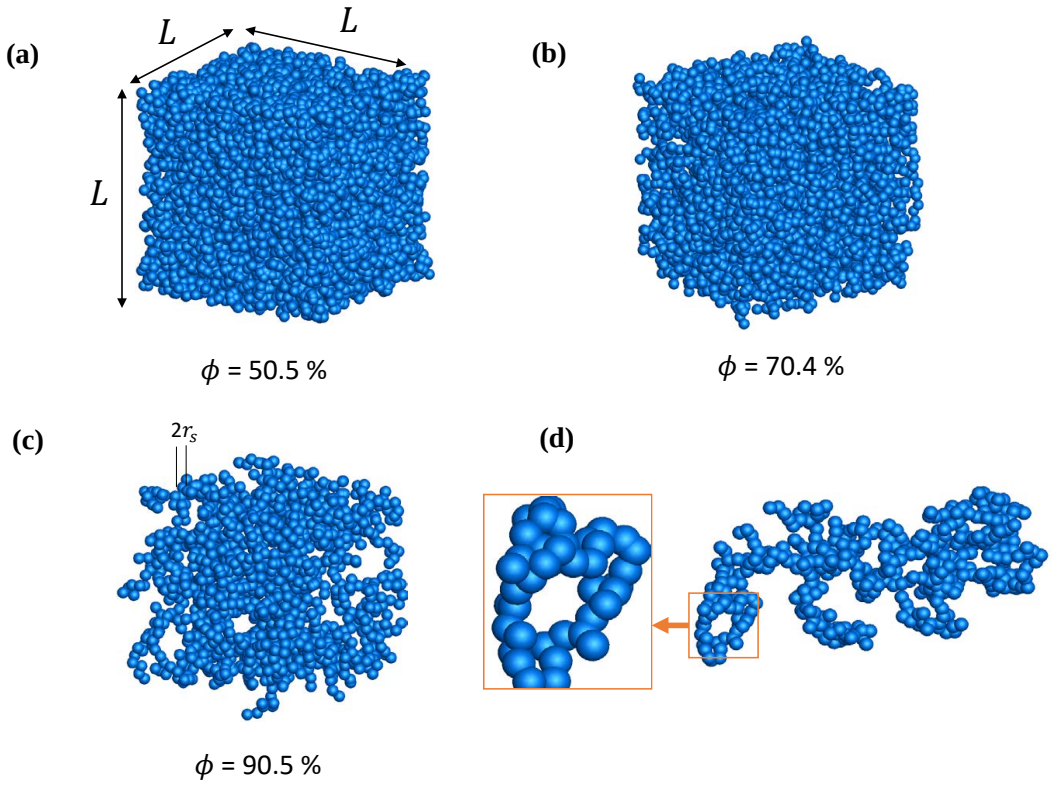

Figure 2.3: Illustrations of surface-contact structures obtained by DLCCA simulations for (a) $\phi = 50.5\%$, (b) $\phi = 70.4\%$, (c) $\phi = 90.5\%$, and (d) zoom-in of a high-porosity computer-generated surface-contact aerogel structure.

2.3.2 Structural characterization - monodisperse nanoparticles

Overlapping distance

Figure 2.4 shows the dimensionless average overlapping distance $\bar{l}_o^* = 1 - \bar{d}/2r_s$ for surface-contact structures with monodisperse nanoparticles as a function of particle volume fraction f_v for particle radius $r_s = 2.5$, 5, and 10 nm. It indicates

that the dimensionless average overlapping distance $\bar{l}_o^*$ increased with particle volume fraction f_v. In other words, the particles overlapped more with decreasing porosity $\phi = 1 - f_v$. This was consistent with experimental observations for denser aerogels obtained wia sintering and featuring lower porosity and larger particle coalescence [7, 49, 87, 88]. It is also interesting to note that the dimensionless average overlapping distance $\bar{l}_o^*$ was independent of the particle radius r_s. Figure

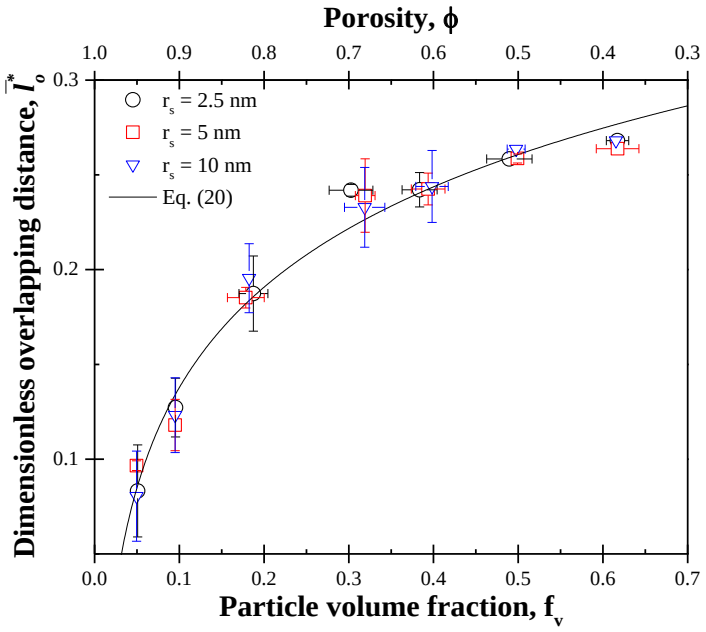

Figure 2.4: Computed dimensionless average overlapping distance $\bar{l}_o^* = 1 - \bar{d}/2r_s$ of an aggregate as a function of particle volume fraction f_v and porosity ϕ for r_s = 2.5, 5, and 10 nm, along with least-square fit given by Equation (2.20).

2.4 also shows a logarithmic fit ($R^2 = 0.98$) of all data points given by

$$\bar{l}_o^* = 0.076\ln(1-\phi) + 0.31 \tag{2.20}$$

where porosity ϕ varied between 35 and 95%, i.e., particle volume fraction f_v ranged between 5 and 65%. Finally, note that more than 99% of the particles in the nanostructures overlapped with other particles for porosity ranging from 60 to 90% and for all radius r_s considered.

Specific surface area and interfacial area concentration

Figure 2.5 shows (a) the specific surface area A_g and (b) the interfacial area concentration A_i as functions of porosity ϕ computed for both point-contact and surface-contact aerogel structures consisting of monodisperse particles. It indicates that the specific surface area $A_{g,PC}$ for point-contact structures computed using Equation (2.8) was in excellent agreement with the theoretical predictions of Equation (2.7). Consequently, good agreement was also observed for $A_{i,PC} = A_{g,PC}\rho_s(1-\phi)$. The specific surface area $A_{g,PC}$ depended only on the particle radius r_s and was independent of porosity ϕ. On the other hand, the interfacial area concentration $A_{i,PC}$ was linearly proportional to porosity ϕ and decreased with increasing particle radius r_s.

Moreover, for surface-contact structures, the specific surface area $A_{g,SC}$ [Equation (2.8)] was systematically lower than that of point-contact structures $A_{g,PC}$ for a given particle radius r_s. Furthermore, $A_{g,SC}$ increased with increasing porosity ϕ, i.e., with decreasing dimensionless average overlapping distance $\bar{l}_o^*$. This suggests that surface-contact structures with higher particle overlap (or coalescence) had lower specific surface area, in agreement with previous studies [68]. Indeed, Iler [68] reported that the theoretical specific surface area $A_{g,PC}$ [Equation (2.7)] was greater than the experimentally measured specific surface area $A_{g,BET}$ of silica aerogels in which the particles were "cemented together". The author detailed that the ratio of the theoretical point-contact and experimental BET specific surface areas $A_{g,PC}/A_{g,BET}$ was greater than 1.1 for silica aerogels featuring strong coalescence between the particles [68]. This ratio was used as an indication of the interparticle overlapping. In the present study, the ratio of the theoretical point-contact to the computed surface-contact specific surface area $A_{g,PC}/A_{g,SC}$, varied from 1.05 to 1.77 as the porosity ϕ decreased from 95 to 40% and the dimensionless average overlapping distance $\bar{l}_o^*$ increased from 0.05 to 0.27. The

specific surface areas $A_{g,SC}$ and $A_{g,PC}$ were found to be related by the following simple ad hoc expression

$$A_{g,SC}(r_s, \phi) = [(1 - \bar{l}_o^*)(\phi - 1) + 1]A_{g,PC}(r_s) \tag{2.21}$$

where $\bar{l}_o^*(\phi)$ was predicted by Equation (2.20). Equation (2.21) was derived to satisfy the following observations: (i) the upper bound of $A_{g,SC}$ as ϕ tended to 100% was $A_{g,PC}$, (ii) overlapping reduced the specific surface area, and (iii) $A_{g,SC}$ increases linearly with porosity ϕ. Figure 2.5(a) indicates that predictions by Equation (2.21) combined with Equation (2.7) for $A_{g,PC}$ and Equation (2.20) for $\bar{l}_o^*$ agreed well with numerical results.

Finally, Figure 2.5 shows measurements of $A_{g,BET}$ reported in the literature [4,5] for silica aerogels and ambigels with porosity ϕ between 76 ± 5 and $92 \pm 5\%$ and particle radius r_s between 1.4 ± 0.05 and 3 ± 0.05 nm. The measured specific surface area $A_{g,BET}$ fell between $A_{g,SC}$ and $A_{g,PC}$. In fact, it was systematically smaller than or equal to the theoretical specific surface area $A_{g,PC}$ for a given particle radius r_s. Therefore, the experimental data was consistent with the fact that $A_{g,PC}(r_s)$ corresponds to the maximum specific surface area for a structure with dense particles of radius r_s, as previously discussed.

Figure 2.6 shows the computed specific surface areas $A_{g,PC}$ and $A_{g,SC}$ as functions of particle radius r_s for point-contact structures and surface-contact structures with monodisperse nanoparticles and porosity $\phi = 40\%$. It also shows predictions of (i) $A_{g,PC}$ by Equation (2.7) for point-contact structures and (ii) $A_{g,SC}$ by Equation (2.21) for surface-contact structures corresponding to $\phi = 40\%$ and a dimensionless average overlapping distance $\bar{l}_o^* = 0.27$ (Figure 2.4). First, Figure 2.6 indicates that the specific surface area $A_{g,PC}$ decreased with increasing particle radius r_s and was in excellent agreement with predictions by Equation (2.7), as previously mentioned. Similarly, the specific surface area $A_{g,SC}$ of surface-contact

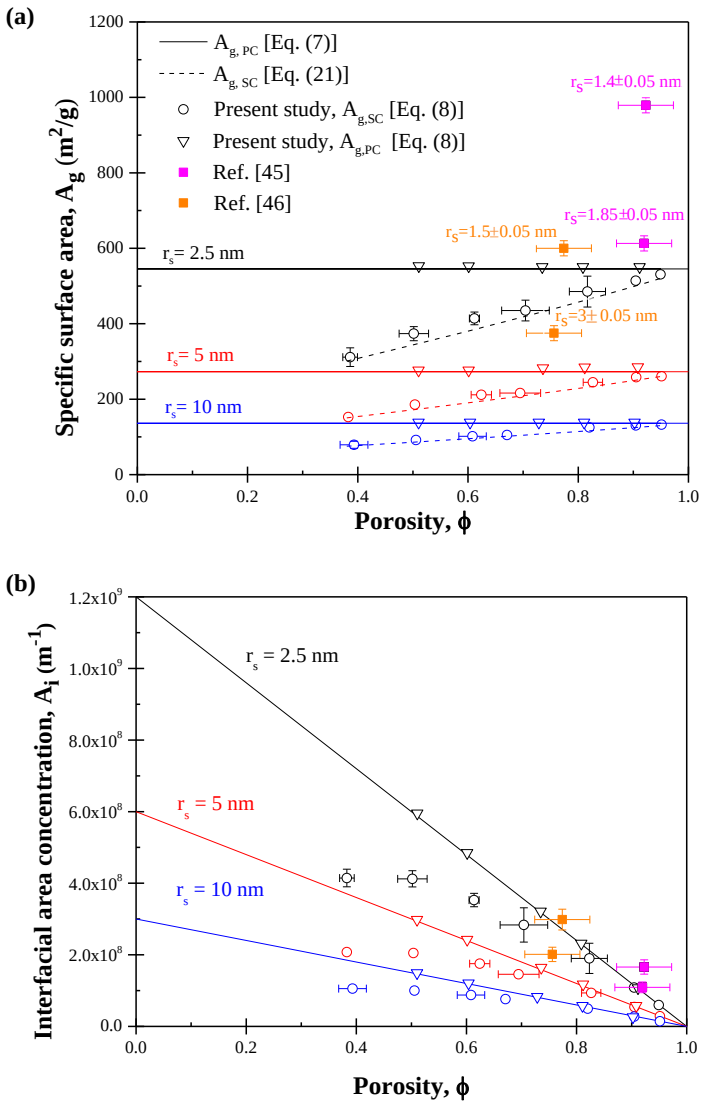

Figure 2.5: Computed (a) specific surface area A_g (in m^2/g) and (b) interfacial area concentration A_i (in m^{-1}) of point-contact and surface-contact structures as functions of porosity ϕ for monodisperse spheres of radius $r_s = 2.5$, 5, and 10 nm, along with predictions by Equations (2.7) and (2.21), and experimental data from Refs. [4, 5].

structures decreased with decreasing r_s and differed by less than 3% with predictions by Equation (2.21). Figure 2.6 also features experimental data $A_{g,BET}$ reported in the literature for silica aerogels [4] and ambigels [5, 6]. It is interest-

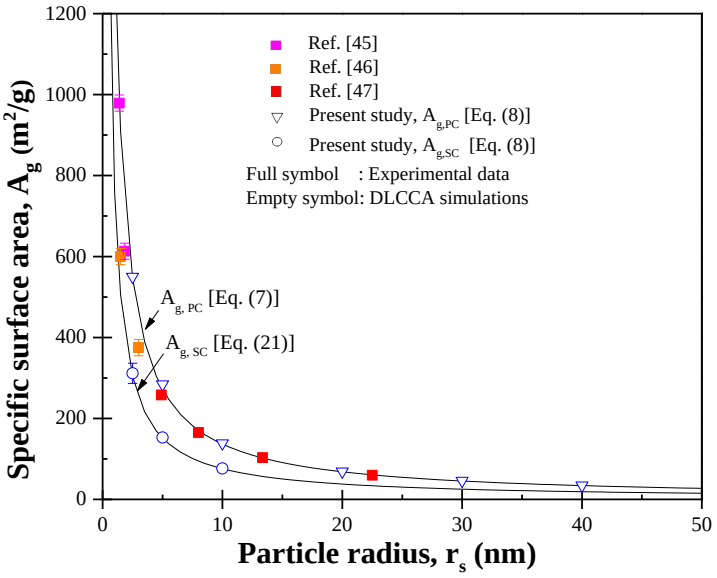

Figure 2.6: Computed specific surface area A_g (in m^2/g) of point-contact and surface-contact structures with monodisperse nanoparticles as a function of particle radius r_s, along with predictions by Equations (2.7) and (2.21) with $\bar{l}_o^* = 0.27$ for $\phi = 40\%$, as well as experimental data from Refs. [4–6].

ing to note that, here also, experimental data for $A_{g,BET}$ fell between predictions for point-contact structures $A_{g,PC}$ and computational results for surface-contact structures $A_{g,SC}$.

Figure 2.7 plots the specific surface area A_g as a function of porosity ϕ measured experimentally for sintered silica aerogels [7] and computed for surface-contact structures $A_{g,SC}$ [Equation (2.21)] with an overlapping distance l_o^* estimated using Equation (2.20). It indicates that $A_{g,SC}$ increased with increasing porosity ϕ. These results were consistent with other experimental data for sintered silica ambigels and aerogels [89,90]. Moreover, predictions by Equation (2.21) were in very good agreement with experimental measurements for $\phi < 80\%$. However, for $\phi > 80\%$, discrepancies were apparent and likely due to the reported average particle radius which corresponded to that of the "secondary particles", i.e., the particles resulting from the agglomeration of primary particles [91]. For larger

porosities, such secondary particles were porous and micropores contributed to the surface area [91]. However, these micropores were ignored in the simulations and collapsed during the sintering process as the porosity decreased [7].

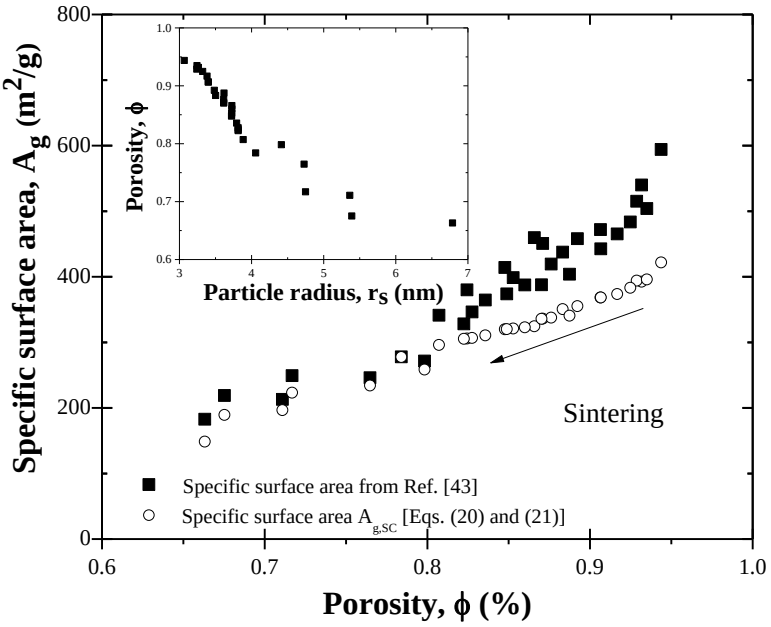

Figure 2.7: Comparison between the specific surface area A_g of sintered silica aerogels from Ref. [7] and the specific surface area $A_{g,SC}$ calculated from Equations (2.20) and (2.21) for aerogels with monodisperse overlapping spherical particles as functions of porosity ϕ. Inset: porosity ϕ of the sintered silica aerogels from Ref. [7] as a function of average particle radius r_s.

Overall, the measured specific surface area $A_{g,BET}$ of aerogels can be used to provide information on the primary particle radius r_s and interparticle coalescence. Indeed, the specific surface area of point-contact structures $A_{g,PC}(r_s)$ represents the maximum specific surface area for structures with monodisperse particle of radius r_s. Thus, an upper limit of the silica aerogel's particle radius can be determined from the measured $A_{g,BET}$ based on Equation (2.7). In addition, a more precise estimate of the particle radius could be determined if the average overlapping distance $\bar{l}_o^*$ of the aggregate was also known. The latter could be inferred from Equation (2.20) and porosity measurement. Finally, the specific surface area is also an indication of the interparticle coalescence such that a ra-

tio $A_{g,PC}/A_{g,BET} \sim 1$ indicates little coalescence (i.e., overlapping) while a ratio $A_{g,PC}/A_{g,BET} > 1.1$ indicates strong coalescence between the particles [68].

Pore size distributions

Figure 2.8 shows (a) the normalized cumulative pore volume $V_{p,cu}/V_{p,tot}$ and (b) the differential pore size distribution $f(d_p)$, obtained by the algorithm previously described, for computer-generated surface-contact structures with monodisperse particles of radius $r_s = 2.5$ nm and porosity ϕ ranging from 40 to 80%. Table 2.1 summarizes the range of pore size and the average pore diameter $\bar{d}_{p,PSD}$ obtained from the differential PSDs [Equation (2.18)] with porosity ϕ between 40 and 80%. Figure 2.8 indicates that the structures with lower porosity ϕ featured smaller pores and narrower pore size distribution. For example, Table 2.1 indicates that the pore diameter d_p ranged (i) from 1.5 to 9.3 nm for porosity $\phi = 39.6\%$, and (ii) from 5.5 to 27.5 nm for porosity $\phi = 79.1\%$. In addition, Figure 2.8(a) plots experimental PSDs for silica ambigels and aerogel with porosity $\phi = 41$, 42, 54, and 80% reported by Harreld et al. [8]. It indicates that the numerically predicted PSDs were in good agreement with experimental measurements. Note that the particle radius r_s of the synthesized mesoporous silica was not reported [8]. However, the measured specific surface area $A_{g,BET}$ for the four silica ambigels and aerogels considered was larger than $A_{g,PC}(r_s = 5$ nm) predicted by Equation (2.7), indicating that, experimentally, the silica nanoparticles were smaller than 5 nm.

Table 2.1 shows that the average pore diameter $\bar{d}_{p,PSD}$ of computer-generated structures ranged from 3.8 to 9.5 nm for porosity ϕ ranging from 39.6 to 79.1%. These results were also in good agreement with experimental measurements for silica ambigels and aerogels with porosity between 41 and 80% reported in Ref. [44].

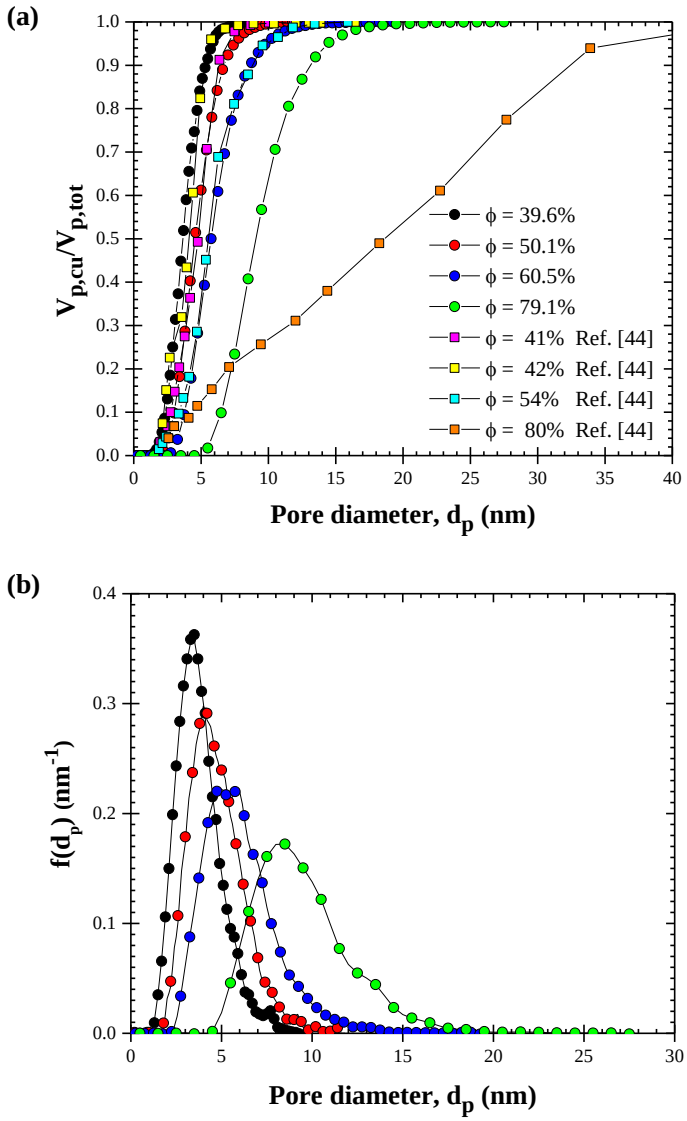

Figure 2.8: (a) Normalized cumulative pore volume $V_{p,cu}/V_{p,tot}$ and (b) differential PSDs $f(d_p)$ of computer-generated surface-contact structures with monodisperse particle radius $r_s = 2.5$ nm and porosity ranging from 39.6 to 89.1% along with experimental measurements from Ref. [8].

Average pore diameter

Figure 2.9 shows the average pore diameter $\bar{d}_p$, estimated by Equation (2.5), (a) as a function of the particle radius r_s for $\phi = 50$ and 80%, and (b) as a function

of porosity ϕ for r_s = 2.5, 5, and 10 nm for computer-generated point-contact and surface-contact structures consisting of monodisperse spheres. It also plots predictions of $\bar{d}_{p,PC}$ by Equation (2.19) and experimental data for silica aerogels reported in the literature for silica aerogels with porosity ϕ around 80% [5–7]. First, Figure 2.9 indicates that both $\bar{d}_{p,PC}$ and $\bar{d}_{p,SC}$ (i) increased linearly with increasing particle radius r_s and (ii) increased sharply with increasing porosity ϕ. It also shows that the average pore diameter of surface-contact structures $\bar{d}_{p,SC}$ was slightly larger than predictions of $\bar{d}_{p,PC}$ for point-contact structures [Equation (2.19)]. The difference between $\bar{d}_{p,PC}$ and $\bar{d}_{p,SC}$ increased with decreasing porosity ϕ due to the larger associated particle overlapping.

Moreover, Figure 2.9(a) shows that the average pore diameters reported in the literature [5–7] were in good agreement with (i) numerical simulations and (ii) predictions of $\bar{d}_{p,PC}$ by Equation (2.19). Moreover, Figure 2.9(b) plots the average pore diameter $\bar{d}_p$ reported for sintered silica aerogels with different porosities [7]. It indicates that the sharp increase in $\bar{d}_p$ with increasing porosity ϕ was also observed experimentally for sintered silica aerogels.

Finally, Figure 2.9(b) plots the average diameter $\bar{d}_{p,PSD}$ obtained from the differential PSDs [Equation (2.18)] of surface-contact structures consisting of monodisperse nanoparticles. It shows that the average diameter $\bar{d}_{p,PSD}$ was in good agreement with the average pore diameter of surface-contact structures $\bar{d}_{p,SC}$ computed using Equation (2.5) for porosity ϕ ranging from 39.6 to 79.1%.

2.3.3 Effect of particle polydispersity

Figure 2.10 shows the specific surface area of surface-contact structures $A_{g,SC}$ consisting of polydisperse particles following a Gaussian distribution with three values of mean radius $\bar{r}_s$ = 2.5, 5, and 10 nm and three values of standard deviation $s = 0$ (monodisperse), $r_s/5$, and $r_s/2.5$. It indicates that the specific surface area

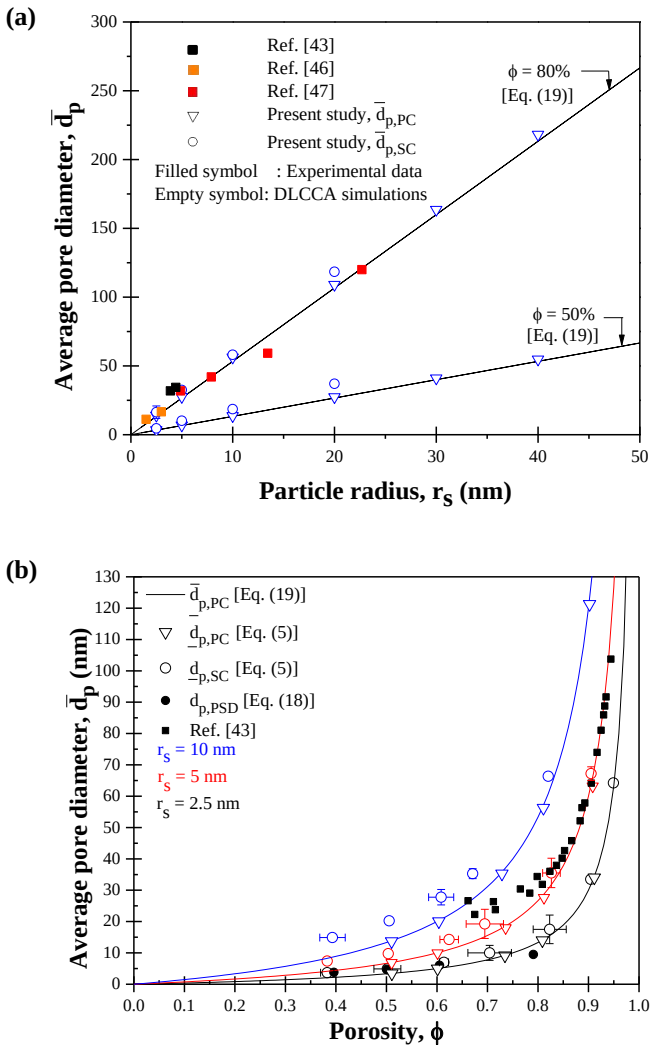

Figure 2.9: Computed average pore diameter $\bar{d}_p$ (in nm) [Equations (2.5) and (2.18)] of point-contact and surface-contact mesoporous structures consisting of monodisperse spheres of radius r_s as a function of (a) particle radius r_s between 2.5 and 40 nm for $\phi = 50$ or 80% and (b) porosity ϕ for $r_s = 2.5$, 5, and 10 nm. Predictions of $\bar{d}_{p,PC}$ [Equation (2.19)] are also shown, as well as experimental data from Refs. [5–7].

of surface-contact structures consisting of polydisperse particles was lower than that of monodisperse particles with the same mean radius. In addition, for a given mean radius $\bar{r}_s$, larger standard deviation s resulted in smaller specific surface area. Note, however, that a smaller fraction of particles overlapped in structures with

polydisperse particles (75-95%) than in structures with monodisperse particles (99%). Finally, polydispersity of the constitutive particles resulted also in lower interfacial area concentration A_i [Equation (2.7)] and larger average pore diameter $\bar{d}_p$ [Equation (2.5)] for both point-contact and surface-contact structures.

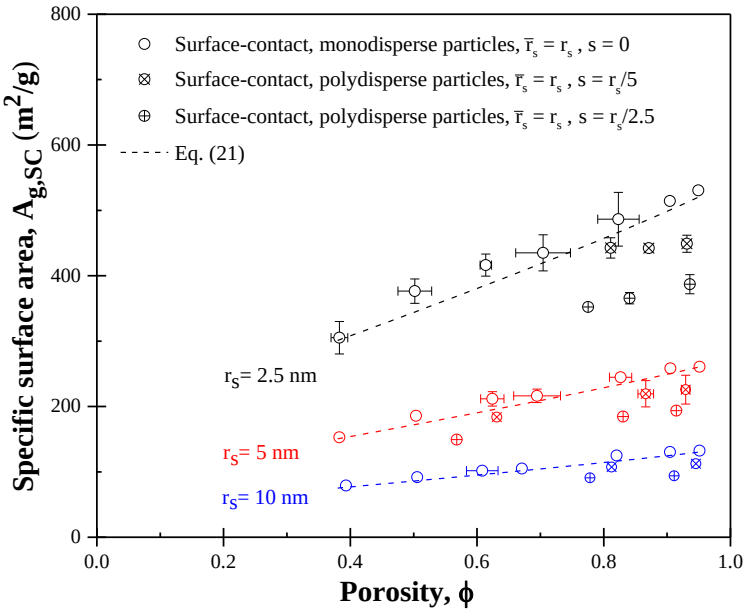

Figure 2.10: Specific surface area $A_{g,SC}$ as a function of porosity ϕ for surface-contact structures of polydisperse nanoparticles of mean radius $\bar{r}_s$ and standard deviation s. Results for the specific surface area of surface-contact structures with monodisperse particles are also shown for reference.

2.4 Conclusion

This study aimed to numerically generate mesoporous structures and assess the effects of porosity, particle radius, polydispersity, and overlapping on the structural characteristics of mesoporous materials. Point-contact and surface-contact structures with either monodisperse or polydisperse particles were generated numerically using the DLCCA method. Porosity was varied from 35 to 95% and particle radius from 2.5 to 40 nm. The computer-generated mesoporous materials were characterized numerically in terms of specific surface area, average pore di-

ameter, and pore size distribution in complete analogy with experimental characterization. In particular, a new algorithm, inspired by gas adsorption porosimetry, was developed to compute the specific surface area and pore size distribution of computer-generated structures. The specific surface area for point-contact structures corresponded to the maximum specific surface area of mesoporous material for a given primary particle radius. For given porosity and particle radius, particles overlapping and/or polydispersity reduced the specific surface area and interfacial concentration but increased the average pore diameter. Finally, the structural properties of the computer-generated structures agree well with those reported for silica aerogel and ambigel. The computational tools and methods can be used in the discovery and optimization of mesoporous materials (e.g., silica, carbon [92], or alumina [93], or ceria [94]) and to relate their nanoscale architecture to their mechanical, optical, and thermal properties.

CHAPTER 3

Revisiting Independent versus Dependent Scattering Regimes in Suspensions and Aggregates of Spherical Particles

This chapter investigates the parameters governing the scattering cross-section and asymmetry factor of systems consisting of non-absorbing spherical particles and the conditions under which dependent and independent scattering regimes prevail for each radiation characteristic. The dimensionless parameters governing the scattering cross-section and asymmetry factor of non-absorbing bispheres, disordered and ordered suspensions and aggregates with up to 8 particles were found to be the particle size parameter χ_s, the relative index of refraction m, the interparticle distance-to-wavelength ratio d^*, and the number of particles. Dependent effects were observed in aggregates with particles of all sizes and were strongly affected by the relative index of refraction in particle systems with $\chi_s \geq 2$ due to large phase shifts across the particles. Moreover, new criteria for the transition between the dependent and independent scattering regimes for the scattering cross-section and the asymmetry factor were derived. For the scattering cross-section of structures with a narrow interparticle distance distribution, the independent scattering regime prevailed when the average interparticle distance-to-wavelength ratio $\bar{d}^*$ exceeded (i) 2 for particles with $\chi_s \leq 2$ and (ii) 5 for particles with $\chi_s > 2$. For the asymmetry factor, the transition from the dependent to the independent regimes for particles with $\chi_s \leq 2$ was achieved for $\bar{d}^*$ as high as 25. These transition criteria could be extended to particle systems with a broad interparticle distance distribution when based on the minimum interparticle distance-to-wavelength ratio d^*_{min}. Finally, the relative index of refraction m did not affect these transition criteria.

3.1 Background

3.1.1 Light scattering by particle suspensions and aggregates

Light scattering characteristics of a suspension or aggregate of spherical particles have been reported to depend not only on the particle (i) size parameter χ_s and (ii) relative complex index of refraction m but also on (iii) the particle volume fraction f_v of the suspension or aggregate [12, 13, 15, 17], (iv) the average clearance-to-wavelength ratio $\bar{c}^* = \bar{c}/\lambda$ where $\bar{c}$ is the average surface-to-surface distance (or clearance distance) between adjacent particles [Figure 3.2(a)] [13, 15], (v) the average interparticle distance-to-wavelength ratio $\bar{d}^* = \bar{d}/\lambda$ where the average interparticle distance $\bar{d}$ is expressed as $\bar{d} = \bar{c}+2r_s$ [17, 95], (vi) the average clearance-to-radius ratio $\bar{c}/r_s$ [14, 15], and/or (vii) the average interparticle distance-to-radius ratio $\bar{d}/r_s$ [12, 16]. The particle volume fraction f_v can be calculated as the ratio of the volume V_s occupied by the particles to the total volume V_{tot} of the suspension. For systems with monodisperse particles of radius r_s, f_v can be expressed as

$$f_v = \frac{V_s}{V_{tot}} \quad \text{with} \quad V_s = 4\pi r_s^3 N_s/3 \tag{3.1}$$

where N_s is the total number of particles in the total volume V_{tot} of the suspension.

When the particle volume fraction f_v is sufficiently low, particles are far from each other and the scattering characteristics of a particle are said to be "unaffected" by the presence of the surrounding particles corresponding to the independent scattering regime [15, 55]. For example, in the independent scattering regime, the effective scattering cross-section C_{sca}^s of the suspensions can be expressed as the sum of the scattering cross-sections $C_{sca}(\chi_{s,i}, m_i, r_{s,i})$ of individual particles, i.e., [55]

$$C_{sca}^s = \sum_{i=1}^{N_s} C_{sca}(\chi_{s,i}, m_i, r_{s,i}). \tag{3.2}$$

Here, the index "i" corresponds to the particle of radius $r_{s,i}$ with size parameter $\chi_{s,i} = 2\pi r_{s,i}/\lambda$ and relative complex index of refraction m_i. Similarly, the asymmetry factor g^s of the suspension can be expressed as [59, 96]

$$g^s = \frac{\sum_{i=1}^{N_s} C_{sca}(\chi_{s,i}, m_i, r_{s,i}) g(\chi_{s,i}, m_i)}{\sum_{i=1}^{N_s} C_{sca}(\chi_{s,i}, m_i, r_{s,i})} \tag{3.3}$$

where $g(\chi_{s,i}, m_i)$ is the asymmetry factor of the i^{th} particle. Note that for suspensions of identical monodisperse particles with size parameter χ_s and relative complex index of refraction m, Equations (3.2) and (3.3) simplify to $C^s_{sca} = N_s$ $C_{sca}(\chi_s,m,r_s)$ and $g^s = g(\chi_s,m)$, respectively.

When particles are in close proximity, light scattering is affected by (i) near-field interactions and (ii) far-field interferences [16, 59, 97]. Near-field interactions originate from multiple scattering corresponding to the situation when the near-field scattered wave from one particle is incident on another particle leading, in turn, to interferences [16, 59, 97]. Far-field interferences refer to interferences between far-field-scattered waves from neighboring particles [16,59,97]. These two phenomena play an important role in the dependent scattering regime such that Equations (3.2) and (3.3) are no longer valid [55].

Previously, experiments or analytical derivations have been used to establish the range of validity of the independent scattering approximation. More recently, numerical algorithms solving Maxwell's equations in complex particulate media have been developed including the discrete dipole approximation (DDA) [98] and the superposition T-matrix method [99, 100]. They have notably been used to analyze the range of applicability of the independent scattering approximation for radiative characteristics such as integral properties, scattering phase function, or scattering matrix elements [20].

3.1.2 Independent versus dependent scattering

Previous studies have investigated the independent and dependent scattering regimes in monodisperse bispheres [12, 14, 16, 59, 95], suspensions of spherical particles [13, 15, 17], or aggregates [13–15, 101, 102] based on experimental measurements [13, 15], analytical derivations [15, 59, 95], or computer simulations [12, 14, 16, 17, 101, 102]. In general, the independent scattering regime was considered to be reached when the radiation characteristic investigated (e.g., C^s_{sca} or g^s) of the particle system fell within 5% of the independent scattering regime predictions [Equations (3.2) and (3.3)]. Note that this criterion was arbitrary and represents a good compromise between the experimental and numerical uncertainties and the need to obtain a reasonable yet conservative criteria for the transition between the two regimes.

Tien and Drolen [15] reviewed experimental studies considering the scattering efficiency factor, scattering cross-section, or scattering coefficient of suspensions of latex particles in water or air [58, 103–107] and of various pigment suspensions in water [108] with $0.05 \leq \chi_s \leq 400$ and $10^{-6} \leq f_v \leq 0.74$. The review also included two analytical studies [97, 109]. The different experimental studies established the transition between the independent and dependent scattering regimes corresponding to $\bar{c}/r_s$ ranging between 0.8 and 1.4 and $\bar{c}^*$ around 0.3-0.5 depending of the suspensions considered. The authors also presented a scattering regime map in the diagram plotting the particle size parameter χ_s versus particle volume fraction f_v based on the work of Yamada et al. [107] for monodisperse latex particles in water or air ($m = 1.2$ or 1.6) with $0.2 \leq \chi_s \leq 90$ and $10^{-3} \leq f_v \leq 0.74$. For $\chi_s \leq 0.388$, the critical particle volume fraction corresponding to the independent/dependent scattering transition was $f_{v,cr} = 0.006$ [15]. On the other hand, for $\chi_s > 0.388$ and $f_v > 0.006$, the transition from independent to dependent scattering was given by

a critical average clearance-to-wavelength ratio of [15]

$$\bar{c}^*_{cr} = 0.5. \tag{3.4}$$

The corresponding critical particle volume fraction $f_{v,cr}$ was calculated by assuming a rhombohedral packing of monodisperse particles and expressed as [15]

$$f_{v,cr} = \left(\frac{0.9047}{\pi/2\chi_s + 1} \right)^3. \tag{3.5}$$

Kaviany and Singh [13] modified the average clearance distance $\bar{c}$ proposed by Tien and Drolen [15] by $\bar{c}+0.2r_s$ where the distance $0.2r_s$ was added in an ad hoc manner to correct for the close-pack separation distance in a rhombohedral packing when the most compact arrangement is obtained (i.e., $f_v = 0.74$) to yield [13]

$$\bar{c}^*_{cr} = 0.5 - 0.1\chi_s/\pi \quad \text{resulting in} \quad f_{v,cr} = \left(\frac{0.9047}{\pi/2\chi_s + 0.9} \right)^3. \tag{3.6}$$

This correction was negligible for systems with particle volume fraction $f_v < 0.3$ but resulted in a significant difference between Equations (3.5) and (3.6) for particle volume fraction $f_v > 0.5$ [13]. Equation (3.6) was shown to predict experimental data for monodisperse latex spheres in water and air [107] more closely than Equations (3.4) and (3.5). Although these studies [13,15] considered experimental data covering a wide range of particle size parameters $0.2 \leq \chi_s \leq 90$, they considered non-absorbing monodisperse particles with relative index of refraction m of either 1.2 (latex particles in water) or 1.6 (latex particles in air). Note that Tien and Drolen [15] did not consider the scattering phase function or asymmetry factor of the suspensions.

Olaofe [95] derived an analytical expression for the scattering cross-section of bispheres by integrating the scattered field intensity obtained from solving

Maxwell's equations. In particular, the author presented the ratio of some scattering efficiency factors of non-absorbing monodisperse bispheres defined as Q^b_{sca} $= C^b_{sca}/\pi r_s^2$ to that of a single sphere Q^M_{sca} predicted by Lorenz-Mie theory. Here, C^b_{sca} was the scattering cross-section of the bisphere at a fixed orientation, the particle size parameter χ_s was 0.5 or 1, and m ranged from 1.05 to 1.50. The ratio Q^b_{sca}/Q^M_{sca} was plotted as a function of the ratio d^* between $1/2\pi$ and $15/\pi$. As the separation distance between the spheres increased, the oscillation amplitude decreased and Q^b_{sca}/Q^M_{sca} tended asymptotically towards 2 corresponding to the independent scattering regime when $Q^b_{sca} = 2Q^M_{sca}$ [95]. Moreover, the oscillation pattern of the ratio Q^b_{sca}/Q^M_{sca} was shown to vary with changes in the bisphere orientation. Finally, Olaofe [95] concluded that the relative index of refraction $m = n_s/n_m$ did not affect the efficiency factor ratio Q^b_{sca}/Q^M_{sca} when all other parameters were kept constant.

Videen et al. [59] developed a general expression for the orientation-averaged asymmetry factor of monodisperse bispheres using an extension of Lorenz-Mie theory. The expression consisted of one term accounting for far-field interferences and another accounting for near-field interactions. The bispheres consisted of two absorbing monodisperse carbon spheres with $\chi_s = 0.628$ or 3.14 and $m = 1.75$ $+ i0.44$. The authors showed that far-field interferences resulted in enhanced forward scattering due to constructive interference in the forward direction. On the other hand, near-field interactions resulted in enhanced backscattering "due to constructive interference of rays reflecting off multiple interfaces" [59]. Lastly, they showed that the asymmetry factor of bispheres tended towards the asymmetry factor of a single sphere when the interparticle distance-to-wavelength ratio d^* exceeded 2.

Quirantes et al. [12] used the T-matrix algorithm to predict the orientation-averaged scattering cross-section ratio $C^b_{sca}/2C^M_{sca}$ of non-absorbing monodisperse bispheres with particle size parameter χ_s varying from 0.1 to 20, interparticle

distance-to-radius ratio d/r_s varying from 2 to 20, and relative index of refraction $m = 1.2$. The critical interparticle distance-to-radius ratio $(d/r_s)_{cr}$ was estimated for bispheres with different particle size parameter χ_s. The authors also hypothesized that the critical criterion obtained for bispheres could be extended to particle suspensions. Then, the critical particle volume fraction $f_{v,cr}$ beyond which dependent scattering prevailed was such that [12]

$$f_{v,cr} = \frac{4}{3}\pi \left(\frac{r_s}{d}\right)^3. \tag{3.7}$$

The authors showed that when $\chi_s < 5.5$ the critical particle volume fraction $f_{v,cr}$ decreased with decreasing χ_s. In particular, suspensions of monodisperse particles such that $\chi_s < 1$ fell in the independent scattering regime for $f_{v,cr} < 0.001$. Note that this criterion contradicts that proposed by Tien and Drolen [15] and such that $f_{v,cr} = 0.006$ for suspensions of particles with $\chi_s < 0.388$.

Mishchenko et al. [16] studied the orientation-averaged phase function and scattering matrix elements of monodisperse bispheres with $\chi_s = 5$ and 15 and $m = 1.5 + i0.005$ using the T-matrix algorithm. The authors showed that, in both cases, the independent scattering regime was reached when the interparticle distance d exceeded four times the particle radius r_s, i.e., $d/r_s \geq 4$. In addition, Mishchenko et al. [17] studied the independent and dependent scattering regimes of 8 non-absorbing monodisperse spheres randomly distributed but in contact with at least another sphere. The particle size parameter was $\chi_s = 4$, the relative index of refraction m was 1.32, and the particle volume fraction f_v varied from 0.0014 to 0.296. The authors showed that the scattering cross-section ratio $C^s_{sca}/8C^M_{sca}$ and forward-scattering phase function ratio $\Phi^s(\Theta = 0)/8\Phi^M(\Theta = 0)$ tended towards 1 when the average interparticle distance-to-wavelength ratio was such that $2\pi\bar{d}^*$ > 30 and $f_v < 0.01$. Here, $\Phi^s(\Theta = 0)$ and $\Phi^M(\Theta = 0)$ are the phase functions of the particle suspension and of a single particle in the forward direction ($\Theta = 0°$),

respectively. Furthermore, the study showed that near-field interactions resulted in enhanced backscattering, in agreement with Videen et al. [59]. Especially, multiple scattering was shown to corroborate with "the interference nature of coherent backscattering".

Ivezić and Mengüç [14] used the discrete dipole approximation (DDA) method to study a system of two monodisperse carbon spheres with $m = 1.75 + i0.75$ and $0.2 \leq \chi_s \leq 1$ under polarized incident radiation. Their study focused on the scattering cross-section and phase function of bispheres at fixed orientations and established that the independent scattering regime was reached for a critical clearance-to-radius ratio given by [14]

$$(c/r_s)_{cr} = 2/\chi_s. \tag{3.8}$$

The authors also studied touching aligned spheres and ordered aggregates (e.g., tetrahedron, body centered cubes, etc.) with up to 12 monodisperse spheres. Orientation-averaged results for agglomerates showed that when $\chi_s \approx 2$, the scattering cross-section and phase function were within 10-20% of the independent scattering regime predictions. Then, they concluded that "dependent effects never disappear" for such systems due to the adjacency of the particles.

Ivezić et al. [101] also studied the effect of the relative index of refraction m on the parameter $(C^s_{sca}/C^M_{sca})(C^M_{abs}/C^s_{abs})(\Phi^s/\Phi^M)$ of aggregates on the basis that dependent effects on C^s_{sca}, C^s_{abs}, and Φ^s "are difficult to separate" [101]. Here, C^s_{abs} is the absorption cross-section of the particle system. Results for compact and linear aggregates with 7 monodisperse spheres with a particle size parameter χ_s varying from 0.025 to 1.57 and for the scattering angles $\Theta = 45$, 135, and 165° were presented. First, the particle index of refraction n_s was taken as $n_s = 1.75$ while the absorption index was $k_s = 0.01$, 0.1, or 1. Second, the absorption index was kept constant as $k_s = 0.75$ and the index of refraction n_s was taken as equal to

1.5, 1.75, or 2.0. The authors concluded that the complex index of refraction had a negligible effect on the parameter $(C^s_{sca}/C^M_{sca})(C^M_{abs}/C^s_{abs})(\Phi^s/\Phi^M)$. The study's conclusion suggests that the complex index of refraction m did not affect the transition between the scattering regimes for particle suspensions.

Ma et al. [102] investigated densely packed disordered aggregates with $N_s = 200$ monodisperse particles with size parameter $\chi_s = 6.964$ (corresponding to $r_s = 500$ nm and $\lambda = 600$ nm) embedded in a virtual spherical domain of radius equal to $10r_s$ in water (i.e., $n_m = 1.33$). The index of refraction of the particles n_s varied from 1.4 to 3.0 and the absorption index k_s from 0 to 1.0. The Mueller matrix elements of the scattering system were computed using the T-matrix method. The authors concluded that the transition between independent and dependent scattering regimes depended not only on the clearance-to-wavelength ratio c^* but also on the complex index of refraction m. However, this conclusion was in contradiction with those of Olaofe [95] and Ivezić et al. [101]. This disagreement could be due to the fact that different particle systems with different particle size parameter χ_s and relative index of refraction m were considered.

Table 3.1 summarizes the range of parameters explored in the different studies previously reviewed and the transition criteria proposed. First, most studies considered a narrow range of particle size parameter χ_s and/or relative complex index of refraction m. Second, major discrepancies appear in the choice of parameters governing the scattering cross-section and asymmetry factor as well as the transition criteria between independent and dependent scattering regimes.

The present study aims to investigate scattering by non-absorbing bispheres, particle suspensions, as well as aggregates with a wide range of particle size parameter ($0.031 \leq \chi_s \leq 8.05$) and relative index of refraction ($0.677 \leq m \leq 2.6$). This study focuses on integral radiative characteristics, namely the scattering cross-section and asymmetry factor, because they are essential in solving the RTE in applications concerned with unpolarized light such as those illustrated in Fig-

ure 3.1. The goal of this study is (i) to determine unequivocally the parameters controlling the scattering cross-section and asymmetry factor of bispheres, suspensions, and aggregates of non-absorbing monodisperse spherical particles, (ii) to assess the validity of the transition criteria between the independent and dependent scattering regimes proposed in the literature (Table 3.1) and, if necessary, propose an alternative criterion, and (iii) to determine whether transition criteria for bispheres can be extrapolated to particle suspensions and aggregates, as previously assumed in the literature [12].

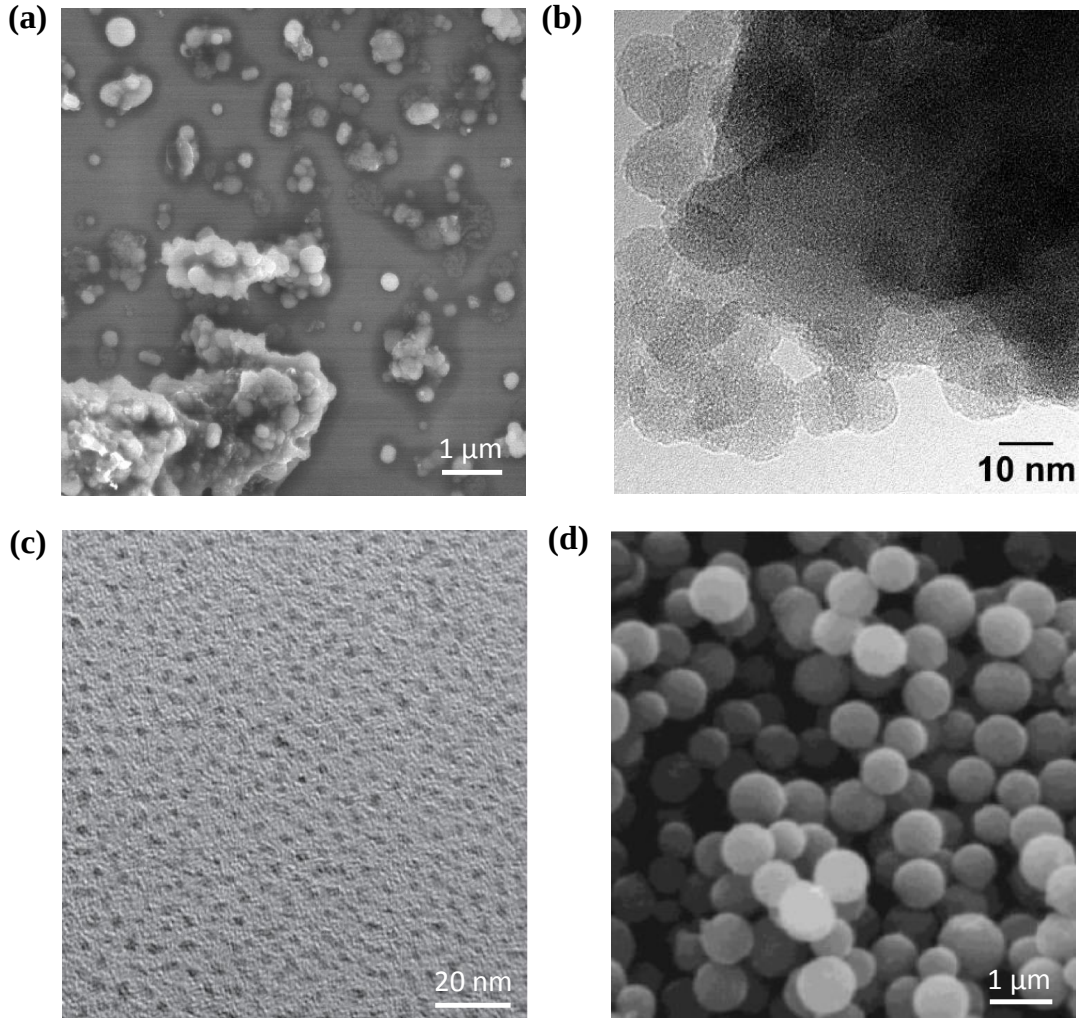

Figure 3.1: Scanning electron microscopy images of (a) aerosol carbon particles (reprinted with permission from Ref. [9], Copyright Taylor & Francis) and (b) silica aerogel (reprinted with permission from Ref. [1], Copyright Springer Nature). (c) Transmission electron image of nickel nanoparticle suspension (reprinted with permission from Ref. [10], Copyright Elsevier) and (d) scanning electron image of titania particles (reprinted with permission from Ref. [11], Copyright John Wiley & Sons).

3.2 Analysis

3.2.1 Computer-generated structures

The radiative characteristics of three types of non-absorbing particle arrangements were investigated namely (i) bispheres, (ii) multiple disordered, monodisperse, non-touching spherical particles representative of particle suspensions, and (iii) multiple ordered monodisperse touching or non-touching spherical particles. Radiative characteristics of bispheres were denoted by the superscript "b" and those of disordered and ordered particle systems were denoted by the superscript "s". Figures 3.2(a)-3.2(c) illustrate the investigated bispheres and the disordered particle systems obtained by randomly generating 4 or 8 particles in a cubic domain of size L and volume $V_{tot} = L^3$. Figures 3.2(d)-3.2(g) display ordered particle systems including tetrahedron and simple cubic structures with $N_s = 4$ or 8 when the particles were touching [Figures 3.2(b) and 3.2(c)] and non-touching [Figures 3.2(d) and 3.2(e)]. For any given arrangement, all spherical particles had a radius r_s ranging from 2.5 nm to 50 nm while wavelength λ was varied so that the particle size parameter χ_s ranged from 0.031 to 8.05. In addition, the non-absorbing particle relative index of refraction m varied from 0.667 to 2.6. To investigate both dependent and independent scattering regimes, the size of the cubic domain or lattice was progressively increased resulting in increasing interparticle distances d. For bispheres, the interparticle distance d ranged from 5 nm to 30 μm. In the case of disordered and ordered particle systems, the average interparticle distance $\bar{d}$ ranged from 25 nm to 1.4 μm.

3.2.2 Scattering characteristics

The discrete-dipole approximation (DDA) algorithm developed by Draine and Flatau [98] was used to compute the scattering cross-section C_{sca} and asymmetry factor g of the different particle systems considered. First, N_d cubic dipoles of

Table 3.1: Literature review of studies on independent and dependent scattering regimes.

Reference	[16]	[15]	[12]	[13]	[17]	[14]
Type of study	Simulations	Review	Simulations	Review	Simulations	Simulations
Data from	T-matrix	Experiments	T-matrix	Experiments	T-matrix	DDA
Particle system	Bisphere	Suspension and aggregate	Bisphere	Suspension and aggregate	Suspension	Bisphere and aggregate
Radiation characteristics	Scattering matrix elements, Q_{sca}	Q_{sca}	C_{sca}	Q_{sca}	C_{sca}, Φ	C_{sca}, Φ
Relative index of refraction m	$1.5+i0.005$	1.2 and 1.6	1.2	1.2 and 1.6	1.32	$1.75+i0.75$
Particle size parameter χ_s	$\chi_s = 5$ and 15	$0.2 \leq \chi_s \leq 90$	$0.1 \leq \chi_s \leq 20$	$0.2 \leq \chi_s \leq 90$	$\chi_s = 4$	$0.2 \leq \chi_s \leq 2$
Particle volume fraction f_v	N/A	$10^{-3} \leq f_v \leq 0.74$	N/A	$10^{-3} \leq f_v \leq 0.74$	$0.0014 \leq f_v \leq 0.30$	N/A
Critical criteria [a]	$(d/r_s)_{cr} \simeq 4$	$\bar{c}^*_{cr} = 0.5$ ($\chi_s > 0.388$)	$(d/r_s)_{cr}$ plotted	$\bar{c}^*_{cr} = 0.5$ - $0.1\chi_s/\pi$	$\bar{d}^*_{cr} \geq 15/\pi$	$(c/r_s)_{cr} = 2/\chi_s$
$f_{v,cr} =$ [a]	N/A	0.006 ($\chi_s < 0.388$) $(\frac{0.9047}{\pi/2\chi_s+1})^3$ (χ_s>0.388)	$\frac{4\pi}{3}(\frac{1}{(c/r_s)_{cr}+2})^3$	$(\frac{0.9047}{\pi/2\chi_s+0.9})^3$	$f_{v,cr}$<0.01	N/A

[a] The independent scattering regime prevailed for values of d^*, c^*, c/r_s, and d/r_s above the critical criteria and values of f_v below $f_{v,cr}$

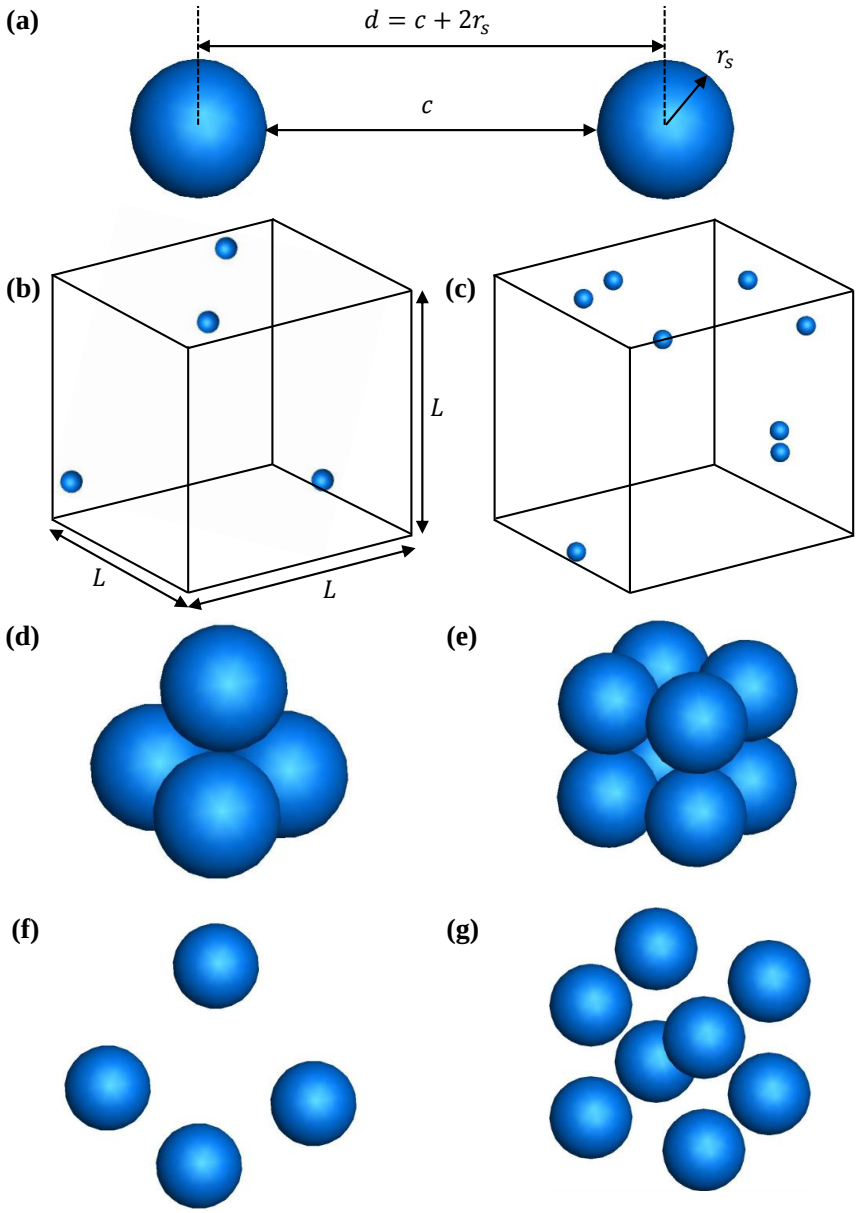

Figure 3.2: Schematics of (a) bisphere, (b)-(c) disordered particle suspensions with $N_s = 4$ and $N_s = 8$, (d) tetrahedron and (e) simple cubic structure with touching particles, and (f) tetrahedron and (g) simple cubic structure with distant particles.

side Δd were generated inside the N_s particles. The dipoles were such that their size Δd was small compared to the particle radius r_s and wavelength λ to achieve numerically converged results independent of the choice of discretization [110]. The input parameters of the DDA method included (i) the position of the N_d cubic dipoles, (ii) the wavelength λ, (iii) the particle relative index of refraction m with respect to the surrounding, and (iv) the equivalent radius r_{eq} defined as the radius of a sphere with the same volume V_s as the particle system and expressed as [110]

$$r_{eq} = \left(\frac{3V_s}{4\pi}\right)^{1/3}. \tag{3.9}$$

Substituting Equation (3.1) into Equation (3.9) simplifies the equivalent radius as $r_{eq} = {N_s}^{1/3} r_s$. The scattering cross-section C_{sca} (in nm^2) of systems consisting of N_s monodisperse particles was expressed as a function of the computed scattering efficiency factor Q_{sca} according to [110]

$$C_{sca} = \pi r_{eq}^2 Q_{sca}. \tag{3.10}$$

The scattering cross-section C_{sca} and asymmetry factor g were averaged over at least 33 orientations for bispheres and simple cubic structures and over at least 115 orientations for tetrahedrons and disordered particle systems to ensure accurate orientation-averaging. Similarly, the number of scattering directions was set greater than 1000 so that the asymmetry factor g can be properly estimated [Equation (1.2)]. Finally, the DDA method was validated against predictions by Lorenz-Mie theory for single spheres with particle size parameter χ_s and relative index of refraction m in the same range as that of the particle systems investigated. In all cases, predictions of C_{sca} and g by the DDA method fell within 3% of those by Lorenz-Mie theory (see Figure B.1 and B.2 in Supporting Information). In fact, the average error between the two methods was 0.89% for the scattering cross-section and 0.85% for the asymmetry factor for all cases considered in the

validation.

3.3 Results and discussion

3.3.1 Bispheres

Governing dimensionless parameters

Figure 3.3 plots (left) the scattering cross-section C^b_{sca} of bispheres as a function of the interparticle distance d and (right) the scattering cross-section ratio $C^b_{sca}/2C^M_{sca}$ as a function of the interparticle distance-to-wavelength ratio $d^* = d/\lambda$ for bispheres with $m = 1.5$ and (a) $\chi_s = 0.031$, (b) $\chi_s = 0.063$, and (c) $\chi_s = 0.126$. Each size parameter χ_s was represented by three cases corresponding to different values of particle radius r_s and wavelength λ. Figure 3.3 indicates that the scattering cross-section C^b_{sca} plotted as a function of d differed significantly among cases with the same particle size parameter χ_s but different particle radius r_s and wavelength λ. By contrast, the scattering cross-section ratio $C^b_{sca}/2C^M_{sca}$ plotted as a function of the interparticle distance-to-wavelength ratio d^* collapsed on a single line for any given particle size parameter χ_s. Similar results were obtained for different values of m including 1.2 and 2 (see Figure B.3 in Supporting Information). These results establish that the ratio $C^b_{sca}/2C^M_{sca}$ was a function of only χ_s, m, and d^*, i.e., $C^b_{sca}(\chi_s,m,d^*,r_s) = 2f^b(\chi_s,m,d^*)C^M_{sca}(\chi_s,m,r_s)$ where f^b is a function to be determined. Note that the parameters c^*, c/r_s, and d/r_s can be expressed in terms of both the interparticle distance-to-wavelength ratio d^* and particle size parameter χ_s such that

$$c^* = d^* - \chi_s/\pi, \quad c/r_s = \frac{2\pi}{\chi_s}d^* - 2, \quad \text{and} \quad d/r_s = \frac{2\pi d^*}{\chi_s}. \tag{3.11}$$

Therefore, $C^b_{sca}(\chi_s,m,d^*,r_s)$ could also be expressed in terms of c^*, c/r_s, or d/r_s instead of d^*. However, plotting $C^b_{sca}/2C^M_{sca}$ versus c^*, c/r_s, or d/r_s for the three

particle size parameter $\chi_s = 0.031$, 0.063, and 0.126 did not result in the collapse of the data on a single line such as that observed when plotting versus d^* (Figure B.4 in Supporting Information). Therefore, χ_s, m, and d^* are the independent parameters determining the scattering cross-section ratio $C^b_{sca}/2C^M_{sca}$ of bispheres.

Moreover, Figure 3.3 shows that when the two spheres were touching (i.e., $d = 2r_s$ and $d^* = \chi_s/\pi$) the bisphere scattering cross-section was 4 times that of a single sphere, i.e., $C^b_{sca} = 4C^M_{sca}$, for the values of χ_s considered. Similar observations were also reported in Refs. [12, 16]. This observation can be explained by the so-called equivalent volume model consisting of approximating the scattering cross-section of a particle aggregate as that of an equivalent sphere with the same volume V_s and an equivalent radius $r_{eq} = {N_s}^{1/3} r_s$ [55]. In fact, since the scattering cross-section of particles in the Rayleigh regime is proportional to the square of the volume V_s [Equation (1.1)], expressing the scattering cross-section C^R_{sca} of an aggregate using Equation (1.1) with $V_s = (4\pi/3)r^3_{eq}$ results in

$$C^R_{sca} = N_s^2 C^M_{sca}. \tag{3.12}$$

In other words, for touching bispheres $C^{b,R}_{sca} = 4C^M_{sca}$. This also indicates that the equivalent volume model was valid for aggregates with touching particles for the size parameter χ_s considered. This was in agreement with previous studies investigating the validity of the equivalent volume model for aggregates with small particles [55].

Figure 3.3 also demonstrates that when the interparticle distance-to-wavelength ratio d^* exceeded 2, independent scattering prevailed since $C^b_{sca} \simeq 2C^M_{sca}$. On the other hand, when $d^* < 2$, the ratio $C^b_{sca}/2C^M_{sca}$ oscillated and exceeded 1 for the values of χ_s and m considered. This was due to dependent effects and notably to interference effects. These results were in agreement with published numerical simulations for bispheres with small size parameter [12, 16].

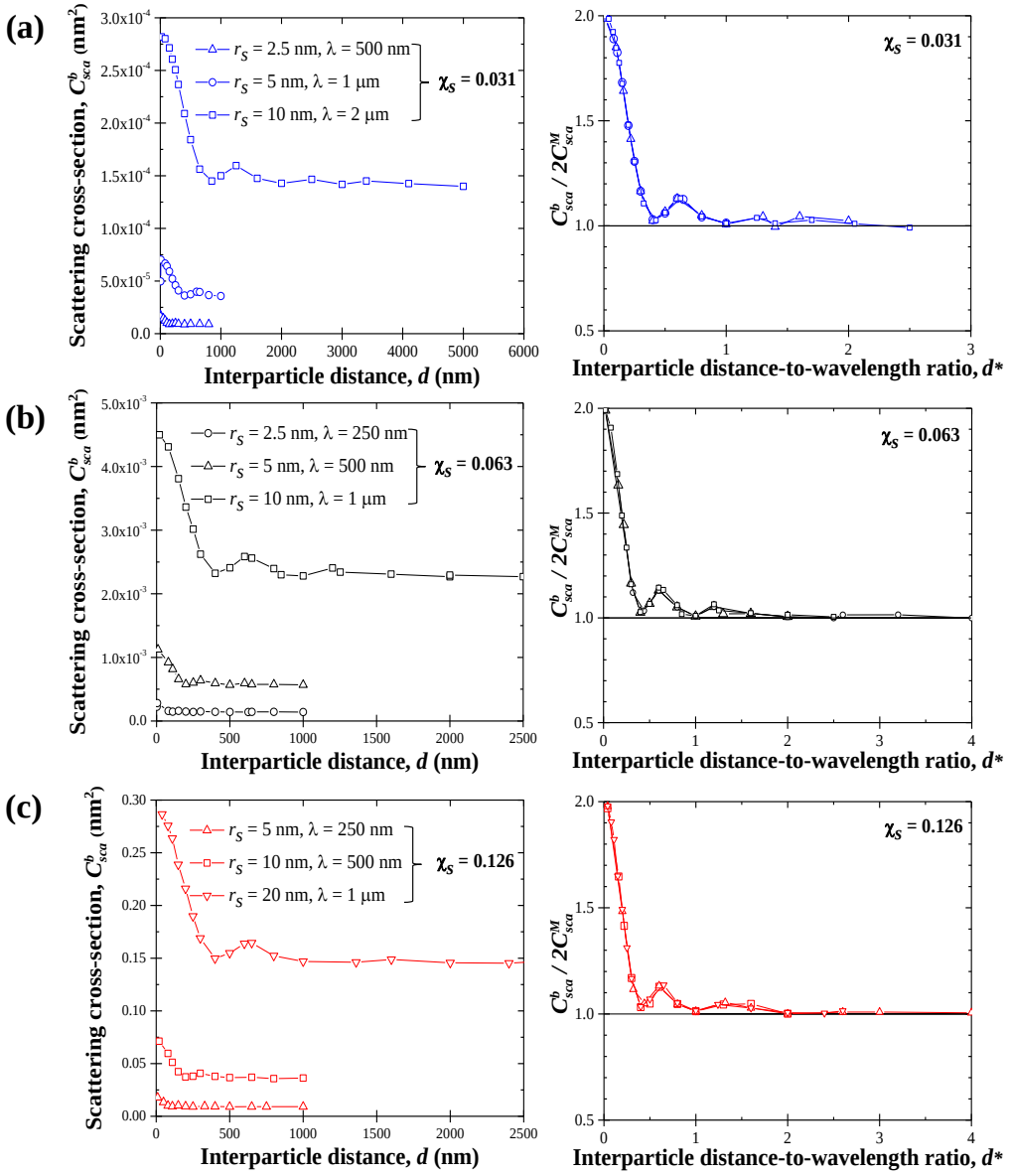

Figure 3.3: (left) Scattering cross-section C^b_{sca} as a function of the interparticle distance d and (right) corresponding scattering cross-section ratio $C^b_{sca}/2C^M_{sca}$ as a function of the interparticle distance-to-wavelength ratio d^* of bispheres for (a) $\chi_s = 0.031$, (b) $\chi_s = 0.063$, and (c) $\chi_s = 0.126$ and $m = 1.5$.

Figure 3.4 shows (left) the asymmetry factor g^b as a function of the interparticle distance d and (right) the asymmetry factor g^b as a function of the interparticle distance-to-wavelength ratio d^* for bispheres with $m = 1.5$ and (a) $\chi_s = 0.031$, (b) $\chi_s = 0.063$, and (c) $\chi_s = 0.126$. The different cases corresponded to those shown in Figure 3.3 for C^b_{sca}. Figure 3.4 indicates that the asymmetry factor g^b of bispheres with the same particle size parameter χ_s but different radius r_s and wavelength λ differed when plotted as a function of d. However, the different plots of g^b for a given value of χ_s overlapped when plotted as functions of d^*. In other words, the asymmetry factor g^b could also be expressed as a function of χ_s, m, and d^*, i.e., $g^b = g^b(\chi_s,m,d^*)$, as previously established for $C^b_{sca}/2C^M_{sca}$. The same conclusions were reached for $m = 1.2$ and 2 (Figure B.5 in Supporting Information). Moreover, the parameters χ_s, m, and d^* were also shown to be the independent parameters controlling the asymmetry factor of bispheres (Figure B.6 in Supporting Information). Finally, it is interesting to note that the bisphere asymmetry factor g^b converged towards that of a single sphere g^M but for $d^* \geq 25$ instead of $d^* \geq 2$ as observed for C^b_{sca} (Figure 3.3).

Bisphere scattering cross-section C^b_{sca}

Figure 3.5 presents the scattering cross-section ratio $C^b_{sca}/2C^M_{sca}$ as a function of the interparticle distance-to-wavelength ratio d^* of bispheres with $m = 1.5$ and (a) $\chi_s \leq 2$ and (b) $\chi_s > 2$. Figure 3.5(a) indicates that for $\chi_s \leq 2$ and $d^* < 2$, dependent effects due to interactions and interferences between the two particles resulted in the scattering cross-section of the bisphere exceeding that of two individual spheres, i.e., $C^b_{sca} > 2C^M_{sca}$, as previously observed in Figure 3.3. Furthermore, the oscillations in $C^b_{sca}/2C^M_{sca}$, observed for $\chi_s \leq 2$ and $d^* < 2$, reached their maxima and minima for the same values of d^* for all particle size parameter χ_s considered. This suggests that the interparticle distance-to-wavelength ratio d^* determined if interferences between waves scattered by each sphere were

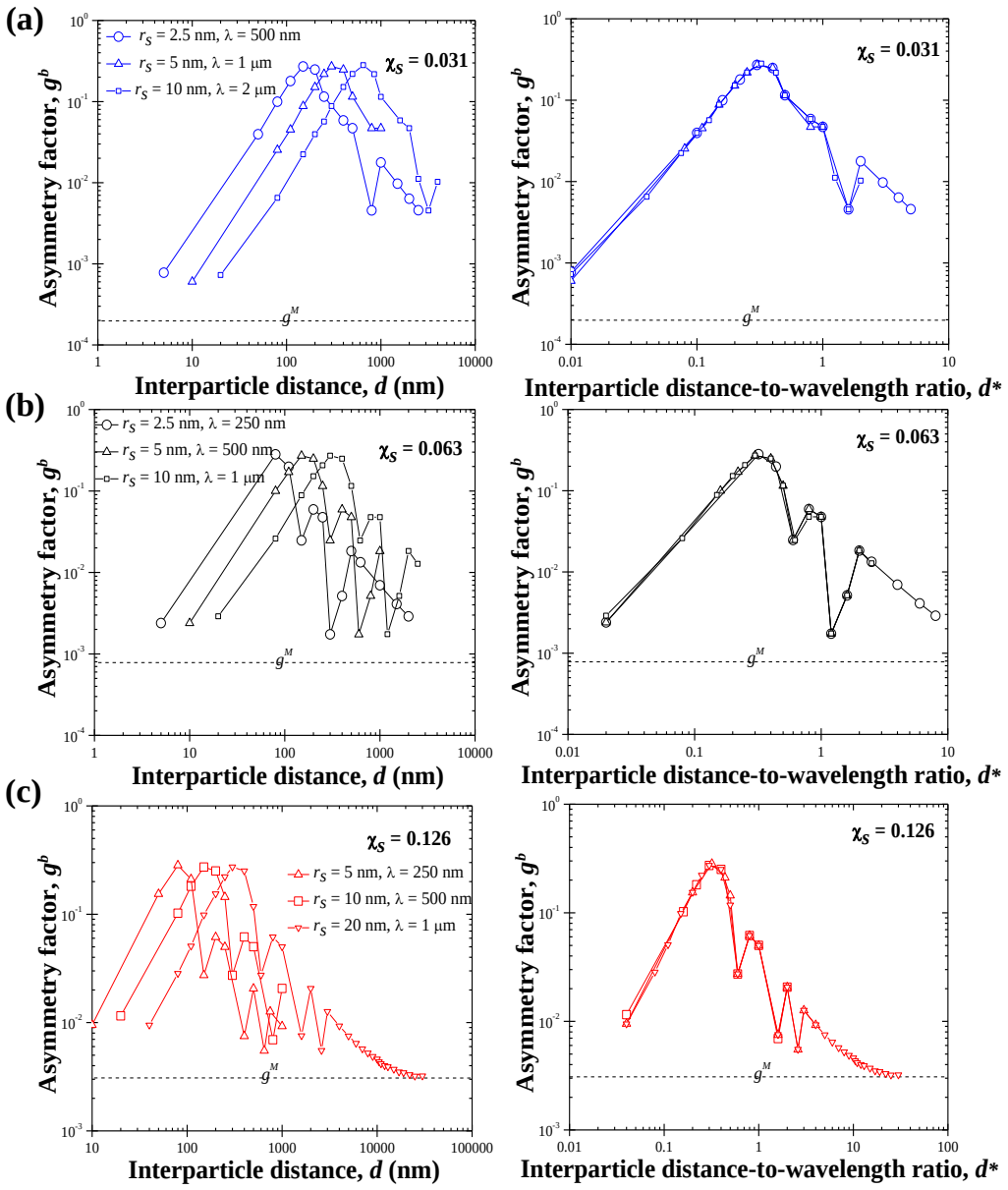

Figure 3.4: (left) Asymmetry factor g^b of bispheres as a function of the interparticle distance d and (right) asymmetry factor g^b as a function of the interparticle distance-to-wavelength ratio d^* of bispheres for (a) $\chi_s = 0.031$, (b) $\chi_s = 0.063$, and (c) $\chi_s = 0.126$ and $m = 1.5$.

constructive or destructive. This also further confirms that χ_s, m, and d^* are the independent parameters determining the effect of dependent scattering on the scattering cross-section of bispheres. Interestingly, the subsequent maxima and minima were spaced by the same interparticle distance-to-wavelength ratio d^* of approximately 1/2. This observation was also made by Videen et al. [59] regarding the subsequent maxima of the interference term of the asymmetry factor. By contrast, Figure 3.5(b) shows that for large bispheres with $\chi_s > 2$, the scattering cross-section ratio $C^b_{sca}/2C^M_{sca}$ did not feature any oscillation. Moreover, dependent effects caused the scattering cross-section C^b_{sca} of the bisphere to be smaller than the scattering cross-section of two individual spheres, i.e., $C^b_{sca} < 2C^M_{sca}$. These observations were consistent with those made in previous studies [12, 16].

Finally, Figure 3.5 establishes that the independent scattering regime for bispheres prevailed, i.e., $C^b_{sca} = 2C^M_{sca}$ when d^* exceeded a critical value d^*_{cr} such that (a) $d^*_{cr} = 2$ for $\chi_s \leq 2$ and $m = 1.5$ and (b) $d^*_{cr} = 5$ for $2 < \chi_s \leq 8.05$ and $m = 1.5$.

Critical interparticle distance-to-radius ratio $(d/r_s)_{cr}$

In some studies, the ratio d/r_s was preferred over $d^* = d/\lambda$ to identify the transition between dependent and independent scattering regimes [12, 16]. As indicated in Equation (3.11), the critical interparticle distance-to-radius ratio $(d/r_s)_{cr}$ can be expressed as a function of the critical interparticle distance-to-wavelength ratio d^*_{cr}. In order to facilitate the comparison of the different studies summarized in Table 3.1, Figure 3.6 displays the critical interparticle distance-to-radius ratio $(d/r_s)_{cr}$ for bispheres or suspensions as a function of particle size parameter χ_s reported in previous studies [12–17] for different particle relative index of refraction m. Note that when particle suspensions were investigated, the parameter considered was in fact the critical average interparticle distance-to-radius ratio

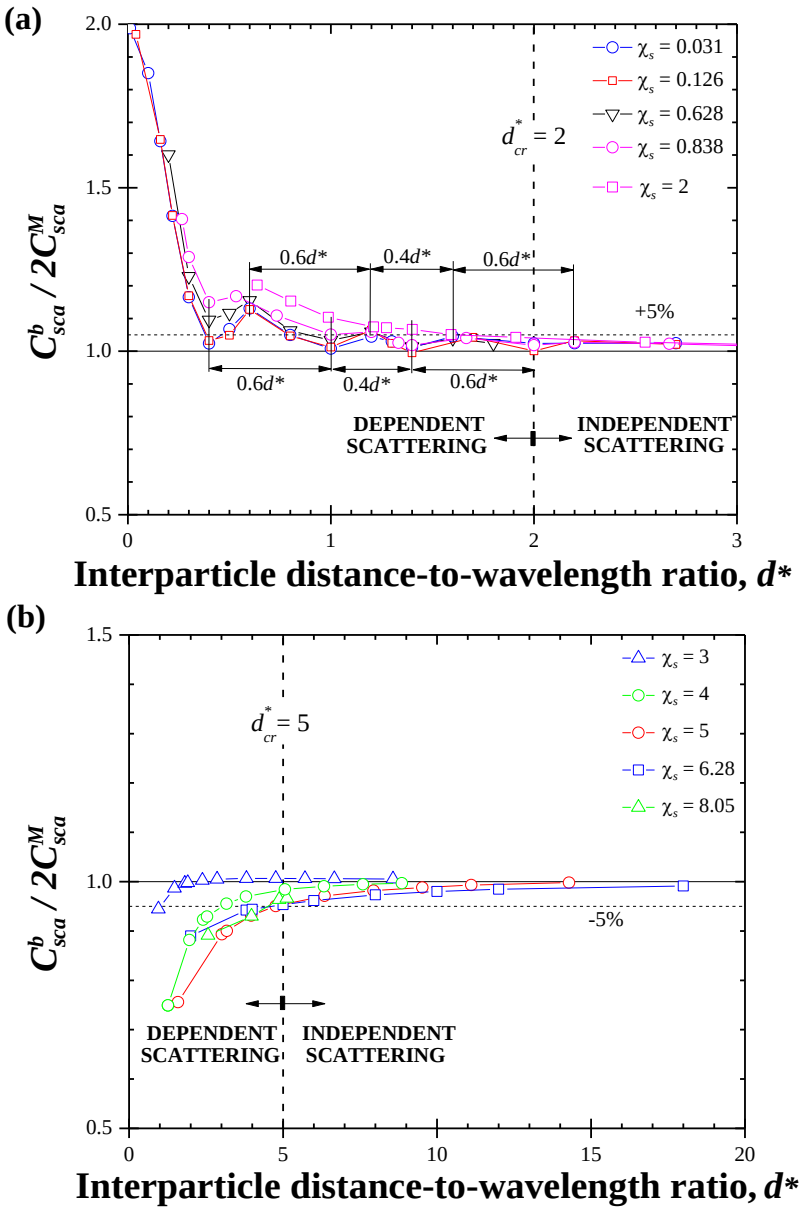

Figure 3.5: Scattering cross-section ratio $C^b_{sca}/2C^M_{sca}$ as a function of the interparticle distance-to-wavelength ratio d^* for bispheres with $m = 1.5$ and (a) $\chi_s \leq 2$ and (b) $\chi_s > 2$.

$(\bar{d}/r_s)_{cr}$ [13,15,17]. In the present study, $m = 1.5$ and d^*_{cr}, used in the calculation of $(d/r_s)_{cr}$, was determined from data shown in Figure 3.5 when the scattering cross-section of bispheres fell within 5% of predictions by Lorenz-Mie theory, i.e., when $|1 - C^b_{sca}/2C^M_{sca}| \leq 0.05$. First, Figure 3.6 indicates that the different models [13–15] and numerical results [12, 16, 17] predicting the transition between the dependent and independent scattering regimes differed significantly from one another and from results obtained in the present study. However, Figure 3.6 indicates that the numerical predictions for $(d/r_s)_{cr}$ reported in Ref. [12] for $m = 1.2$ were in qualitative agreement with those of the present study for $m = 1.5$.

Finally, Figure 3.6 indicates that the transition criteria $d^*_{cr} = 2$ for $\chi_s \leq 2$ and $d^*_{cr} = 5$ for $\chi_s > 2$ from dependent to independent scattering regimes encompass all the criteria previously reported. In practice, the critical interparticle distance d_{cr} to ensure the independent scattering regime was such that $d_{cr} \geq 6.5r_s$ for $\chi_s \geq 2$. However, for $\chi_s < 0.2$, independent scattering prevailed for interparticle distance d hundreds of time larger than the particle radius r_s, i.e., $d_{cr} \geq 100r_s$.

Bisphere asymmetry factor g^b

Figure 3.7 plots the ratio g^b/g^M of the asymmetry factor g^b for bispheres to that predicted by Lorenz-Mie theory g^M for a single particle as a function of the interparticle distance-to-wavelength ratio d^* for spheres with $m = 1.5$ and (a) $\chi_s < 2$ and (b) $\chi_s \geq 2$. First, Figure 3.7 indicates that for particle size parameter $\chi_s \leq 2$, the asymmetry factor ratio g^b/g^M vs. d^* featured oscillations whose magnitude tended to decrease with increasing χ_s. In fact, these oscillations disappeared for $\chi_s \geq 2$ [Figure 3.7(b)], as also observed in $C^b_{sca}/2C^M_{sca}$ vs. d^* [Figure 3.5(b)]. Furthermore, for $\chi_s < 2$ the oscillations reached their maxima and minima for the same values of d^* as observed for $C^b_{sca}/2C^M_{sca}$ [Figure 3.5(a)]. Moreover, g^b/g^M reached a global maximum around $d^* = 1/4$ and the subsequent

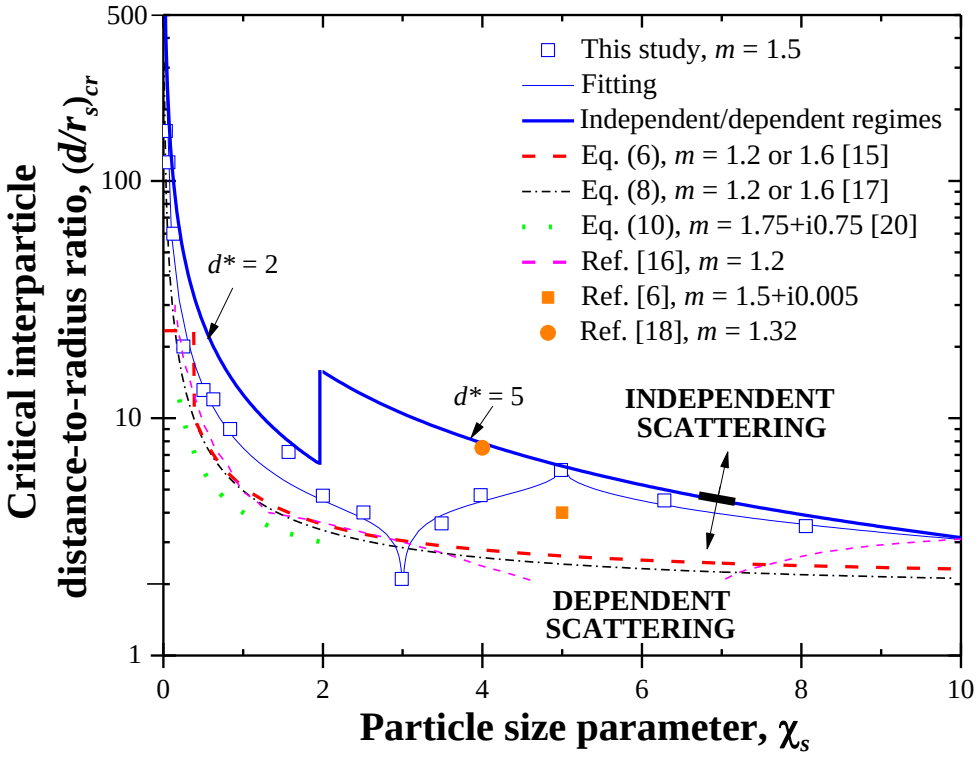

Figure 3.6: Critical interparticle distance-to-radius ratio $(d/r_s)_{cr}$ as a function of particle size parameter χ_s for bispheres with $m = 1.5$ along with data and predictions from expressions reported in the literature [12–17] and summarized in Table 3.1. The data points collected for the present study were fitted to a power series to guide the eye.

maxima and minima occured at intervals of approximately 1/2, in agreement with observations made by Videen et al. [59]. The global maximum was attributed to destructive interferences of the scattered radiation by individual particles.

Finally, Figure 3.7 indicates that g^b/g^M converged towards unity (i.e., $g^b = g^M$) as d^* increased beyond a critical interparticle distance-to-wavelength ratio d^*_{cr} when independent scattering regime prevailed. For small particles such that $\chi_s < 2$, the smaller the particles, the larger the critical interparticle distance-to-wavelength ratio d^*_{cr}. For example, the critical interparticle distance-to-wavelength ratio d^*_{cr} was 2 for $\chi_s \geq 0.628$ but reached 25 for $\chi_s = 0.126$. On the other hand, for large particles such that $\chi_s \geq 2$, independent scattering for g^b prevailed for d^* ≥ 5, as obtained also for C^b_{sca}.

Overall, this study showed that the particle size parameter χ_s and interparticle distance-to-wavelength ratio d^* are the dimensionless parameters governing the scattering cross-section and asymmetry factor of bispheres. The fact that χ_s is one parameter controlling scattering of light is well-known for single-particles [56]. However, to the best of our knowledge, this has not been demonstrated for particle systems. Similarly, the present study establishes unequivocally that d^* is the dimensionless distance parameter controlling interference effects. Note that all the results discussed so far for C^b_{sca} and g^b of bispheres were obtained for the same value of relative particle index of refraction $m = n_s/n_m = 1.5$. Thus, it is essential to consider different values of m to fully assess the validity of the above conclusions.

3.3.2 Effect of the relative index of refraction m

Effect of m on the scattering cross-section C^b_{sca}

Figure 3.8 plots the scattering cross-section ratio $C^b_{sca}/2C^M_{sca}$ as a function of the interparticle distance-to-wavelength ratio d^* for bispheres with particle size param-

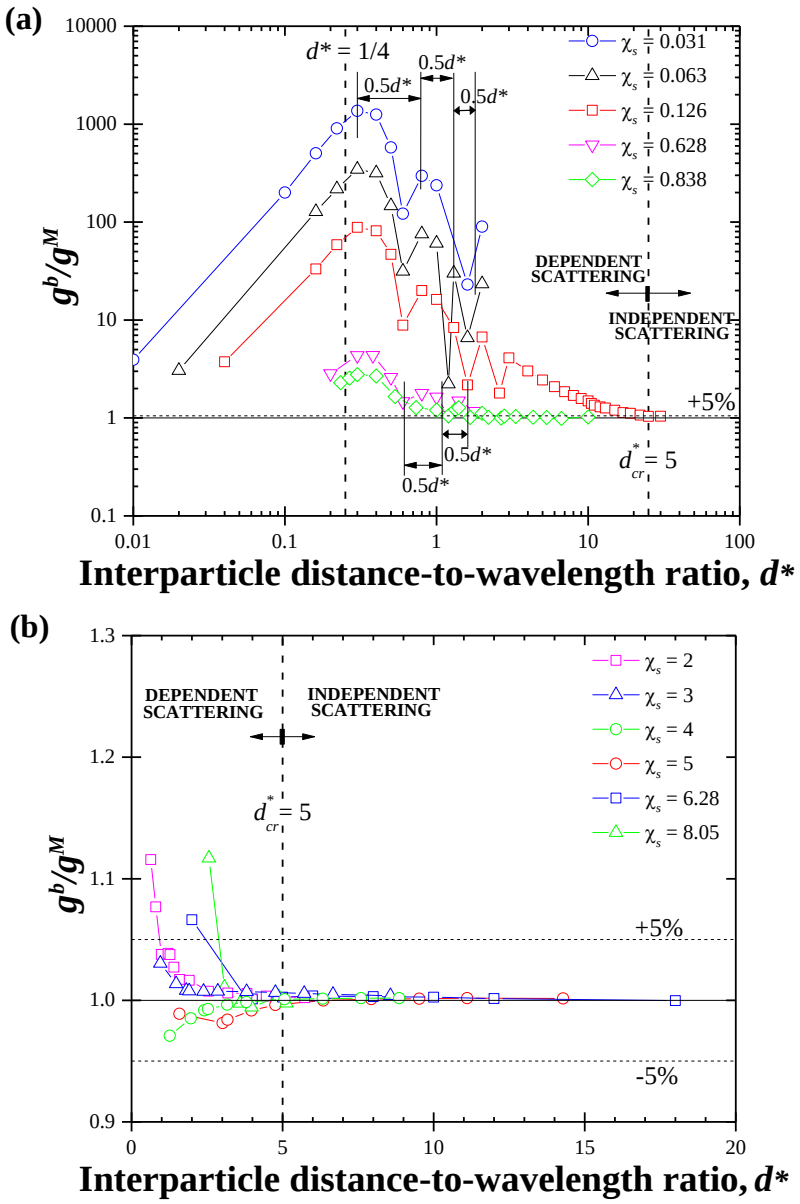

Figure 3.7: Asymmetry factor ratio g^b/g^M as a function of the interparticle distance-to-wavelength ratio d^* for bispheres with $m = 1.5$ and (a) $\chi_s \leq 2$ and (b) $\chi_s > 2$.

eter (a) $\chi_s = 0.063$ or 0.628 and (b) $\chi_s = 2$ or 4 and relative index of refraction m varying between 0.667 and 2.6. It indicates that the scattering cross-section ratio $C^b_{sca}/2C^M_{sca}$ of bispheres was independent of the relative index of refraction m for very small particle size parameter such as $\chi_s = 0.063$ as well as for $\chi_s = 0.628$ with small index mismatch ($m \leq 1.2$). This could be attributed to the fact that for small size parameter χ_s (i) the phase shift $\beta = 2\chi_s|m-1|$ was negligible and (ii) scattering was isotropic ($g^M \simeq 0$). Then, interference and interaction effects were independent of m. These results establish that C^b_{sca} can be expressed as $C^b_{sca} = 2f^b(d^*)C^M_{sca}(\chi_s,m,r_s)$ for $\chi_s|m-1| \ll 1$ where $f^b(d^*)$ is a function to be determined.

By contrast, the scattering cross-section ratio $C^b_{sca}/2C^M_{sca}$ of bispheres with $\chi_s = 2$ and 4 as well as $\chi_s = 0.628$ and $m \geq 1.5$ depended on the relative index of refraction m. Here, the phase shift across the particles was significant (e.g., $\beta = 2$ for $\chi_s = 0.628$ and $m = 2.6$) and interference effects were affected by changes in m. Moreover, scattering of the particles was anisotropic and more sensitive to m.

Finally, Figure 3.8 establishes that, here also, and regardless of m, the independent scattering regime, characterized by $C^b_{sca} = 2C^M_{sca}$, prevailed when $d^* > d^*_{cr}$ with the critical interparticle distance-to-wavelength ratio d^*_{cr} such that $d^*_{cr} = 2$ for $\chi_s \leq 2$ and $d^*_{cr} = 5$ for $\chi_s > 2$. However, note that these criteria are conservative estimates. In fact, for bispheres with $\chi_s \geq 2$ and different relative index of refraction m, the independent scattering regime was reached for different values of d^* smaller than $d^*_{cr} = 5$.

Effect of m ***on the asymmetry factor*** g^b

Figure 3.9 presents the asymmetry factor g^b as a function of d^* for bispheres with (a) $\chi_s = 0.063$ or 0.628 and (b) $\chi_s = 2$ or 4 and particle relative index of refraction m varying between 0.667 and 2.6. Here also, the asymmetry factor of bispheres

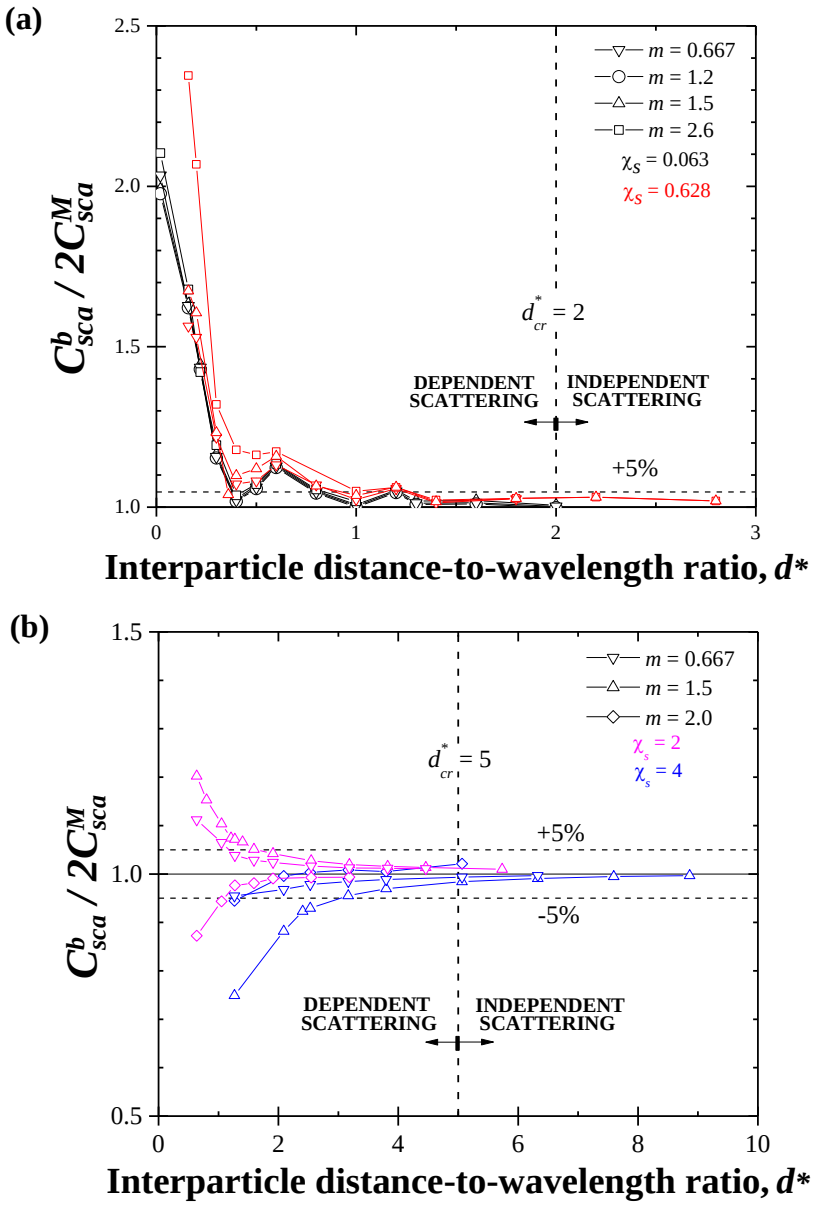

Figure 3.8: Scattering cross-section ratio $C^b_{sca}/2C^M_{sca}$ as a function of the interparticle distance-to-wavelength ratio d^* for bispheres with m varying between 0.667 and 2.6 and (a) $\chi_s = 0.063$ and 0.628 and (b) $\chi_s = 2$ and 4.

with $\chi_s = 0.063$ was not affected by the relative index of refraction m due to negligible phase shift β across the particles, as previously discussed. However, as observed for $C^b_{sca}/2C^M_{sca}$, the asymmetry factor g^b of bispheres with larger values of χ_s varied with relative index of refraction m due to the non-negligible phase shift β. In addition, Figures 3.9(c) and 3.9(d) plot the ratio g^b/g^M as a function of d^* for bispheres with the same particle size parameters and relative indices of refraction presented in Figure 3.9(a) and 3.9(b), respectively. Figure 3.9(d) establishes that for bispheres with $\chi_s \geq 2$ and any relative index of refraction m, the transition from dependent to independent scattering occurred for $d^* \geq d^*_{cr} = 2$. On the other hand, for $\chi_s < 2$, d^*_{cr} was larger than 2 for all relative index of refraction m considered [Figure 3.9(c)].

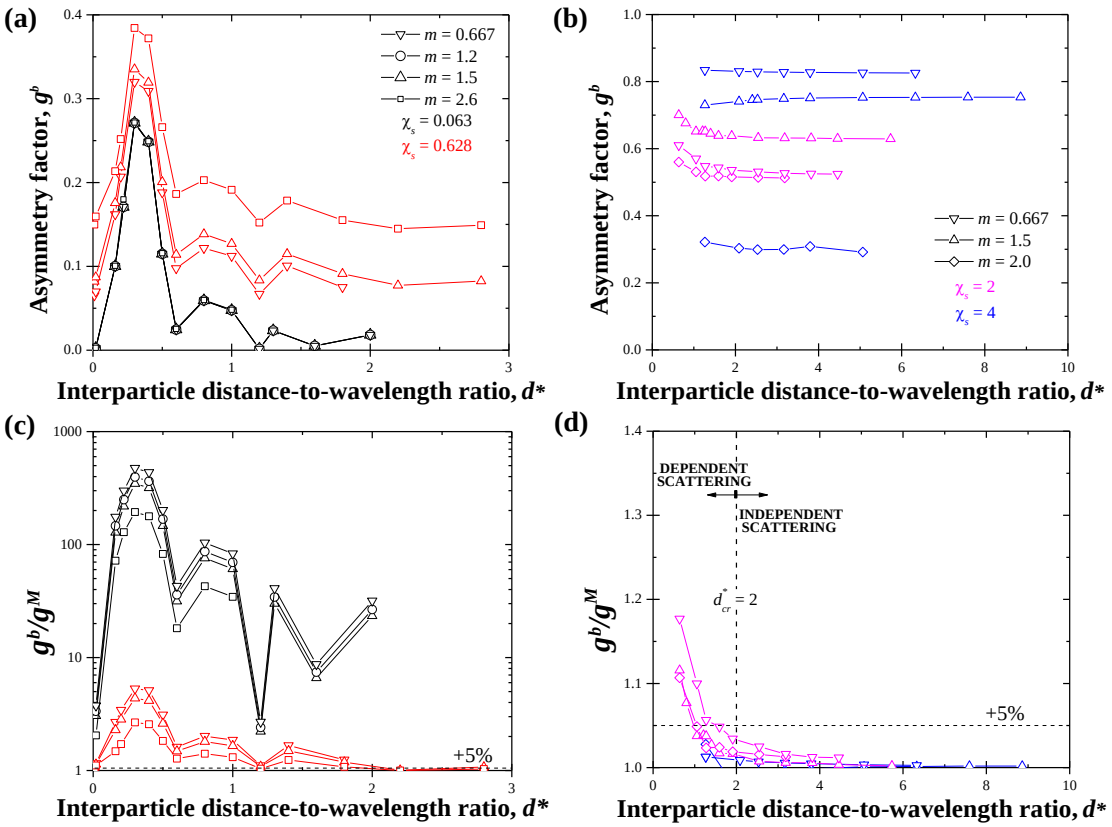

Figure 3.9: Asymmetry factor g^b as a function of the interparticle distance-to-wavelength ratio d^* for bispheres with m varying between 0.667 and 2.6 and (a) $\chi_s = 0.063$ and 0.628 and (b) $\chi_s = 2$ and 4.

Overall, Figures 3.8 and 3.9 indicate that the effect of the relative index of refraction m on dependent effects was negligible for systems with small particle size parameter $\chi_s < 2$, as observed by Olaofe [95] for bispheres and by Ivezić et al. [101] for aggregates. However, the radiation characteristics of bispheres with large particle size parameter $\chi_s \geq 2$ were affected by m. This was in agreement with conclusions made by Ma et al. [102] for aggregates.

3.3.3 Particle suspensions and aggregates

Scattering cross-section C^s_{sca}

A similar analysis to that previously performed for bispheres was conducted for a 4 particle tetrahedron to identify the parameters governing the scattering characteristics of suspensions and aggregates. The scattering cross-section ratio $C^s_{sca}/N_s C^M_{sca}$ and asymmetry factor g^s of the tetrahedron were found to be also functions of (i) the particle size parameter χ_s, (ii) the relative index of refraction m, and (iii) the interparticle distance-to-wavelength ratio d^* (Figures B.6 and B.7 in Supporting Information).

Figure B.9 in Supporting Information plots the scattering cross-section ratio of bispheres, disordered, and ordered particle systems ($N_s = 2$, 4, or 8) as a function of the average interparticle distance-to-wavelength ratio $\bar{d}^*$ with a relative index of refraction $m = 1.5$. First, Figure B.9 indicates that the oscillations for disordered particle suspensions with small particle size parameter χ_s were not as well structured as those obtained for bispheres and ordered particle systems. This was due to variations in the interparticle distance among pairs of particles. Moreover, Figure S9 shows that ordered particle systems with $N_s = 4$ and 8 featured a critical average interparticle distance-to-wavelength ratio $\bar{d}^*_{cr} = 2$ beyond which independent scattering prevailed for $\chi_s = 0.031$, 0.126, and 0.628 and $\bar{d}^*_{cr} = 5$ for $\chi_s = 3$, as observed for bispheres. However, disordered particle systems featured

transition from the dependent to the independent scattering regimes for higher critical average interparticle distance-to-wavelength ratio. In fact, the criterion $\bar{d}^*_{cr} = 2$ developed for bispheres with $\chi_s = 0.031$, 0.126, and 0.628 did not apply to disordered particle systems with the same particle size parameter. This was due to the fact that disordered particle systems had a broader interparticle distance distribution and especially smaller minimum interparticle distances d_{min} than ordered particle systems. These observations establish that bispheres were not representative of actual disordered particle suspensions contradicting the hypothesis made by Quirantes et al. [12]. Instead, results for bispheres provided the lower limit for the critical distance d_{cr} among pairs of particles required to reach the independent scattering regime.

Figure 3.10 presents the scattering cross-section of bispheres, disordered, and ordered particle systems ($N_s = 2$, 4, or 8) as a function of the minimum interparticle distance-to-wavelength ratio $d^*_{min} = d_{min}/\lambda$ with a relative index of refraction $m = 1.5$. Figure 3.10 shows that the criteria (i) $d^*_{min,cr} = 2$ for $\chi_s \leq 2$ and (ii) $d^*_{min,cr} = 5$ for $\chi_s > 2$ developed for bispheres could also be applied conservatively to disordered and ordered particle systems with various interparticle distance distribution. Note that Figure 3.10 also indicates that ordered particle systems fell under the independent scattering regime for slightly larger values of d^*_{min} than that observed for bispheres. This suggests that the total number of particles N_s affected slightly dependent scattering effects.

Figures S9 and 3.10 establish that for small particle size parameter $\chi_s = 0.031$, 0.126, and 0.628, (i) dependent effects resulted in $C^s_{sca} \geq N_s C^M_{sca}$ and (ii) the scattering cross-section ratio $C^s_{sca}/N_s C^M_{sca}$ increased with increasing number of particles N_s, as predicted by Equation (3.12). These observations were due to the fact that scattering by small particles was isotropic leading to increased multiple scattering with increasing N_s. It is also interesting to note that for simple cubic systems ($N_s = 8$) with small touching spheres such that $\chi_s = 0.031$ and 0.126,

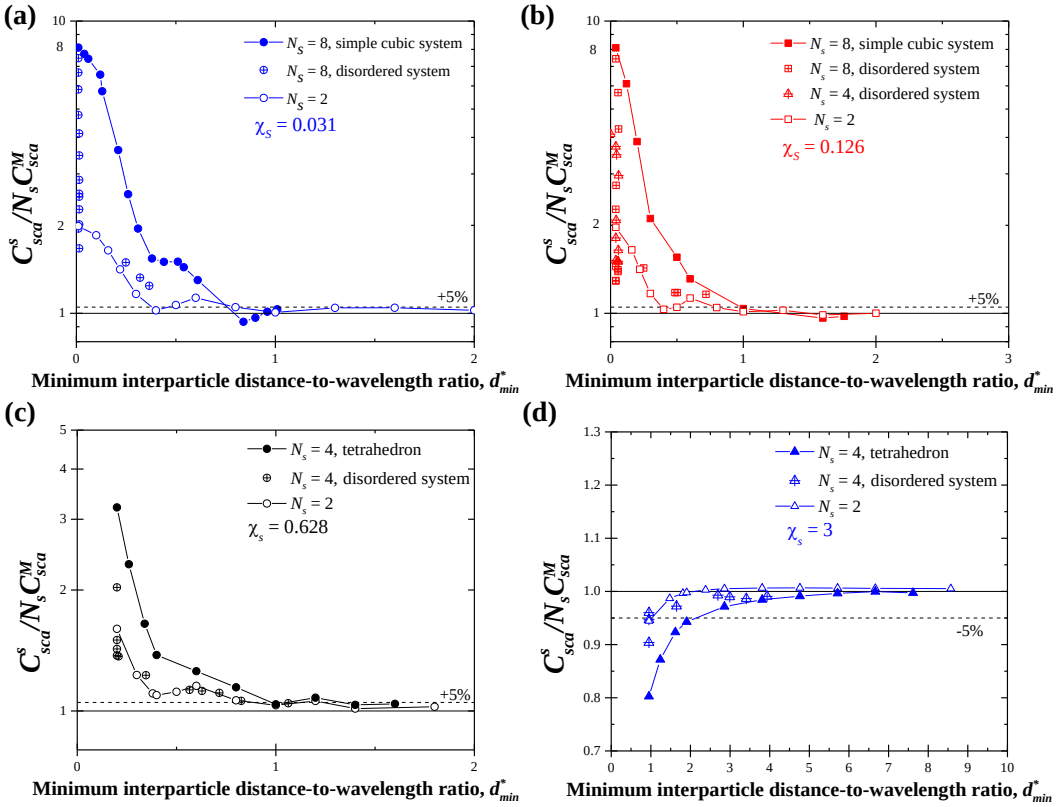

Figure 3.10: Scattering cross-section ratio as a function of the minimum interparticle distance-to-wavelength ratio d^*_{min} for bisphere ($N_s = 2$), ordered, and disordered particle suspensions or aggregates with $N_s = 4$ or 8 for $m = 1.5$ and (a) $\chi_s = 0.031$, (b) $\chi_s = 0.126$, (c) $\chi_s = 0.628$, and (d) $\chi_s = 3$.

$C^s_{sca} = 64C^M_{sca}$, as predicted by the volume equivalent model [Equation (3.12)].

Finally, note that the critical particle volume fraction $f_{v,cr} = 0.006$ proposed by Tien and Drolen [15] and below which independent scattering prevailed for $\chi_s < 0.388$ was found to be inadequate for both the disordered and ordered particle systems simulated in the present study. Indeed, for $\chi_s = 0.031$ and 0.126, the independent scattering regime prevailed for much lower volume fractions (see Figure S10 of Supporting Information).

Asymmetry factor g^s

Figure B.11 in Supporting Information presents the asymmetry factor g^b and g^s of bispheres, disordered, and ordered particle systems as functions of the average interparticle distance-to-wavelength ratio $\bar{d}^*$. First, Figures B.11(a)-B.11(c) show that the asymmetry factor increased with increasing particle number N_s and that oscillations were present for disordered and ordered particle systems for $\chi_s = 0.031$, 0.126, and 0.628. Moreover, Figures B.11(b)-B.11(d) indicate that the asymmetry factor of ordered particle systems with $\chi_s \geq 0.1$ and $N_s = 4$ or 8 tended towards those of bispheres ($N_s = 2$) for $\bar{d}^* \geq 2$, unlike that of disordered particle systems. This was due to the broader interparticle distance distribution of disordered systems, as mentioned previously.

Figure 3.11 presents the asymmetry factor g^b and g^s of bispheres, disordered, and ordered particle systems as functions of the minimum interparticle distance-to-wavelength ratio d^*_{min} for the same cases considered in Figure 3.10. Figure 3.11 shows that the asymmetry factor of disordered and ordered particle systems with $\chi_s \geq 0.1$ converged towards that of bispheres for $d^*_{min} \geq 2$. Therefore, Figure 3.11 suggests that particle suspensions with $\chi_s = 0.628$ and 3 reached the independent scattering regime for the same critical minimum interparticle distance-to-wavelength ratio as bispheres, i.e., when $d^*_{min} \geq d^*_{min,cr} \simeq 5$. On the

other hand, for $\chi_s = 0.031$, Figure 3.11 indicates that the independent scattering regime was reached for $d^*_{min} \geq d^*_{min,cr} > 5$.

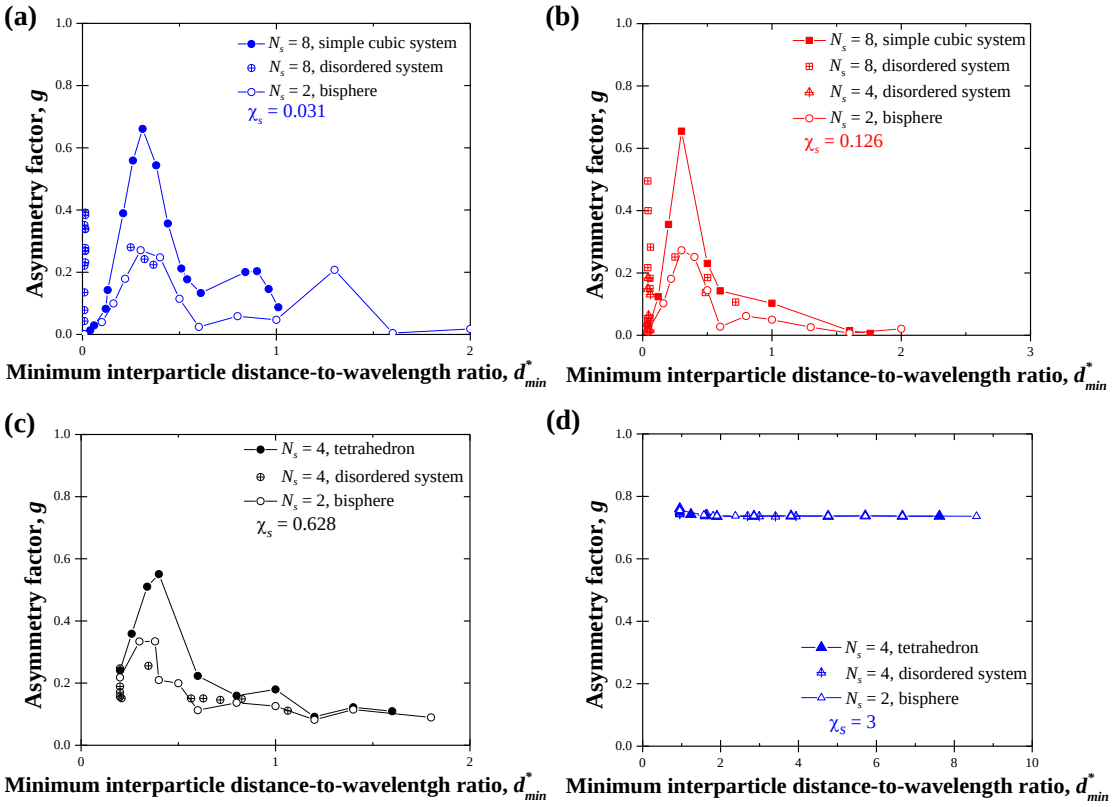

Figure 3.11: Asymmetry factor as a function of the minimum interparticle distance-to-wavelength ratio d^*_{min} for bisphere ($N_s = 2$), ordered, and disordered particle systems with $N_s = 4$ or 8 with $m = 1.5$ and (a) $\chi_s = 0.031$, (b) $\chi_s = 0.126$, (c) $\chi_s = 0.628$, and (d) $\chi_s = 3$.

3.4 Conclusion

This study determined (1) the parameters governing the scattering cross-section and asymmetry factor of bispheres, disordered and ordered particle suspensions, and aggregates of non-absorbing spherical particles and (2) the conditions under which dependent and independent scattering regimes prevail for each radiation characteristic. A wide range of parameters was investigated using the DDA method including (i) particle size parameter χ_s varying from 0.031 to 8.05, (ii)

relative index of refraction m ranging from 0.667 to 2.6, and (iii) average interparticle distance-to-wavelength ratio $\bar{d}^*$ varying between χ_s/π (touching particles) and 30. The scattering cross-section ratio $C_{sca}/N_s C_{sca}^M$ and asymmetry factor g were shown to be functions exclusively of the number of particles N_s, their size parameter χ_s, their relative index of refraction m, and the interparticle distance-to-wavelength ratio d^*. Additionally, the transition between independent and dependent scattering regimes was shown to be different for the scattering cross-section and the asymmetry factor. For all cases considered, the criteria $\bar{d}^* \geq 2$ for $\chi_s \leq 2$ and $\bar{d}^* \geq 5$ for $\chi_s > 2$ were shown to ensure conservatively that the independent scattering approximation was valid for the scattering cross-section of structures featuring interparticle distances with relatively small standard deviation and for all values of m considered. Similarly, the critical average interparticle distance-to-wavelength ratio $\bar{d}_{cr}^*$ associated with the asymmetry factor (i) reached values as high as 25 for $\chi_s < 2$ and (ii) was equal to $\bar{d}_{cr}^* = 5$ for $\chi_s \geq 2$. Finally, this study demonstrated that results obtained for bispheres could be extended to the disordered particle systems considered provided the transition criteria were based on the minimum interparticle distance-to-wavelength ratio d_{min}^* instead of on the average interparticle distance-to-wavelength ratio $\bar{d}^*$.

CHAPTER 4

Scattering Characteristic Approximations for Non-Absorbing Aggregates

This chapter demonstrates that the integral scattering characteristics of non-absorbing aggregates consisting of spherical particles with size parameter less than 1 can be rapidly estimated as those of homogeneous spheres with the same volume and effective refractive index. The so-called equivalent effective property (EEP) approximation predicted the scattering cross-section and asymmetry factor when dependent scattering prevailed. Dependent scattering effects were shown to increase with decreasing particle size parameter x_s. The results also established that overlapping of particles had a negligible effect on the scattering cross-section and asymmetry factor of non-absorbing aggregates.

4.1 Background

4.1.1 Scattering regimes map

Figure 4.1 illustrates the scattering regime map plotting the particle size parameter x_s versus the average interparticle distance-to-wavelength ratio $\bar{d}/\lambda$ [111]. The transition from dependent to independent scattering regimes corresponds to a relative difference in the predicted scattering cross-section exceeding 5%. The transition occurs for an average interparticle distance-to-wavelength ratio $\bar{d}/\lambda = 2$ for $x_s \leq 2$ and $\bar{d}/\lambda = 5$ for $x_s > 2$. Note that for the aggregate asymmetry factor, the transition from the dependent to the independent scattering regimes for particles with $x_s > 2$ was also achieved for $\bar{d}/\lambda = 5$. However, for $x_s \leq 2$ the transition was achieved for $\bar{d}/\lambda$ as high as 25 [111]. The effect of the relative refractive index

m was shown to be negligible when varied between 0.67 and 2.6 [111]. Figure 4.1 also maps x_s and $\bar{d}/\lambda$ of typical particle systems consisting of non-absorbing aggregates, as those previously mentioned. It indicates that dependent scattering of light can prevail for various particle systems such as mesoporous materials or atmospheric aerosols.

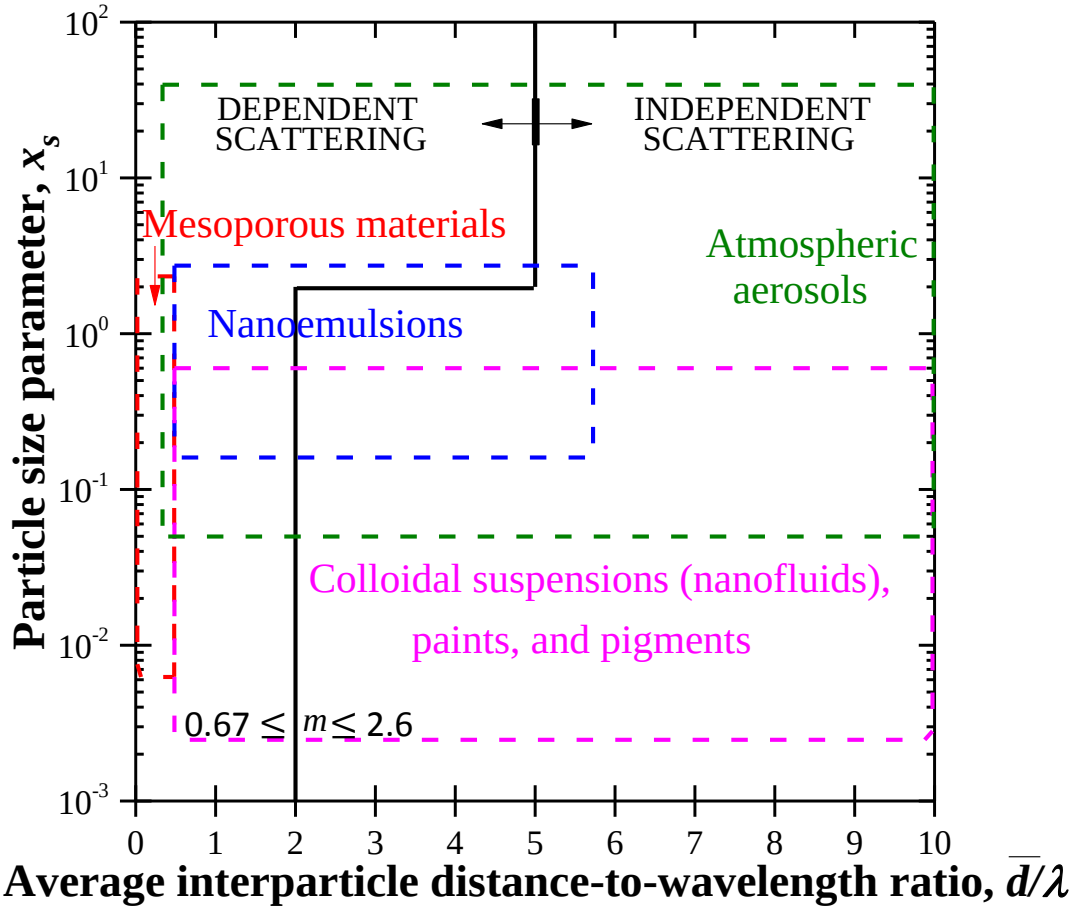

Figure 4.1: Scattering regime map for the scattering cross-section plotting zones of typical particle systems with respect to their particle size parameter x_s and average interparticle distance-to-wavelength ratio between constituent particles.

4.1.2 Scattering approximations

There exists numerous approximations predicting the scattering cross-section C^a_{sca} and asymmetry factor g^a of fractal aggregates consisting of monodisperse particles.

All approximations require knowing (i) the particle size parameter x_s, (ii) the particle relative complex refractive index $m = (n_s + ik_s)/n_m$, and (iii) the spatial arrangement of the particles in the aggregate.

For example, the Rayleigh-Debye-Gans (RDG) theory and the anomalous diffraction approximation assume that the phase shift of the wave passing through optically soft spheres satisfies the condition $|m - 1| \ll 1$ [112, 113]. On the one hand, the RDG theory predicts the scattering and absorption cross-sections, and the asymmetry factor of aggregates with monodisperse point-contact spheres such that $x_s \ll 1$. Expressions for C^a_{abs}, C^a_{sca}, and g^a not only depend on (i) x_s and (ii) m but also on the aggregate's (iii) fractal dimension, (vi) radius of gyration, (v) structure factor, and (vi) number of particles N_s [112, 113]. On the other hand, the anomalous diffraction approximation considers aggregates consisting of large point-contact particles such that $x_s \gg 1$ [114]. The scattering cross-section C^a_{sca} of the aggregates can be predicted based on (i) x_s, (ii) m, (iii) the path of light through the particles in the aggregate, and (iv) the aggregate's projected area [114].

Alternatively, other approximations model aggregates as equivalent homogeneous spheres. These approximations necessitate relatively few structural information about the aggregate and can also be used for aggregates with surface-contact particles. Two of the most commonly used approximations includes the equivalent volume (EV) [15, 55] and the equivalent effective properties (EEP) [15, 19–21] approximations illustrated in Figure 4.2. The EV approximation models the aggregate as an equivalent sphere with the same complex index of refraction as the particles m_s and effective radius r_{eff} such that the volume of the equivalent sphere matched the volume V_s of the aggregate occupied by the particles, i.e.,

$$\frac{4\pi}{3} r^3_{eff} = V_s = f_v V_t \tag{4.1}$$

where V_t is the total volume of the aggregate and f_v is the particle volume fraction calculated as the ratio of the volume V_s occupied by the particles to the total volume V_t of the aggregate, i.e., $f_v = V_s/V_t$. For aggregates with monodisperse point-contact particles of radius r_s, V_s can be expressed as $V_s = 4\pi r_s^3 N_s/3$ and Equation (4.1) simplifies to $r_{eff} = r_s N_s^{1/3}$.

Moreover, the EEP approximation models the aggregate as an equivalent sphere of radius R_s encompassing the aggregate such that [21]

$$R_s = (3V_t/4\pi)^{1/3}. \tag{4.2}$$

Here, the equivalent sphere has an effective refractive index n_{eff} given by some effective medium approximation (EMA) [Figure 4.2(c)]. In this study, the 3D Maxwell-Garnett EMA was used to predict n_{eff} according to

$$n_{eff}^2 = n_m^2 \left[1 - \frac{3f_v(n_m^2 - n_s^2)}{2n_m^2 + n_s^2 + f_v(n_m^2 - n_s^2)}\right]. \tag{4.3}$$

In both the EV and EEP approximations, the scattering cross-sections, denoted by C_{sca}^{EV} and C_{sca}^{EEP}, and the asymmetry factors, g^{EV} and g^{EEP}, of their respective equivalent spheres can be predicted using the Lorenz-Mie theory [56].

4.1.3 Equivalent sphere approximations

Previous studies have investigated the applicability of the EV [18,55] and EEP [18–21] approximations for predicting the radiation characteristics of non-absorbing aggregates [18, 21] and suspensions [19, 20] with monodisperse spherical particles. Drolen and Tien [18] studied the scattering and absorption cross-sections of spherical, cubical, and ellipsoidal clusters and linear chains of monodisperse particles with $x_s = 0.00785$, 0.037, and 0.0393 and aggregate size parameter $\chi_s \leq 5$ defined as $\chi_s = 2\pi R_s/\lambda$. The number of particles N_s in the aggregates was less than

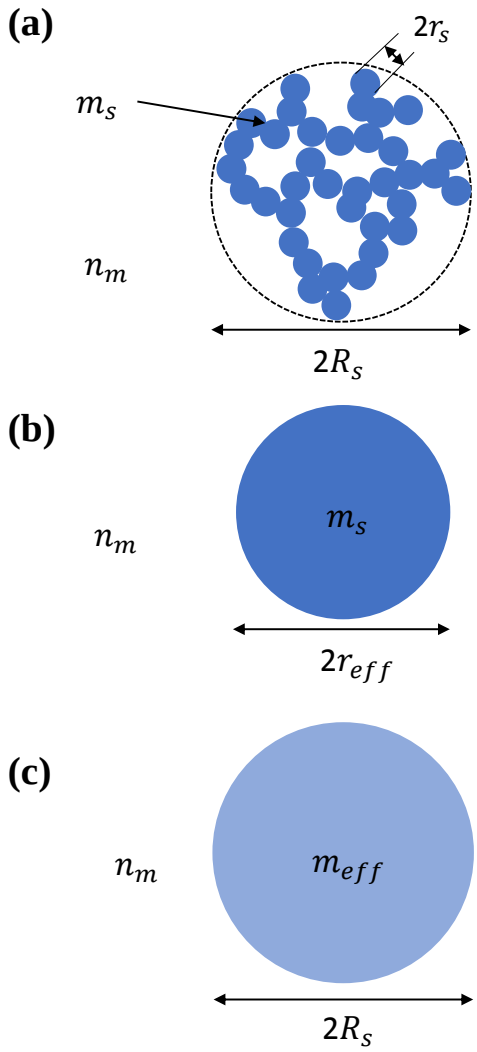

Figure 4.2: (a) Particle aggregate and its equivalent representations (b) in the EV approximation and (c) in the EEP approximation.

136, the particle volume fraction f_v varied from 0.05 to 0.95, and the particle relative complex index of refraction was $m = m_s/n_m = 2.0+i0.95$, $3.5+i3$, and $1.5+i10^{-6}$. The authors compared the EV and EEP approximations based on the Maxwell-Garnett EMA for both n_{eff} and k_{eff} with predictions from an analytical model based on the solution of Maxwell's equations for spheres in the Rayleigh scattering regime [109, 115]. The study showed that predictions by the EV approximation were in good agreement with results from the analytical model for chains with a small number of particles ($N_s < 30$) and for all clusters considered. By contrast, the EEP model was in good agreement with the analytical model for all aggregates investigated.

Lagarrigue et al. [21] investigated the scattering cross-section of non-absorbing aggregates with particle size parameter $x_s \leq 0.63$, number of particles $N_s > 13$, and aggregate size parameter $\chi_s \leq 3.14$. The relative refractive index of the monodisperse particles was $m = n_s/n_m = 2.35$ or 2.58. The aggregates were generated in spherical and cubic domains as well as cylindrical or ellipsoidal domains featuring aspect ratios varying from 1/20 to 20. The aggregates' particle volume fractions f_v varied from 0.0605 to 0.605. The generalized multiparticle Mie theory algorithm was used to compute the aggregates scattering cross-section. The authors showed that the applicability of the EEP approximation, based also on the Maxwell-Garnett EMA, depended on the aspect ratio of the aggregate. As the aspect ratio deviated from unity, the EEP approximation differed from the numerical predictions. The study also concluded that the effect of the particle size on the validity of the EEP approximation was negligible. An empirical expression for the scattering cross-section of aggregates was derived by fitting the scattering cross-section of 1,792 aggregates with various shapes, sizes, particle size parameters, relative refractive index, and aspect ratios and was given by [21]

$$C_{sca} = 0.81 f_v^{0.11} \bar{d}_s^{-0.66} C_{sca}^{EEP}. \tag{4.4}$$

Here, $\bar{d}_s$ is the average interparticle distance of the aggregate normalized by the aggregate radius R_s and C_{sca}^{EEP} is the scattering cross-section calculated using the EEP approximation for a sphere of radius R_s.

Mishchenko et al. [19] used the T-matrix method to compute the elements of the normalized scattering matrix of randomly distributed non-touching and non-absorbing spherical particles and compared them to the EEP approximation based on the Maxwell-Garnett EMA. The non-touching particles featured x_s = 0.3, 0.5, or 1 and were embedded in a spherical domain with size parameter χ_s = 10. The particle refractive index was $n_s = 1.55$ and that of the surrounding medium was $n_m = 1.33$. The aggregates' particle volume fraction f_v was 0.216 or 0.2 and the number of particles N_s varied from 216 to 8,000. The authors showed that suspensions with particles such that $x_s = 0.3$ and 0.5 were within the range of validity of the EEP approximation while those consisting of particles with $x_s = 1$ fell outside. In addition, by comparing results for suspensions with the same particle size parameter $x_s = 0.3$ and different number of particles ($N_s = 500$ and 8,000) the authors concluded that N_s should be sufficiently large to ensure the validity of the EEP approximation. However, the authors wrote that "*the threshold value of x_s and N_s can be expected to depend on the refractive indices of the host and the inclusions as well as on the size parameter of the host and should be further analyzed and quantified*".

Mishchenko et al. [20] extended the analysis of Ref. [19] to non-touching particle suspensions with a wider range of particle size parameter x_s and suspension size parameter χ_s representative of air bubbles ($n_s = 1$) and hematite inclusions ($m_s = 3.102+i0.0925$) in dust material ($n_m = 1.6$). For air bubbles, x_s varied from 0.15 to 1.09, $\chi_s = 4$ or 8, and N_s ranged from 1 to 3,035. For hematite inclusions, x_s varied from 0.1 to 0.5, $\chi_s = 4$ or 8, and N_s ranged from 10 to 10,240. Results were also presented for non-absorbing suspensions of particles with x_s = 0.3 or 0.6, $\chi_s = 10$, N_s = 1,000 and 8,000, refractive index n_s varying from 1.4

to 2, and $n_m = 1.32$. The particle volume fraction was $f_v = 0.02$ for air bubbles and hematite particles and $f_v = 0.216$ for other non-absorbing suspensions. The elements of the scattering matrix, the scattering and absorption cross-sections, and the asymmetry factor of the suspensions were calculated using the T-matrix method and the EEP approximation based on the Maxwell-Garnett EMA for both n_{eff} and k_{eff}. For all cases considered, predictions of the scattering cross-section and asymmetry factor by the EEP approximation fell within 6.5% of those by the T-matrix method. However, predictions of the elements of the scattering matrix by the EEP approximation differed significantly from the T-matrix calculations for aggregates with $x_s \geq 0.5$. In addition, the difference between predictions of the two methods increased with increasing suspension size parameter and refractive index mismatch between the particles and their surrounding. The authors concluded that a larger refractive index mismatch restricted the range of validity of the EEP approximation to aggregates with smaller particles. This observation suggests that the validity of the EEP approximation depends on the phase shift $x_s|m-1|$.

Finally, Figure 4.3 illustrates the ranges of particle size parameter x_s, aggregate or suspension size parameter χ_s, and phase shift $x_s|m-1|$ used in the different studies investigating the validity of the EV and EEP approximations for systems consisting of non-absorbing spherical particles [15, 19–21]. It indicates that previous studies were limited to relatively small particle size parameter x_s (≤ 1.09) and aggregate size parameter χ_s (≤ 10). Although the refractive index n_s of the particle was sometimes large [21], the particles were relatively small and, therefore, the range of the phase shift $x_s|m-1|$ explored was limited to 0.85. Moreover, none of the previous studies investigated the effect of particle overlapping on the applicability of the EEP approximation. The present study aims to systematically assess the validity of the EEP model for predicting the scattering cross-section C^a_{sca} and the asymmetry factor g^a of aggregates with point-contact and surface-contact par-

ticles over a large range of relevant parameters. In particular, it is interesting to determine if this approximation is also valid in the dependent scattering regime.

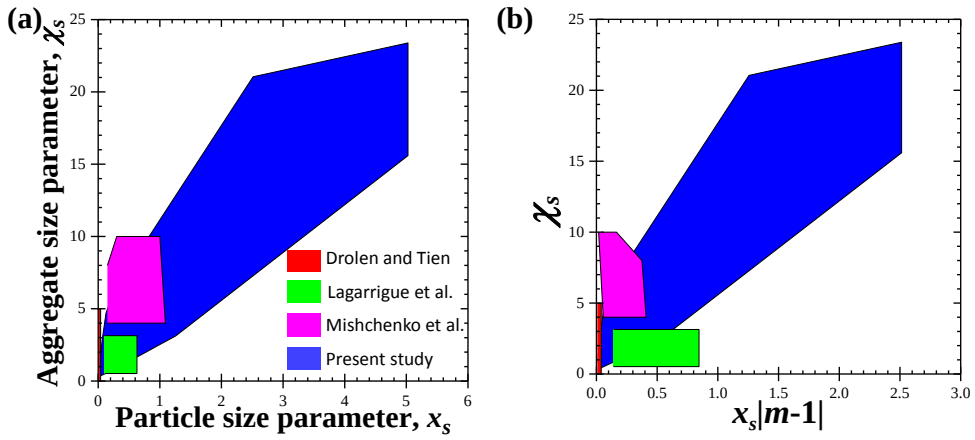

Figure 4.3: Aggregate size parameter χ_s as a function of (a) the particle size parameter x_s and (b) the optical phase shift $x_s|m-1|$ for computer-generated aggregates investigated in Refs. [18–21].

4.2 Analysis

4.2.1 Computer-generated aggregates

The DLCCA algorithm [116] was used to generate aggregates consisting of N_s spherical monodisperse particles of radius r_s positioned in a three-dimensional spherical simulation domain of radius R_s or in a cubic domain of side L. For cubic simulation domains, the radius R_s encompassing the aggregate was defined as the radius of a sphere having the same total volume as the aggregate, i.e., $V_t = L^3$ and was calculated from Equation (4.2). Two types of structures were generated namely (1) aggregates with point-contact particles where spherical particles may touch each other at a point but do not overlap and (2) aggregates with surface-contact particles consisting of overlapping spherical particles [116]. The particle radius r_s ranged from 2.5 to 400 nm, R_s varied from 6 nm to 1860 nm, and the wavelength λ was set to 500 nm corresponding to x_s varying from 0.031 to 5.03

and χ_s varying from 0.08 to 23. The number of particles N_s ranged from 5 to 30,000 and the refractive index n_s of the particles was set to $n_s = 1.5$ while the surrounding medium was vacuum, i.e., $n_m = 1$ resulting in $m = 1.5$. Finally, the particle volume fraction f_v of all computer-generated structures was 33±2%. This choice of f_v was arbitrary. However, if the EV or EEP approximations are found to be valid for $f_v = 33\pm2\%$, it is reasonable to expect them to be valid for other values of f_v whose effect is accounted for through the equivalent sphere radius r_{eff} [Equation (4.1)] or via the effective refraction index n_{eff} [Equation (4.3)].

4.2.2 Scattering characteristics

The multiple sphere T-matrix (MSTM) code developed by Mackowski [117] and based on the superposition T-matrix method [118] was used to predict the scattering efficiency factor Q^a_{sca} and the asymmetry factor g^a of the computer-generated aggregates with point-contact particles generated numerically. The input parameters of the MSTM code included (i) the position of the constitutive monodisperse particles, (ii) their size parameter $x_s = 2\pi r_s/\lambda$, and (iii) their relative refractive index m.

To consider the complex geometry of aggregates with surface-contact particles, the discrete-dipole approximation (DDA) algorithm developed by Draine and Flatau [98] was employed. First, N_d dipoles of size Δd were generated inside the N_s particles of the numerically-generated aggregates such that $\sum_{i=1}^{N_d}(\Delta d)^3 = V_s$. The dipoles were such that their size Δd was small compared to the particle radius r_s and wavelength λ to achieve numerically converged results independent of the choice of discretization [110]. The input parameters of the DDA method included (i) the position of the N_d dipoles, (ii) the wavelength λ, (iii) the relative refractive index m, and (iv) the effective radius of the aggregate r_{eff} which can also be expressed as $r_{eff}=(3V_s/4\pi)^{1/3}$.

The integral radiative characteristics can be predicted either for aggregates with a given orientation or for randomly oriented aggregates. However, fixed-orientation and orientation-averaged scattering efficiency factors were found to differ by less than 1% and the asymmetry factors by less than 4% for both point-contact and surface-contact aggregates with $x_s \leq 0.13$ (see Table C.1 in Supporting Information). This observation was likely due to the fact that particles with small x_s scatter radiation isotropically resulting in very similar scattering characteristics for different aggregates' orientations. Therefore, simulations for aggregates with point-contact particles with $x_s \leq 0.13$ and large aggregate size parameter χ_s were performed for a fixed orientation to reduce the computational time. On the other hand, for aggregates with particles such that $x_s > 0.16$, the reported scattering cross-section and asymmetry factor were those of the orientation-averaged aggregates averaged over at least 55 orientations.

The scattering cross-section C^a_{sca} (in nm^2) of aggregates consisting of N_s monodisperse point-contact and surface-contact particles can be calculated from the radius r_{eff} and the computed efficiency factor Q^a_{sca} such that [110, 117]

$$C^a_{sca} = \pi r^2_{eff} Q^a_{sca}. \tag{4.5}$$

Finally, the scattering coefficient σ_s of the aggregate was calculated according to [55]

$$\sigma_s = C^a_{sca}/V_t. \tag{4.6}$$

4.3 Results and discussion

4.3.1 Dependent effects in aggregates

Figure 4.4 presents the absorption and scattering cross-section ratios $C^a_{abs}/N_s C^M_{abs}$ and $C^a_{sca}/N_s C^M_{sca}$, and asymmetry factor ratio g^a/g^M as functions of χ_s for fractal

aggregates with point-contact particles with size parameter $x_s = 0.031$ and 0.63, particle volume fraction $f_v = 33 \pm 2\%$, and relative refractive index $m = n + ik$ such that $n = 1.5$ and $0 \leq k \leq 0.5$. Here, C_{abs}^M, C_{sca}^M, and g^M are the absorption cross-section, scattering cross-section, and asymmetry factor of a particle of size parameter x_s calculated using Lorenz-Mie theory. Ratios $C_{abs}^a / N_s C_{abs}^M$, $C_{sca}^a / N_s C_{sca}^M$, and g^a / g^M equal to unity would indicate that the radiation characteristics of the aggregates represent the cumulated effects of individual constitutive particles, i.e., the particles scattered and absorbed independently of each other. First, Figures 4.4(a)-4.4(d) establish that dependent effects prevailed in the absorption and scattering of the aggregates considered, as all ratios exceeded or fell below 1. However, the ratio $C_{sca}^a / N_s C_{sca}^M$ increased significantly more than $C_{abs}^a / N_s C_{abs}^M$ with increasing χ_s. These observations were in agreement with results reported in previous studies [119, 120]. Figures 4.4(c) and 4.4(d) also suggest that the increase in the aggregate scattering cross-section ratio $C_{sca}^a / N_s C_{sca}^M$ was larger for aggregates with small particle size parameter x_s. These results indicate that for applications with small absorbing nanoparticles ($x_s \leq 0.1$) such as those found in nanofluids for solar energy applications [10, 121–123], the nanoparticles can be assumed to absorb independently (i.e., $C_{abs}^a \approx N_s C_{abs}^M$), but dependent scattering prevailed (i.e., $C_{sca}^a > N_s C_{sca}^M$).

Figures 4.4(a) and 4.4(b) also show that the ratio $C_{abs}^a / N_s C_{abs}^M$ decreased with increasing relative absorption index k for any given aggregate size parameter $\chi_s > 0.6$. For very large values of k, C_{abs}^a was even smaller than C_{abs}^M. The same findings were presented in Ref. [120] for aggregates consisting of monodisperse particles with $x_s = 1$, $n = 1.0165$, $0 \leq k \leq 0.5$, and $N_s < 1000$. This observation was attributed to the so-called "shielding" or "shading" effect of the aggregate's inner particles by those located outside responsible for the increased attenuation of the electromagnetic wave before reaching the inner particles. In addition, Figures 4.4(c) and 4.4(d) indicate that the scattering cross-section ratio $C_{sca}^a / N_s C_{sca}^M$ was

not affected by absorption for $\chi_s \leq 0.7$. However, for $\chi_s > 1$, the ratio $C^a_{sca}/N_s C^M_{sca}$ decreased with increasing relative absorption index k for any given value of χ_s.

Finally, Figures 4.4(e) and 4.4(f) show that dependent scattering effects in aggregates with large size parameter χ_s and small particle size parameter x_s were significant and resulted in $g^a > g^M$. In addition, the effect of the particle relative absorption index k on the asymmetry factor ratio g^a/g^M was negligible despite its effect on $C^a_{sca}/N_s C^M_{sca}$. Note that the same conclusions were reached for all three ratios $C^a_{abs}/N_s C^M_{abs}$, $C^a_{sca}/N_s C^M_{sca}$, and g^a/g^M for particle size $x_s = 2.51$, as presented in Figure C.1 in Supporting Information.

Overall, Figure 4.4 shows the importance of studying the scattering characteristics C^a_{sca} and g^a of particle aggregates for a wide range of particle x_s and aggregate χ_s size parameters.

4.3.2 Equivalent models for non-absorbing fractal aggregates

Scattering cross-section C^a_{sca}

Figure 4.5(a) plots the scattering cross-section C^a_{sca} predicted by the T-matrix method [117, 118] as a function of the aggregate size parameter χ_s for fractal aggregates with particle volume fraction $f_v = 33 \pm 2\%$ generated in cubic or spherical domains with point-contact particles of size parameter x_s ranging from 0.031 to 5.03 and relative refractive index $m = 1.5$. Figure 4.5(a) also displays the scattering cross-section of the same aggregates predicted by the EV and EEP approximations. First, Figure 4.5(a) indicates that the scattering cross-section of aggregates C^a_{sca} increased with increasing aggregate size parameter χ_s for all particle size parameter x_s. Figure 4.5(a) also establishes that both the EV and EEP approximations were in good agreement with the T-matrix method predictions of C^a_{sca} for relatively small aggregates with $\chi_s \leq 1$. These observations were consistent with those of Ref. [15]. For $\chi_s > 1$, the scattering cross-section C^a_{sca} of the

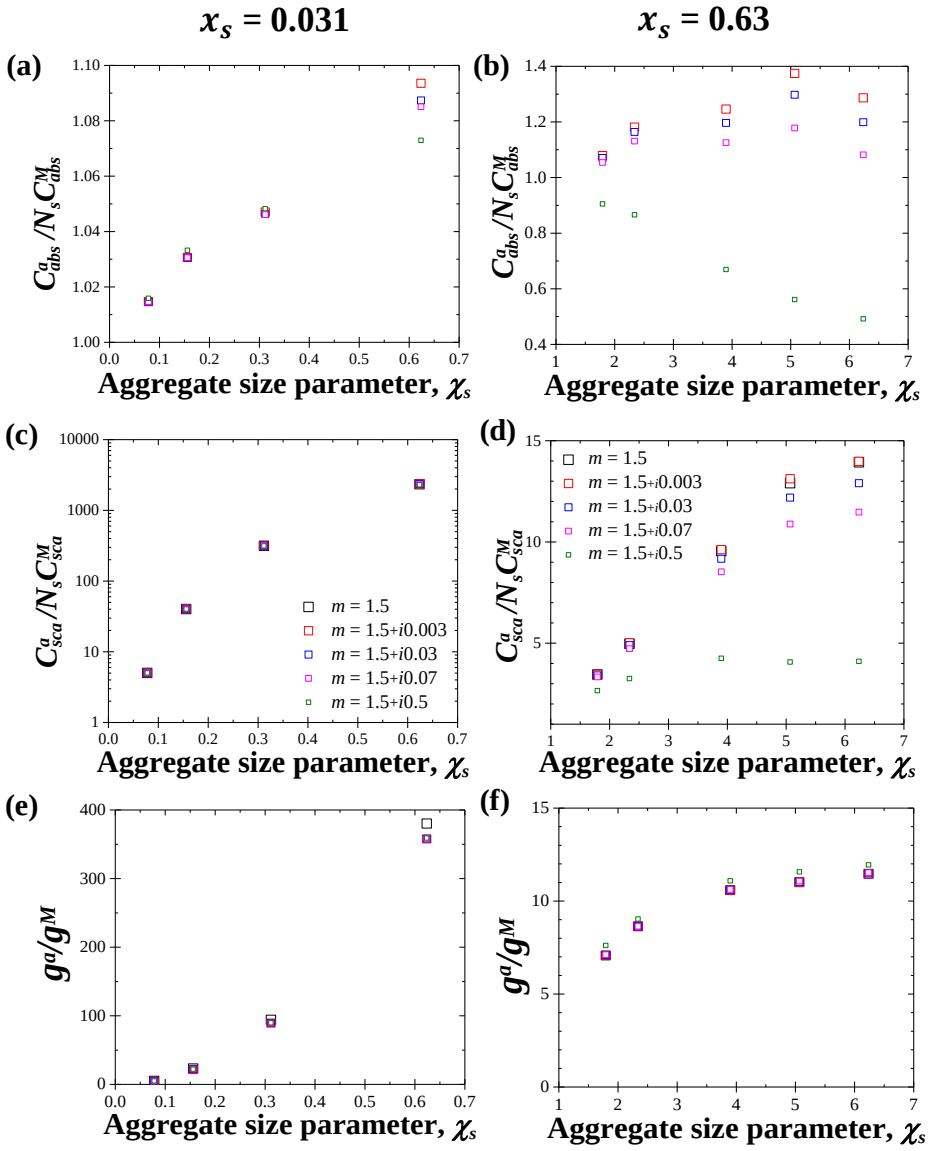

Figure 4.4: (a)-(b) Absorption cross-section ratio $C^a_{abs}/N_sC^M_{abs}$, (c)-(d) scattering cross-section ratio $C^a_{sca}/N_sC^M_{sca}$, and (e)-(f) asymmetry factor ratio g^a/N_sg^M as functions of the aggregate size parameter χ_s for aggregates with particle size parameter (a, c, e) $x_s = 0.031$ and (b, d, f) $x_s = 0.63$, particle volume fraction $f_v = 33\pm2\%$, and relative refractive index m between 1.5 and 1.5+i0.5.

aggregates differed significantly from that predicted by the EV approximation.

In addition, Figure C.2(a) in Supporting Information presents the relative error in the scattering cross-section $|C^a_{sca}\text{-}C^{EEP}_{sca}|/C^a_{sca}$ between numerical predictions and EEP approximation, with respect to the aggregate χ_s and particle x_s size parameters. Figure C.2(a) shows that the relative error $|C^a_{sca}\text{-}C^{EEP}_{sca}|/C^a_{sca}$ varied between 0 and 80% for χ_s varying from 0.08 to 23 and x_s from 0.031 to 5.03. Interestingly, Figure C.2(a) also indicates that $|C^a_{sca}\text{-}C^{EEP}_{sca}|/C^a_{sca} \leq 15\%$ when $x_s < 1.1$, $x_s|m-1| < 0.55$, and any χ_s considered. When $x_s \geq 1.1$, the ratio C^a_{sca}/C^{EEP}_{sca} varied between 0 and 80% with varying x_s and χ_s, but no clear and systematic effect of x_s or χ_s could be identified.

Asymmetry factor g^a

Figure 4.5(b) presents the asymmetry factor g^a as a function of the aggregate size parameter χ_s for non-absorbing aggregates with point-contact particles with x_s varying between 0.031 and 5.03, $m = 1.5$, and particle volume fraction $f_v = 33\pm2\%$. It also plots predictions obtained by the EV and EEP approximations. Figure 4.5(b) shows that the asymmetry factor g^a depended not only on the aggregate size χ_s but also on the particle size x_s. For given values of χ_s and f_v, aggregates with smaller particles had larger asymmetry factor g^a indicating that they scattered more in the forward direction. Moreover, Figure 4.5(b) indicates that the predictions of the EEP approximation of the asymmetry factor of aggregates were in good agreement with those of the T-matrix method for particles such that $x_s \leq 0.63$. However, the EV approximation failed to predict g^a accurately for all cases considered.

Figure C.2(b) presents the relative error in the asymmetry factor $|g^a - g^{EEP}|/g^a$, where g^{EEP} is the asymmetry factor predicted by the EEP model, as a function of the aggregate χ_s and particle x_s size parameters. First, Figure C.2(b) shows clear

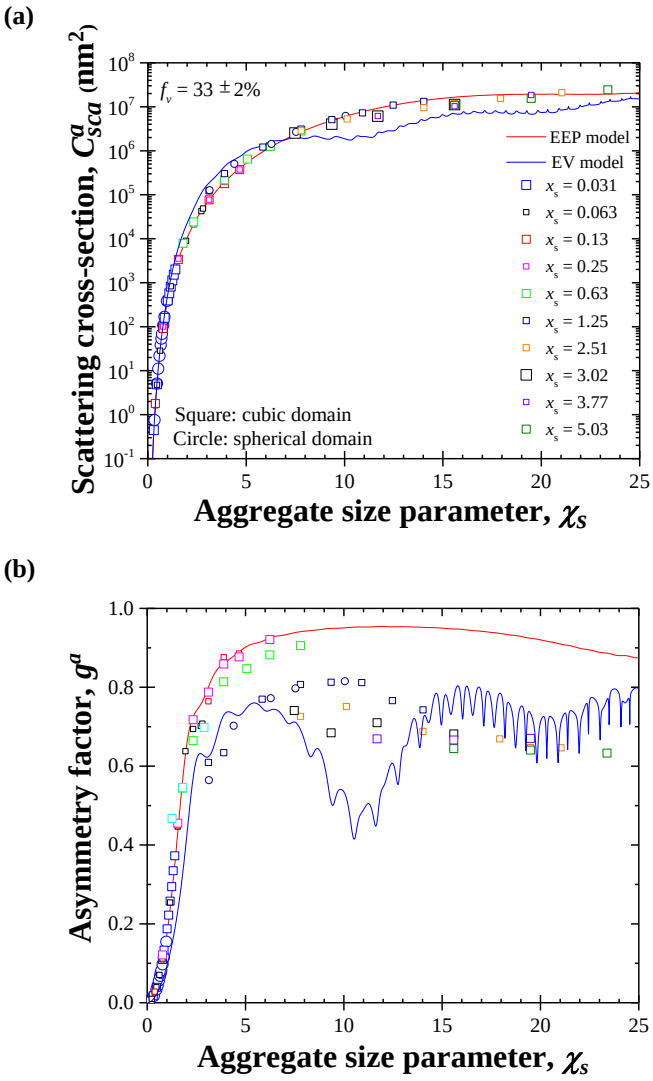

Figure 4.5: (a) Scattering cross-section C^a_{sca} and (b) asymmetry factor g^a of point-contact particle aggregates as functions of the aggregate size parameter χ_s for particle size parameter x_s ranging from 0.031 to 5.03, particle volume fraction f_v = 33±2%, and relative refractive index m = 1.5.

variations in $|g^a - g^{EEP}|/g^a$ with varying x_s and χ_s, contrary to $|C^a_{sca}\text{-}C^{EEP}_{sca}|/C^a_{sca}$ [Figure C.2(a)]. In fact, Figure C.2(b) indicates that the ratio $|g^a - g^{EEP}|/g^a$ increased from 0 to 50% with decreasing particle size parameter x_s and aggregate size parameter χ_s. Moreover, Figure C.2(b) indicates that the relative error $|g^a - g^{EEP}|/g^a$ was within 15% for aggregates with $x_s < 1.1$ and any χ_s considered.

Scattering coefficient σ_s

Figure 4.6 presents the scattering coefficient σ_s [Equation (4.5)] of spherical and cubic aggregates as a function of the size parameter χ_s for particle volume fraction $f_v = 33 \pm 2\%$ and point-contact particles featuring x_s between 0.031 and 5.03 and $m = 1.5$. It also plots predictions by the EEP approximation. First, Figure 4.6 indicates that the scattering coefficient σ_s increased sharply with increasing χ_s to reach a maximum for $\chi_s = 10$, corresponding to $2R_s \approx 3\lambda$. However, as χ_s increased above 10, σ_s decreased and the EEP approximation featured oscillations for $\chi_s \geq 25$. Moreover, Figure 4.6 shows that numerical predictions of σ_s were independent of x_s and of the aggregate shape when $\chi_s \leq 4$. For $\chi_s > 4$, σ_s depended slightly on the particle size x_s and the aggregate shape. Note that the predictions given by the EEP approximation decreased as χ_s increased and did not converged (see Figure C.3 in Supporting Information). This observation suggests that the scattering coefficient of aggregates does not reach a plateau with increasing χ_s and converge towards that of films, monoliths, or bulk materials consisting of the same porous medium. This indicates that representing porous monoliths, films, or bulk materials by aggregates to predict their radiative properties, as done in the literature [123–125], is not an appropriate approach.

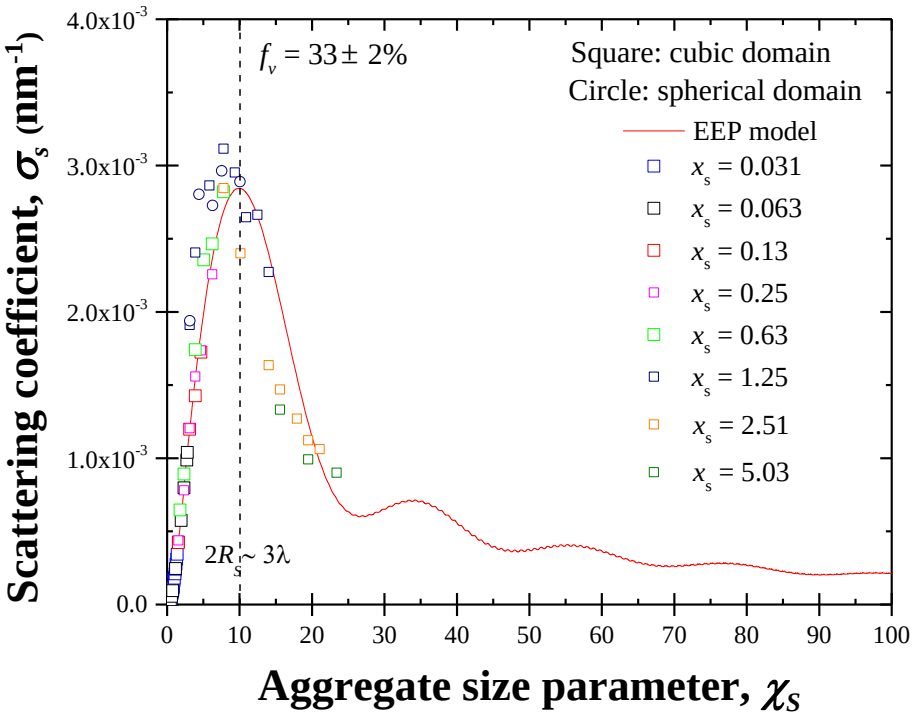

Figure 4.6: Scattering coefficient σ_s of point-contact particle aggregates as a function of the aggregate size parameter χ_s for particle size parameter x_s ranging from 0.031 to 5.03, particle volume fraction $f_v = 33\pm2\%$, and relative refractive index $m = 1.5$.

Dependent scattering effects

Figure 4.7 plots the relative (a) scattering cross-section ratio $C^a_{sca}/N_sC^M_{sca}$ and (b) asymmetry factor ratio g^a/g^M as functions of the aggregate size parameter χ_s for the same range of parameters considered previously including $0.031 \leq x_s \leq 5.03$ and $m = 1.5$. First, Figure 4.7 indicates that C^a_{sca} deviated from $N_sC^M_{sca}$ more strongly for small values of x_s. Indeed, smaller particles scatter radiation isotropically resulting in increased multiple scattering in the aggregates. This observation was consistent with the conclusions of Ref. [111] for aggregates and suspensions with $2 \leq N_s \leq 8$. Moreover, Figure 4.7 indicates that dependent scattering effects resulted in $C^a_{sca}/N_sC^M_{sca} > 1$ and $g^a/g^M > 1$ for $x_s < 2.51$ and in $C^a_{sca}/N_sC^M_{sca} < 1$ and $g^a/g^M \sim 1$ for $x_s \geq 2.51$. Interestingly, Figure 8(a) suggests that $C^a_{sca}/N_sC^M_{sca}$ reached its maximum when $\chi_s \simeq 10$ and then decreased with decreasing χ_s, similarly to σ_s. On the other hand, the asymmetry factor ratio g^a/g^M increased with increasing χ_s and then reached a plateau when $\chi_s > 2$. Finally, Figure 4.7 establishes that the EEP model predicted the scattering cross-section and asymmetry factor with a relative error of 15% of aggregates with $x_s|m-1| < 0.55$ when dependent scattering prevailed.

4.3.3 Effect of particle overlapping

Figure 4.8 plots (a) the scattering cross-section C^a_{sca} and (b) asymmetry factor g^a of aggregates as functions of χ_s for cubic aggregates with $f_v = 33\pm2\%$ and with point-contact and surface-contact particles with x_s ranging from 0.063 and 1.25. It also shows predictions by the EEP and EV approximations. First, Figure 4.8 indicates that overlapping between particles did not strongly affect the scattering characteristics of the aggregates. Indeed, the scattering cross-section C^a_{sca} of aggregates with surface-contact particles fell within 15% of that of aggregates with point-contact particles with the same aggregate size χ_s, particle size x_s, and

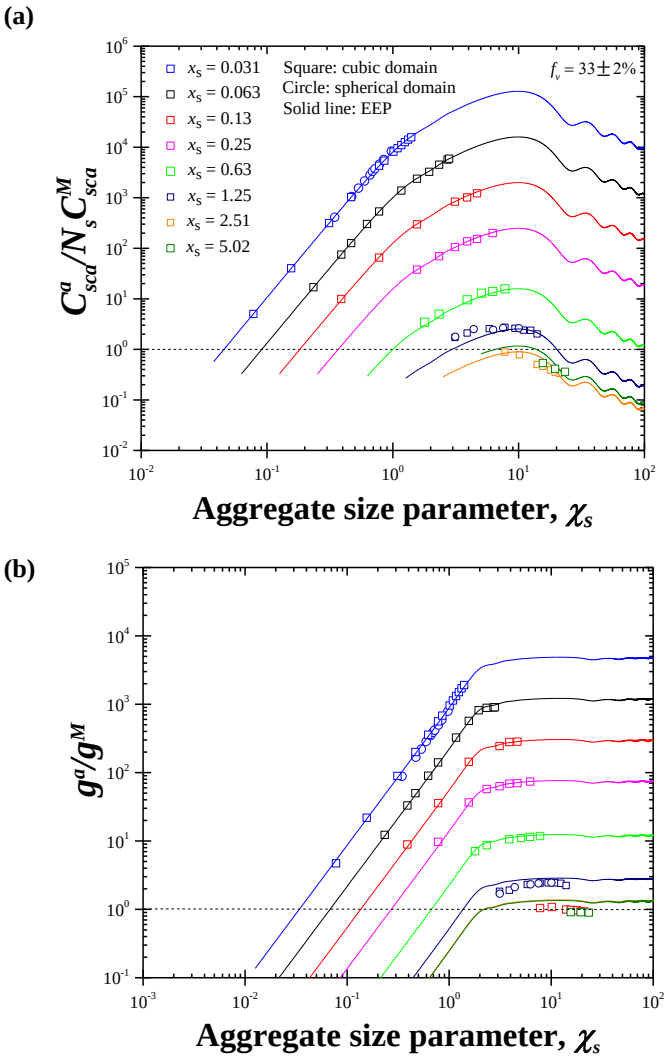

Figure 4.7: (a) Scattering cross-section ratio $C^a_{sca}/N_sC^M_{sca}$ and (b) asymmetry factor ratio g^a/g^M of point-contact particle aggregates as functions of the aggregate size parameter χ_s for particle size parameter x_s ranging from 0.031 to 5.03, particle volume fraction $f_v = 33\pm2\%$, and relative refractive index $m = 1.5$.

similar particle volume fraction f_v (see Table C.2 in Supporting Information). Similarly, the asymmetry factor g^a of aggregates with surface-contact particles fell within 10% of that of the equivalent aggregates but with point-contact particles and similar f_v. This observation suggests that the scattering cross-section and asymmetry factor of non-absorbing aggregates were mainly dependent on (i) the aggregate size parameter χ_s, (ii) the particle volume fraction f_v, and (iii) the relative refractive index m of the particles.

4.4 Conclusion

This study investigated the scattering cross-section and asymmetry factor of aggregates consisting of non-absorbing spherical particles and the validity of the EEP approximation. A wide range of parameters was studied using the multiple sphere T-matrix and DDA methods, including (i) point-contact and surface-contact particles, (ii) particle size parameter x_s varying from 0.031 to 5.03, and (iii) aggregate size parameter χ_s up to 23. The results established that dependent scattering effects in aggregates were more significant than dependent absorption effects. The former increased with decreasing particle size parameter for both absorbing and non-absorbing aggregates. Furthermore, the predictions of the scattering coefficient σ_s by the EEP approximation showed that σ_s does not reach a plateau as χ_s increased, suggesting that the scattering coefficient of aggregates cannot be used to model porous monoliths, films, or bulk materials. This study also showed that particle overlapping had no effect on the scattering cross-section and asymmetry factor of non-absorbing aggregates for all sizes considered. Finally, the study demonstrated that the EEP approximation could predict the scattering cross-section and asymmetry factor of non-absorbing aggregates with $x_s|m-1| < 0.55$ in the dependent scattering regime.

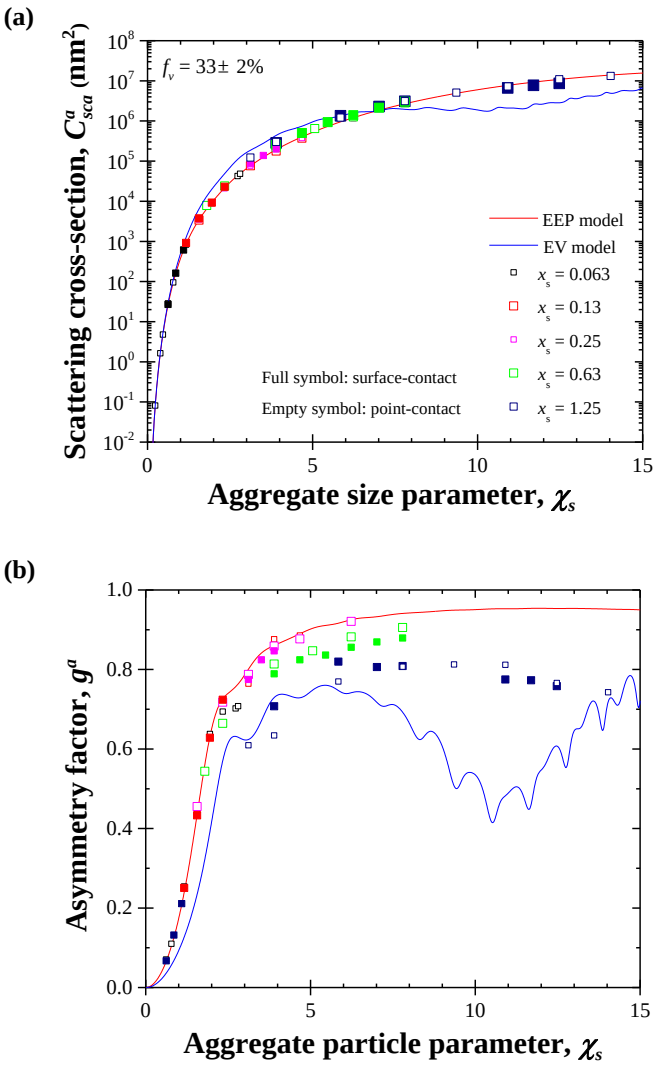

Figure 4.8: (a) Scattering cross-section C^a_{sca} and (b) asymmetry factor g^a of point-contact and surface-contact particle aggregates as functions of the aggregate size parameter χ_s for particle size parameter x_s between 0.063 and 1.25, particle volume fraction $f_v = 33\pm2\%$, and $m = 1.5$. Also shown are predictions by the EEP and EV approximations.

CHAPTER 5

Drying of Mesoporous Monoliths: from Transparent to White to Transparent Again

This chapter explains the changes in appearance observed in sol-gel synthesis of mesoporous monoliths during drying under ambient conditions. First, the gel monoliths remained transparent during the constant rate period when the gels shrank. Then, the mesoporous monoliths turned white during the so-called falling rate period when the pores started emptying, before becoming transparent again at the end of the drying process. The haziness and white appearance were attributed to scattering by growing drained regions encompassing multiple pores and featuring a refractive index mismatch with the surrounding wet monolith. The scattering coefficient and asymmetry factor of the drained regions were modeled by approximating the wet and dry mesoporous regions as homogeneous, non-absorbing, and polydisperse domains with some effective refractive indices. Then, the radiative transfer equation was solved by the Monte Carlo method to predict the transmittance and haze of a 2 mm thick monolith. The model predictions were in good agreement with experimental measurements obtained during drying of water-based nanoparticle-based mesoporous silica monoliths.

5.1 Background

Drying of all gels can be divided into two consecutive stages namely the constant rate period and the falling rate period [49, 126–128]. During the constant rate period, solvent evaporation occurs at the monolith's surface. The monolith shrinks uniformly and the pores remain filled with solvent. Once the monolith becomes

too stiff to shrink, the drying process enters the falling rate period as air replaces the evaporating solvent. Brinker and Scherer [49, 126] further divided the falling rate period into two successive regimes namely (i) the first falling rate period and (ii) the second falling rate period. During the first falling rate period, the solvent was predominantly transported along pore walls to the monolith's surface where it evaporated [49]. During this period, some solvent also evaporated within the monolith and was transported to the outside by diffusion. The second falling rate period started when isolated pockets of solvent appeared in the monolith. Then, evaporation only occurred within the monolith and the gaseous solvent diffused out of the monolith through the open pores [49]. More recently, Thiery et al. [127, 128] studied ambiently dried particle-based silica monoliths with particle diameter varying from 6 nm to 45 μm, and revisited the drying mechanisms occurring during the falling rate period. Their studies indicate that the drying mechanisms depended on the pore size. For particle diameter larger than 40 nm, solvent transport and vapor diffusion occurred simultaneously in monoliths after the constant rate period. In fact, these monoliths featured (i) a drying front advancing inward thanks to vapor diffusion through the dry porous region and (ii) an homogeneous desaturation in the wet region progressively drained through liquid solvent flow [128]. On the other hand, for particle diameter less than 40 nm, only solvent transport occurred during the falling rate period such that the solvent remained homogeneously distributed in the monolith [127, 128].

Figure 5.1 shows a sequence of photographs illustrating how nanoparticle-based mesoporous silica monoliths [129] appear transparent, white, and transparent again during the course of the drying process. Two potential causes of scattering in drying porous monoliths responsible for their milky appearance have been commonly mentioned, namely (1) the refractive index mismatch between the air entrapped in the pores and the solid phase [49, 126] and (2) scattering by regions of drained or wet pores [49, 127]. First, Brinker and Scherer [49] hy-

pothesized that "the saturated body is translucent or transparent because of the similarity in refractive index of the solid and liquid, but the lower index of air causes scattering of light". This reasoning explains the opacity of dry and drying porous monoliths consisting of large particles and pores, comparable to the wavelength of visible light. Indeed, as large pores empty and feature a significant refractive index mismatch with the solid particle network, they scatter light. However, pores in the nanoparticle-based monolith of Figure 5.1 were less than 12 nm, much smaller than the wavelength of visible light, and featured a narrow size distribution causing limited scattering and resulting in transparent monoliths when fully dry [129]. Therefore, the difference in refractive index between the solvent and the air in individual mesopores cannot explain the transition from transparent to white during the drying stage (Figure 5.1). Alternatively, drained pores can form relatively large mesoporous regions - with size on the order or larger than the wavelength of visible light - and feature strong refractive index mismatch with the surrounding wet monolith. Although the same observations as those illustrated in Figure 5.1 have been mentioned anecdotally in the literature [49, 126, 127], to the best of our knowledge, the observed changes in appearances during the drying step of the sol-gel process have never been rigorously documented, physically modeled, or theoretically investigated.

5.2 Experiments

5.2.1 Material Synthesis

The water-based synthesis method used to synthesize nanoparticle-based silica monoliths was described in detail in Ref. [129] and need not be repeated here. In brief, a commercially available aqueous colloidal solution of silica nanoparticles Nalco 2326 (15 wt% in water, NH_3 stabilized, Nalco^{TM} Chemical Company, Naperville, IL) with an average particle diameter of 9 nm was poured in a solid

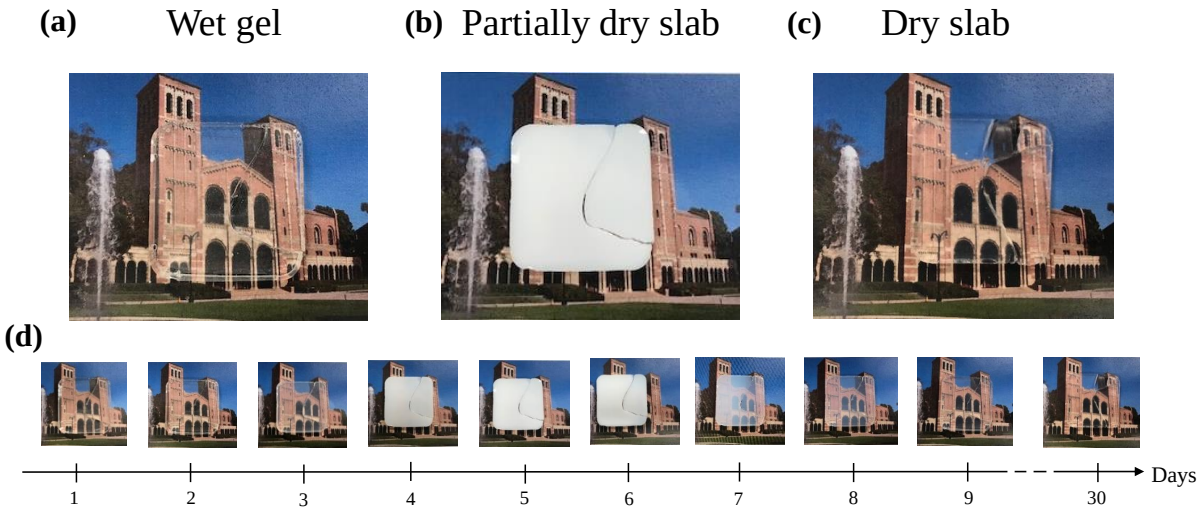

Figure 5.1: Photographs of the (a) wet, (b) partially dry, and (c) dry nanoparticle-based mesoporous silica monolith dried from water. (d) Photographs of the same mesoporous silica monolith drying over 30 days. The monolith was photographed on an image of UCLA Royce Hall [22] (modified and redistributed with permission from Ref. [23] Copyright Prayitno).

PTFE mold. Water slowly evaporated resulting in gelation and aging of the monoliths at room temperature. Then, the monoliths were dried at ambient temperature and atmospheric pressure in a covered or open dish. Note that the monoliths continued aging during the drying process due to the presence of water in the pores. At the end of the drying stage, the monoliths were calcined for 4 hours at 450 °C in oxygen to remove any trace of water and organic residues.

5.2.2 Characterization

The total mass $m_m(t)$ of the mesoporous silica monoliths was measured at regular time intervals t during drying using an Entris balance (Sartorius, Gottingen, Germany). The mass fraction of water $x_w(t)$ remaining in the mesoporous silica monoliths was estimated according to

$$x_w(t) = \frac{m_m(t) - m_s}{m_s} \tag{5.1}$$

where m_s is the mass of silica in the monolith corresponding to the mass of the calcined and fully dried monoliths. The monolith dimensions were also monitored to calculate its shrinkage throughout the drying process.

The normal-hemispherical transmittance $T_{nh,\lambda}$ of the mesoporous silica monoliths was measured at each time interval with a double-beam UV-Vis spectrophotometer (Shimadzu 3101-PC, Kyoto, Japan) and an integrating sphere with an internal diameter of 60 mm (Shimadzu ISR 3100). The reference signal B_λ and the normal-hemispherical transmitted signal $S_{nh,\lambda}$ through the sample were measured under collimated and normally incident radiation and corrected for the dark signal D_λ to yield the sample normal-hemispherical transmittance given by

$$T_{nh,\lambda} = \frac{S_{nh,\lambda} - D_\lambda}{B_\lambda - D_\lambda}. \tag{5.2}$$

The dark signal D_λ was collected when no light entered the integrating sphere. The reference signal B_λ was measured in the same configuration as for $S_{nh,\lambda}$ but without sample.

The haze of the mesoporous monolith, characterizing its cloudiness, can be defined as [130]

$$h_\lambda = \frac{S_{d,\lambda}}{S_{nh,\lambda}} - \frac{M_\lambda}{B_\lambda} \tag{5.3}$$

where the diffuse transmitted signal $S_{d,\lambda}$ represents the fraction of the collimated and normally incident radiation that is scattered and eventually transmitted by the sample in directions other than the incident direction. The signal $S_{d,\lambda}$ was measured by removing the highly reflecting plate facing the sample in the integrating sphere so that the unscattered light escaped. Here, M_λ is the signal measured in the same configuration as for $S_{d,\lambda}$ but without sample.

The visible transmittance T_{vis} and haze h_{vis} were calculated by weighting the spectral normal-hemispherical transmittance $T_{nh,\lambda}$ and haze h_λ by the photopic spectral luminous efficiency function V_λ of the human eye in daytime between

wavelength of 380 and 780 nm [54, 131], i.e.,

$$T_{vis} = \frac{\int_{380}^{780} V_\lambda T_{nh,\lambda} \mathrm{d}\lambda}{\int_{380}^{780} V_\lambda \mathrm{d}\lambda} \quad \text{and} \quad h_{vis} = \frac{\int_{380}^{780} V_\lambda h_\lambda \mathrm{d}\lambda}{\int_{380}^{780} V_\lambda \mathrm{d}\lambda}. \tag{5.4}$$

Here, V_λ was tabulated in Ref. [131].

Finally, low-temperature nitrogen adsorption-desorption isotherms of the final calcined monoliths were measured at -196°C using a surface area and porosity analyzers TriStar II 3020 (Micromeritics Instrument Corp., Norcross, GA, USA). The pore size distribution and final porosity ϕ_F were retrieved from adsorption isotherms of the calcined monoliths using the Barrett-Joyner-Halenda (BJH) method [83]. The monolith porosity $\phi(t)$ during the constant rate period can be estimated from the measured volume shrinkage and the final porosity ϕ_F. During the falling rate period, as shrinkage stopped, the porosity can also be assumed to be equal to ϕ_F.

5.3 Analysis

The objective of this section is to develop a radiation transfer model predicting the normal-hemispherical transmittance and haze of the mesoporous monoliths during the constant rate and falling rate periods. Then, the model predictions can be compared with experimental measurements to validate the model hypotheses and confirm the causes of changes in the appearance of sol-gel monoliths during drying.

5.3.1 Assumptions

During both the constant rate and falling rate periods, the mesoporous monolith was assumed to be non-absorbing in the visible. Specifically, during the constant rate period, when the monolith is fully wet, light scattering by the pores can also be ignored, since the latter are much smaller than the wavelength. Then,

the monolith can be approximated as that of a plane-parallel, homogeneous, and transparent monolith with optically smooth surfaces. During the falling rate period, we hypothesize that the mesoporous monoliths appeared white and hazy due to volumetric scattering by dry regions forming and growing within the wet gel, as illustrated in Figure 5.2. The monolith was assumed to contain $N_T(t)$ polydisperse and spherical dry regions per unit volume of monolith (in $\#/\mu\text{m}^3$), homogeneously distributed and embedded in domains of solvent-filled mesopores, as illustrated in Figure 5.2(a). The dry and wet domains were assumed to be homogeneous with effective refractive index $n_{D,\lambda}$ and $n_{W,\lambda}$, respectively [Figures 5.2(b) and 5.2(c)]. The refractive indices of air $n_{a,\lambda}$, water $n_{w,\lambda}$, and silica $n_{s,\lambda}$ were assumed to be constant and were taken as $n_{a,\lambda} = 1$, $n_{w,\lambda} = 1.33$, and $n_{s,\lambda} = 1.5$, respectively [132]. Note that this model is consistent with the drying mechanism of solvent transport identified for nanoparticle-based silica monoliths in Refs. [127,128]. At the end of the falling rate period, the monolith is fully dry and can be approximated as that of a plane-parallel, homogeneous, and transparent monolith, similarly to the fully wet monolith.

5.3.2 Water mass fraction x_w

During the constant rate period, the monolith shrinks while remaining fully wet. Its water mass fraction x_w can be expressed as

$$x_w(t) = \frac{m_m(t) - m_s}{m_s} = \frac{m_w(t)}{m_s} = \frac{\rho_w}{\rho_s}\frac{\phi(t)}{1-\phi(t)} \tag{5.5}$$

where $\rho_s = 2.2$ g/cm^3 is the density of silica [50] and $\rho_w = 1$ g/cm^3 is the density of liquid water at room temperature. At the transition between the constant rate and the falling rate periods at time $t = t_F$, the wet monolith stops shrinking and reaches its final porosity, i.e., $\phi(t_F) = \phi_F$, such that $x_w(t_F) = x_{w,F}$. In other words, during the constant rate period $x_w(t) > x_{w,F}$.

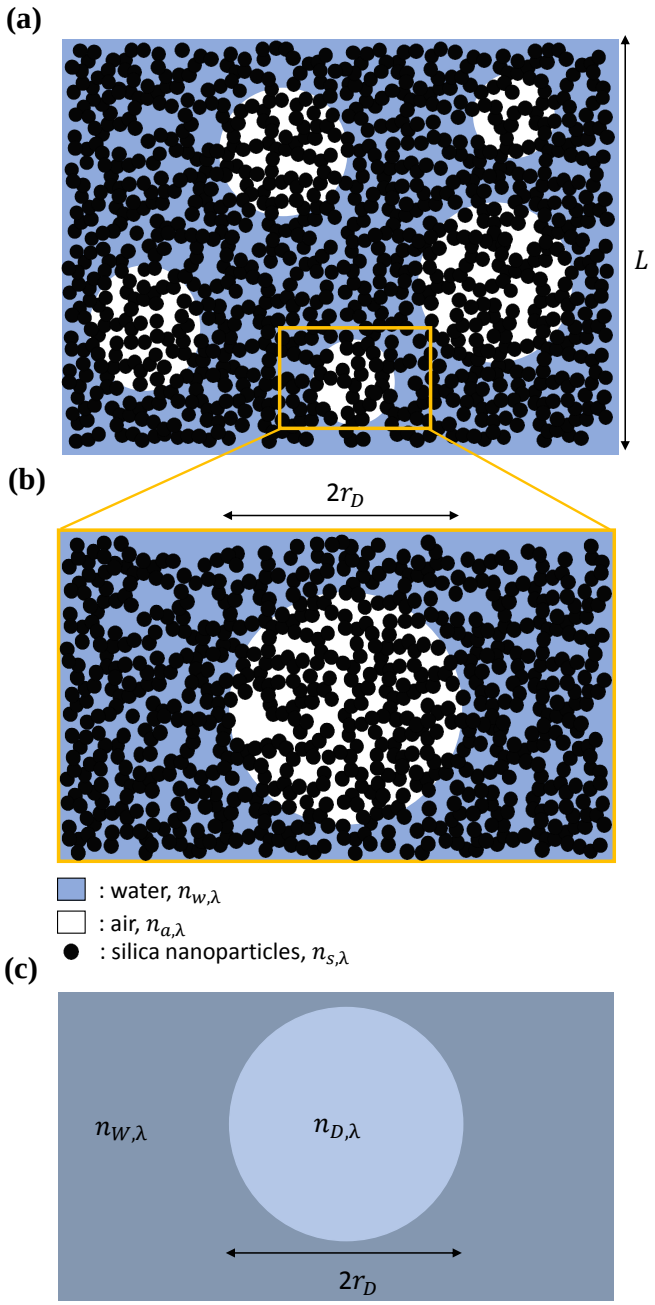

Figure 5.2: (a) Mesoporous monolith containing polydisperse spherical drained domains surrounded by a wet matrix. (b) Dry spherical domain with radius r_D of a mesoporous silica monolith and (c) its equivalent homogeneous sphere representation.

During the falling rate period, the water mass fraction $x_w(t)$ in the mesoporous monoliths can be expressed as

$$x_w(t) = x_{w,F}[1 - f_D(t)]. \tag{5.6}$$

Here, $f_D(t)$ is the volume fraction of the dry domains at time t, i.e., the ratio of the volume occupied by the dry mesoporous domains to that of the monolith. When the monolith is fully dry, $f_D = 1$ and $x_w = 0$.

5.3.3 Constant rate period and calcined monoliths

As previously mentioned, during the constant rate period the monolith is fully wet and can be assumed to be an homogeneous and non-scattering monolith with normal-hemispherical transmittance expressed as [132]

$$T_{nh,\lambda} = \frac{(1 - r_\lambda)^2}{1 - r_\lambda^2} \quad \text{with} \quad r_\lambda = \frac{(n_{m,\lambda} - 1)^2}{(n_{m,\lambda} + 1)^2}. \tag{5.7}$$

Here, the monolith's effective refractive index $n_{m,\lambda}$ can be estimated by the Maxwell-Garnett effective medium approximation (EMA) as [133]

$$n_{m,\lambda}^2 = n_{s,\lambda}^2 \left[1 - \frac{3\phi(t)(n_{s,\lambda}^2 - n_{d,\lambda}^2)}{2n_{s,\lambda}^2 + n_{d,\lambda}^2 + \phi(t)(n_{s,\lambda}^2 - n_{d,\lambda}^2)}\right] \tag{5.8}$$

where the subscript "s" refers to the continuous silica phase and the subscript "d" refers to the discontinuous phase contained in the pores, i.e., the solvent ($n_{d,\lambda}$ = $n_{w,\lambda}$ = 1.33) when the sample is wet. The same assumptions apply to the dry monoliths and Equations (5.7) and (5.8) can also be used with $n_{d,\lambda} = n_{a,\lambda} = 1$. Note that the Maxwell-Garnett EMA has been validated both numerically [134] and experimentally [111, 135] for dry mesoporous silica films. In addition, as a first order approximation, the haze h_λ is assumed to vanish for the fully wet or dry monoliths [Figures 5.1(a) and 5.1(c)].

5.3.4 Falling rate period

During the falling rate period, pores empty and dry domains appear in the mesoporous monolith [Figure 5.2(a)]. First, for a given water mass fraction x_w, the dry domains were assumed to be spherical with radius r_D and follow the Gaussian size distribution $\psi(x_w, r_D)$ (in $\#/\mu\text{m}^4$) given by

$$\psi(x_w, r_D) = \frac{N_T(x_w)}{S\sqrt{2\pi}} \exp\left(-\frac{1}{2}\left[\frac{r_D - \bar{r}_D(x_w)}{S}\right]^2\right). \tag{5.9}$$

Here, $\bar{r}_D(x_w)$ is the average radius of the dry domains and S is the associated standard deviation. Note that during the falling rate period, the monolith does not shrink anymore. Therefore, its volume and porosity are constant and the volume fraction of dry domains $0 \leq f_D \leq 1$ can be expressed as

$$f_D = \int_0^{+\infty} \frac{4\pi}{3} r_D^3 \psi(x_w, r_D) \mathrm{d}r_D = N_T(x_w) \bar{V}_D(x_w) \tag{5.10}$$

where $\bar{V}_D$ is the average volume of the dry domains defined as

$$\bar{V}_D = \int_0^{+\infty} \frac{4\pi}{3} r_D^3 \frac{e^{-\frac{1}{2}\left[\frac{r_D - \bar{r}_D(x_w)}{S}\right]^2}}{S\sqrt{2\pi}} \mathrm{d}r_D. \tag{5.11}$$

Note that $\bar{V}_D$ can be analytically expressed as a function of $\bar{r}_D$ and S (see Supporting Information) given by

$$\bar{V}_D = \frac{2}{3}\sqrt{2\pi}\left(\left[\bar{r}_D^2 + 2S^2\right] S \exp\left(-\frac{\bar{r}_D^2}{2S^2}\right) + \sqrt{\frac{\pi}{2}}\left[3\bar{r}_D S^2 + \bar{r}_D^3\right]\left[1 + \mathrm{erf}\left(\frac{\bar{r}_D}{S}\right)\right]\right). \tag{5.12}$$

At the beginning of the falling rate period, $x_w = x_{w,F}$, $f_D = 0$, and $N_T = 0$ since the mesoporous monolith is fully wet. On the other hand, as the monolith dries, x_w approaches 0, f_D tends to 1, and N_T decreases and ≈ 0.

The one-dimensional RTE was solved to predict the normal-hemispherical

transmittance $T_{nh,\lambda}$, the diffuse transmittance $T_{d,\lambda}$, and the haze h_λ of mesoporous silica monoliths during the falling rate period. The input parameters were the monolith effective (i) scattering coefficient $\sigma_{s,\lambda}$, (ii) asymmetry factor $g_{m,\lambda}$, (iii) refractive index $n_{m,\lambda}$, and (iv) thickness L. The regions of drained pores [Figure 5.2(b)] were modeled as spherical scatterers with radius r_D and effective refractive index $n_{D,\lambda}$ [Figure 5.2(c)], as previously explained. The surrounding medium was homogeneous wet mesoporous silica with effective refractive index $n_{W,\lambda}$. Here also, the effective refractive indices $n_{D,\lambda}$ and $n_{W,\lambda}$ can be estimated using the Maxwell-Garnett EMA [Equation (5.8)] using $n_{d,\lambda} = n_{a,\lambda} = 1$ and $n_{d,\lambda} = n_{w,\lambda} = 1.33$, respectively. The spectral scattering cross-section $C_{sca,\lambda}(r_D)$ and asymmetry factor $g_\lambda(r_D)$ of the spherical dry domains of radius r_D were computed using the Lorenz-Mie theory [55]. The input parameters included (i) the relative refractive index of the dry domains defined as $n_{D,\lambda}/n_{W,\lambda}$ and (ii) their size parameter equal to $2\pi r_D n_{W,\lambda}/\lambda$. Moreover, it was assumed that the spherical dry regions scattered independently so that the scattering coefficient of the monolith during drying can be defined as [55]

$$\sigma_{s,\lambda}(x_w) = \int_0^{+\infty} C_{sca,\lambda}(r_D)\psi(x_w, r_D)\mathrm{d}r_D. \tag{5.13}$$

In addition, the asymmetry factor of the monolith containing polydisperse drained spherical domains can be expressed as [55]

$$g_{m,\lambda}(x_w) = \frac{1}{\sigma_{s,\lambda}(x_w)} \int_0^{+\infty} C_{sca,\lambda}\psi(x_w, r_D)g_\lambda(r_D)\mathrm{d}r_D. \tag{5.14}$$

The refractive index of the three-phase mesoporous silica monolith $n_{m,\lambda}$ during the falling rate period was computed using the Maxwell-Garnett EMA given by [136]

$$n_{m,\lambda}^2 = n_{s,\lambda}^2 \left[1 + \frac{\frac{\phi_w(n_{w,\lambda}^2 - n_{s,\lambda}^2)}{n_{s,\lambda}^2 + (n_{w,\lambda}^2 - n_{s,\lambda}^2)/3} + \frac{\phi_a(n_{a,\lambda}^2 - n_{s,\lambda}^2)}{n_{s,\lambda}^2 + (n_{a,\lambda}^2 - n_{s,\lambda}^2)/3}}{1 - \frac{\phi_w(n_{w,\lambda}^2 - n_{s,\lambda}^2)}{2n_{s,\lambda}^2 + n_{w,\lambda}^2} - \frac{\phi_a(n_{a,\lambda}^2 - n_{s,\lambda}^2)}{2n_\lambda^2 + n_{a,\lambda}^2}} \right]. \tag{5.15}$$

Here, ϕ_w and ϕ_a are the fractions of the porosity occupied by water and air, respectively, and such that $\phi_F = \phi_w + \phi_a$. They can be expressed in terms of the overall volume fraction f_D of dry mesoporous silica domains and the final porosity ϕ_F of the monolith as $\phi_w = \phi_F(1 - f_D)$ and $\phi_a = \phi_F f_D$. Lastly, the thickness of the simulated nanoparticle-based mesoporous silica monolith was $L = 2$ mm.

The 1D RTE was solved using the Monte Carlo method. To do so, the numbers of photons $N_{nh,\lambda}$ transmitted in all directions and $N_{d,\lambda}$ transmitted outside of a cone of transmission angle 16° were counted. The latter corresponds to the solid angle of the integrating sphere's back port opened for diffuse transmittance measurements. Then, the normal-hemispherical and diffuse $T_{nh,\lambda}$ and $T_{d,\lambda}$ transmittances were obtained according to

$$T_{nh,\lambda} = \frac{N_{nh,\lambda}}{N_{i,\lambda}} \quad \text{and} \quad T_{d,\lambda} = \frac{N_{d,\lambda}}{N_{i,\lambda}} \tag{5.16}$$

where $N_{i,\lambda}$ is the number of incident photons. Similarly, the haze h_λ was defined as [130]

$$h_\lambda = \frac{T_{d,\lambda}}{T_{nh,\lambda}} = \frac{N_{d,\lambda}}{N_{nh,\lambda}}. \tag{5.17}$$

Figure 5.3 summarizes the computational procedure used to predict the temporal evolution of the normal-hemispherical transmittance $T_{nh,\lambda}$ and haze h_λ of mesoporous silica monoliths during the falling rate period. The input parameters included (i) the water mass fraction $x_w(t)$, (ii) the standard deviation S of the dry domains size distribution, and (iii) the number $N_T(t)$ of dry domains per unit volume of monolith. The water mass fraction $x_w(t)$, as that measured experimentally, progressively decreased from $x_{w,F}$ to 0.08 as the drying process proceeded. The dry domain standard deviation was arbitrarily taken as $S = 0.1\bar{r}_D$. Lastly, the number N_T of dry domains per unit volume of monolith was determined by trial and error to obtain a good agreement between experimental and modeled transmittance and haze. Several functions commonly used in population balances

satisfying the conditions $N_T(x_{w,F}) = 0$ and $N_T(x_w \to 0) \approx 0$ were tested. Here, the expression used for microbial cell populations generated good agreement between model and measurements [137]. It was expressed as

$$N_T(x_w) = A(x_{w,F} - x_w)\exp\left(-\frac{x_{w,F} - x_w}{s_w}\right), \tag{5.18}$$

where A and s_w are fitting constants. The fraction f_D of porosity occupied by the dry domains was calculated using Equation (5.6), i.e., f_D = 1 - $x_w(t)/x_{w,F}$. Then, the average radius $\bar{r}_D(x_w)$ of the dry domains was obtained by considering that Equations (5.10) and (5.11) simplify to $f_D \simeq 4.31\bar{r}_D^3 N_T$ when $S = 0.1\bar{r}_D$. Knowing $\bar{r}_D$ and $S = 0.1\bar{r}_D$ enables one to predict the size distribution $\psi(x_w,r_D)$ of the polydisperse dry domains [Equation (5.9)]. Here, $\psi(x_w,r_D)$ was assumed to be contained between $\bar{r}_D$-$2S$ and $\bar{r}_D$+$2S$. Then, the scattering cross-section $C_{sca,\lambda}$ and asymmetry factor g_λ of the dry domains of radius r_D were estimated using Lorenz-Mie theory. The scattering coefficient $\sigma_{s,\lambda}$ and asymmetry factor $g_{m,\lambda}$ of the monolith were predicted using Equations (5.13) and (5.14), respectively. The normal-hemispherical transmittance $T_{nh,\lambda}$ and haze h_λ were computed by solving the RTE using the Monte Carlo method. Finally, the visible transmittance T_{vis} and haze h_{vis} were calculated using Equation (5.4).

5.4 Results and discussion

Several nanoparticle-based mesoporous monoliths dried from water either in a covered or open dish were observed during drying. Special attention was paid to nanoparticle-based monoliths dried from water in a covered dish since their slower evaporation rate allowed for time-dependent measurements of their water mass fraction and optical properties, as illustrated in Figure 5.1. Although the monoliths dried with different evaporation rates, they all underwent the same optical changes (Figures D.1 and D.2 in Supporting Information). Some parts of

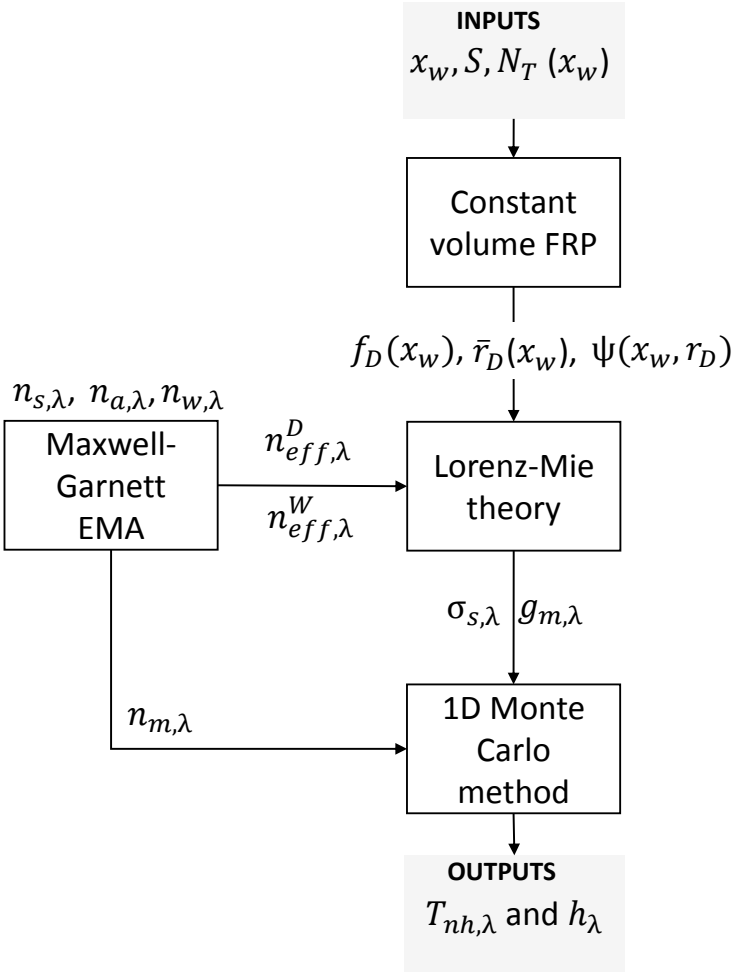

Figure 5.3: Block diagram of the procedure used to predict the normal-hemispherical transmittance $T_{nh,\lambda}$ and haze h_λ of drying mesoporous silica monoliths during the falling rate period (FRP).

the monoliths may turn white or transparent faster than others. Note, however, that all the observed monoliths were completely white at some point in the drying process. These observations suggest that dry and wet regions were homogeneously distributed throughout the monoliths.

5.4.1 Structural and optical characterization

Figure 5.4 shows (a) the adsorption-desorption isotherms and (b) the pore size distribution of the calcined nanoparticle-based mesoporous monolith illustrated in Figure 5.1. The isotherms were of type IV(a) according to the IUPAC classification [28] confirming that the monolith was mesoporous. In addition, the monolith featured a H2(b) hysteresis loop indicating that the pores were constricted by neck but that the neck size distribution was broad. The monolith featured pores with diameter d_p ranging from 2.4 to 12 nm, and a porosity ϕ_F of 49±2%.

Figure 5.5 presents the spectral (a) normal-hemispherical transmittance $T_{nh,\lambda}$ and (b) haze h_λ of the drying mesoporous monolith over the course of the drying process. Figure 5.5 also displays the days corresponding to the measurements. Figure 5.5(a) shows that $T_{nh,\lambda}$ decreased from Day 1 to Day 6, and then increased from Day 6 until its calcination on Day 30. Moreover, Figure 5.5(a) indicates that the spectral normal-hemispherical transmittance $T_{nh,\lambda}$ was almost constant when the mesoporous monolith was wet (Days 1 through 3) and fully dry (Day 30). On the other hand, between Days 4 and 8, $T_{nh,\lambda}$ increased with increasing wavelength. Similarly, Figure 5.5(b) shows that h_λ increased from Day 1 to Day 6, and then decreased from Day 6 until Day 30. Figure 5.5(b) also shows that the haze was higher than 96% and almost constant on Days 5 and 6 when the monolith was white. This observation indicates that almost all of the transmitted light was scattered with a scattering angle larger than 16°. Figure D.3 in Supporting Information presents the 3D plots of the spectral transmittance and haze as functions of the monolith's water mass content.

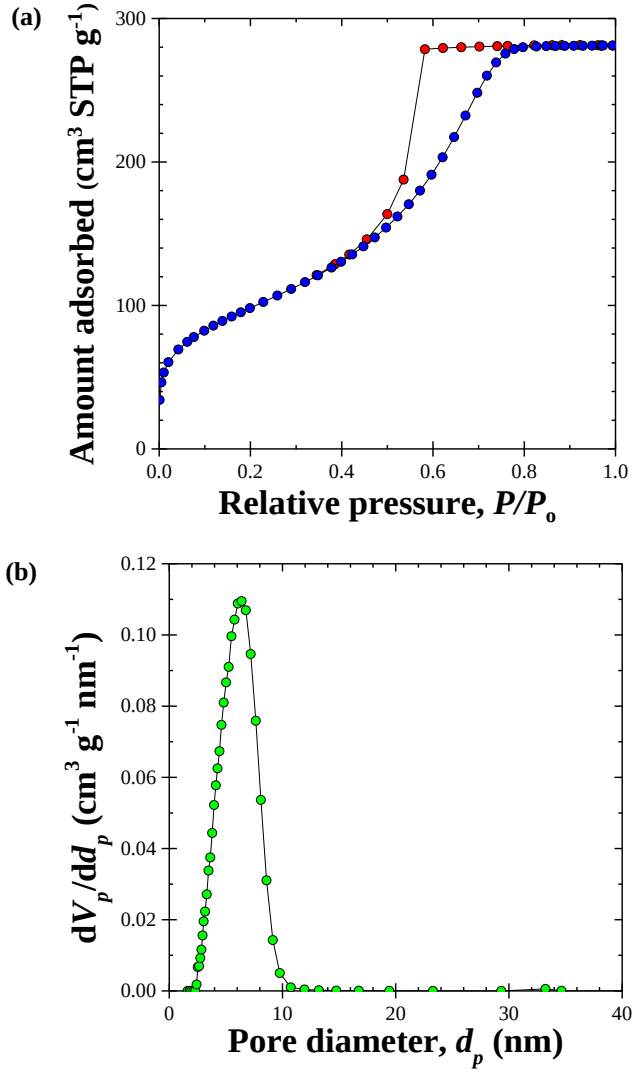

Figure 5.4: (a) Adsorption-desorption isotherms and (b) pore size distribution of the calcined nanoparticle-based mesoporous silica monolith (Table 5.1 and Figure 5.1).

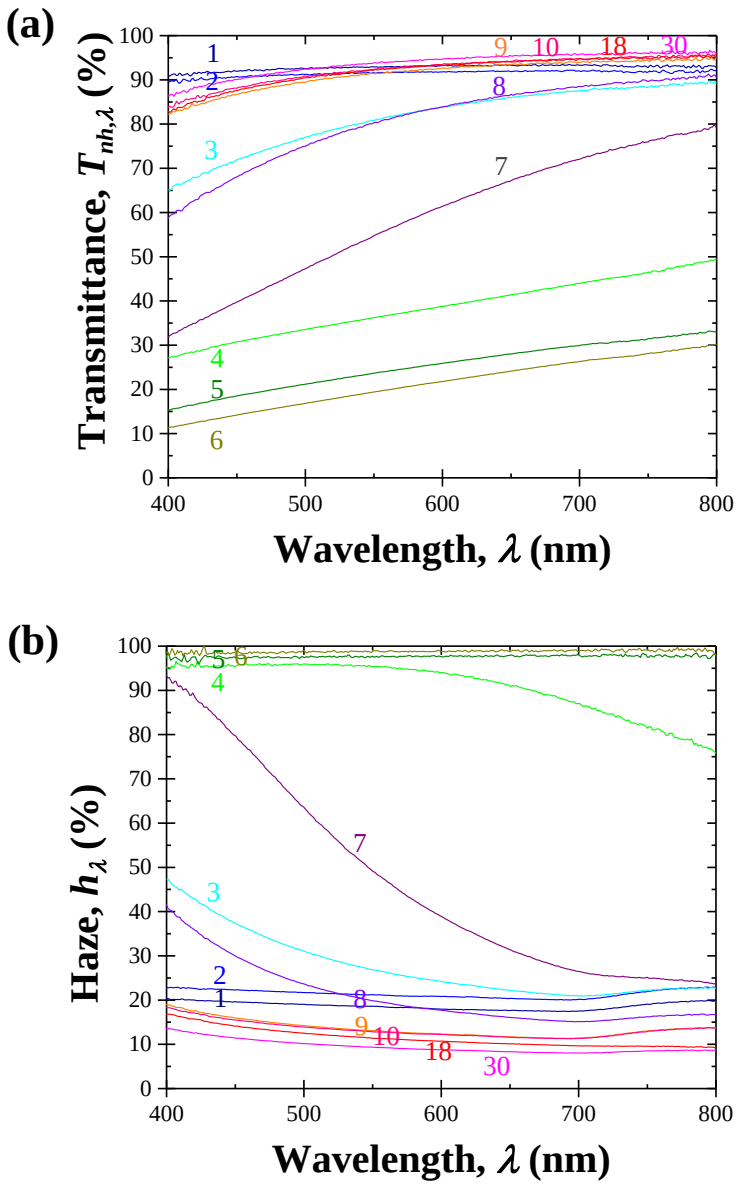

Figure 5.5: Spectral (a) normal-hemispherical transmittance $T_{nh,\lambda}$ and (b) haze h_λ of a nanoparticle-based mesoporous monolith (pictures in Figure 1) over the course of drying. Days of measurements are also indicated on the graphs.

Table 5.1 summarizes the evolution of the water mass fraction, volume shrinkage, and visible transmittance and haze during drying of the water-based mesoporous silica monolith over 30 days. It indicates that during the first three days of drying, the water mass fraction x_w decreased while the monolith shrank by 20%, corresponding to the constant rate period [49]. During these three days, the monolith remained transparent with visible transmittance T_{vis} decreasing slightly from 92 to 81% and visible haze h_{vis} increasing from 18 to 27%. This was likely due to the appearance of cracks and defects. Between Days 3 and 4, the shrinkage stopped signaling the beginning of the falling rate period when pores started emptying suggesting $0.46 \leq x_{w,F} \leq 0.51$. On Day 4, the monolith turned white and the visible transmittance T_{vis} decreased to 37% while the visible haze h_{vis} increased abruptly to 95%. These observations were in agreement with those of Brinker and Scherer [49]. The monolith remained white for two more days, the visible transmittance T_{vis} was below 25% and the visible haze h_{vis} exceeded 95%. On Day 7, the monolith became translucent and featured increasing transmittance $T_{vis} = 56\%$ and decreasing haze $h_{vis} = 48\%$. Then, the monolith's optical quality continued improving until the last traces of water were removed by calcination. It is also interesting to note that from Day 9 until calcination, the water mass fraction x_w remained constant ($x_w = 0.08$), and the optical properties barely changed. This suggests that $x_w = 0.08$ was the residual water mass fraction resulting from capillary condensation of the surrounding humidity and that the drying process had stopped.

Figure 5.6 plots the visible normal-hemispherical transmittance T_{vis} and the corresponding haze h_{vis} for the nanoparticle-based mesoporous silica monolith pictured in Figure 5.1 as functions of the measured water mass fraction x_w [Equation (5.1)]. Figure 5.6 also displays the drying stages that were identified from Table 5.1. It indicates that the different drying stages had very distinct optical features. First, the constant rate period corresponded to $0.46 < x_w \leq 1.01$ and coincided

Table 5.1: Water mass fraction $x_w(t)$ and optical characteristics T_{vis} and $h_{vis}$of the nanoparticle-based mesoporous silica monolith drying from water over 30 days.

Day	**Water mass fraction** $x_w(t)$	**Appearance**	**Transmittance** T_{vis} (%)	**Haze** h_{vis} (%)	**Volume shrinkage** (%)
1	1.01	Transparent	92.4	18.4	100
2	0.71	Transparent	91.7	21.1	95
3	0.51	Slightly hazy	81.3	26.7	80
4	0.46	White	36.7	94.8	80
5	0.42	White	24	97.7	80
6	0.38	White	19.8	98.8	80
7	0.25	Translucent	56.2	48.1	80
8	0.20	Slightly hazy	81.1	19.8	80
9	0.08	Transparent	91.5	13.0	80
10	0.08	Transparent	92.5	12.8	80
18	0.08	Transparent	92.3	11.4	80
30	0	Transparent	92.3	9.3	80

with low haze h_{vis} and high transmittance T_{vis}. During this stage, the haze and transparency of the monolith were mainly controlled by reflection at the monolith/air interface, random defects, and surface roughness. Figure 5.6 also shows that the monolith featured the lowest haze and highest transmittance after calcination when $x_w = 0$. In this case, haze and transparency of the calcined monolith were also controlled by reflection and potential scattering at the monolith surface.

Figure 5.6 also establishes that at the beginning of the falling rate period when $x_w \simeq 0.46$, the haze h_{vis} abruptly increased and T_{vis} decreased. We hypothesized that these observations were the result of volumetric scattering of growing dry domains within the monolith with characteristic size on the order or larger than the wavelength λ. As drying proceeded with $x_w < 0.4$, these drained domains occupied more volume but were significantly less numerous resulting in decreasing haze and increasing transmittance.

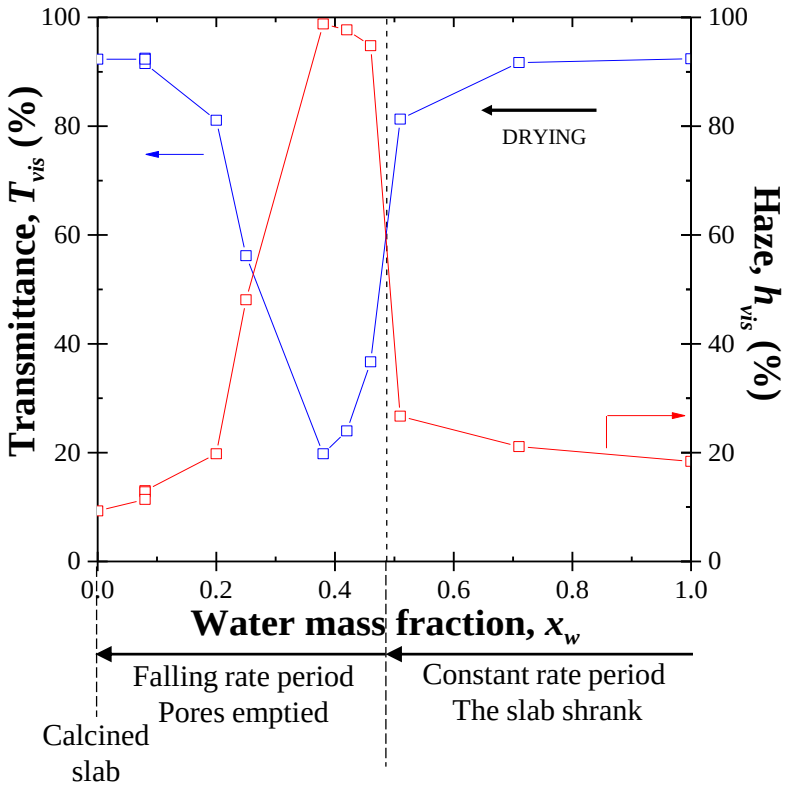

Figure 5.6: Measured visible normal-hemispherical transmittance T_{vis} and haze h_{vis} of a 2 mm thick nanoparticle-based mesoporous silica monolith dried from water as functions of its water mass fraction x_w (Table 5.1 and Figure 5.1).

5.4.2 Modeling

Structural characteristics

First, the theoretical water mass fraction of $x_{w,F}$ at the transition between the constant rate and falling rate periods of a mesoporous monolith was calculated as $x_{w,F} = 0.44$ using Equation (5.5) for porosity $\phi_F = 49\%$ obtained experimentally. Then, Figure 5.7(a) plots the volume fraction $f_D(x_w)$ of dry domains predicted by Equation (5.6) as a function of its water mass fraction $x_w(t)$ for a drying nanoparticle-based monolith (Figure 5.1 and Table 5.1) as well as details of its appearance. Figure 5.7(a) indicates that the monolith turned white for $x_w \simeq 0.46$ suggesting the start of the falling rate period as discussed previously. In other words, the water mass fraction at the transition between constant rate and falling rate periods obtained visually was consistent with that predicted by Equation (5.6).

In addition, the average dry domain radius $\bar{r}_D(x_w)$ can be obtained from Equations (5.10) and (5.11). The trial and error fitting of the model parameters A and s_w that minimized the least square error between the measured and predicted visible transmittance and haze yielded $A = 7.9$ and $s_w = 0.015$. Figure 5.7 also presents (b) the number N_T of dry domains per unit volume of monolith [Equation (5.18)] and (c) their average dry domain radius $\bar{r}_D$ [Equation (5.10)] as functions of the water mass fraction x_w. Figures 5.7(b) and 5.7(c) indicate that as the water mass fraction x_w decreased from 0.44 to 0.4, N_T and $\bar{r}_D$ increased. This suggests that at the early stage of the falling rate period, the number of dry domains appearing in the monolith increased rapidly and their size grew. Moreover, when x_w fell below $x_{w,F} = 0.44$, the emerging dry scattering domains featured a radius $r_D \approx 0.3$ μm, comparable to the wavelength of visible light. Then, for $x_w < 0.4$, N_T decreased and $\bar{r}_D$ increased. This implies that dry regions expanded and probably grew by merging with other dry regions as the drying proceeded.

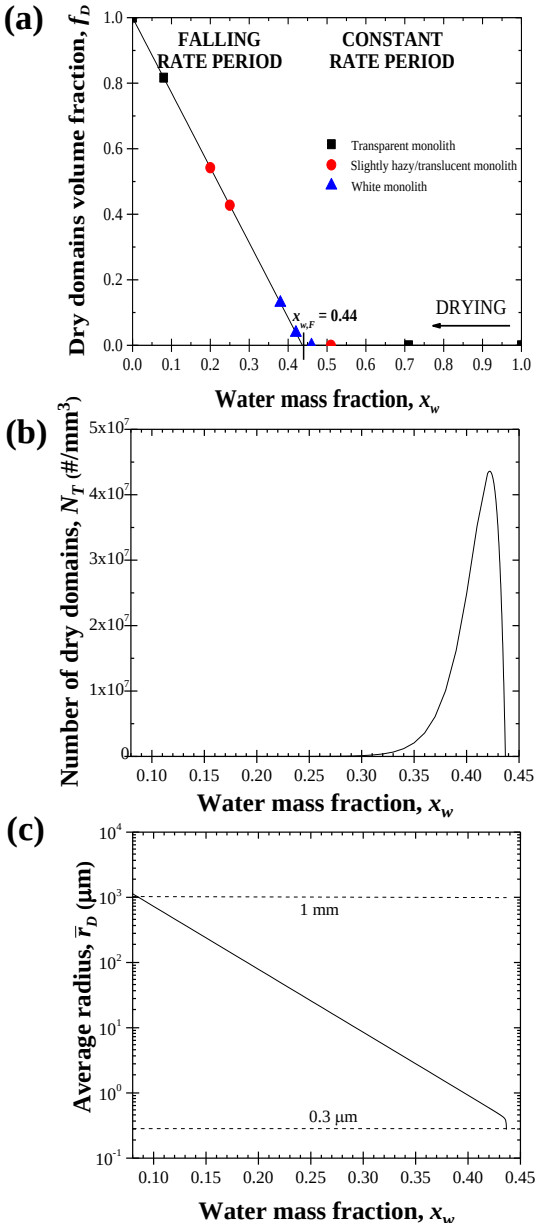

Figure 5.7: (a) Dry domain volume fraction f_D of a mesoporous silica monolith with porosity $\phi = 49\%$ as a function of the water mass fraction x_w, predicted by Equation (5.6). (b) Number N_T of dry domains per unit volume of monolith [Equation (5.18)] and (c) their average radius $\bar{r}_D$ as functions of the water mass fraction x_w in the mesoporous monolith.

Normal-hemispherical transmittance and haze

Figure D.4 of the Supporting Information plots the scattering coefficient $\sigma_{s,\lambda}$ [Equation (5.13)] and asymmetry factor $g_{m,\lambda}$ [Equation (5.14)] as functions of the water mass fraction x_w, used in the computation of the visible transmittance T_{vis} and haze h_{vis} of a mesoporous silica monolith with thickness $L = 2$ mm and porosity $\phi_F = 49\%$. Figure S4(a) indicates that the scattering coefficient $\sigma_{s,\lambda}$ exceeded the value of 0.5 mm^{-1} during the falling rate period. This establishes that the white color of the monoliths resulted from multiple light scattering as the optical thickness $\tau_\lambda = L\sigma_{s,\lambda} \geq 1$ [15]. Moreover, Figure S4(a) shows that overall the scattering coefficient $\sigma_{s,\lambda}$ decreased with increasing wavelength suggesting enhanced scattering of the dry domains in the shorter wavelengths. In addition, Figure S4(b) shows that the asymmetry factor $g_{m,\lambda} > 0.9$ indicating that the dry domains scattered most of the light in the forward direction.

Figure 5.8 plots the modeled and experimental visible transmittance T_{vis} and haze h_{vis} of a drying nanoparticle-based silica monolith with thickness $L = 2$ mm and porosity $\phi_F = 49\%$ as functions of the water mass fraction x_w. First, Figure 5.8 shows that the model estimations and experimental measurements were in good agreement thanks to the trial and error fitting of A and s_w. The model reproduced the drastic decrease in transmittance T_{vis} and the sharp increase in haze h_{vis} at the transition between the constant rate and falling rate periods when $x_w = x_{w,F}$. In fact, the model estimations and experimental measurements featured transmittance $T_{vis} \leq 20\%$ and haze $h_{vis} \geq 95\%$ when $x_w \simeq 0.4$. This observation indicates that the white appearance of the monolith was due to volumetric light scattering by drained regions. Also, Figure 5.8(a) shows that the model reproduced properly the increasing transmittance when x_w decreased from 0.35 to 0.08. This confirms that as the number of dry domains decreased significantly and they became larger than 3 μm [Figures 5.7(b) and 5.7(c)], scattering by the monolith

decreased and its transparency improved. Furthermore, the modeled visible haze h_{vis} presented in Figure 5.8(b) depicted the measured decrease when $x_w \approx 0.25$. Figure 5.8(b) shows that the modeled h_{vis} was higher than the measured one when $x_w < 0.3$. This difference between measurements and model estimations for h_{vis} was likely due to the approximation of the scattering phase function. In the Monte Carlo method, the scattering direction of the photons was assumed to be characterized by the Henyey-Greenstein phase function. Overall, Figure 5.8 suggests that the amount of light scattered by the dry domains was correctly simulated by the model and that the direction of scattering was not as well estimated.

Figure D.5 in Supporting Information plots the modeled spectral normal-hemispherical transmittance $T_{nh,\lambda}$ and haze h_λ of a nanoparticle-based monolith with porosity $\phi_F = 49\%$ and thickness $L = 2$ mm. Figure S5(a) shows that at the beginning of the falling rate period when $0.22 < x_w \leq 0.44$, $T_{nh,\lambda}$ increased with increasing wavelength indicating greater scattering of the dry domains in the shorter wavelengths, as observed experimentally [Figure 5.5(a)] and as suggested by the predicted scattering coefficient [Figure S4(a)]. When $x_w \geq 0.22$, $T_{nh,\lambda}$ was constant. On the other hand, h_λ was overall constant and did not feature the same variations with varying wavelength as observed experimentally. This difference in measured and modeled spectral haze was probably also due to the approximation of the scattering phase function, as mentioned previously.

5.5 Conclusion

The optical changes in mesoporous monoliths from transparent to white to transparent again have been mentioned anecdotely and some qualitative explanations have been provided in the literature. For the first time, the present study documents quantitatively the changes in water content, transmittance, and haze during drying of nanoparticle-based mesoporous monoliths. Moreover, this study shows,

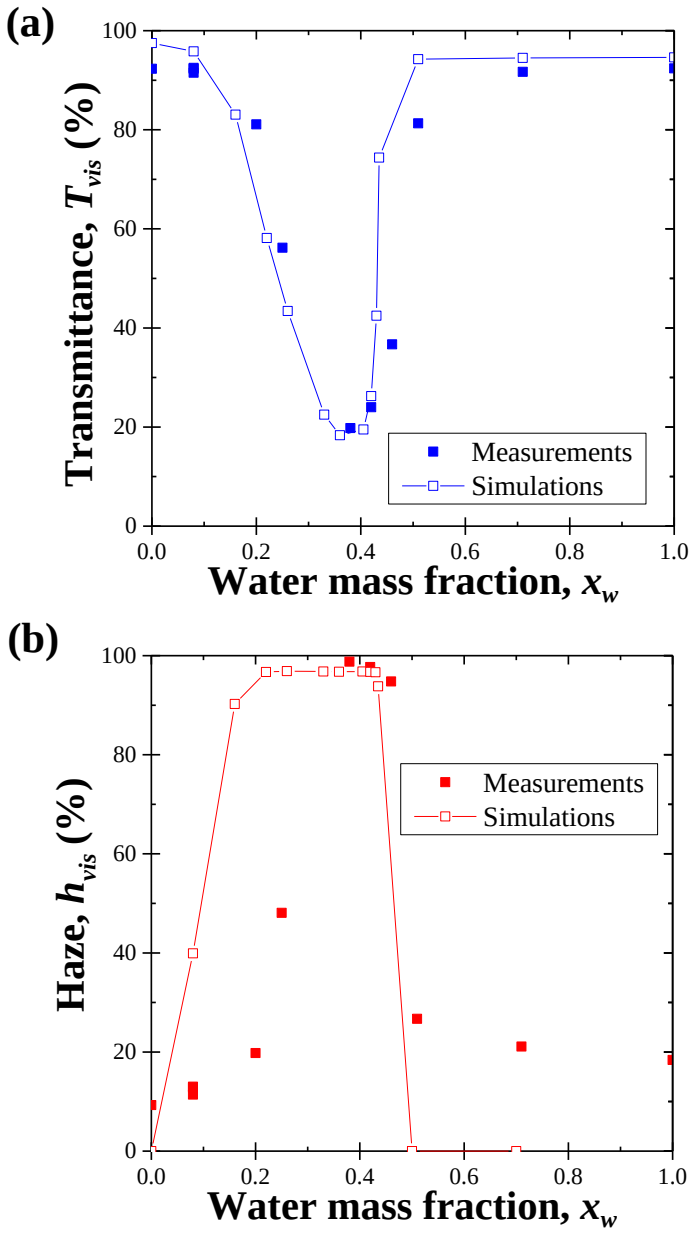

Figure 5.8: Simulated and experimental (a) normal-hemispherical transmittance $T_{nh,500}$ and (b) haze h_{500} at wavelength $\lambda = 500$ nm for a 2 mm thick nanoparticle-based silica monolith (Figure 5.1, Table 5.1) with final porosity $\phi_F = 49\%$.

through a light transfer model, that dry domains emerging during the falling rate period caused the changes in appearances of drying monoliths. Light transfer through the mesoporous monolith accounted for volumetric light scattering by polydisperse spherical drained domains encompassing several pores and surrounded by the wet gel. In other words, the white appearance of the monolith resulted from the refractive index mismatch between dry and wet domains. The dry domains and wet gel were approximated as homogeneous domains with some effective refractive index. The scattering cross-section and asymmetry factor of the dry domains were calculated using Lorenz-Mie theory. Finally, the Monte Carlo method was used to estimate the transmittance and haze of the monoliths. The model was able to reproduce the sharp changes observed in the measured transmittance and haze during the falling rate period.

CHAPTER 6

Comparing Methods for Measuring Thickness, Refractive Index, and Porosity of Mesoporous Thin Films

This chapter compares systematically contact profilometry, interferometry, ellipsometric porosimetry for measuring thickness, effective refractive index, porosity, and/or pore size of mesoporous thin films. Here, sol-gel and nanoparticle-based mesoporous silica and silica-titania thin films were synthesized and characterized with the aforementioned methods. The synthesis recipe and deposition conditions were varied to achieve a wide range of compositions (silica:titania molar ratio from 100:0 to 70:30), thickness (80 nm $\leq L \leq$ 630 nm), effective refractive index (1.11 $\leq n_{eff,\lambda} \leq$ 1.75), porosity (0% $\leq \phi \leq$ 70%), and peak pore diameter (1 nm $\leq d_p \leq$ 20 nm). Overall, the thickness, effective refractive index, and/or porosity obtained from contact profilometry, interferometry, ellipsometry, and ellipsometric porosimetry agreed very well. However, porosity and pore size distribution obtained from nitrogen porosimetry on powder samples differed significantly from those of the equivalent thin films.

6.1 Background

6.1.1 Effective medium approximations

Effective medium approximations (EMAs) treat heterogeneous materials as homogeneous with some effective properties. For example, EMAs predict the effective refractive index of heterogeneous media based on the optical properties and volume fractions of its constituent materials, assumed to be known. For mesoporous materials, this approach is valid if the pore size is much smaller than the wavelength

λ of the incident light so that scattering by pores can be ignored [133, 138, 139]. In addition, the films should be thick compared to the pore size to consider a sufficiently large representative volume of the film [134, 140].

The most commonly used EMAs include (1) the symmetric Bruggeman model [133,139,141], (2) the Maxwell-Garnett model [142], (3) the asymmetrical Bruggeman model [143], (4) the Lorentz-Lorenz model [144,145], and (5) the volume averaging theory (VAT) [140]. The symmetric Bruggeman model relates the effective refractive index of a two-phase mixture $n_{eff,\lambda}$ to its total porosity ϕ as [133]

$$\phi \frac{n_{d,\lambda}^2 - n_{eff,\lambda}^2}{n_{d,\lambda}^2 + 2n_{eff,\lambda}^2} + (1-\phi)\frac{n_{c,\lambda}^2 - n_{eff,\lambda}^2}{n_{c,\lambda}^2 + 2n_{eff,\lambda}^2} = 0 \tag{6.1}$$

where the subscript "*c*" refers to the "continuous" phase (e.g., silica), and the subscript "*d*" refers to the "dispersed" phase (e.g., air or toluene). Similarly, the Maxwell-Garnett model was derived for randomly monodisperse spherical inclusions in a continuous matrix and is expressed as [133]

$$n_{eff,\lambda}^2 = n_{c,\lambda}^2 \left[1 - \frac{3\phi(n_{c,\lambda}^2 - n_{d,\lambda}^2)}{2n_{c,\lambda}^2 + n_{d,\lambda}^2 + \phi(n_{c,\lambda}^2 - n_{d,\lambda}^2)} \right]. \tag{6.2}$$

The asymmetrical Bruggeman model considers polydisperse spheres distributed in a continuous matrix [146]. It predicts the effective refractive index $n_{eff,\lambda}$ of the mesoporous material based on the following implicit relationship [133]

$$1 - \phi = \frac{\dfrac{n_{eff,\lambda}^2}{n_{c,\lambda}^2} - \dfrac{n_{d,\lambda}^2}{n_{c,\lambda}^2}}{\left(\dfrac{n_{eff,\lambda}^2}{n_{c,\lambda}^2}\right)^{1/3} \left(1 - \dfrac{n_{d,\lambda}^2}{n_{c,\lambda}^2}\right)}. \tag{6.3}$$

The Lorentz-Lorenz model was derived for monodisperse spherical particles in air

and expresses the effective refractive index implicitly according to [147–149]

$$\frac{n_{eff,\lambda}^2 - 1}{n_{eff,\lambda}^2 + 2} = (1 - \phi)\frac{n_{c,\lambda}^2 - 1}{n_{c,\lambda}^2 + 2} + \phi\frac{n_{d,\lambda}^2 - 1}{n_{d,\lambda}^2 + 2}. \tag{6.4}$$

The Maxwell-Garnett and Bruggeman models have been generalized to ellipsoidal and spheroidal inclusions to account for the shape and orientation of the inclusions [150–152]. On the other hand, the VAT model was derived by volume averaging the Maxwell's equations and disregards the inclusions shape, size, and spatial distribution. It expresses the effective refractive index $n_{eff,\lambda}$ of a non-absorbing two-phase composite as [153]

$$n_{eff,\lambda}^2 = \phi n_{d,\lambda}^2 + (1 - \phi)n_{c,\lambda}^2. \tag{6.5}$$

Hutchinson et al. [134, 135] numerically solved Maxwell's equations through mesoporous silica films with different porosities and morphologies and compared the porosity retrieved from different EMAs based on reflectance spectrum simulated numerically. The authors concluded that the Maxwell-Garnett model could predict the effective refractive index $n_{eff,\lambda}$ while the asymmetrical Bruggeman model predicted the absorption index $k_{eff,\lambda}$ of mesoporous films with spherical pores regardless of their spatial arrangement. Similarly, Braun and Pilon [140] recommended the VAT model for non-absorbing films consisting of aligned cylindrical pores in a continuous matrix. Stenzel [138] recommended the Lorentz-Lorenz model for highly porous films regardless of their morphology. Despite the different recommendations, the above mentioned EMAs yield similar predictions for mesoporous materials with relatively small mismatch in refractive indices between the continuous and the dispersed phases such as mesoporous silica (see Figure E.1 in Supporting Information).

6.1.2 Interferometry

Interferometry relies on interference patterns present in UV-Vis reflectance spectra of thin films to measure their thickness and refractive index. The theoretical spectral reflectance of a non-absorbing, non-scattering, optically homogeneous, and isotropic thin film deposited on a reflective substrate (Figure 6.1) for unpolarized light can be expressed as [132]

$$R_{pred,\lambda} = \frac{|r_{\perp,\lambda}|^2 + |r_{\parallel,\lambda}|^2}{2} \tag{6.6}$$

where $r_{\perp,\lambda}$ and $r_{\parallel,\lambda}$ are the amplitude reflection coefficients for the perpendicular and parallel polarizations, respectively. They can be expressed as [132]

$$r_{\perp,\lambda} = \frac{r_{12,\perp,\lambda} + r_{23,\perp,\lambda}e^{-2i\beta_\lambda}}{1 + r_{12,\perp,\lambda}r_{23,\perp,\lambda}e^{-2i\beta_\lambda}} \quad \text{and} \quad r_{\parallel,\lambda} = \frac{r_{12,\parallel,\lambda} + r_{23,\parallel,\lambda}e^{-2i\beta_\lambda}}{1 + r_{12,\parallel,\lambda}r_{23,\parallel,\lambda}e^{-2i\beta_\lambda}} \tag{6.7}$$

where $r_{12,\lambda}$ and $r_{13,\lambda}$ are the Fresnel's coefficients defined as [132]

$$r_{ij,\perp,\lambda} = \frac{m_{i,\lambda}\cos\theta_i - m_{j,\lambda}\cos\theta_j}{m_{i,\lambda}\cos\theta_i + m_{j,\lambda}\cos\theta_j} \quad \text{and} \quad r_{ij,\parallel,\lambda} = \frac{m_{j,\lambda}\cos\theta_i - m_{i,\lambda}\cos\theta_j}{m_{j,\lambda}\cos\theta_i + m_{i,\lambda}\cos\theta_j}. \tag{6.8}$$

Here, $m_{1,\lambda} = n_{1,\lambda}$ is the refractive index of the transparent surrounding medium, $m_{2,\lambda} = n_{2,\lambda}$ is the refractive index of the non-absorbing film, and $m_{3,\lambda} = n_{3,\lambda} - \mathrm{i}k_{3,\lambda}$ is the complex refractive index of the substrate. In addition, $\beta_\lambda = 2\pi n_{2,\lambda} L\cos\theta_2/\lambda$ is the phase difference between interfering waves while θ_1 is the angle of the collimated incident radiation defined with respect to the outward normal vector to the film. Moreover, θ_2 is the angle of transmission at the air/film interface and θ_3 is a complex angle [132]. The angles θ_2 and θ_3 can be calculated using Snell's law [132] according to $n_{1,\lambda}\sin\theta_1 = n_{2,\lambda}\sin\theta_2$ and $n_{2,\lambda}\sin\theta_2 = m_{3,\lambda}\sin\theta_3$. If the substrate is non-absorbing, θ_3 is real and corresponds to the angle of transmission at the film/substrate interface (Figure 6.1).

Fitting the experimental reflectance spectrum from a thin film on a substrate

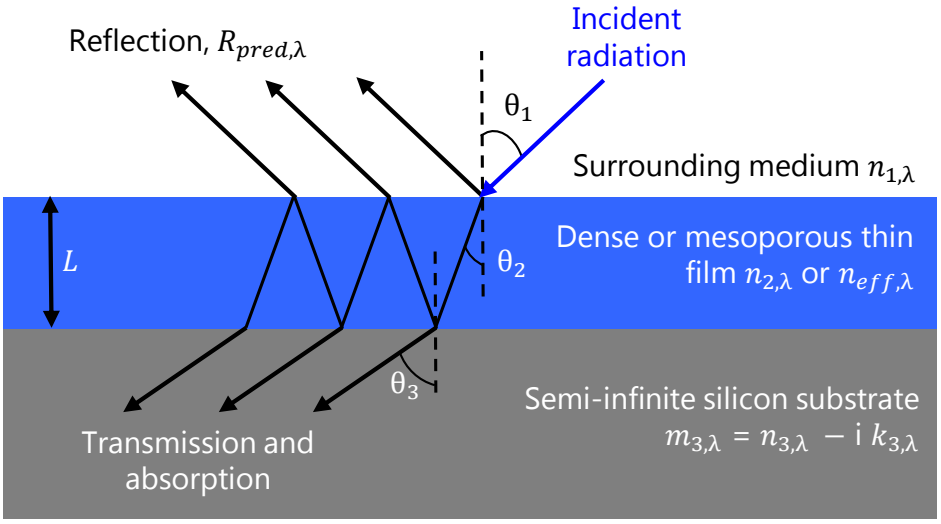

Figure 6.1: Schematic of dense or mesoporous thin films deposited on a silicon substrate exposed to collimated light incident at angle θ_1.

of known optical properties $m_{3,\lambda}$ using Equations (6.6)-(6.8) yields the thickness L and refractive index $n_{2,\lambda}$ of the film. When the film is absorbing, the complex refractive index $m_{2,\lambda}$ can also be retrieved by interferometry by including the adsorption index $k_{2,\lambda}$ in the fitting procedure. Note that this procedure also requires prior knowledge of the complex index of refraction of the surrounding medium $m_{1,\lambda}$ (if different from air) and of the incident angle θ_1. Furthermore, Equation (6.7) is valid when the substrate is thick enough to be treated as semi-infinite. Finally, a reflective substrate is preferred to maximize the signal-to-noise ratio and to measure strong interference fringes.

For mesoporous thin films, this procedure retrieves the effective refractive index $n_{eff,\lambda}$ ($= n_{2,\lambda}$) that can then be used to retrieve the porosity ϕ based on some EMAs. In this study, the Maxwell-Garnett model [Equation (6.2)] was chosen for $n_{eff,\lambda}$ since it was validated both numerically [134] and experimentally [135] for sol-gel mesoporous silica films. Moreover, note that the porosity ϕ retrieved by interferometry based on some EMAs is the total porosity including both the open and closed porosities. By contrast, porosimetry techniques, including ellipsometric porosimetry and nitrogen porosimetry, measure only the open porosity

ϕ_o accessible to the probing molecule. Figure 6.2(a) illustrates the procedure of interferometry used in the present study.

6.1.3 Ellipsometry

Spectroscopic ellipsometry measures changes in polarization between the linearly polarized incident radiation and the reflected radiation from a film as a function of wavelength in the UV to IR regions. After reflection by the film and its substrate, the polarization of the electromagnetic wave changes from linear to elliptical. The measured reflected intensity is characterized by two angles Δ_λ and Ψ_λ where Δ_λ represents the phase difference between the parallel and perpendicular polarizations of the reflected electric field while $\tan\Psi_\lambda$ represents the change in their amplitude ratio. The amplitude reflection coefficients $r_{\perp,\lambda}$ and $r_{\parallel,\lambda}$ of the perpendicular and parallel components of polarization are such that their ratio is given by [154]

$$\frac{r_{\parallel,\lambda}}{r_{\perp,\lambda}} = \tan\Psi_\lambda \exp(i\Delta_\lambda). \tag{6.9}$$

For a mesoporous thin film on a reflective substrate, the ratio $r_{\parallel,\lambda}/r_{\perp,\lambda}$ depends on the film's thickness L and on its effective refractive index $n_{eff,\lambda}$ [Equations (6.7)]. Therefore, fitting the spectral angles Δ_λ and Ψ_λ to a model based on thin film optics enables the retrieval of both L and $n_{eff,\lambda}$ of non-absorbing mesoporous thin films. Then, $n_{eff,\lambda}$ can be used to calculate the total porosity ϕ of the film using one of the EMAs previously discussed.

6.1.4 Ellipsometric porosimetry

Ellipsometric porosimetry (EP) combines ellipsometry and gas adsorption measurements by measuring the mesoporous thin film's thickness and refractive index as a gas (i.e., adsorbate) progressively fills the pores. This method yields (i) the thickness L, (ii) the spectral effective refractive index $n_{eff,\lambda}$, (iii) the adsorption

and desorption isotherms, (iv) the open porosity ϕ_o, and (v) the pore size distribution. The thickness L and the effective refractive index $n_{eff,\lambda}$ are retrieved by the ellipsometry method previously described. This method is also used to retrieve the thicknesses $L(P)$ and effective refractive indices $n_{eff,\lambda}(P)$ of the film filled with adsorbate retrieved for different pressures P. Then, the amount of adsorbate adsorbed/desorbed in the mesoporous film can be calculated as a function of the relative pressure P/P_0 where P_0 is the adsorbate saturation pressure. Since the processes are not necessarily reversible, the resulting adsorption and desorption isotherms feature hysteresis loops that can be classified into four types and provide information on the pore connectivity and shape [28]. In the case of ellipsometric porosimetry, the volume adsorbed ratio $r_a(P)$ at adsorbate pressure P, defined as the ratio of the volume of adsorbate in pores to the volume occupied by the film, is calculated from the thickness $L(P)$ and effective refractive index $n_{eff,\lambda}(P)$ using some EMA. For example, when using the Lorentz-Lorenz model, the volume adsorbed ratio $r_a(P)$ can be expressed as [144]

$$r_a(P) = \frac{V_m}{\alpha_a L(P)} \left[D(P)L(P) - D(0)L(0) \right] \tag{6.10}$$

where V_m is the molecular volume of the adsorbate (in cm^3), α_a is the molecular polarizability of the adsorbate (in cm^3), and $D(P)$ is defined as $D(P) = [n_{eff,\lambda}(P)^2 - 1]/[n_{eff,\lambda}(P)^2 + 2]$.

Then, the open porosity ϕ_o is calculated using the Lorentz-Lorenz EMA [Equation (6.4)] based on the effective refractive indices measured when the pores are completely empty and when the accessible pores are completely filled with the adsorbate close to saturation P_0 such that

$$\phi_o = r_a(P_0) = \frac{D(P_0) - D(0)}{\dfrac{n_{d,\lambda}(P_0)^2 - 1}{n_{d,\lambda}(P_0)^2 + 2}} \tag{6.11}$$

where $n_{d,\lambda}(P_0)$ is the refractive index of the adsorbate, assumed to be known.

Finally, the pore size distribution can be calculated from the isotherms using the Barrett-Joyner-Halenda (BJH) [83] algorithm which assumes that the pores are cylindrical. The model relies on the Kelvin equation relating the pore filling pressure to the radius of curvature of the adsorbate phase [84]. This estimate is then corrected for the layer of adsorbate present on the pore walls, using the measured or estimated statistical film thickness curve [155]. Figure 6.2(b) shows a diagram of the procedure.

6.1.5 Nitrogen porosimetry

Nitrogen porosimetry is a gas adsorption technique that measures (i) adsorption and desorption isotherms, (ii) the specific surface area S_a (in m^2/g), (iii) the total pore volume $v_{p,tot}$ (in cm^3/g) and open porosity ϕ_o, and (iv) the pore size distribution of bulk mesoporous materials. Adsorption-desorption isotherms report the amount of adsorbed nitrogen, calculated from the difference in numbers of moles that are (i) dosed into the sample tube and (ii) left in the gas phase in the sample tube after adsorption is complete, as a function of the relative pressure P/P_0. The specific surface area S_a can be obtained by the Brunauer-Emmett-Teller (BET) method based on the expression [82]

$$S_a = N_A C_{N_2} N_m \tag{6.12}$$

where N_A is the Avogadro constant (in mol^{-1}) and C_{N_2} is the cross-sectional area of a N_2 molecule adsorbed in a monolayer (in m^2) while N_m is the measured monolayer capacity (in mol/g), defined as the number of moles of N_2 needed to cover the surface of the pores in 1 g of porous material with a monolayer of N_2. The total pore volume $v_{p,tot}$ can be calculated by converting the number of moles of nitrogen adsorbed at a relative pressure P/P_0 close to saturation to

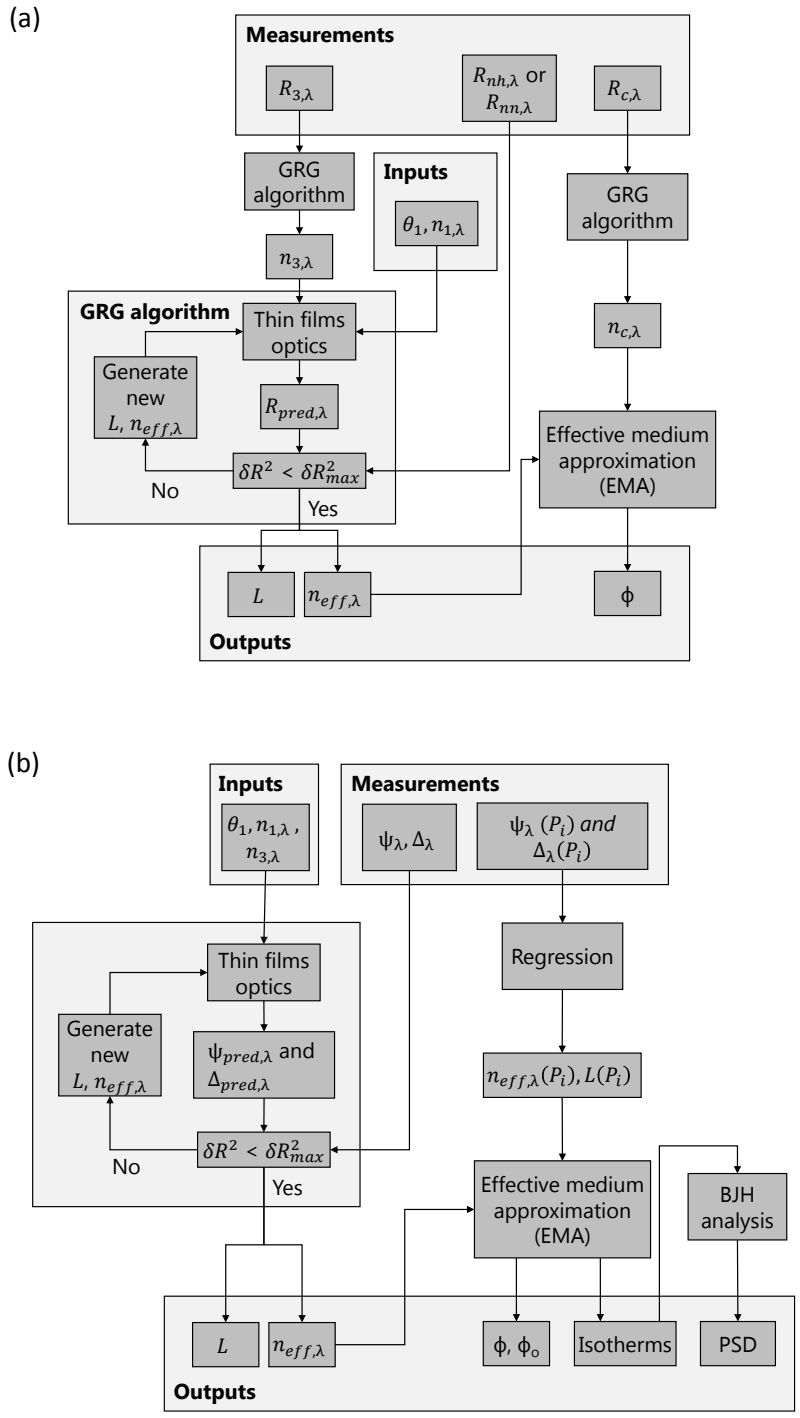

Figure 6.2: Block diagrams of (a) interferometry and (b) ellipsometric porosimetry.

the volume of liquid nitrogen based on the liquid nitrogen molar density of 34.38 cm^3mol^{-1} [156, 157]. Then, the open porosity ϕ_o can be calculated from the total pore volume $v_{p,tot}$ according to [157]

$$\phi_o = \frac{V_t\rho}{1 + V_t\rho} \tag{6.13}$$

where ρ is the density of the solid phase. Here also, the pore size distribution of mesoporous materials is obtained from the BJH method [83] using the Kelvin equation and the statistical film thickness of the adsorbate on the pore walls to estimate the pore size [85]. Nitrogen porosimetry is mainly used for characterizing mesoporous powders available in sufficiently large quantities.

Interferometry is a simple and well-established technique for measuring thickness and refractive index of dense thin films and has been implemented in commercial devices [158]. Several studies used interferometry to retrieve thickness and effective refractive index of mesoporous thin films and to estimate their porosity using some EMAs [159–162]. However, to the best of our knowledge, no comprehensive comparison of interferometry with other well-established methods for measuring the thickness, effective refractive index, and porosity of mesoporous thin films is available in the literature. Notably, this method has never been used for multicomponent mesoporous thin films such as silica-titania films. In addition, this study aims at determining if nitrogen porosimetry measurements on equivalent powders can be used as a substitute to measurements on thin films.

6.2 Materials and methods

6.2.1 Materials

The following materials were obtained from commercial suppliers and used without further purification: (1) ammonia-stabilized colloidal suspension of silica

nanoparticles (15 wt% of silica in water, measured mean particle diameter 9 nm, Nalco 2326, Nalco Chemical Company), (2) triblock copolymer Pluronic P123 ($EO_{20}PO_{70}EO_{20}$, M_w = 5800 Da, BASF), (3) triblock copolymer Pluronic F127 ($EO_{100}PO_{65}EO_{100}$, M_w = 12600 Da, BASF), (4) tetraethyl orthosilicate (TEOS) (98%, Acros Organics), (5) titanium isopropoxide (TIPO) (95%, Acros Organics), (6) hydrochloric acid (38 wt% in water, Certified ACS Plus, Fisher Scientific), (7) and ethanol (200 proof, Rossville Gold Shield).

6.2.2 Synthesis

Mesoporous silica and silica-titania thin films were prepared by evaporation-induced self-assembly [45,47,49] using either molecular precursors of silica (TEOS) and titania (TIPO) or silica nanoparticles as the building blocks along with Pluronic F127 or P123 as the structure directing agents. The porosity, pore size, and pore wall thickness of the thin films were controlled by adjusting the mass ratio M of the polymer to the inorganic components (i.e., the sum of silica and titania). The exact synthesis is described in the following paragraphs. Note that nanoparticle-based mesoporous silica-titania films were not prepared because solutions of silica and titania nanoparticles were unstable due to uncontrolled aggregation and precipitation caused by their opposing surface charges. Indeed, the silica nanoparticles were stabilized in NH_3 at pH 9 resulting in a negative surface charge while the titania nanoparticles were stabilized in solution at pH 3 resulting in a positive surface charge [163].

Mesoporous silica thin films

The solution of molecular silica precursor was prepared by dissolving 25 mg of either Pluronic F127 or Pluronic P123 in 0.6 mL of ethanol and 0.16 mL of 0.05 M aqueous HCl by magnetic stirring. Then, TEOS was added in the amount

corresponding to the desired polymer to silica mass ratio M between 0.1 and 2.5 g/g. Similarly, the solution of silica nanoparticles and structure directing agents was prepared by dissolving 0.678 g of either Pluronic F127 or Pluronic P123 in 3 mL of deionized water by magnetic stirring. Then, the colloidal suspension of silica nanoparticles was added in the amount corresponding to M between 0.1 and 2 g/g.

Sol-gel and nanoparticle-based mesoporous silica thin films were synthesized by spin-coating 80 μL of one of the above solutions onto a 1" x 1" single-crystal p-doped silicon substrate (μ = 0.005-0.01 Ω.cm). The film thickness was varied by changing the spin speed between 1,000 and 4,000 rpm. The as-spun films were calcined in air at 350°C for 30 min using a temperature ramp of 2°C/min to remove the polymer and then cooled in air to room temperature.

Silica-titania thin films

The synthesis of sol-gel mesoporous silica-titania films was adapted from the literature [164]. The desired amount of Pluronic F127 was dissolved in a solution of ethanol, HCl, and H_2O that was rapidly stirred at 60°C. Then, the desired amount of TEOS was added to the solution followed by a dropwise addition of TIPO, and the stirring was continued for another 5 hours at 60°C. The amount of Pluronic F127 was adjusted to correspond to a polymer to inorganic components mass ratio M between 1 and 2.5 g/g while the amount of the remaining components of the solution were defined by a molar ratio ethanol:HCl:H_2O:TEOS:TIPO = 50:6.1:0.06:x:(1-x) where x = 10, 20, and 30 determined the molar ratio of silica and titania in the prepared thin films. The sol-gel mesoporous silica-titania thin films were synthesized by spin-coating (1,000-4,000 rpm) 80 μL of the above silica-titania solution onto a 1" x 1" single-crystal p-doped silicon substrate (μ = 0.005-0.01 Ω.cm). The as-spun films were calcined in flowing oxygen at 400°C for

2 hours using a temperature ramp of 1°C/min to remove the polymer and then cooled in flowing oxygen to room temperature.

Moreover, dense sol-gel silica-titania thin films with compositions identical to those of the sol-gel mesoporous silica-titania films were prepared using the same procedure but without Pluronic F127. These films were used to measure the refractive index of the silica-titania continuous phase $n_{c,\lambda}$ necessary to retrieve porosity of the sol-gel mesoporous silica-titania films using an EMA.

Mesoporous silica and silica-titania powders

Finally, sol-gel and nanoparticle-based mesoporous silica powders and sol-gel mesoporous silica-titania powders were synthesized from the same solutions as those used to prepare the corresponding silica and silica-titania thin films. The solutions were evaporated in a Petri dish for at least 2 days, at relative humidity above 50%. The resulting powders were calcined in a tube furnace in flowing oxygen at 400°C for 10 to 12 hours using a temperature ramp of 5°C/min to remove the polymer template. They were then cooled in flowing oxygen to room temperature. These powders were characterized by nitrogen porosimetry.

6.2.3 Characterization

Mesoporous thin films were characterized by (i) scanning electron microscopy (SEM), (ii) contact profilometry, (iii) interferometry, (iv) ellipsometry, and (v) ellipsometric porosimetry (EP). Note that the porosity retrieved by interferometry and ellipsometry combined with the Maxwell-Garnett model corresponded to the total porosity ϕ of the mesoporous films while that measured by ellipsometric porosimetry represented the open porosity ϕ_o [157]. The open porosity of mesoporous powders was characterized by low-temperature nitrogen porosimetry. All details of these measurements and calculations are provided in Supporting

Information.

6.3 Results and discussion

Table 6.1 summarizes the structure, composition, thickness L, spectral effective refractive index $n_{eff,\lambda}$, open porosity ϕ_o, and peak pore diameter d_p, characterized by ellipsometric porosimetry, for sol-gel silica (denoted by SG) and silica-titania (ST) as well as nanoparticle-based silica (NP) mesoporous thin films using Pluronic F127 (F) or P123 (P) with different polymer to inorganic components mass ratio M. Here, the pore size distribution was calculated from the adsorption branch of the isotherm and the peak pore diameter d_p was defined as the diameter for which the pore size distribution reached its maximum. In the following discussion, ellipsometric porosimetry was used as the reference method to characterize mesoporous thin films.

Table 6.1: Structure, composition, thickness L, spectral effective refractive index $n_{eff,\lambda}$, and open porosity ϕ_o of the different mesoporous sol-gel silica (SG) and silica-titania (ST) thin films and nanoparticle-based silica (NP) films investigated in the present study.

Sample	**Structure**	**Polymer**	**Mass ratio M** (g/g)	**Silica:titania molar ratio**	**Film thickness L** (nm)	**Effective refractive index $n_{eff,\lambda}$** (λ = 400 -800 nm)	**Open porosity ϕ_o** (%)	**Peak pore diameter d_p** (nm)
SGF-2.5	sol-gel	F127	2.5	100:0	628	1.11	58	15.2
SGF-2	sol-gel	F127	2	100:0	374	1.17-1.18	65	11.5
SGF-1.7	sol-gel	F127	1.7	100:0	235	1.22	45	8.1
SGF-1.4	sol-gel	F127	1.4	100:0	255	1.22	46	8.1
SGF-1.2	sol-gel	F127	1.2	100:0	198	1.25-1.26	41	8.7
SGF-1.2-2	sol-gel	F127	1.2	100:0	337	1.20-1.21	54	15.0
SGF-0.6	sol-gel	F127	0.6	100:0	156	1.35	31	7.6
SGF-0.4	sol-gel	F127	0.4	100:0	231	1.37-1.39	22	6
SGP-1.5	sol-gel	P123	1.5	100:0	460	1.18-1.19	65	5.2
SGP-0.8	sol-gel	P123	0.8	100:0	297	1.23-1.24	47	8
SGP-0.2	sol-gel	P123	0.2	100:0	80.5	1.41	8	2.5
NPF-1.7	NP	F127	1.7	100:0	526	1.15-1.6	59	16.4
NPF-1.5	NP	F127	1.5	100:0	524	1.15-1.16	40	13.9
NPF-1.2	NP	F127	1.2	100:0	401	1.21-1.22	53	13.3
NPF-1.2-2	NP	F127	1.2	100:0	530	1.21-1.22	61	12.7
NPF-1	NP	F127	1	100:0	368	1.19-1.20	55	10.8
NPF-0.5	NP	F127	0.5	100:0	406	1.29	33	5.8
NPF-0.3	NP	F127	0.3	100:0	399	1.29-1.30	34	2.8
NPP-2	NP	P123	2	100:0	456	1.19	56	12.3
NPP-1.5	NP	P123	1.5	100:0	461	1.17-1.18	68	13.2
NPP-0.5	NP	P123	0.5	100:0	396	1.25-1.26	40	6.4
NPP-0.2	NP	P123	0.2	100:0	438	1.27-1.28	36	4.4
STF91-1	sol-gel	F127	1	90:10	242	1.33-1.35	36	4.1
STF82-2.2	sol-gel	F127	2.2	80:20	571	1.27	58	4.5
STF82-2	sol-gel	F127	2	80:20	508	1.28	53	4.9
STF82-1.7	sol-gel	F127	1.7	80:20	445	1.29-1.31	42	4
STF82-1.5	sol-gel	F127	1.5	80:20	424	1.32-1.34	41	4
STF82-1	sol-gel	F127	1	80:20	321	1.32-1.37	39	3.7
STF73-1.5	sol-gel	F127	1.5	70:30	452	1.33-1.35	48	4
STF73-1	sol-gel	F127	1	70:30	369	1.40-1.43	32	4

6.3.1 Scanning Electron Microscopy

Figure 6.3 shows SEM images of three representative mesoporous thin films namely (a) SGF-1.2 sol-gel silica film prepared using Pluronic F127 with polymer to silica mass ratio M = 1.2 g/g, (b) NPP-1.5 nanoparticle-based silica film prepared using Pluronic P123 with M = 1.5 g/g, and (c) STF73-1.5 sol-gel silica-titania film prepared using Pluronic F127 with M = 1.5 g/g and a silica:titania molar ratio of 70:30. The images indicate that the films were mesoporous with somewhat uniform but disordered pores. The backbone of the sol-gel silica and silica-titania films consisted of continuous silica and silica-titania networks that were created by condensation of the molecular precursor(s) [Figures 6.3(a) and 6.3(c)]. By contrast, the backbone of the nanoparticle-based silica film consisted of a network of aggregated silica nanoparticles that served as building blocks of the mesoporous

structure [Figure 6.3(b)].

6.3.2 Reference measurements

Refractive index of dense silica-titania $n_{c,\lambda}$

Figure 6.4 plots the spectral refractive index $n_{c,\lambda}$ of dense silica-titania films for wavelength λ between 400 and 800 nm retrieved by interferometry and ellipsometry for silica:titania molar ratio of 100:0 [24], 90:10, 80:20, and 70:30 using Cauchy's dispersion law given by [155]

$$n_{c,\lambda} = A + \frac{B}{\lambda^2} + \frac{C}{\lambda^4} \tag{6.14}$$

where A, B (in μm^2), and C (in μm^4) are fitting coefficients with λ expressed in μm. First, Figure 6.4 shows that the refractive index $n_{c,\lambda}$ measured by interferometry was in very good agreement with that measured by ellipsometry. Table E.1 summarizes the values of A, B, and C for the different silica:titania molar ratios considered. In fact, the relative error in refractive index $n_{c,\lambda}$ between the two methods was less than 6% (Table E.2 and Figure E.2).

Figure 6.4 also indicates that the refractive index of the dense silica-titania films increased with decreasing silica:titania molar ratio. This was expected since amorphous titania has a larger refractive index than silica [165], i.e., 2-2.6 vs. 1.45 in the 400-800 nm wavelength range. In addition, the refractive index $n_{c,\lambda}$ of dense silica-titania films varied from 0.03 to 0.07 in the 400-800 nm wavelength range as the silica:titania molar ratio ranged from 90:10 to 70:30 while that of silica did not vary by more than 0.02. Thus, the spectral nature of the refractive index of silica-titania $n_{c,\lambda}$, given by the dispersion law of Equation (6.14), must be considered in order to achieve good fitting of the reflectance spectra. However, the refractive index $n_{c,\lambda}$ of silica can be assumed to be constant and equal to 1.459

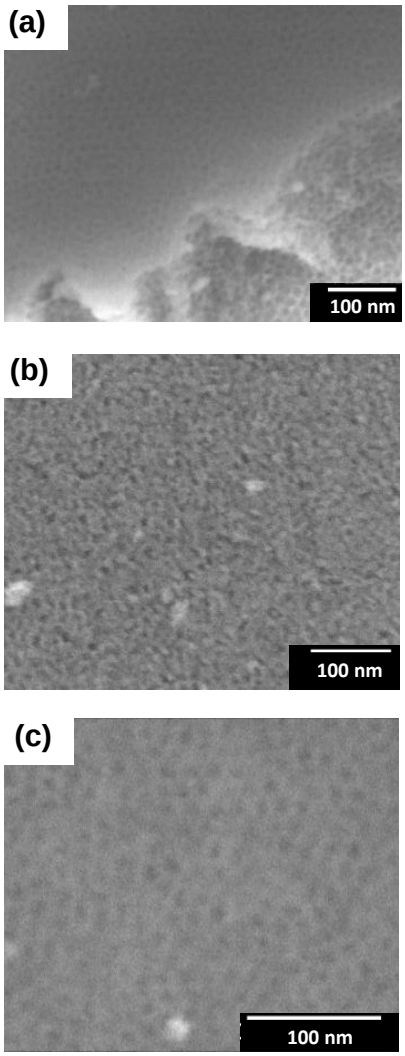

Figure 6.3: SEM images of (a) sol-gel mesoporous silica film templated with Pluronic F127 with a mass ratio M of 1.2 g/g (SGF-1.2), (b) nanoparticle-based mesoporous silica film templated with Pluronic P123 with $M = 1.5$ g/g (NPP-1.5), and (c) sol-gel mesoporous silica-titania film templated with Pluronic F127 and $M = 1.5$ g/g and with a silica:titania molar ratio of 70:30 (STF73-1.5). Silica matrix or nanoparticles appear in grey and pores appear in black.

(see section 6.1 in Supporting Information).

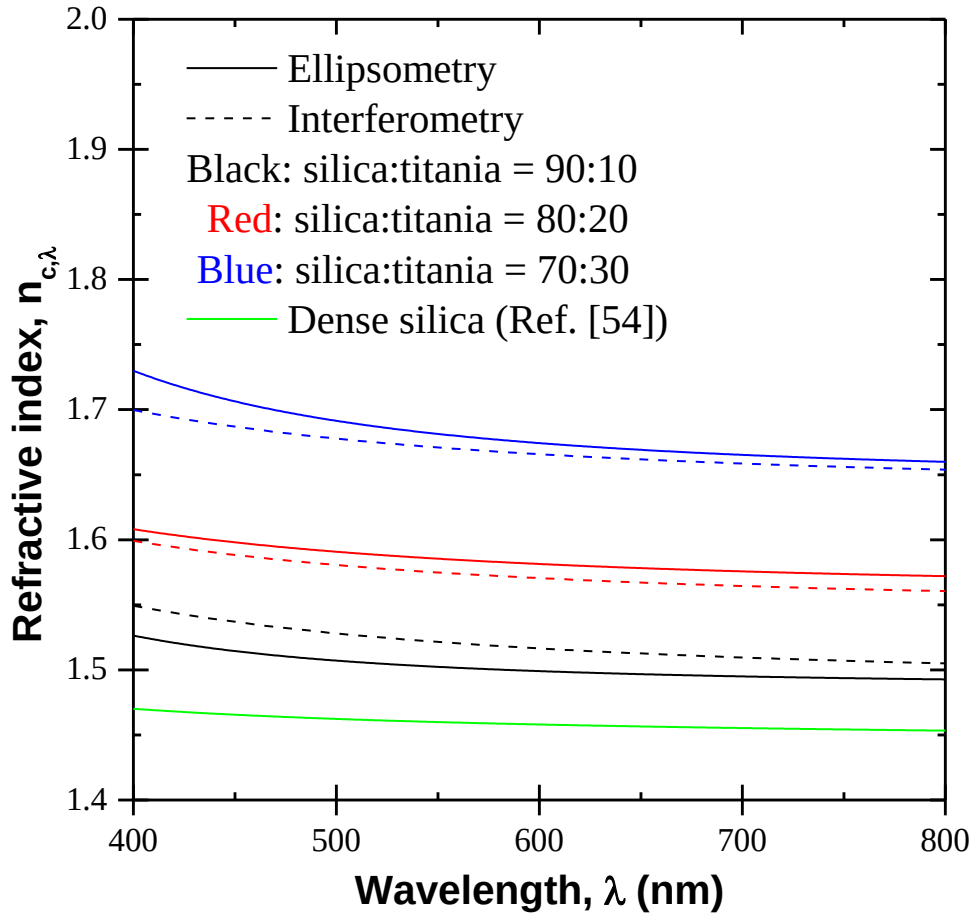

Figure 6.4: Spectral refractive index $n_{c,\lambda}$ of dense silica-titania films with silica:titania molar ratio of 90:10, 80:20, and 70:30 retrieved from ellipsometry (solid lines) and interferometry (dashed lines). The refractive index of silica from Ref. [24] is also plotted for comparison.

Adsorption-desorption isotherms

Figure 6.5 shows toluene adsorption-desorption isotherms of the (a) sol-gel mesoporous silica films (SGF), (b) nanoparticle-based mesoporous silica films (NPF), and (c) sol-gel mesoporous silica-titania films (STF) with silica:titania molar ratios of 90:10, 80:20, and 70:30 all prepared using Pluronic F127 with different polymer to inorganic components mass ratio M. All isotherms were of the type IV(a) ac-

cording to the IUPAC classification [28] confirming that all films were mesoporous. The isotherms of the sol-gel mesoporous (i) silica films with a mass ratio $M < 2$ g/g and (ii) silica-titania films featured H2(a) hysteresis loops indicating that the mesopores were constricted by necks with narrow size distribution [28]. The latter resulted in pore-blocking apparent through the very steep desorption close to the cavitation point of toluene. This indicates that the pores were likely spherical and the narrow connections between them served as the constricting necks. The isotherms of (a) the sol-gel mesoporous silica films prepared using Pluronic F127 with $M = 2$ and 2.5 g/g (SGF-2 and SGF-2.5) and (b) all nanoparticle-based mesoporous silica films prepared using Pluronic F127 featured H2(b) hysteresis loops indicating that the mesopores were similarly constricted by necks but in these films the neck size distribution was broader [28]. The latter was likely due to the broader pore size distributions in the sol-gel films with high mass ratio M and in all nanoparticle-based films.

Figure 6.6 presents the toluene adsorption-desorption isotherms of the sol-gel mesoporous silica films (SGP-0.2 to 1.5) and of the nanoparticle-based mesoporous silica films (NPP-0.2 to 2) templated with Pluronic P123, instead of Pluronic F127. Figure 6.6(a) shows that SGP-0.2 had an isotherm of type I(b) and featured an irreversible adsorption isotherm, i.e., the adsorption and desorption branches did not coincide even below the cavitation point of toluene, likely due to trapping of toluene in the network of very small pores. This was likely due to the very small amounts of block copolymer used for the synthesis of this film that resulted in small pores [28]. The isotherms of the other sol-gel and nanoparticle-based silica films prepared using Pluronic P123 were all of the type IV(a) indicating the presence of mesopores [28]. The SGP-0.8 film featured an H2(a) hysteresis loop while the SGP-1.5, NPP-0.2, NPP-0.5, NPP-1.5, and NPP-2 films featured H2(b) hysteresis loops.

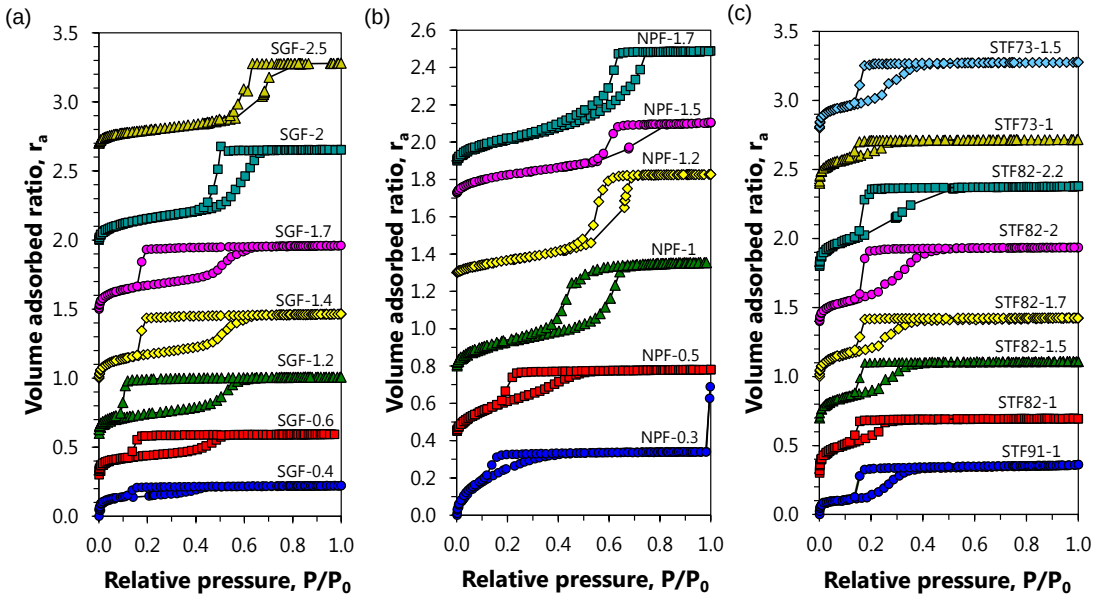

Figure 6.5: Toluene adsorption-desorption isotherms measured by ellipsometric porosimetry of the (a) sol-gel mesoporous silica films, (b) nanoparticle-based mesoporous silica films, and (c) sol-gel mesoporous silica-titania films with silica:titania molar ratios of 90:10, 80:20, and 70:30 all prepared using Pluronic F127 with different polymer to inorganic components mass ratio M. Isotherms were shifted for better visibility.

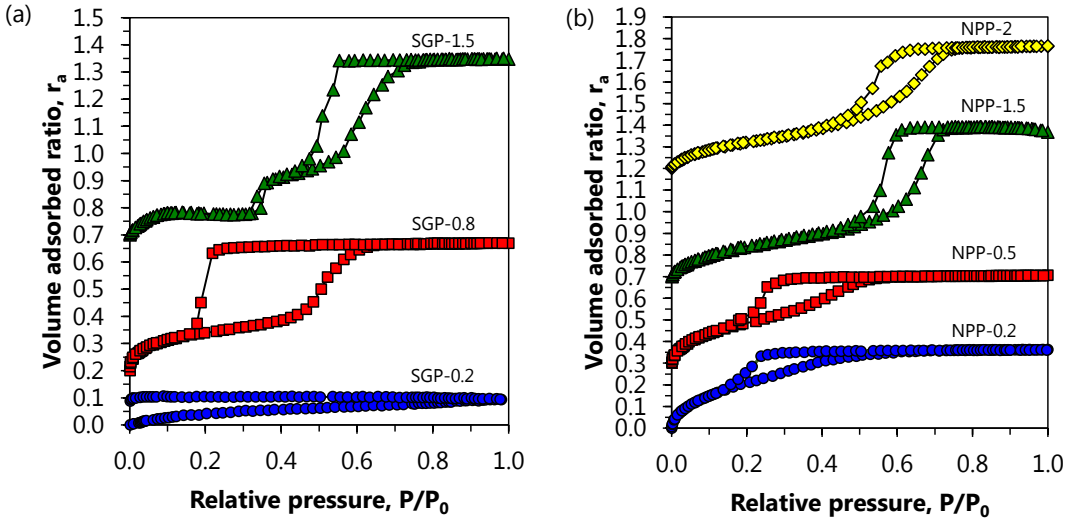

Figure 6.6: Toluene adsorption-desorption isotherms measured by ellipsometric porosimetry of the (a) sol-gel mesoporous silica and (b) nanoparticle-based mesoporous silica thin films all templated with Pluronic P123. Toluene isotherms were shifted by 0, 0.2, and 0.7 for SGP-1.5, SGP-0.8, SGP-0.2 films and by 0, 0.3, 0.7 and 1.2 for NPP-0.2, NPP-0.5, NPP-1.5, and NPP-2 films.

Porosity

Figure 6.7 depicts the open and total porosities retrieved by ellipsometric porosimetry and by interferometry for (a) sol-gel mesoporous silica, (b) nanoparticle-based mesoporous silica, and (c) sol-gel mesoporous silica-titania films (see Table 6.1) as a function of polymer to inorganic components mass ratio M. Figure 6.7 indicates that the porosity of all films generally increased with increasing mass ratio M. However, some films synthesized using high mass ratio M showed reduced porosity. For example, the open porosity ϕ_o of the sol-gel mesoporous silica films prepared using Pluronic F127 increased from 22 to 65% as M increased from 0.4 to 2 g/g. However, ϕ_o decreased to 58% for $M = 2.5$ g/g. Similarly, the open and total porosities of the nanoparticle-based silica films, prepared using Pluronic P123, increased from 36 to over 63% when M increased from 0.2 to 1.5 g/g but ϕ_o decreased to 56% and ϕ to 60% for $M = 2$ g/g. This observation was likely due to the fact that the films synthesized using high mass ratio M were more fragile, resulting in a partial collapse of the mesostructure during calcination. As a result, the porosity did not exceed 70% regardless of the polymer to inorganic components mass ratio M used for the synthesis.

Moreover, Figure 6.7 shows that the minimum porosity of the sol-gel silica films was much lower (8% for $M = 0.2$ g/g) than that of the nanoparticle-based silica films (34-36% for $M = 0.2$-0.3 g/g). This can be attributed to the fact that condensation of molecular precursors formed a continuous silica network that, in the absence of polymer template, completely filled the available space forming dense silica films. By contrast, silica nanoparticles aggregate spontaneously and leave empty space between them, even for $M = 0$ g/g, resulting in films with porosity above 26%, corresponding to the porosity of ordered close-packed monodisperse spheres [166].

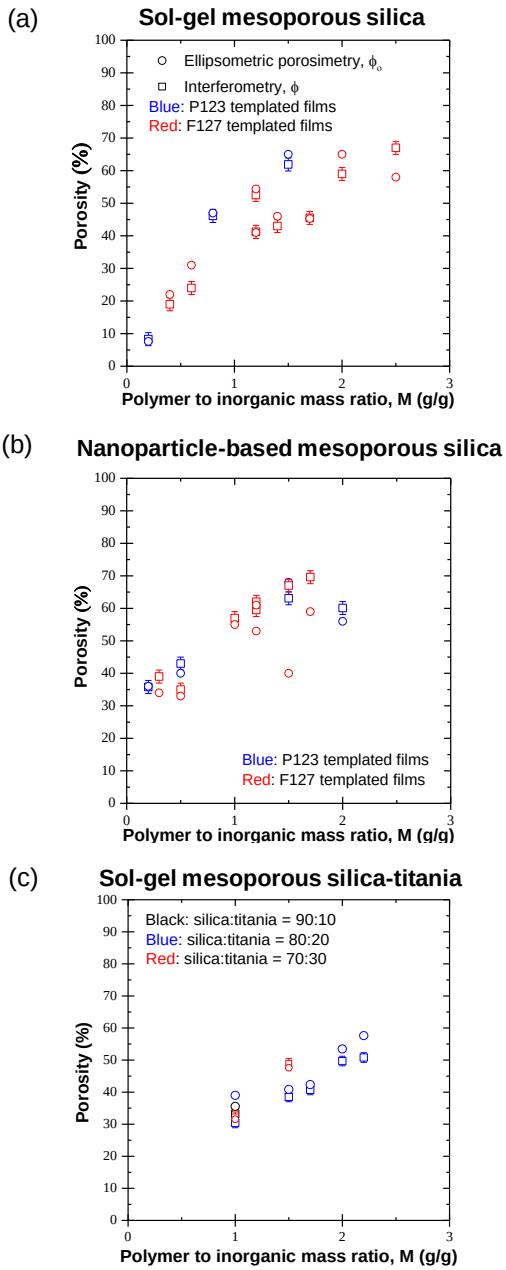

Figure 6.7: Porosity as a function of the polymer to inorganic component mass ratio M for (a) sol-gel mesoporous silica, (b) nanoparticle-based mesoporous silica, and (c) sol-gel mesoporous silica-titania films measured by ellipsometric porosimetry and interferometry.

Pore size distribution

Table 6.1 shows that the peak pore diameter d_p of the mesoporous silica and silica-titania films generally increased with increasing polymer to inorganic components mass ratio M. Moreover, Figure 6.8 shows the pore size distributions retrieved from ellipsometric porosimetry for (a) sol-gel, (b) nanoparticle-based mesoporous silica, and (c) sol-gel mesoporous silica-titania thin films templated with Pluronic F127. They indicate that the pore size distributions of mesoporous silica films broadened with increasing mass ratio M. This was caused by the increase in block copolymer concentration that resulted in increasing micelles' size and broadening of their size distribution [164]. The latter also caused broadening of the neck size distribution reflected in the aforementioned changes of the hysteresis loops from H2(a) to H2(b) for the sol-gel mesoporous silica films (see Figure 6.5(a) for SGF-0.4 to 2.5 and Figure 6.6(a) for SGP-0.2 to 1.5). Finally, Figure 6.9 shows similar trend for the pore size distributions of sol-gel and nanoparticle-based mesoporous silica films templated with Pluronic P123.

6.3.3 Comparison of characterization methods

Tables E.3 to E.5 in Supporting Information summarize the thickness, spectral effective refractive index, and porosity measured by contact profilometry, interferometry, ellipsometric porosimetry, and/or nitrogen porosimetry of all synthesized films and their corresponding powders.

Film thickness L

Figure 6.10(a) plots the thickness L of all mesoporous thin films investigated and measured using contact profilometry and interferometry as a function of the film thickness measured by ellipsometry. It shows that, in general, all three methods

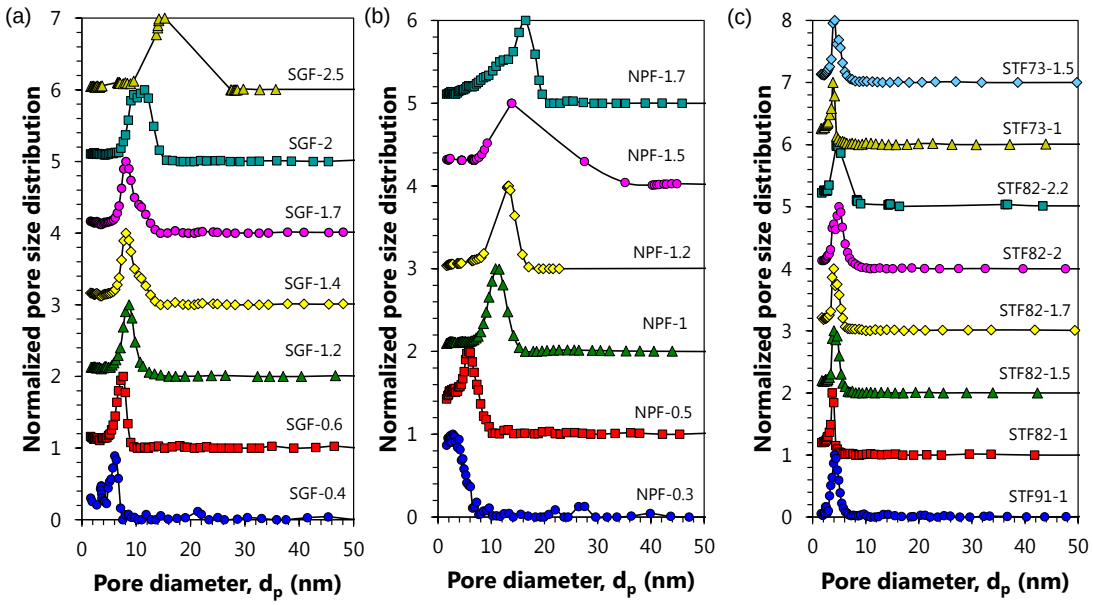

Figure 6.8: Pore size distributions measured by ellipsometric porosimetry of the (a) sol-gel mesoporous silica films, (b) nanoparticle-based mesoporous silica films, and (c) sol-gel mesoporous silica-titania films with silica:titania molar ratios of 90:10, 80:20, and 70:30 all prepared using Pluronic F127 with different polymer to inorganic components mass ratio M. Pore size distributions were shifted by increments of 1.

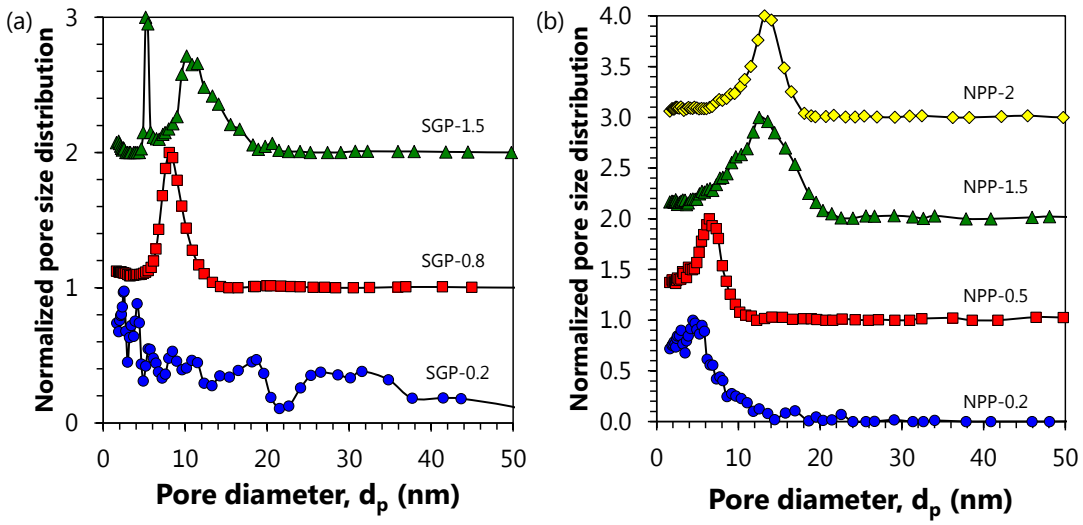

Figure 6.9: Pore size distributions measured by ellipsometric porosimetry of the (a) sol-gel mesoporous silica and (b) nanoparticle-based mesoporous silica thin films all templated with Pluronic P123. Pore size distributions were shifted by increments of 1.

considered were consistent. In fact, the thickness measured by contact profilometry and interferometry fell within 10% of the value measured using ellipsometry. However, the thickness of the SGF-2.5, NPF-1.2-2, and NPP-1.5 films showed significant inconsistency among the three methods resulting in differences in excess of 10%. This was probably due to the non-uniformity of the film thickness since each method probed different parts of the film. Finally, note that the thickness of some mesoporous thin films less than $\sim$ 250 nm thick and of dense silica-titania films could not be measured using contact profilometry because of the difficulty in preparing the samples due to the chipping of the films or the fact that they were too hard.

Effective refractive index $n_{eff,\lambda}$

Figure 6.10(b) plots the effective refractive index $n_{eff,\lambda}$ measured at wavelength $\lambda = 500$ nm by interferometry as a function of that measured using ellipsometry for all mesoporous thin films investigated. It shows that the measurements from both methods fell within 5% of each other for all samples.

Porosity

Figure 6.10(c) plots the total porosity ϕ retrieved by interferometry using the Maxwell-Garnett EMA [Equation (6.2)] as a function of the open porosity ϕ_o measured by ellipsometric porosimetry, based on Lorentz-Lorenz EMA [Equation (6.11)], for all mesoporous thin films synthesized. It also shows the total porosity retrieved by ellipsometry using the measured effective refractive index and the Maxwell-Garnett EMA along with the open porosity measured from nitrogen adsorption porosimetry performed on equivalent powders. First, Figure 6.10(c) shows that the total porosity ϕ measured by interferometry and ellipsometry agreed very well for most films. It also indicates that, for most samples,

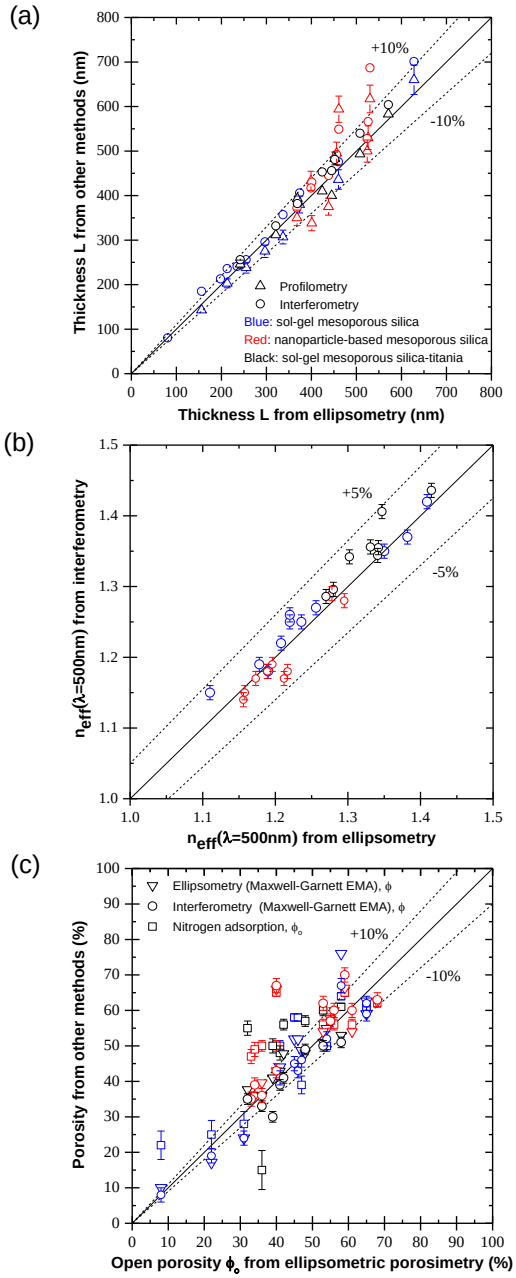

Figure 6.10: (a) Thickness L, (b) effective refractive index $n_{eff}(\lambda = 500$ nm), and (c) porosity of sol-gel mesoporous silica films (Table E.3), nanoparticle-based mesoporous silica films (Table E.4), and sol-gel mesoporous silica-titania films (Table E.5) measured by contact profilometry, interferometry, ellipsometry, and/or ellipsometric porosimetry. Dashed lines represent relative errors of 5 or 10%.

the total porosity obtained from interferometry was generally within 10% of the open porosity measured by ellipsometric porosimetry. This difference could be attributed to experimental uncertainty associated with both methods. It also suggests that the closed porosity of the films did not contribute significantly to their total porosity.

Figure 6.10(c) also shows that the total porosity of several mesoporous films retrieved by interferometry or ellipsometry was unexpectedly lower than the open porosity measured with ellipsometric porosimetry. In the case of all mesoporous silica films and most mesoporous silica-titania films, the total and open porosities fell within a relative error of 15% or an absolute error of 7%. This may be due to experimental uncertainty associated with both methods. For sol-gel mesoporous silica-titania films, it may also be due to the fact that the sol-gel derived dense films used to retrieve $n_{c,\lambda}$ might have been slightly porous. This would lead to an underestimation of the refractive index $n_{c,\lambda}$ resulting in underestimation of the total porosity by interferometry based on the Maxwell-Garnett model. However, the differences observed were not significant and the accurate total and open porosities were within the experimental uncertainties.

Finally, the fact that the total porosity ϕ of most mesoporous silica-titania films measured by interferometry was in good agreement (within 10%) with that measured by ellipsometry establishes that interferometry is a simple and reliable method to estimate the porosity of multicomponent mesoporous films.

6.3.4 Mesoporous thin films versus equivalent powders

Tables E.6 and E.7 present the structural characteristics of the powders measured by nitrogen porosimetry. Powders were designated with the letter P followed by references to their structure (SG, NP, ST), the template used (F for Pluronic F127 or P for Pluronic P123), and the mass ratio M.

Structure

Figures 6.11 shows the nitrogen adsorption-desorption isotherms of the powders equivalent to the (a) sol-gel mesoporous silica films, (b) nanoparticle-based mesoporous silica films, and (c) sol-gel mesoporous silica-titania films with silica:titania molar ratios of 90:10, 80:20, and 70:30, all prepared using Pluronic F127. Comparing Figures 6.5 and 6.11 indicates that, in general, the equivalent powders had porous structures different from their corresponding thin films. For example, SGF-0.4 and SGF-0.6 films were mesoporous based on their type IV(a) toluene isotherms but their equivalent powders, P-SGF-0.4 and P-SGF-0.6, had isotherms of type I(a) according to the IUPAC classification indicating a microporous structure [28]. Moreover, for the SGF-1.7, SGF-2, SGF-2.5, NPF-1.2, NPF-1.5, and NPF-1.7 films, the toluene isotherms featured only one clear adsorption step related to the capillary condensation in the pores whereas the nitrogen isotherms of the corresponding powders featured two steps indicating a bimodal pore size distribution. These discrepancies can be attributed to the fact that sol-gel synthesis is very sensitive to the drying conditions [167] and that the drying rate in spin-coating of thin films is much larger than in synthesizing equivalent powders. The same observations were made for mesoporous silica films and powders templated with Pluronic P123 (Figures 6.6 and 6.12).

Pore size distribution

Figures 6.13 shows the pore size distributions measured by nitrogen porosimetry of the powders equivalent to the (a) sol-gel mesoporous silica films, (b) nanoparticle-based mesoporous silica films, and (c) sol-gel mesoporous silica-titania films with silica:titania molar ratio of 90:10, 80:20, and 70:30 all prepared with Pluronic F127. Comparing Figures 6.8 and 6.13 indicates that, overall, the pore size increased with increasing polymer to silica mass ratio M for both mesoporous films and powders.

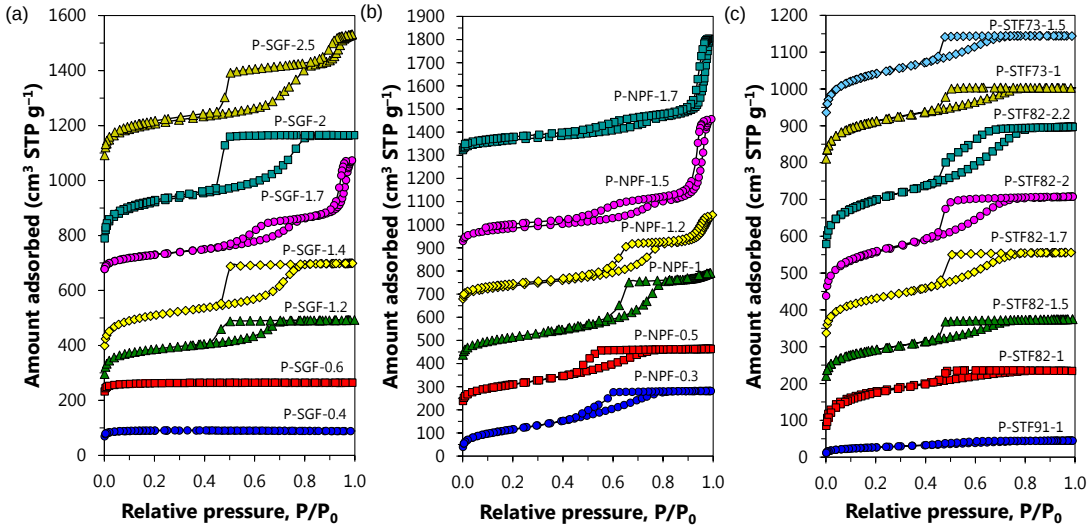

Figure 6.11: Nitrogen adsorption-desorption isotherms of the (a) sol-gel mesoporous silica powders, (b) nanoparticle-based mesoporous silica powders, and (c) sol-gel mesoporous silica-titania powders with silica:titania molar ratios of 90:10, 80:20, and 70:30 all prepared using Pluronic F127 with different polymer to inorganic components mass ratio M. Isotherms were shifted for better visibility.

However, films and their equivalent powders had different pore size distributions and peak pore diameter d_p. Contrary to thin films, powders often had bimodal pore size distributions such as P-SGF-1.4, P-SGF-1.7, or P-NPF-1.5. Similar discrepancies could be observed for the sol-gel and nanoparticle-based mesoporous silica films and powders templated with Pluronic P123 (Figure 6.9 and 6.14). This was due to the different drying conditions between the mesoporous films and the equivalent powders that affected their structural evolution, as previously discussed. Note that the kinetic diameter of toluene molecules is 0.61 nm [168] and that of nitrogen is 0.37 nm [169]. Therefore, since the measured pores featured a diameter equal or greater than 1.6 nm, both molecules should probe the same pore sizes [157].

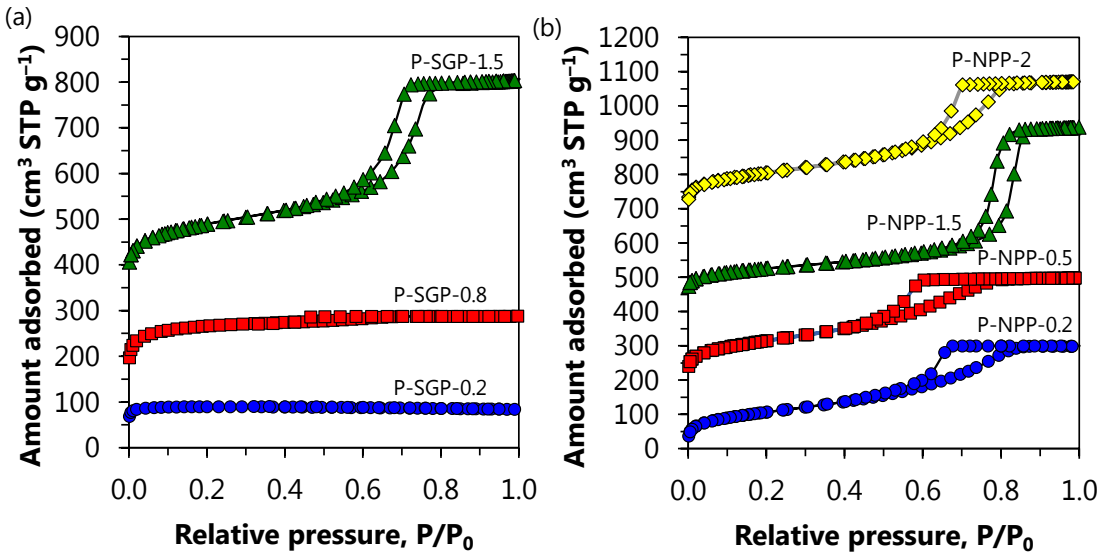

Figure 6.12: Nitrogen adsorption-desorption isotherms of the (a) sol-gel mesoporous silica and (b) nanoparticle-based mesoporous silica powders all templated with Pluronic P123. Nitrogen isotherms were shifted by 0, 100, and 350 cm^3 STP g^{-1} for P-SGP-1.5, P-SGP-0.8, P-SGP-0.2 powders and by 0, 200, 450, and 700 cm^3 STP g^{-1} for P-NPP-0.2, P-NPP-0.5, P-NPP-1.5, and P-NPP-2 powders.

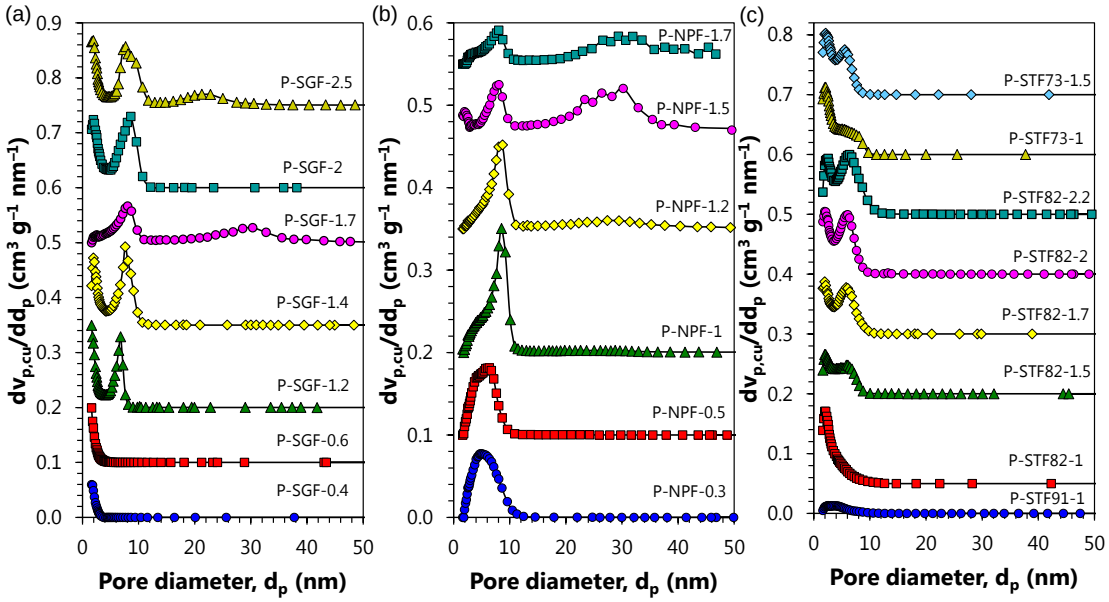

Figure 6.13: Pore size distributions measured by nitrogen porosimetry of the (a) sol-gel mesoporous silica powders, (b) nanoparticle-based mesoporous silica powders, and (c) sol-gel mesoporous silica-titania powders with silica:titania molar ratios of 90:10, 80:20, and 70:30 all prepared using Pluronic F127 with different polymer to inorganic components mass ratio M. Pore size distributions were shifted for better visibility.

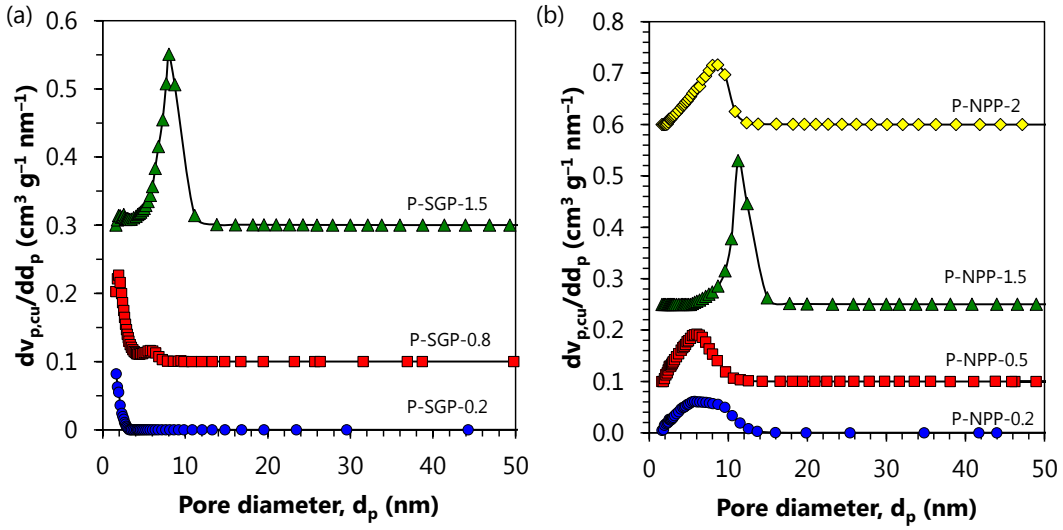

Figure 6.14: Pore size distributions measured by nitrogen porosimetry of the (a) sol-gel mesoporous silica and (b) nanoparticle-based mesoporous silica powders all templated with Pluronic P123. Pore size distributions were shifted by 0, 0.1, and 0.3 $cm^3\ g^{-1}\ nm^{-1}$ for P-SGP-1.5, P-SGP-0.8, P-SGP-0.2 powders and by 0, 0.1, 0.25, and 0.6 $cm^3\ g^{-1}\ nm^{-1}$ for P-NPP-0.2, P-NPP-0.5, P-NPP-1.5, and P-NPP-2 powders.

Porosity

Figure 6.10(c) indicates that the open porosity ϕ_o obtained from nitrogen porosimetry on the powders equivalent to the sol-gel mesoporous silica and silica-titania films generally differed by more than 10% from the open porosity ϕ_o of films measured by ellipsometric porosimetry. It is interesting to note that the porosity ϕ_o of the powders equivalent to the nanoparticle-based mesoporous silica films measured by nitrogen porosimetry was in good agreement (within 10%) with the porosity obtained from ellipsometric porosimetry or from interferometry in the case of the NPF-1.2, NPF-1.5, and NPF-1.7 films, except for films with low polymer to silica mass ratio $M \leq 0.5$ g/g.

Overall, these results establish that using the equivalent powders as a substitute to perform the structural characterization of thin films is inappropriate.

6.4 Conclusion

This study compared systematically contact profilometry, interferometry, ellipsometry, and ellipsometric porosimetry for measuring the thickness, effective refractive index, porosity, and/or pore size distribution of mesoporous thin films. To do so, mesoporous silica and silica-titania thin films with different thicknesses, structures (sol-gel or nanoparticle-based), compositions (silica or silica-titania), porosities, and pore sizes were synthesized and characterized. For most films, the thickness measured using contact profilometry and interferometry agreed within 15% with that measured using ellipsometry. Interferometry and ellipsometry should be preferred as they are non-destructive methods, unlike contact profilometry. The effective refractive index measured by interferometry agreed within 5% with that measured by ellipsometry. Finally, the porosity measured by interferometry fell within 15% with that measured by ellipsometric porosimetry for most films indicating that closed pores did not contribute significantly to the total

porosity. Occasionally, interferometry was more appropriate for porosity measurements than ellipsometric porosimetry since it measures the total porosity of the film instead of the open porosity.

Moreover, the open porosity and pore size distribution measured by nitrogen adsorption porosimetry on equivalent powders disagreed with measurements made on the corresponding mesoporous thin films. These observations were attributed to the different drying conditions between spin coating of films and drying of powders. Therefore, characterization of equivalent powders cannot be used as representative of thin films.

Overall, the study showed that interferometry is a robust and simple alternative to ellipsometry for measuring the film thickness, effective refractive index, and total porosity of non-absorbing multicomponent mesoporous thin films.

CHAPTER 7

Conclusions and Future Work

7.1 Conclusions

The objectives of this dissertation were to (i) computationally generate and characterize realistic mesoporous materials, (ii) explore how their structures affect their scattering characteristics, and (iii) apply the knowledge gained in light scattering to understand light transfer through drying mesoporous monoliths and optical characterization of thin films.

The first objective was achieved by developing numerical methods to generate and fully characterize realistic three-dimensional computer-generated mesoporous materials (Chapter 2). First, new tools were developed to numerically generate and characterize mesoporous structures in terms of specific surface area, average pore diameter, and pore size distribution, in complete analogy with experimental characterization including gas adsorption porosimetry. Notably, Chapter 2 established that the specific surface area for point-contact structures corresponded to the maximum specific surface area of mesoporous material for a given primary particle radius. For given porosity and particle radius, particles overlapping and/or polydispersity reduced the specific surface area and interfacial concentration and increased the average pore diameter.

The second objective was achieved in Chapters 3 and 4. Chapter 3 determined (1) the parameters governing the scattering cross-section and asymmetry factor of bispheres, disordered and ordered particle suspensions, and aggregates of non-absorbing spherical particles and (2) the conditions under which dependent and independent scattering regimes prevail for their scattering cross-section and asym-

metry factor. These integral radiation characteristics were shown to be functions exclusively of the number of particles, their size parameter, their relative index of refraction, and the interparticle distance-to-wavelength ratio. Transition criteria between the dependent and independent scattering regimes obtained for bispheres could be extended to disordered particle systems provided the transition criteria were based on the minimum interparticle distance-to-wavelength ratio instead of on the average interparticle distance-to-wavelength ratio. Furthermore, Chapter 4 showed that (1) dependent effects prevailed in all aggregates and were stronger in aggregates with smaller particles, (2) particle overlapping did not affect the scattering cross-section and asymmetry factor of aggregates, and (3) non-absorbing aggregates constitutive of mesoporous materials could be approximated as spheres with the same volume and effective refractive index corresponding to the so-called equivalent effective properties (EEP) approximation.

The third objective was achieved in Chapters 5 and 6. In Chapter 5, the changes in appearance observed experimentally in sol-gel synthesis of mesoporous monoliths during drying under ambient conditions were explained. Chapter 5 confirmed, through a light transfer model based on the EEP approximation (Chapter 4), that dry domains emerging during the falling rate period caused the temporary white appearance of drying mesoporous monoliths. Finally, Chapter 6 compared systematically contact profilometry, interferometry, ellipsometry, and ellipsometric porosimetry for measuring the film thickness, effective refractive index, and total porosity of non-absorbing multicomponent mesoporous thin films. It demonstrated that interferometry is a robust and simple alternative to ellipsometry. Moreover, the open porosity and pore size distribution measured by nitrogen adsorption porosimetry on equivalent powders disagreed with measurements made on the corresponding mesoporous thin films. These observations were attributed to the different drying conditions between spin coating of films and drying of powders. Therefore, characterization of equivalent powders cannot be used

as representative of thin films.

7.2 Future work

7.2.1 Effect of absorption on thermal performances of mesoporous materials

Chapters 3 and 4 investigated the scattering characteristics of transparent mesoporous materials in the visible when absorption is negligible. However, in the infrared (IR), absorption of mesoporous materials such as mesoporous silica is no longer negligible [170]. In fact, the radiative characteristics in the IR may affect the thermal conductivity of mesoporous materials with high porosity [76]. Therefore, in the perspective of using mesoporous materials in window solutions, it would be insightful to study both the scattering and absorption cross-sections and the asymmetry factor of fractal aggregates in the IR.

7.2.2 Predicting transmittance, reflectance, and haze of mesoporous materials

Chapter 6 indicated that mesoporous thin films are non-scattering. However, thick mesoporous monoliths scatter light. In fact, Chapter 5 assumed that fully dry and fully wet mesoporous monoliths could also be considered as non-scattering. However, the predicted normal-hemispherical transmittances of dry and wet monoliths were slightly higher than the measured ones while the measured hazes were non-negligible. These differences between measurements and predictions were due to scattering of light by the mesopores. Therefore, it would be of great practical interest to develop a numerical model computing the transmittance and haze of mesoporous materials from their structural characteristics, i.e., particle size, porosity, and pore size distribution. Such models exist, however, to the best of our knowledge, they do not account for dependent scattering effects whereas

Chapters 3 and 4 established these effects are significant in mesoporous materials under visible light.

References

[1] F. Klenert, J. Fruhstorfer, C. G. Aneziris, U. Gross, D. Trimis, I. Reichenbach, D. Vijay, and A. Horn, "Microstructure and transmittance of silica gels for application as transparent heat insulation materials", *Journal of Sol-Gel Science and Technology*, vol. 75, no. 3, pp. 602–616, 2015.

[2] H. Ma, E. Ding, and W. Wang, "Power reduction with enhanced sensitivity for pellistor methane sensor by improved thermal insulation packaging", *Sensors and Actuators B: Chemical*, vol. 187, pp. 221–226, 2013.

[3] S.-W. Hwang, H.-H. Jung, S.-H. Hyun, and Y.-S. Ahn, "Effective preparation of crack-free silica aerogels via ambient drying", *Journal of Sol-Gel Science and Technology*, vol. 41, no. 2, pp. 139–146, 2007.

[4] M.-A. Einarsrud, E. Nilsen, A. Rigacci, G. M. Pajonk, S. Buathier, D. Valette, M. Durant, B. Chevalier, P. Nitz, and F. Ehrburger-Dolle, "Strengthening of silica gels and aerogels by washing and aging processes", *Journal of Non-Crystalline Solids*, vol. 285, no. 1, pp. 1–7, 2001.

[5] M.-A. Einarsrud and E. Nilsen, "Strengthening of water glass and colloidal sol based silica gels by aging in TEOS", *Journal of Non-Crystalline Solids*, vol. 226, no. 1, pp. 122–128, 1998.

[6] J. Ramsey, *Sol-Gel Processing*, Butterworth, Oxford, UK, 1994.

[7] A. Emmerling, J. Gross, R. Gerlach, R. Goswin, G. Reichenauer, J. Fricke, and H.-G. Haubold, "Isothermal sintering of SiO_2 aerogels", *Journal of Non-Crystalline Solids*, vol. 125, no. 3, pp. 230–243, 1990.

[8] J. Harreld, T. Ebina, N. Tsubo, and G. Stucky, "Manipulation of pore size distributions in silica and ormosil gels dried under ambient pressure conditions", *Journal of Non-Crystalline Solids*, vol. 298, no. 2, pp. 241–251, 2002.

[9] K. Wittmaack, "Characterization of carbon nanoparticles in ambient aerosols by scanning electron microscopy and model calculations", *Journal of the Air & Waste Management Association*, vol. 54, no. 9, pp. 1091–1098, 2004.

[10] Y. Kameya and K. Hanamura, "Enhancement of solar radiation absorption using nanoparticle suspension", *Solar Energy*, vol. 85, no. 2, pp. 299–307, 2011.

[11] H. K. Park, D. K. Kim, and C. H. Kim, "Effect of solvent on titania particle formation and morphology in thermal hydrolysis of $TiCl_4$", *Journal of the American Ceramic Society*, vol. 80, no. 3, pp. 743–749, 1997.

[12] A. Quirantes, F. Arroyo, and J. Quirantes-Ros, "Multiple light scattering by spherical particle systems and its dependence on concentration: a T-matrix study", *Journal of Colloid and Interface Science*, vol. 240, no. 1, pp. 78–82, 2001.

[13] M. Kaviany and B. P. Singh, "Radiative heat transfer in porous media", in *Advances in Heat Transfer*, vol. 23, pp. 133–186. 1993.

[14] Z. Ivezić and M. P. Mengüç, "An investigation of dependent/independent scattering regimes using a discrete dipole approximation", *International Journal of Heat and Mass Transfer*, vol. 39, no. 4, pp. 811–822, 1996.

[15] C.-L. Tien and B. Drolen, "Thermal radiation in particulate media with dependent and independent scattering", *Annual Review of Heat Transfer*, vol. 1, no. 1, pp. 1–32, 1987.

[16] M. I. Mishchenko, D. W. Mackowski, and L. D. Travis, "Scattering of light by bispheres with touching and separated components", *Applied Optics*, vol. 34, no. 21, pp. 4589–4599, 1995.

[17] M. I. Mishchenko, L. Liu, and G. Videen, "Conditions of applicability of the single-scattering approximation", *Optics Express*, vol. 15, no. 12, pp. 7522–7527, 2007.

[18] B. Drolen and C.-L. Tien, "Absorption and scattering of agglomerated soot particulate", *Journal of Quantitative Spectroscopy and Radiative Transfer*, vol. 37, no. 5, pp. 433–448, 1987.

[19] M. Mishchenko, Z. Dlugach, and N. Zakharova, "Direct demonstration of the concept of unrestricted effective-medium approximation", *Optics letters*, vol. 39, no. 13, pp. 3935–3938, 2014.

[20] M. I. Mishchenko, J. M. Dlugach, M. A. Yurkin, L. Bi, B. Cairns, L. Liu, R. L. Panetta, L. D. Travis, P. Yang, and N. T. Zakharova, "First-principles modeling of electromagnetic scattering by discrete and discretely heterogeneous random media", *Physics Reports*, vol. 632, pp. 1–75, 2016.

[21] M. Lagarrigue, S. Jacquier, J. Debayle, J.-C. Pinoli, and F. Gruy, "Approximation for the light scattering cross-section of optically hard aggregates", *Journal of Quantitative Spectroscopy and Radiative Transfer*, vol. 113, no. 9, pp. 704–714, 2012.

[22] Prayitno, "UCLA Royce Hall", *https://www.flickr.com/photos/prayitnophotography.*

[23] "Creative commons license", *https://creativecommons.org/licenses/by/2.0.*

[24] I. Malitson, "Interspecimen comparison of the refractive index of fused silica", *Journal of the Optical Society of America*, vol. 55, no. 10, pp. 1205–1209, 1965.

[25] M. Baklanov and K. Mogilnikov, "Non-destructive characterisation of porous low-k dielectric films", *Microelectronic Engineering*, vol. 64, no. 1, pp. 335–349, 2002.

[26] D. Yang, R. Opila, G. Jiang, V. Pallem, and D. Gidley, "Porosity and pore interconnectivity characterization and understanding using positron annihilation lifetime spectroscopy, ellipsometric porosimetry and x-ray reflectivity", in *Frontiers of Characterization and Metrology for Nanoelectronics Conference*, National Institute of Standards and Technology, Gaithersburg, MD, 2013.

[27] "Single-pane highly insulating efficient lucid designs (SHIELD)", Tech. Rep. AR-311-10.15, Advanced Research Projects Agency (ARPA-E) U.S. Department of Energy, 2015.

[28] M. Thommes, K. Kaneko, A. Neimark, J. Olivier, F. Rodriguez-Reinoso, J. Rouquerol, and K. Sing, "Physisorption of gases, with special reference to the evaluation of surface area and pore size distribution (IUPAC technical report)", *Pure and Applied Chemistry*, vol. 87, no. 9-10, pp. 1051–1069, 2015.

[29] J. Rouquerol, D. Avnir, C. Fairbridge, D. Everett, J. Haynes, N. Pernicone, J. Ramsay, K. Sing, and K. Unger, "Recommendations for the characterization of porous solids (technical report)", *Pure and Applied Chemistry*, vol. 66, no. 8, pp. 1739–1758, 1994.

[30] T. Yanagisawa, T. Shimizu, K. Kuroda, and C. Kato, "The preparation of alkyltriinethylaininonium–kaneinite complexes and their conversion to microporous materials", *Bulletin of the Chemical Society of Japan*, vol. 63, no. 4, pp. 988–992, 1990.

[31] F. Schüth, "Non-siliceous mesostructured and mesoporous materials", *Chemistry of Materials*, vol. 13, no. 10, pp. 3184–3195, 2001.

[32] J. Vivero-Escoto, Y.-D. Chiang, K. Wu, and Y. Yamauchi, "Recent progress in mesoporous titania materials: adjusting morphology for innovative applications", *Science and Technology of Advanced Materials*, vol. 13, no. 1, pp. 013003, 2012.

[33] S. Xiong, C. Yuan, X. Zhang, B. Xi, and Y. Qian, "Controllable synthesis of mesoporous co3o4 nanostructures with tunable morphology for application in supercapacitors", *Chemistry-A European Journal*, vol. 15, no. 21, pp. 5320–5326, 2009.

[34] M. Hartmann, "Ordered mesoporous materials for bioadsorption and biocatalysis", *Chemistry of Materials*, vol. 17, no. 18, pp. 4577–4593, 2005.

[35] S. Wang, "Ordered mesoporous materials for drug delivery", *Microporous and Mesoporous Materials*, vol. 117, no. 1, pp. 1–9, 2009.

[36] M. Vallet-Regí, "Ordered mesoporous materials in the context of drug delivery systems and bone tissue engineering", *Chemistry-A European Journal*, vol. 12, no. 23, pp. 5934–5943, 2006.

[37] A. Walcarius, "Mesoporous materials and electrochemistry", *Chemical Society Reviews*, vol. 42, no. 9, pp. 4098–4140, 2013.

[38] H.-C. Kim, S.-M. Park, and W. Hinsberg, "Block copolymer based nanostructures: materials, processes, and applications to electronics", *Chemical reviews*, vol. 110, no. 1, pp. 146–177, 2009.

[39] B. Scott, G. Wirnsberger, and G. Stucky, "Mesoporous and mesostructured materials for optical applications", *Chemistry of Materials*, vol. 13, no. 10, pp. 3140–3150, 2001.

[40] U. Berardi, "The development of a monolithic aerogel glazed window for an energy retrofitting project", *Applied Energy*, vol. 154, pp. 603–615, 2015.

[41] T. Gao, T. Ihara, S. Grynning, B. Jelle, and A. Lien, "Perspective of aerogel glazings in energy efficient buildings", *Building and Environment*, vol. 95, pp. 405–413, 2016.

[42] T. Coquil, E. Richman, N. Hutchinson, S. Tolbert, and L. Pilon, "Thermal conductivity of cubic and hexagonal mesoporous silica thin films", *Journal of Applied Physics*, vol. 106, no. 3, pp. 034910, 2009.

[43] D. Rolison and B. Dunn, "Electrically conductive oxide aerogels: new materials in electrochemistry", *Journal of Materials Chemistry*, vol. 11, no. 4, pp. 963–980, 2001.

[44] D. Zhao, J. Feng, Q. Huo, N. Melosh, G. Fredrickson, B. Chmelka, and G. Stucky, "Triblock copolymer syntheses of mesoporous silica with periodic 50 to 300 angstrom pores", *Science*, vol. 279, no. 5350, pp. 548–552, 1998.

[45] C. Brinker, Y. Lu, A. Sellinger, and H. Fan, "Evaporation-induced self-assembly: nanostructures made easy", *Advanced Materials*, vol. 11, no. 7, pp. 579–585, 1999.

[46] B. Smarsly and M. Antonietti, "Block copolymer assemblies as templates for the generation of mesoporous inorganic materials and crystalline films", *European Journal of Inorganic Chemistry*, vol. 2006, no. 6, pp. 1111–1119, 2006.

[47] D. Grosso, F. Cagnol, G. d. A. Soler-Illia, E. Crepaldi, H. Amenitsch, A. Brunet-Bruneau, A. Bourgeois, and C. Sanchez, "Fundamentals of mesostructuring through evaporation-induced self-assembly", *Advanced Functional Materials*, vol. 14, no. 4, pp. 309–322, 2004.

[48] A. Dorcheh and M. Abbasi, "Silica aerogel; synthesis, properties and characterization", *Journal of Materials Processing Technology*, vol. 199, no. 1, pp. 10–26, 2008.

[49] C. Brinker and G. Scherer, *Sol-Gel Science*, Academic Press, London, UK, 2013.

[50] R. Iler, *The Chemistry of Silica*, John Wiley & Sons, Chichester, UK, 1979.

[51] J. Long, K. Swider-Lyons, R. Stroud, and D. Rolison, "Design of pore and matter architectures in manganese oxide charge-storage materials", *Electrochemical and Solid-State Letters*, vol. 3, no. 10, pp. 453–456, 2000.

[52] C. Brinker, A. Hurd, P. Schunk, G. Frye, and C. Ashley, "Review of sol-gel thin film formation", *Journal of Non-Crystalline Solids*, vol. 147, pp. 424–436, 1992.

[53] L. B. N. Laboratory, *Window software*.

[54] N. F. R. C. Incorporated, *Procedure for Determining Fenestration Product U-factors*.

[55] M. Modest, *Radiative Heat Transfer*, Academic Press, San Diego, CA, USA, 2013.

[56] C. Bohren and D. Huffman, *Absorption and Scattering of Light by Small Particles*, John Wiley & Sons, New York, NY, USA, 1983.

[57] H. C. van de Hulst, *Light Scattering by Small Particles*, Courier Corporation, North Chelmsford, MA, USA, 1981.

[58] M. Brewster and C.-L. Tien, "Radiative transfer in packed fluidized beds: dependent versus independent scattering", *ASME Journal of Heat Transfer*, vol. 104, no. 4, pp. 573–579, 1982.

[59] G. Videen, R. Pinnick, D. Ngo, Q. Fu, and P. Chỳlek, "Asymmetry parameter and aggregate particles", *Applied Optics*, vol. 37, no. 6, pp. 1104–1109, 1998.

[60] E. Cuce, P. Cuce, C. Wood, and S. Riffat, "Toward aerogel based thermal superinsulation in buildings: a comprehensive review", *Renewable and Sustainable Energy Reviews*, vol. 34, pp. 273–299, 2014.

[61] C. Buratti and E. Moretti, "Glazing systems with silica aerogel for energy savings in buildings", *Applied Energy*, vol. 98, pp. 396–403, 2012.

[62] K. Duer and S. Svendsen, "Monolithic silica aerogel in superinsulating glazings", *Solar Energy*, vol. 63, no. 4, pp. 259–267, 1998.

[63] Y. Yan, S. C. King, M. Li, T. Galy, M. Marszewski, J. S. Kang, L. Pilon, Y. Hu, and S. H. Tolbert, "Exploring the effect of porous structure on thermal conductivity in templated mesoporous silica films", *The Journal of Physical Chemistry C*, vol. 123, no. 35, pp. 21721–21730, 2019.

[64] Y. Yan, M. Li, S. King, T. Galy, M. Marszewski, J. S. Kang, L. Pilon, Y. Hu, and S. H. Tolbert, "Controlling thermal conductivity in mesoporous silica films using pore size and nanoscale architecture", *The Journal of Physical Chemistry Letters*, vol. 11, no. 9, pp. 3731–3737, 2020.

[65] S. C. King, M. Li, T. Galy, Y. Yan, J. S. Kang, Y. Li, M. Marszewski, L. Pilon, Y. Hu, and S. H. Tolbert, "Controlling thermal conductivity in mesoporous silica films using pore size and nanoscale architecture", *The Journal of Physical Chemistry Letters (submitted)*, 2020.

[66] D. Schaefer, "Polymers, fractals, and ceramic materials", *Science*, vol. 243, no. 4894, pp. 1023–1027, 1989.

[67] J. Martin and D. Adolf, "The sol-gel transition in chemical gels", *Annual Review of Physical Chemistry*, vol. 42, no. 1, pp. 311–339, 1991.

[68] R. Iler, *The Colloid Chemistry of Silica and Silicates*, vol. 80, Cornell University Press, Ithaca, NY, 1955.

[69] P. Meakin, T. Vicsek, and F. Family, "Dynamic cluster-size distribution in cluster-cluster aggregation: Effects of cluster diffusivity", *Physical Review B*, vol. 31, no. 1, pp. 564, 1985.

[70] J. Primera, A. Hasmy, and T. Woignier, "Numerical study of pore sizes distribution in gels", *Journal of Sol-Gel Science and Technology*, vol. 26, no. 1, pp. 671–675, 2003.

[71] J. Primera, T. Woignier, and A. Hasmy, "Pore structure simulation of gels with a binary monomer size distribution", *Journal of Sol-Gel Science and Technology*, vol. 34, no. 3, pp. 273–280, 2005.

[72] V. Morales-Flórez, M. Pinero, N. De La Rosa-Fox, L. Esquivias, J. Anta, and J. Primera, "The cluster model: A hierarchically-ordered assemblage of random-packing spheres for modelling microstructure of porous materials", *Journal of Non-Crystalline Solids*, vol. 354, no. 2, pp. 193–198, 2008.

[73] H.-S. Ma, A. P. Roberts, J.-H. Prévost, R. Jullien, and G. W. Scherer, "Mechanical structure–property relationship of aerogels", *Journal of Non-Crystalline Solids*, vol. 277, no. 2-3, pp. 127–141, 2000.

[74] V. Morales-Flórez, N. De La Rosa-Fox, M. Pinero, and L. Esquivias, "The cluster model: a simulation of the aerogel structure as a hierarchically-ordered arrangement of randomly packed spheres", *Journal of Sol-Gel Science and Technology*, vol. 35, no. 3, pp. 203–210, 2005.

[75] A. Hasmy, M. Foret, E. Anglaret, J. Pelous, R. Vacher, and R. Jullien, "Small-angle neutron scattering of aerogels: simulations and experiments", *Journal of Non-Crystalline Solids*, vol. 186, pp. 118–130, 1995.

[76] S. Lallich, F. Enguehard, and D. Baillis, "Experimental determination and modeling of the radiative properties of silica nanoporous matrices", *ASME Journal of Heat Transfer*, vol. 131, no. 8, pp. 082701, 2009.

[77] J.-J. Zhao, Y.-Y. Duan, X.-D. Wang, and B.-X. Wang, "A 3-D numerical heat transfer model for silica aerogels based on the porous secondary nanoparticle aggregate structure", *Journal of Non-Crystalline Solids*, vol. 358, no. 10, pp. 1287–1297, 2012.

[78] L. Gelb and K. Gubbins, "Pore size distributions in porous glasses: a computer simulation study", *Langmuir*, vol. 15, no. 2, pp. 305–308, 1999.

[79] S. Gavalda, K. Gubbins, Y. Hanzawa, K. Kaneko, and K. Thomson, "Nitrogen adsorption in carbon aerogels: A molecular simulation study", *Langmuir*, vol. 18, no. 6, pp. 2141–2151, 2002.

[80] J.-C. Cuillière, "An adaptive method for the automatic triangulation of 3D parametric surfaces", *Computer-Aided Design*, vol. 30, no. 2, pp. 139–149, 1998.

[81] M. Thommes, "Physical adsorption characterization of ordered and amorphous mesoporous materials", *Nanoporous Materials: Science and Engineering*, vol. 11, pp. 317–364, 2004.

[82] S. Brunauer, P. Emmett, and E. Teller, "Adsorption of gases in multimolecular layers", *Journal of the American Chemical Society*, vol. 60, no. 2, pp. 309–319, 1938.

[83] E. Barrett, L. Joyner, and P. Halenda, "The determination of pore volume and area distributions in porous substances. I. computations from nitrogen isotherms", *Journal of the American Chemical Society*, vol. 73, no. 1, pp. 373–380, 1951.

[84] L. Skinner and J. Sambles, "The kelvin equation: a review", *Journal of Aerosol Science*, vol. 3, no. 3, pp. 199–210, 1972.

[85] M. Jaroniec, M. Kruk, and J. Olivier, "Standard nitrogen adsorption data for characterization of nanoporous silicas", *Langmuir*, vol. 15, no. 16, pp. 5410–5413, 1999.

[86] G. Scherer, "Effect of drying on properties of silica gel", *Journal of Non-Crystalline Solids*, vol. 215, no. 2-3, pp. 155–168, 1997.

[87] T. Woignier, J. Reynes, A. H. Alaoui, I. Beurroies, and J. Phalippou, "Different kinds of structure in aerogels: relationships with the mechanical properties", *Journal of Non-Crystalline Solids*, vol. 241, no. 1, pp. 45–52, 1998.

[88] G. Scherer, S. Calas, and R. Sempéré, "Sintering aerogels", *Journal of Sol-Gel Science and Technology*, vol. 13, no. 1-3, pp. 937–943, 1998.

[89] G. Scherer, S. Calas, and R. Sempéré, "Densification kinetics and structural evolution during sintering of silica aerogel", *Journal of Non-crystalline Solids*, vol. 240, no. 1-3, pp. 118–130, 1998.

[90] S. Haereid, M. Dahle, S. Lima, and M.-A. Einarsrud, "Preparation and properties of monolithic silica xerogels from TEOS-based alcogels aged in silane solutions", *Journal of Non-Crystalline Solids*, vol. 186, pp. 96–103, 1995.

[91] J. Fricke, "SiO_2 aerogels: modifications and applications", *Journal of Non-Crystalline Solids*, vol. 121, no. 1-3, pp. 188–192, 1990.

[92] C. Moreno-Castilla and F. Maldonado-Hódar, "Carbon aerogels for catalysis applications: An overview", *Carbon*, vol. 43, no. 3, pp. 455–465, 2005.

[93] G. Zu, J. Shen, L. Zou, W. Wang, Y. Lian, Z. Zhang, and A. Du, "Nanoengineering super heat-resistant, strong alumina aerogels", *Chemistry of Materials*, vol. 25, no. 23, pp. 4757–4764, 2013.

[94] C. Laberty-Robert, J. Long, E. Lucas, K. Pettigrew, R. Stroud, M. Doescher, and D. Rolison, "Sol-gel-derived ceria nanoarchitectures: synthesis, characterization, and electrical properties", *Chemistry of Materials*, vol. 18, no. 1, pp. 50–58, 2006.

[95] G. O. Olaofe, "Scattering cross-section for two spheres", *The Quarterly Journal of Mechanics and Applied Mathematics*, vol. 27, no. 4, pp. 403–422, 1974.

[96] V. V. Tuchin, L. Wang, and D. A. Zimnyakov, *Optical Polarization in Biomedical Applications*, Springer Science & Business Media, Berlin, Germany, 2006.

[97] J. Cartigny, Y. Yamada, and C.-L. Tien, "Radiative transfer with dependent scattering by particles: Part 1 - theoretical investigation", *ASME Journal of Heat Transfer*, vol. 108, no. 3, pp. 608–613, 1986.

[98] B. Draine and P. Flatau, "Discrete-dipole approximation for scattering calculations", *Journal of the Optical Society of America A*, vol. 11, no. 4, pp. 1491–1499, 1994.

[99] D. W. Mackowski, "A general superposition solution for electromagnetic scattering by multiple spherical domains of optically active media", *Journal of Quantitative Spectroscopy and Radiative Transfer*, vol. 133, pp. 264–270, 2014.

[100] D. W. Mackowski and M. I. Mishchenko, "A multiple sphere t-matrix fortran code for use on parallel computer clusters", *Journal of Quantitative Spectroscopy and Radiative Transfer*, vol. 112, no. 13, pp. 2182–2192, 2011.

[101] Ž. Ivezić, M. P. Mengüç, and T. G. Knauer, "A procedure to determine the onset of soot agglomeration from multi-wavelength experiments", *Journal of Quantitative Spectroscopy and Radiative Transfer*, vol. 57, no. 6, pp. 859–865, 1997.

[102] L. Ma, J. Tan, J. Zhao, F. Wang, C. Wang, and Y. Wang, "Dependent scattering and absorption by densely packed discrete spherical particles: effects of complex refractive index", *Journal of Quantitative Spectroscopy and Radiative Transfer*, vol. 196, pp. 94–102, 2017.

[103] H. Hottel, A. Sarofim, W. Dalzell, and I. Vasalos, "Optical properties of coatings. Effect of pigment concentration", *AIAA Journal*, vol. 9, no. 10, pp. 1895–1898, 1971.

[104] S. W. Churchill, G. C. Clark, and C. M. Sliepcevich, "Light-scattering by very dense monodispersions of latex particles", *Discussions of the Faraday Society*, vol. 30, pp. 192–199, 1960.

[105] R. Harding, B. Golding, and R. Morgen, "Optics of light-scattering films. study of effects of pigment size and concentration", *Journal of the Optical Society of America*, vol. 50, no. 5, pp. 446–455, 1960.

[106] A. Ishiniaru and Y. Kuga, "Attenuation constant of a coherent field in a dense distribution of particles", *Journal of the Optical Society of America*, vol. 72, no. 10, pp. 1317–1320, 1982.

[107] Y. Yamada, J. Cartigny, and C.-L. Tien, "Radiative transfer with dependent scattering by particles: Part 2 - experimental investigation", *ASME Journal of Heat Transfer*, vol. 108, no. 3, pp. 614–618, 1986.

[108] W. Blevin and W. Brown, "Effect of particle separation on the reflectance of semi-infinite diffusers", *Journal of the Optical Society of America*, vol. 51, no. 2, pp. 129–134, 1961.

[109] A. Jones, "Electromagnetic wave scattering by assemblies of particles in the Rayleigh approximation", *Proceedings of the Royal Society of London. A. Mathematical and Physical Sciences*, vol. 366, no. 1724, pp. 111–127, 1979.

[110] B. Draine and P. Flatau, *User guide for the discrete-dipole approximation code DDSCAT 7.3*, 2013.

[111] T. Galy, M. Marszewski, S. King, Y. Yan, S. H. Tolbert, and L. Pilon, "Comparing methods for measuring thickness, refractive index, and porosity of mesoporous thin films", *Microporous and Mesoporous Materials*, vol. 291, pp. 109677, 2020.

[112] C. Sorensen, "Light scattering by fractal aggregates: a review", *Aerosol Science & Technology*, vol. 35, no. 2, pp. 648–687, 2001.

[113] T. Farias, M. d. G. Carvalho, Ü. Köylü, and G. Faeth, "Computational evaluation of approximate Rayleigh–Debye–Gans/fractal-aggregate theory for the absorption and scattering properties of soot", *Journal of Heat Transfer*, vol. 117, no. 1, pp. 152–159, 1995.

[114] S. Jacquier and F. Gruy, "Anomalous diffraction approximation for light scattering cross section: case of ordered clusters of non-absorbent spheres", *Journal of Quantitative Spectroscopy and Radiative Transfer*, vol. 109, no. 5, pp. 789–810, 2008.

[115] A. Jones, "Scattering efficiency factors for agglomerates for small spheres", *Journal of Physics D: Applied Physics*, vol. 12, no. 10, pp. 1661, 1979.

[116] T. Galy, D. Mu, M. Marszewski, and L. Pilon, "Computer-generated mesoporous materials and associated structural characterization", *Computational Materials Science*, vol. 157, pp. 156–167, 2019.

[117] D. Mackowski and M. Mishchenko, "A multiple sphere T-matrix fortran code for use on parallel computer clusters", *Journal of Quantitative Spectroscopy and Radiative Transfer*, vol. 112, no. 13, pp. 2182–2192, 2011.

[118] D. Mackowski, "A general superposition solution for electromagnetic scattering by multiple spherical domains of optically active media", *Journal of Quantitative Spectroscopy and Radiative Transfer*, vol. 133, pp. 264–270, 2014.

[119] L. Liu and M. I. Mishchenko, "Effects of aggregation on scattering and radiative properties of soot aerosols", *Journal of Geophysical Research: Atmospheres*, vol. 110, no. D11211, 2005.

[120] R. Kandilian, R.-L. Heng, and L. Pilon, "Absorption and scattering by fractal aggregates and by their equivalent coated spheres", *Journal of Quantitative Spectroscopy and Radiative Transfer*, vol. 151, pp. 310–326, 2015.

[121] R. A. Taylor, P. E. Phelan, T. P. Otanicar, R. Adrian, and R. Prasher, "Nanofluid optical property characterization: towards efficient direct absorption solar collectors", *Nanoscale Research Letters*, vol. 6, no. 1, pp. 2–11, 2011.

[122] R. Saidur, T. Meng, Z. Said, M. Hasanuzzaman, and A. Kamyar, "Evaluation of the effect of nanofluid-based absorbers on direct solar collector", *International Journal of Heat and Mass Transfer*, vol. 55, no. 21-22, pp. 5899–5907, 2012.

[123] M. Du and G. Tang, "Optical property of nanofluids with particle agglomeration", *Solar Energy*, vol. 122, pp. 864–872, 2015.

[124] S. Banerjee, "Simulation of a film of random particulate medium containing aggregates of metal nanospheres", in *Nanoengineering: Fabrication, Properties, Optics, and Devices XI*. International Society for Optics and Photonics, 2014, vol. 9170, p. 91700M.

[125] D. H. Schneiderheinze, T. R. Hillman, and D. D. Sampson, "Modified discrete particle model of optical scattering in skin tissue accounting for multiparticle scattering", *Optics Express*, vol. 15, no. 23, pp. 15002–15010, 2007.

[126] G. Scherer, "Theory of drying", *Journal of the American Ceramic Society*, vol. 73, no. 1, pp. 3–14, 1990.

[127] J. Thiery, S. Rodts, E. Keita, X. Chateau, P. Faure, D. Courtier-Murias, T. Kodger, and P. Coussot, "Water transfer and crack regimes in nanocolloidal gels", *Physical Review E*, vol. 91, no. 4, pp. 042407, 2015.

[128] J. Thiery, S. Rodts, D. Weitz, and P. Coussot, "Drying regimes in homogeneous porous media from macro-to nanoscale", *Physical Review Fluids*, vol. 2, no. 7, pp. 074201, 2017.

[129] M. Marszewski, S. King, Y. Yan, T. Galy, M. Li, A. Dashti, D. Butts, J. Kang, P. McNeil, E. Lan, B. Dunn, Y. Hu, S. Tolbert, and L. Pilon, "Thick transparent nanoparticle-based mesoporous silica monolithic slabs for thermally insulating window materials", *ACS Applied Nano Materials*, vol. 2, no. 7, pp. 4547–4555, 2019.

[130] A. Standard, "D1003-07 (2007): Standard test method for haze and luminous transmittance of transparent plastics", *ASTM International, West Conshohocken, PA*, 2007.

[131] R. Hunt, *The Reproduction of Colour*, John Wiley & Sons, Tolworth, UK, 2004.

[132] M. Q. Brewster, *Thermal Radiative Transfer and Properties*, John Wiley & Sons, New York, NY, USA, 1992.

[133] A. Sihvola, *Electromagnetic Mixing Formulas and Applications*, The Institution of Electrical Engineers, London, UK, 1999.

[134] N. Hutchinson, T. Coquil, A. Navid, and L. Pilon, "Effective optical properties of highly ordered mesoporous thin films", *Thin Solid Films*, vol. 518, no. 8, pp. 2141–2146, 2010.

[135] N. Hutchinson, T. Coquil, E. Richman, S. Tolbert, and L. Pilon, "Reflectance of surfactant-templated mesoporous silica thin films: Simulations versus experiments", *Thin Solid Films*, vol. 518, no. 8, pp. 2134–2140, 2010.

[136] A. Sihvola and J. Kong, "Effective permittivity of dielectric mixtures", *IEEE Transactions on Geoscience and Remote Sensing*, vol. 26, no. 4, pp. 420–429, 1988.

[137] D. Ramkrishna, *Population balances: Theory and applications to particulate systems in engineering*, Elsevier, 2000.

[138] O. Stenzel, *The Physics of Thin Film Optical Spectra*, Springer-Verlag, Heidelberg, Germany, 2005.

[139] R. Gehr and R. Boyd, "Optical properties of nanostructured optical materials", *Chemistry of Materials*, vol. 8, no. 8, pp. 1807–1819, 1996.

[140] M. Braun and L. Pilon, "Effective optical properties of non-absorbing nanoporous thin films", *Thin Solid Films*, vol. 496, no. 2, pp. 505–514, 2006.

[141] M. Khardani, M. Bouaïcha, and B. Bessaïs, "Bruggeman effective medium approach for modelling optical properties of porous silicon: comparison with experiment", *Physica Status Solidi C*, vol. 4, no. 6, pp. 1986–1990, 2007.

[142] E. Pedrueza, J. Valdés, V. Chirvony, R. Abargues, J. Hernández-Saz, M. Herrera, S. Molina, and J. Martínez-Pastor, "Novel method of preparation of gold-nanoparticle-doped TiO_2 and SiO_2 plasmonic thin films: optical characterization and comparison with Maxwell–Garnett modeling", *Advanced Functional Materials*, vol. 21, no. 18, pp. 3502–3507, 2011.

[143] D. Bouvard, J.-M. Chaix, R. Dendievel, A. Fazekas, J. Létang, G. Peix, and D. Quenard, "Characterization and simulation of microstructure and properties of EPS lightweight concrete", *Cement and Concrete Research*, vol. 37, no. 12, pp. 1666–1673, 2007.

[144] M. Baklanov, K. Mogilnikov, V. Polovinkin, and F. Dultsev, "Determination of pore size distribution in thin films by ellipsometric porosimetry", *Journal of Vacuum Science & Technology B*, vol. 18, no. 3, pp. 1385–1391, 2000.

[145] P. Mezza, J. Phalippou, and R. Sempere, "Sol–gel derived porous silica films", *Journal of Non-Crystalline Solids*, vol. 243, no. 1, pp. 75–79, 1999.

[146] D. Bruggeman, "The calculation of various physical constants of heterogeneous substances. I. the dielectric constants and conductivities of mixtures composed of isotropic substances", *Annals of Physics*, vol. 416, pp. 636–791, 1935.

[147] L. Lorenz, "Ueber die refractionsconstante", *Annalen der Physik und Chemie*, vol. 247, no. 9, pp. 70–103, 1880.

[148] H. Lorentz, "Ueber die beziehung zwischen der fortpflanzungsgeschwindigkeit des lichtes und der köperdichte", *Annalen der Physik und Chemie*, vol. 245, no. 4, pp. 641–665, 1880.

[149] D. Aspnes, "Optical properties of thin films", *Thin Solid Films*, vol. 89, no. 3, pp. 249–262, 1982.

[150] R. Cohen, G. Cody, M. Coutts, and B. Abeles, "Optical properties of granular silver and gold films", *Physical Review B*, vol. 8, no. 8, pp. 3689, 1973.

[151] M. Koledintseva, R. DuBroff, and R. Schwartz, "Maxwell-Garnett rule for dielectric mixtures with statistically distributed orientations of inclusions", *Progress in Electromagnetics Research*, vol. 99, pp. 131–148, 2009.

[152] B. Schulz, "Thermal conductivity of porous and highly porous materials", *High Temperatures-High Pressures*, vol. 13, no. 6, pp. 649–660, 1981.

[153] J. de Río and S. Whitaker, "Maxwell's equations in two-phase systems I: Local electrodynamic equilibrium", *Transport in Porous Media*, vol. 39, no. 2, pp. 159–186, 2000.

[154] D. Gonçalves and E. A. Irene, "Fundamentals and applications of spectroscopic ellipsometry", *Química Nova*, vol. 25, no. 5, pp. 794–800, 2002.

[155] *Semilab Co. Ltd., Spectroscopic Ellipsometry Analyzer User's Reference Manual*, 2012.

[156] M. Kruk and M. Jaroniec, "Gas adsorption characterization of ordered organic-inorganic nanocomposite materials", *Chemistry of Materials*, vol. 13, no. 10, pp. 3169–3183, 2001.

[157] J. Rouquerol, F. Rouquerol, P. Llewellyn, G. Maurin, and K. Sing, *Adsorption by Powders and Porous Solids: Principles, Methodology and Applications*, Academic Press, Cambridge, MA, 2013.

[158] S. A. Chalmers and R. S. Geels, "Thin-film metrology using spectral reflectance with an intermediate in-line reference", Mar. 10 2009, US Patent 7,502,119.

[159] V. A. Sterligov, "Scattering and reflective properties of ordered mesoporous silica films", *Applied Optics*, vol. 44, no. 21, pp. 4538–4546, 2005.

[160] Y. K. Hwang, K. R. Patil, S. H. Jhung, J.-S. Chang, Y. J. Ko, and S.-E. Park, "Control of pore size and condensation rate of cubic mesoporous silica thin films using a swelling agent", *Microporous and Mesoporous Materials*, vol. 78, no. 2-3, pp. 245–253, 2005.

[161] Y. K. Hwang, A. S. Mamman, K. Patil, L. K. Kim, J. S. Hwang, and J. S. Chang, "Reflectometry studies of mesoporous silica thin films", in *Solid State Phenomena*. Trans Tech Publ, 2008, vol. 135, pp. 31–34.

[162] T. Matsubara, T. Oishi, and A. Katagiri, "Determination of porosity of tio2 films from reflection spectra", *Journal of The Electrochemical Society*, vol. 149, no. 2, pp. C89–C93, 2002.

[163] D. Lee, D. Omolade, R. E. Cohen, and M. F. Rubner, "ph-dependent structure and properties of TiO_2/SiO_2 nanoparticle multilayer thin films", *Chemistry of Materials*, vol. 19, no. 6, pp. 1427–1433, 2007.

[164] D. Dunphy, P. Sheth, F. L. Garcia, and C. Brinker, "Enlarged pore size in mesoporous silica films templated by pluronic F127: use of poloxamer mixtures and increased template/SiO_2 ratios in materials synthesized by evaporation-induced self-assembly", *Chemistry of Materials*, vol. 27, no. 1, pp. 75–84, 2014.

[165] A. Forouhi and I. Bloomer, "Optical dispersion relations for amorphous semiconductors and amorphous dielectrics", *Physical Review B*, vol. 34, no. 10, pp. 7018, 1986.

[166] F. Dullien, *Porous Media: Fluid Transport and Pore Structure*, Academic Press, London, UK, 2012.

[167] C. Brinker, G. Frye, A. Hurd, and C. Ashley, "Review of sol-gel thin film formation", *Thin solid films*, vol. 201, no. 1, pp. 97–108, 1991.

[168] S. Van der Perre, T. Van Assche, B. Bozbiyik, J. Lannoeye, D. E. De Vos, G. V. Baron, and J. F. Denayer, "Adsorptive characterization of the zif-68 metal-organic framework: a complex structure with amphiphilic properties", *Langmuir*, vol. 30, no. 28, pp. 8416–8424, 2014.

[169] R. C. Weast, M. J. Astle, W. H. Beyer, et al., *CRC Handbook of Chemistry and Physics*, vol. 69, CRC press Boca Raton, FL, 1988.

[170] R. Kitamura, L. Pilon, and M. Jonasz, "Optical constants of silica glass from extreme ultraviolet to far infrared at near room temperature", *Applied Optics*, vol. 46, no. 33, pp. 8118–8133, 2007.

[171] G. Jellison and F. Modine, "Optical functions of silicon at elevated temperatures", *Journal of Applied Physics*, vol. 76, no. 6, pp. 3758–3761, 1994.

[172] B. Prasai, B. Cai, M. K. Underwood, J. Lewis, and D. Drabold, ", *J. Mater. Sci.*, vol. 47, no. 21, pp. 7515–7521, 2012.

[173] M. Kruk, M. Jaroniec, and A. Sayari, "Application of large pore mcm-41 molecular sieves to improve pore size analysis using nitrogen adsorption measurements", *Langmuir*, vol. 13, no. 23, pp. 6267–6273, 1997.

APPENDIX A

Supplementary Materials for Chapter 2

A.1 Validation of discretization method for overlapping particles

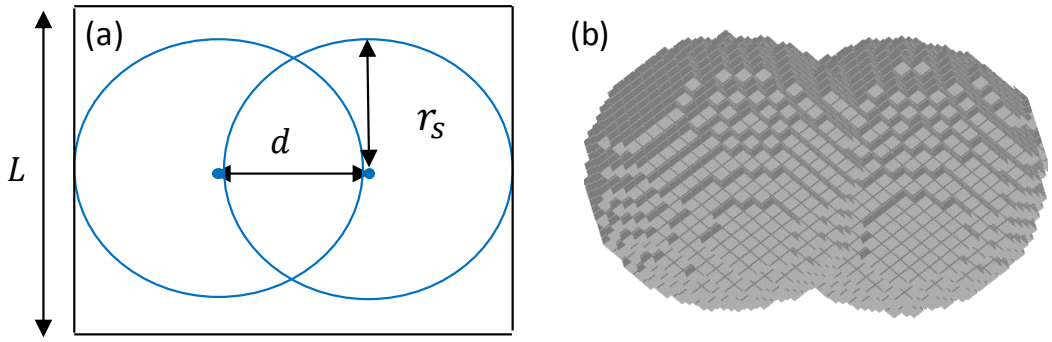

Figure A.1: Illustrations of (a) the overlapping spheres and (b) the cube discretization method to compute porosity ϕ, surface area S, and specific surface area A_g. Here $r_s = L/3 = 2$ nm, $d = 2$ nm, and $\Delta_x = 0.04$ nm.

Table A.1: Theoretical and computed porosity ϕ, surface area S, and specific surface area A_g of two overlapping spheres.

	Actual Value	**Simulation Results**
Porosity (%)	73.8	73.8
Surface area (nm^2)	74.3	76.5
Specific surface area (m^2/g)	597.3	614.2

A.2 Validation of pore size distribution algorithm

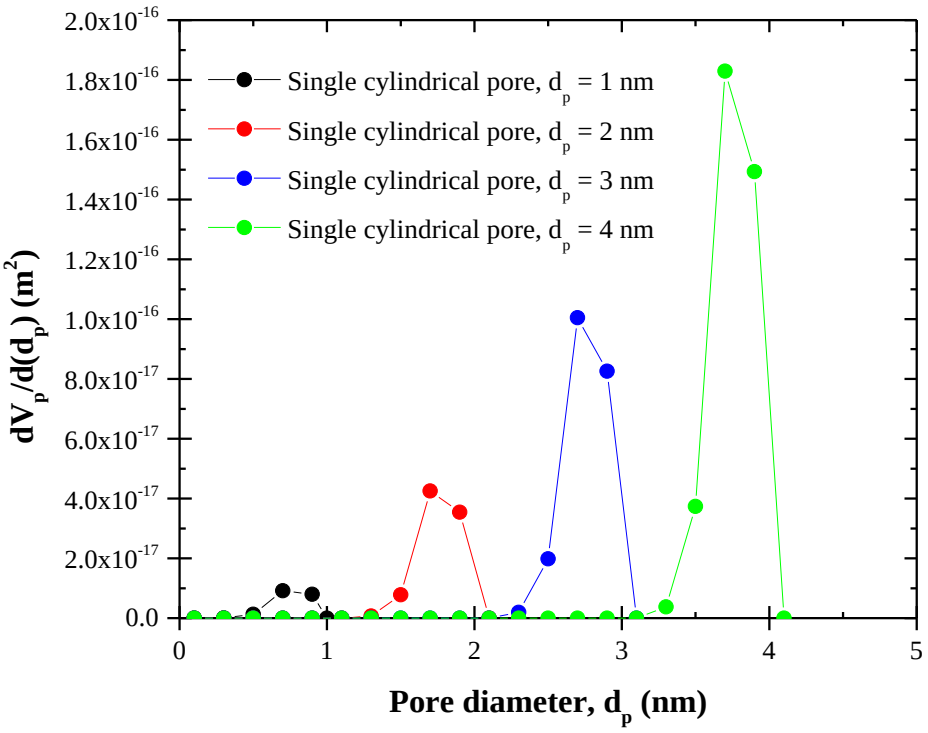

Figure A.2: Differential pore size distribution of four structures with single cylindrical pore of d_p = 1, 2, 3, and 4 nm.

Table A.2: "Adsorbate" layer thickness Δt and relative error on the total pore volume $\delta V_{p,tot}$ for structures with one cylindrical pore used for validation of pore size distribution algorithm.

Pore diameter d_p (nm)	**"Adsorbate" layer thickness Δt (nm)**	**Relative error $\delta V_{p,tot}$ (%)**
1.0	0.10	5.97
2.0	0.10	10.07
3.0	0.15	10.07
4.0	0.20	10.07

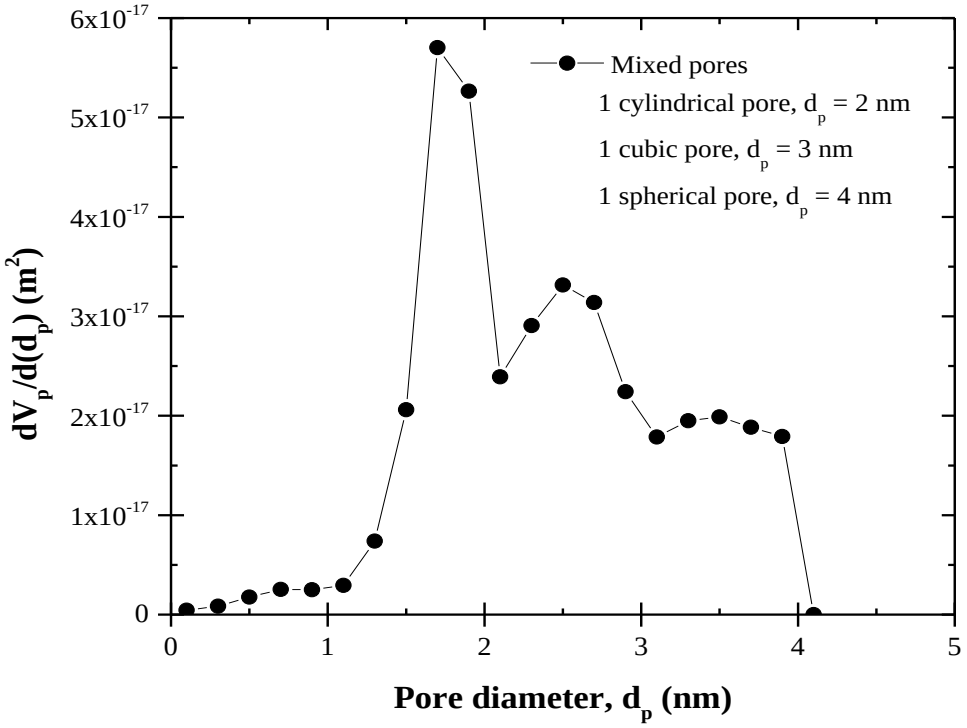

Figure A.3: Differential pore size distribution of a structure with three pores of different shapes (cylindrical, cubic, and spherical) and size (d_p= 2, 3 and 4 nm).

Table A.3: "Adsorbate" layer thickness Δt and relative error on the total pore volume $\delta V_{p,tot}$ for the structure with pores of different shapes used for validation of pore size distribution algorithm.

"Adsorbate" layer thickness Δt (nm)	**Relative error $\delta V_{p,tot}$ (%)**
0.1	2.0

APPENDIX B

Supplementary Materials for Chapter 3

B.1 DDA validation

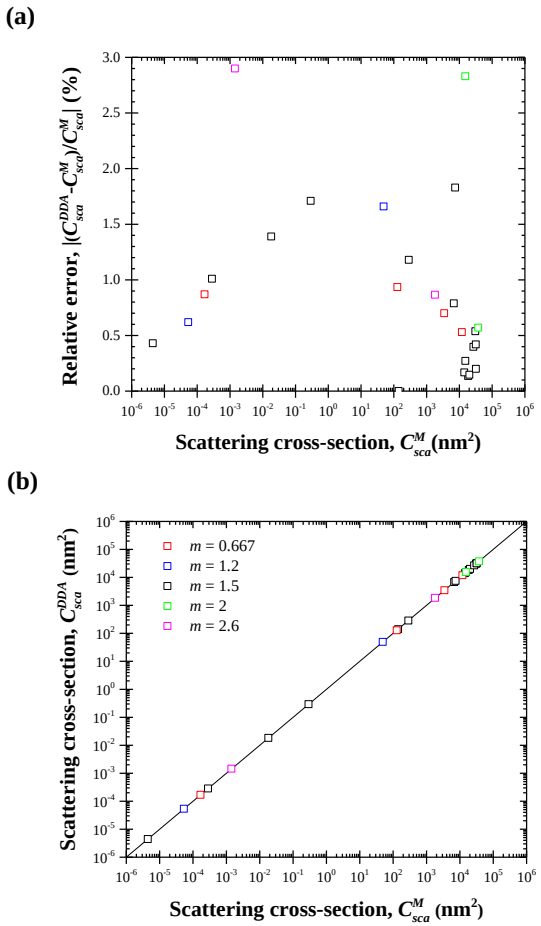

Figure B.1: (a) Scattering cross-section of single spheres C_{sca}^{DDA} computed using the DDA method and (b) relative error between the scattering cross-sections computed using the DDA and Lorenz-Mie methods as functions of the scattering cross-section C_{sca}^{M} predicted by Lorenz-Mie theory.

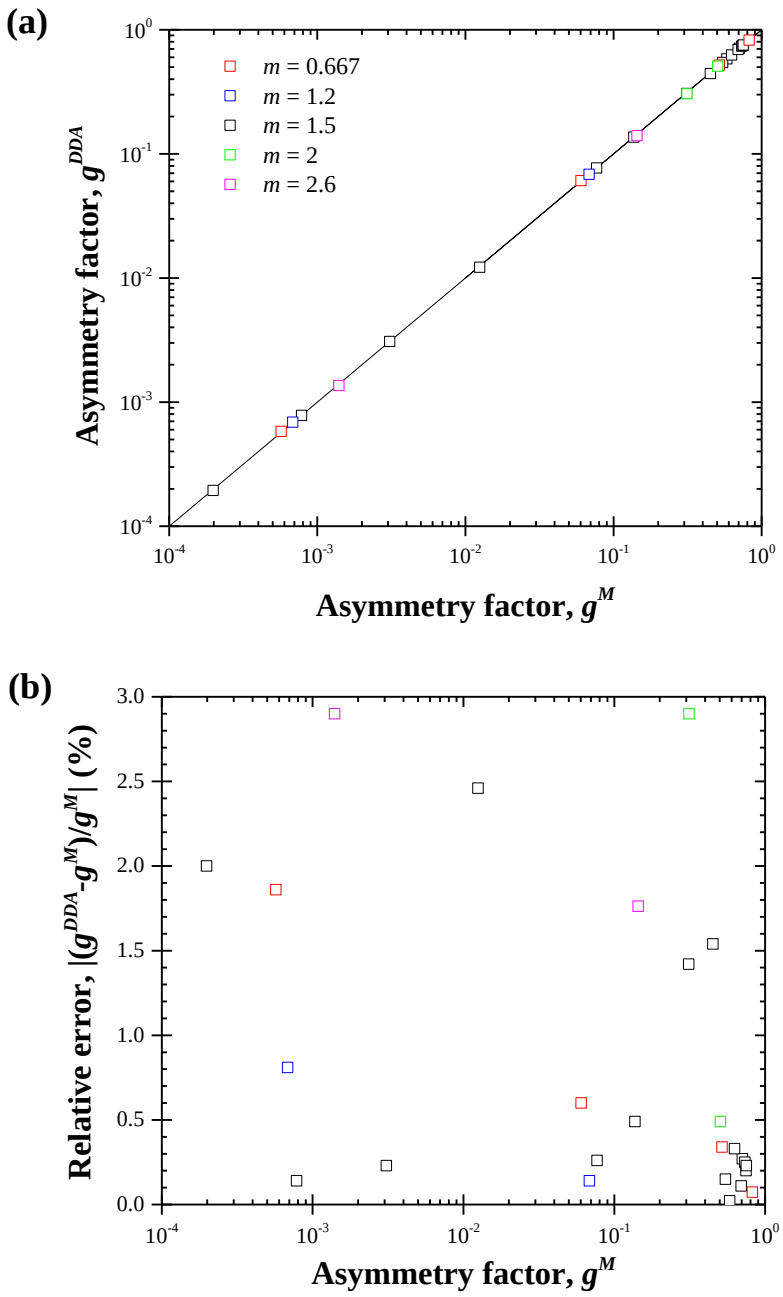

Figure B.2: (a) Asymmetry factor of single spheres g^{DDA} computed using the DDA method and (b) relative error between the asymmetry factors computed using the DDA and Lorenz-Mie methods as functions of the asymmetry factor g^M predicted by Lorenz-Mie theory.

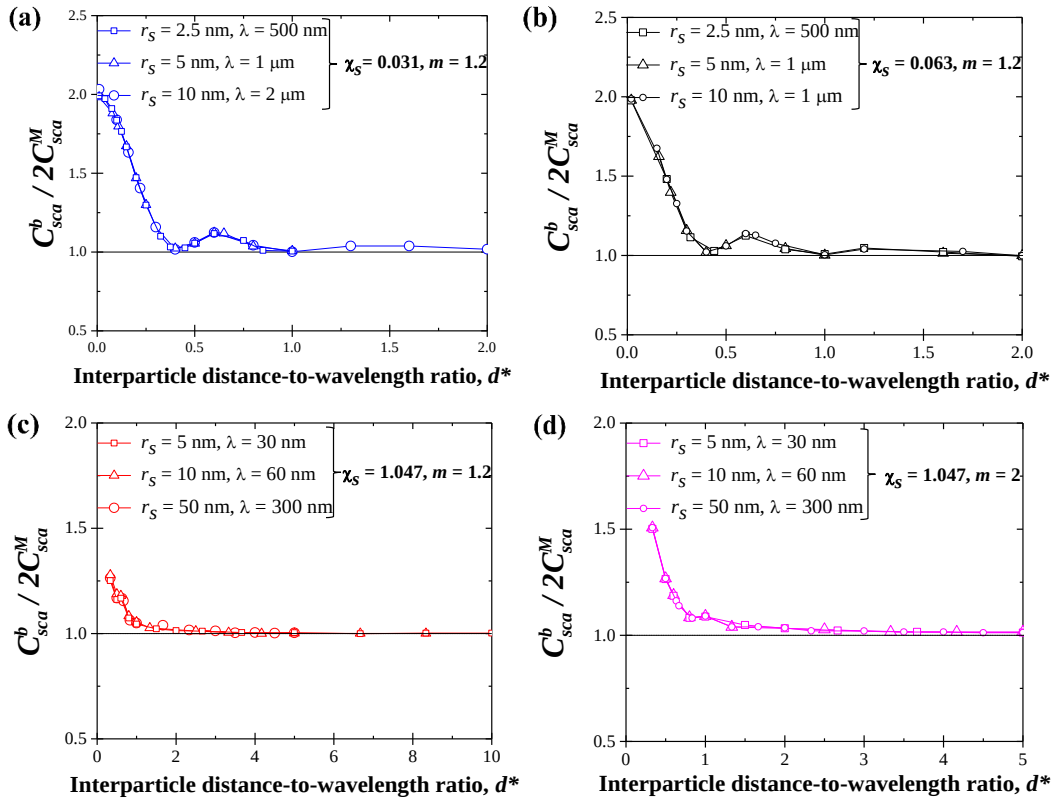

Figure B.3: Scattering cross-section ratio $C^b_{sca}/2C^M_{sca}$ as a function of the interparticle distance-to-wavelength ratio d^* for bispheres with (a) $\chi_s = 0.031$, (b) $\chi_s = 0.063$, (c) $\chi_s = 1.047$ and m = 1.2, and (d) $\chi_s = 1.047$ and m = 2.

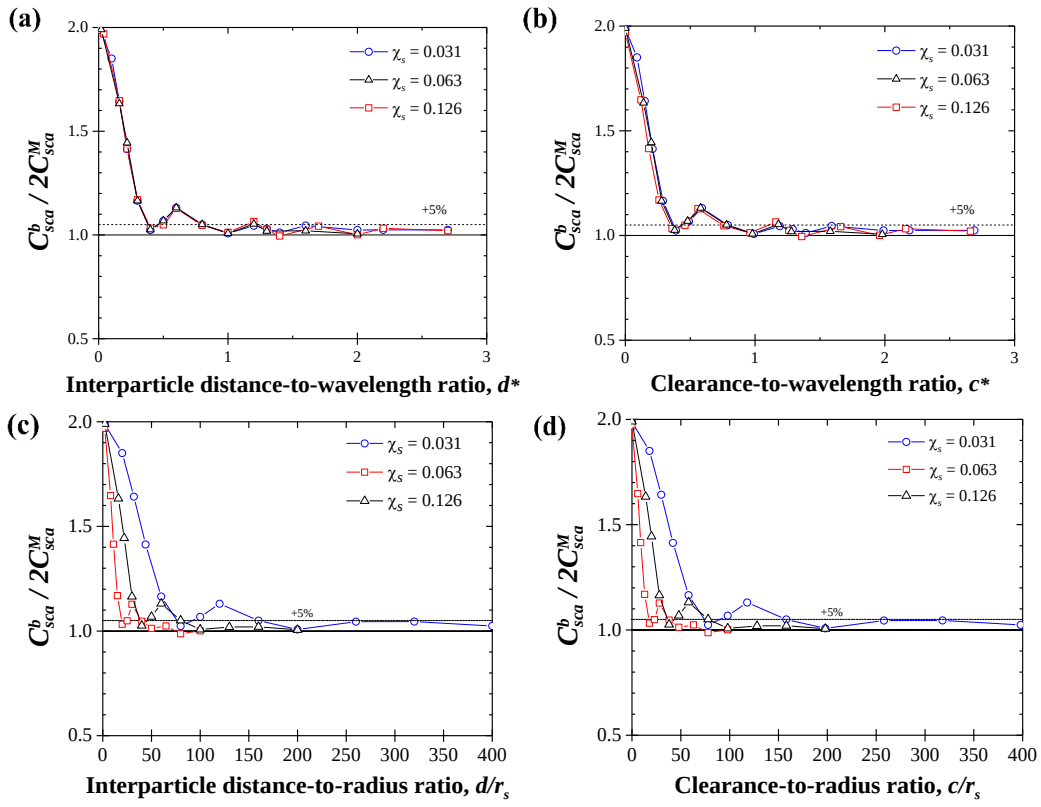

Figure B.4: Scattering cross-section ratio $C^b_{sca}/2C^M_{sca}$ as a function of (a) the interparticle distance-to-wavelength ratio d*, (b) clearance-to-wavelength ratio c^*, (c) interparticle distance-to-radius ratio d/r_s, and (d) clearance-to-wavelength ratio c/r_s for bispheres with $\chi_s = 0.031$, 0.063, and 0.126 and $m = 1.5$.

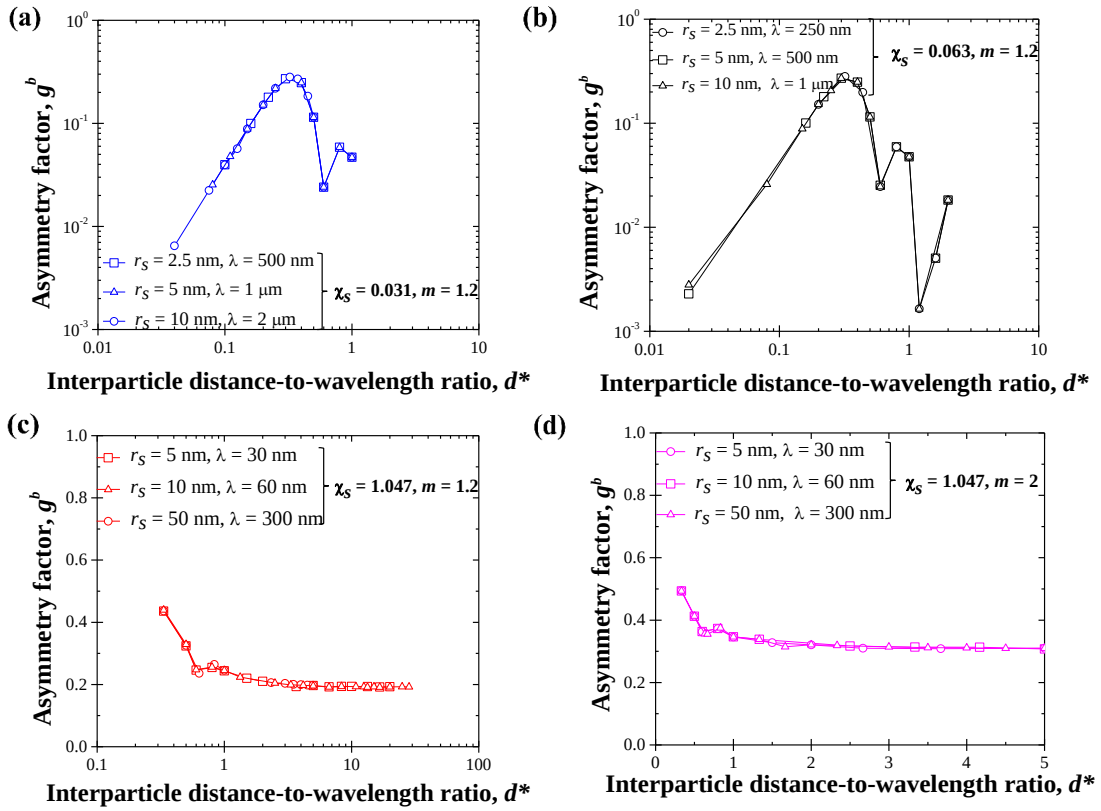

Figure B.5: Asymmetry factor g^b as a function of the interparticle distance-to-wavelength ratio d^* for bispheres with (a) $\chi_s = 0.031$, (b) $\chi_s = 0.063$, (c) $\chi_s = 1.047$ and $m = 1.2$, and (d) $\chi_s = 1.047$ and $m = 2$.

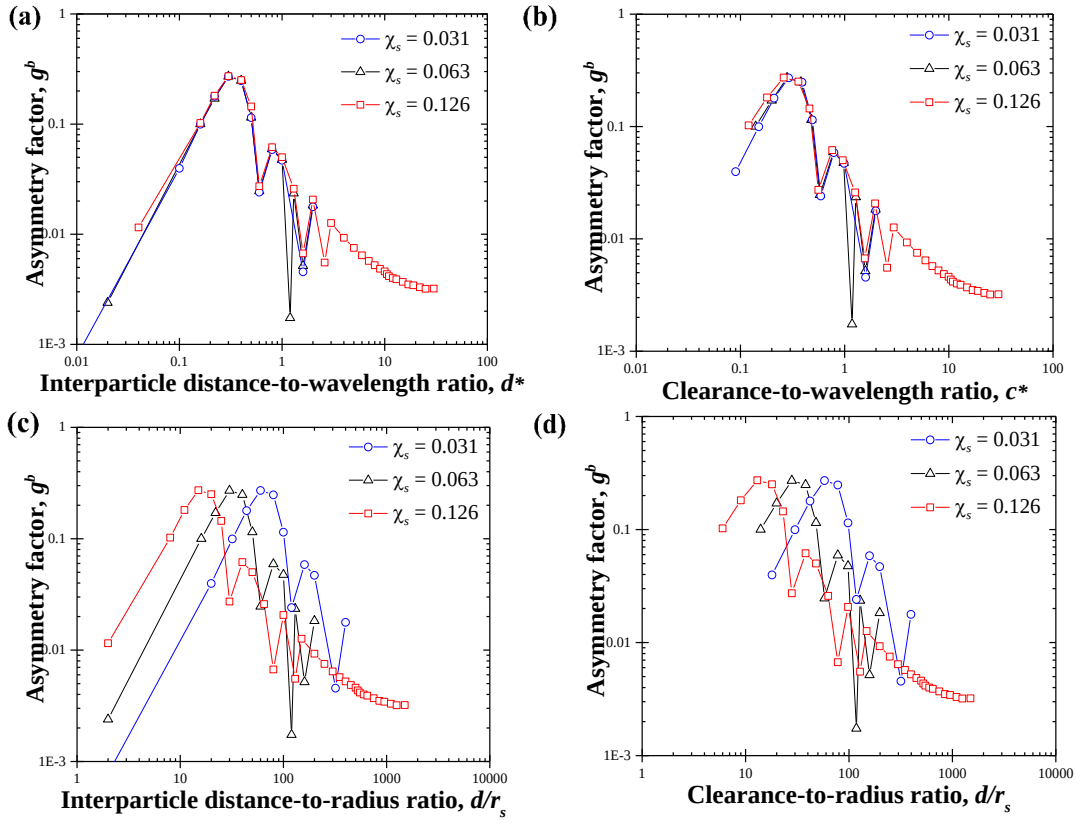

Figure B.6: Asymmetry factor g^b as a function of (a) the interparticle distance-to-wavelength ratio d^*, (b) clearance-to-wavelength ratio c^*, (c) interparticle distance-to-radius ratio d/r_s, and (d) clearance-to-wavelength ratio c/r_s for bi-spheres with $\chi_s = 0.031$, 0.063, and 0.126 and $m = 1.5$.

B.2 Ordered and disordered particle systems

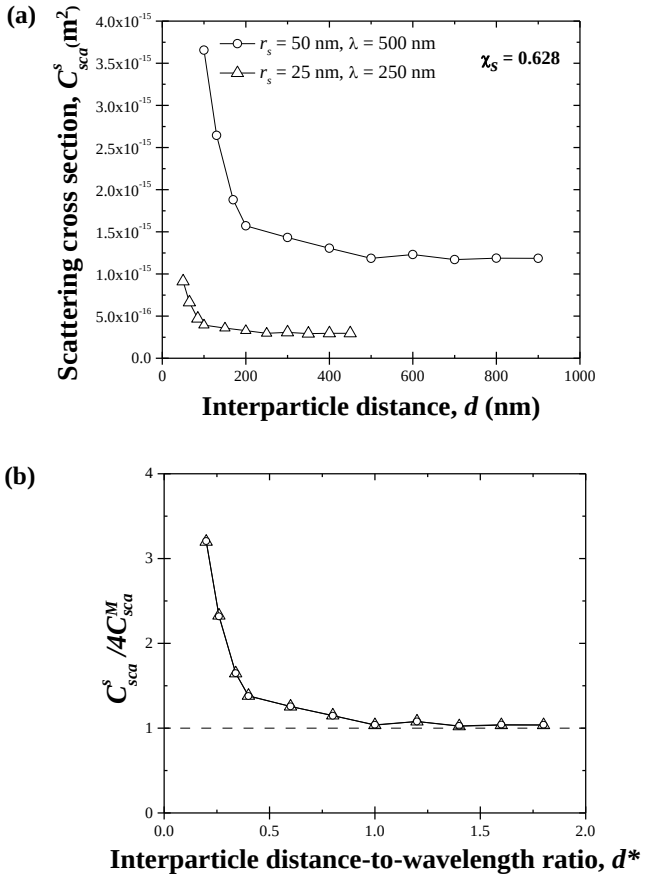

Figure B.7: (a) Scattering cross-section C^b_{sca} as a function of the interparticle distance d and (b) scattering cross-section ratio $C^b_{sca}/4C^M_{sca}$ as a function of the interparticle distance-to-wavelength ratio d^* for tetrahedrons with $\chi_s = 0.628$ and $m = 1.5$.

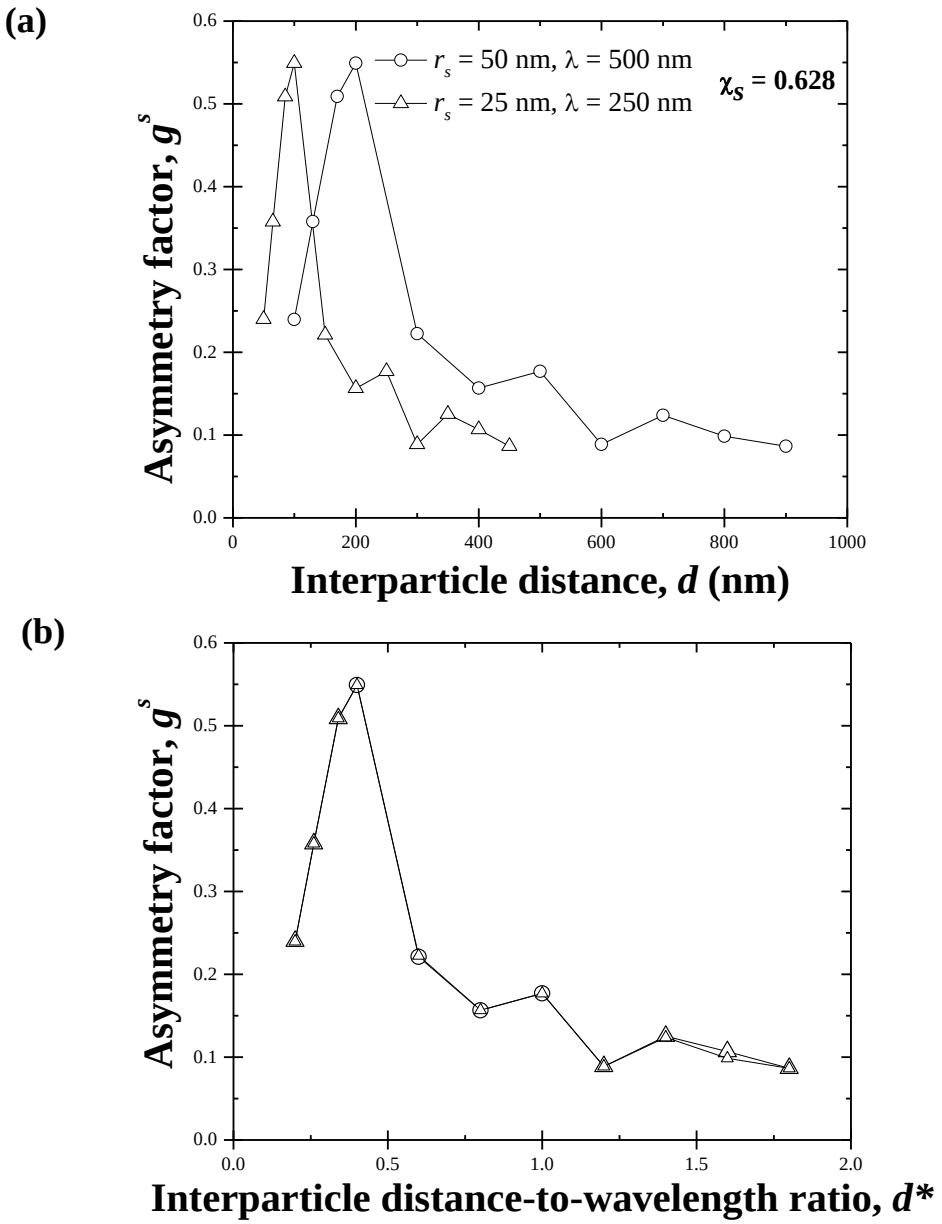

Figure B.8: Asymmetry factor as a function of (a) the interparticle distance d and (b) the interparticle distance-to-wavelength ratio d^* for tetrahedrons with $\chi_s = 0.628$ and $m = 1.5$.

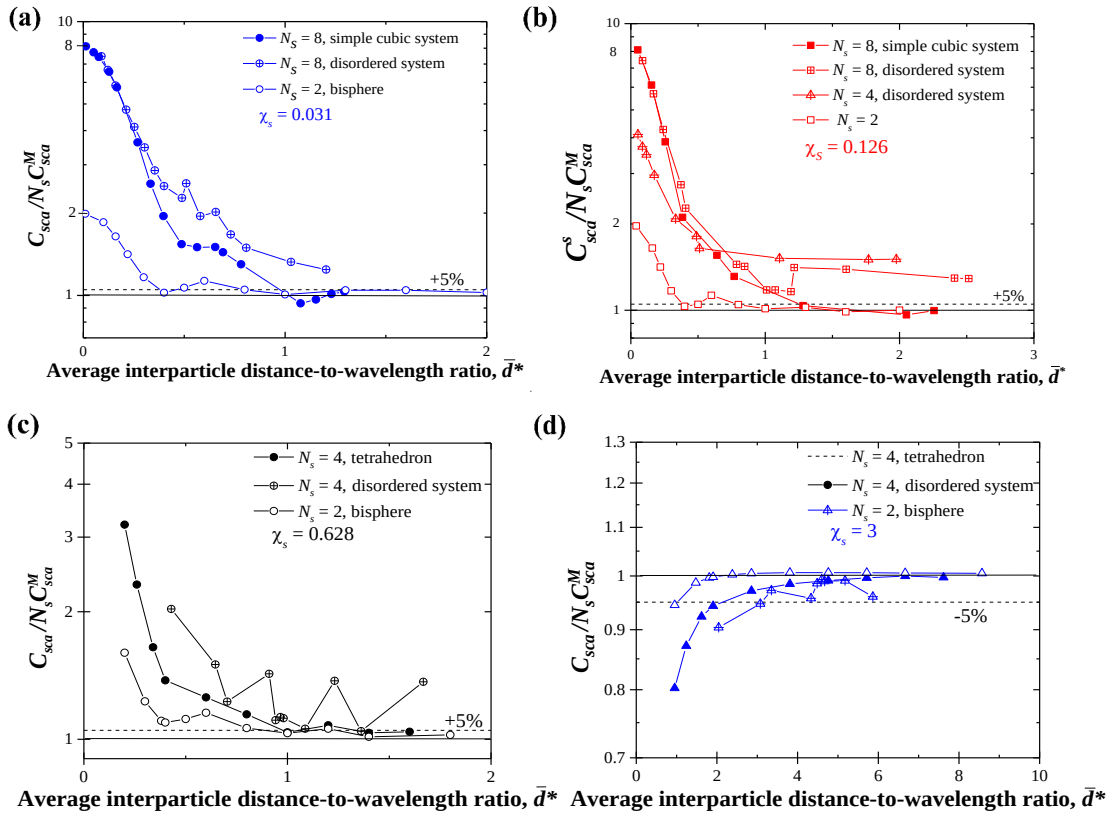

Figure B.9: Scattering cross-section ratio $C^s_{sca}/N_s\, C^M_{sca}$ as a function of the average interparticle distance-to-wavelength ratio $\bar{d}^*$ for (a) $\chi_s = 0.031$, (b) $\chi_s = 0.126$, (c) $\chi_s = 0.628$, and (d) $\chi_s = 3$ and $m = 1.5$.

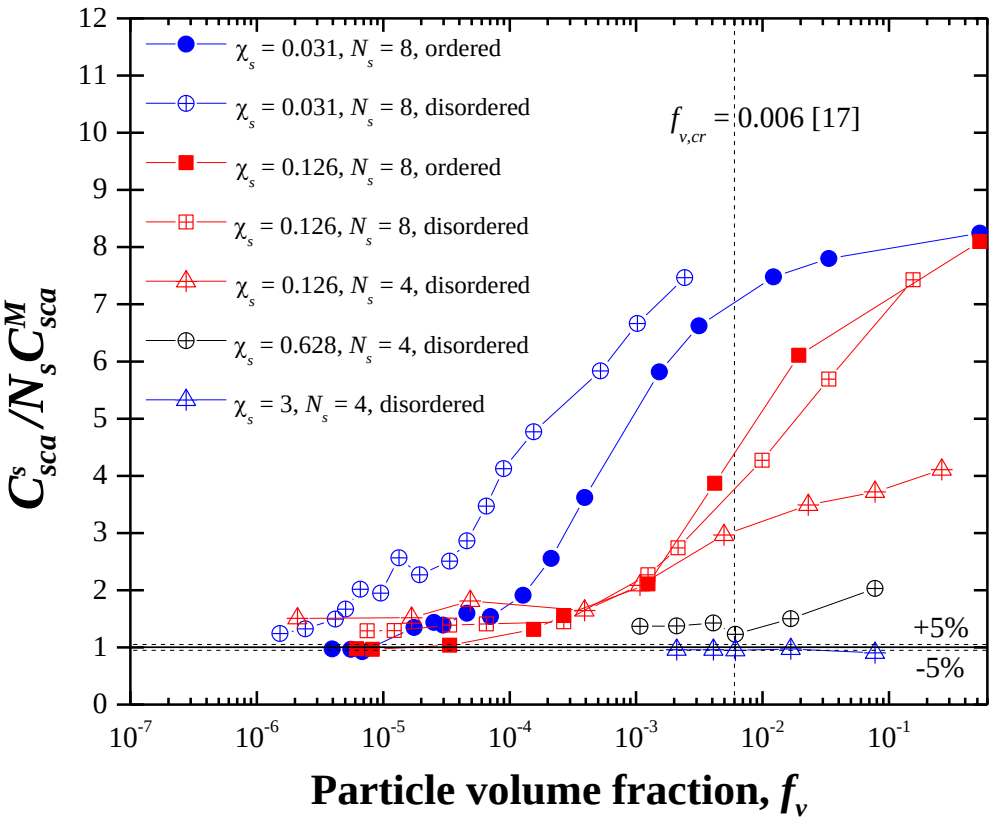

Figure B.10: Scattering cross-section ratio $C^s_{sca}/N_s\ C^M_{sca}$ as a function of the particle volume fraction f_v for ordered and disordered particle systems with N_s= 4 or 8, $m = 1.5$, and $\chi_s = 0.031$, 0.126, 0.628, and 3.

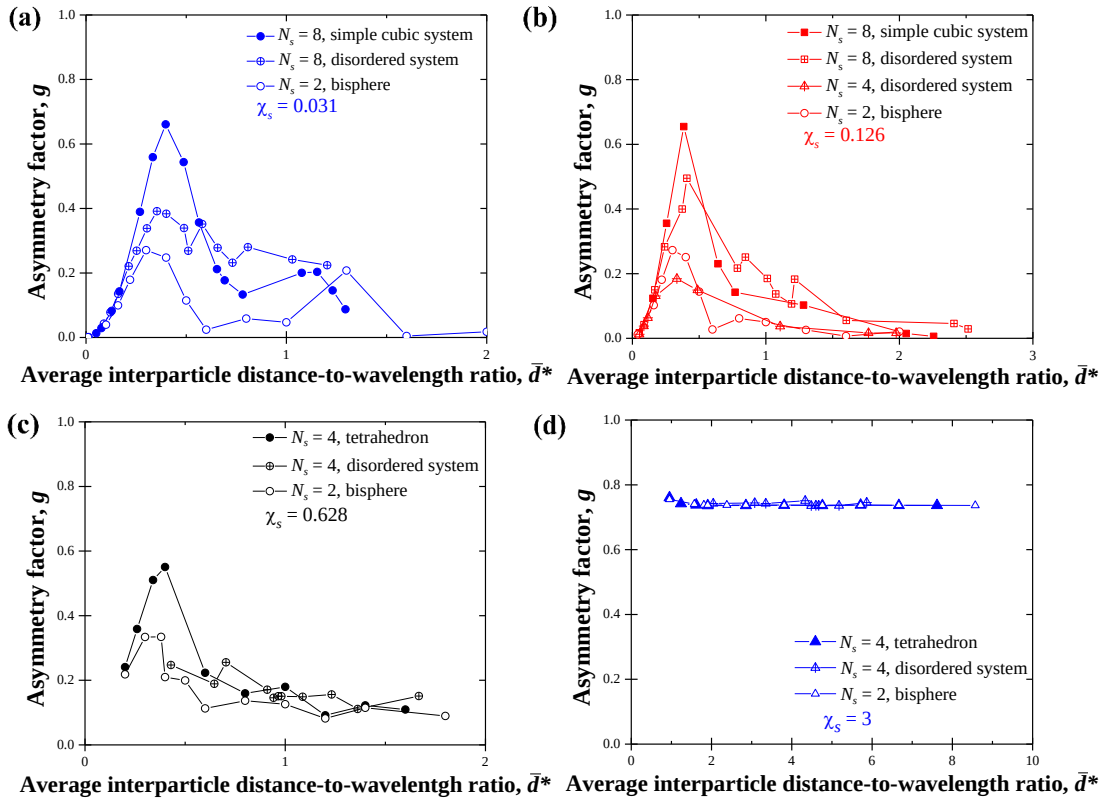

Figure B.11: Asymmetry factor g^s as a function of the average interparticle distance-to-wavelength ratio $\bar{d}^*$ for (a) $\chi_s = 0.031$, (b) $\chi_s = 0.126$, (c) $\chi_s = 0.628$, (d) $\chi_s = 3$, and $m = 1.5$.

APPENDIX C

Supplementary Materials for Chapter 4

Table C.1: Orientation-averaged and fixed scattering efficiency factor and asymmetry factor of aggregates with point-contact particles computed using the T-matrix method.

Particle size parameter x_s	**Aggregate size parameter** χ_s	**Porosity** ϕ (%)	**Orientation-averaged**		**Fixed orientation**		**Relative error**	
			Q^a_{sca}	g^a	Q^a_{sca}	g^a	$\lvert Q^f_{sca} - Q^o_{sca}\rvert / Q^o_{sca}$ (%) [a]	$\lvert g^f - g^o\rvert / g^o$ (%)
0.031	0.72	66	0.013	0.082	0.014	0.083	0.26	0.7
0.031	0.79	66.2	0.018	0.1	0.018	0.1	0	0.06
0.031	0.85	66.1	0.024	0.12	0.024	0.11	0.8	3.3
0.031	0.47	67.3	0.00237	0.039	0.00239	0.04	0.6	2.22
0.031	0.78	66.8	0.017	0.11	0.017	0.11	0.11	1.47
0.063	0.78	67	0.016	0.11	0.016	0.11	0.1	0.9
0.063	1.17	67.1	0.064	0.25	0.064	0.26	0.8	3.9
0.063	1.56	66.8	0.147	0.45	0.146	0.46	0.5	3
0.13	1.56	67	0.147	0.45	0.146	0.46	0.7	3
0.25	3.12	67	0.835	0.79	0.835	0.74	0.05	5.7
0.25	3.9	67.1	1.35	0.86	1.28	0.87	5.3	1.1
0.63	3.9	66.5	1.49	0.81	1.4	0.82	6.3	0.9
0.63	7.8	67	4.89	0.91	5	0.92	2.5	1.56
1.26	7.8	66.5	5.34	0.81	5.4	0.74	1.15	8.5
1.26	9.35	66.8	6.11	0.81	6.5	0.75	6.42	7.5
1.26	10.9	67.6	6.5	0.81	7.05	0.76	8.5	6.2
1.26	12.5	67.3	6.54	0.8	7.42	0.77	13.6	4.2
2.51	14	66.1	5	0.69	4.67	0.68	6.76	28.1
2.51	15.6	66.9	5.1	0.68	5.56	0.74	9.52	22
2.51	17.9	66.4	5	0.67	3.78	0.64	24.3	31.5
2.51	19.5	67.2	4.88	0.65	4.1	0.61	16	34.4
2.51	21	67.1	5	0.65	4.38	0.64	12.1	30.1

[a] "ò" refers to orientation-averaged and "f" refers to fixed orientation.

Table C.2: Scattering cross-section and asymmetry factor of aggregates with point-contact and surface-contact particles.

Particle size parameter x_s	**Aggregate size parameter** χ_s	**Point-contact particles** ϕ (%)	C^a_{sca} (**nm**^{2})	g^a	**Surface-contact particles** ϕ (%)	C^a_{sca} (**nm**^{2})	g^a	**Relative error** $\lvert C^{PC}_{sca} - C^{SC}_{sca}\rvert / C^{SC}_{sca}$ (%) [a]	$\lvert g^{PC} - g^{SC}\rvert / g^{SC}$ (%)
1.26	3.9	66.4	3.01x10^5	0.63	68.9	2.83x10^5	0.71	6	10
1.26	5.9	67.2	1.21x10^6	0.77	67.8	1.35x10^5	0.82	10	6
1.26	7.8	66.5	3.11x10^6	0.81	67.6	3.09x10^6	0.81	0.6	0
1.26	10.9	67.6	7.26x10^6	0.81	66	6.66x10^6	0.78	9	5
1.26	12.5	67.3	9.61x10^6	0.8	66.6	8.62x10^6	0.76	11	6
0.63	3.9	66.5	2.18x10^5	0.81	66.2	2.56x10^5	0.79	15	3
0.63	6.3	67.5	1.26x10^6	0.88	67.7	1.39x10^6	0.86	9	3
0.63	7.8	67	2.82x10^6	0.91	66.9	3.01x10^6	0.88	6	3
0.25	3.11	67	7.71x10^4	0.79	66.6	8.67x10^4	0.78	11	2
0.25	3.9	67.1	1.95x10^5	0.86	67.9	2.05x10^5	0.85	5	1
0.13	1.56	66.8	3.38x10^3	0.45	66.7	3.74x10^3	0.43	10	4
0.063	0.62	65.9	28.4	0.07	67.7	26.8	0.67	6	5

[a] "PC" refers to aggregates with point-contact particles and "SC" refers to aggregates with surface-contact particles.

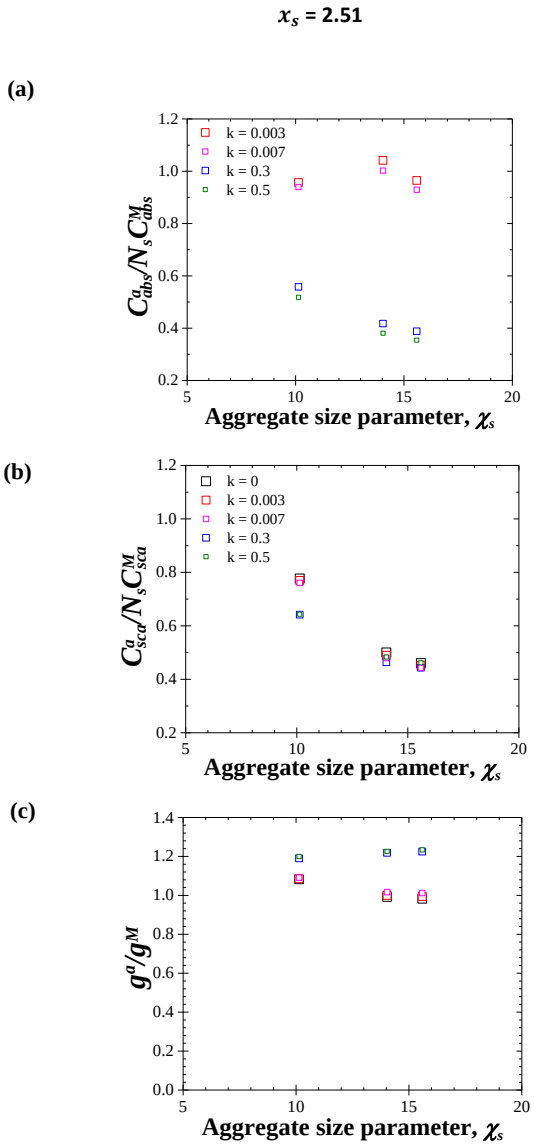

Figure C.1: (a) Absorption cross-section ratio $C^a_{abs}/N_sC^M_{abs}$, (b) scattering cross-section ratio $C^a_{sca}/N_sC^M_{sca}$, and (c) asymmetry factor ratio g^a/g^M as functions of the aggregate size parameter χ_s for aggregates with particle size parameter x_s = 2.51, particle volume fraction f_v = 33±2%, and relative refractive index m between 1.5 and 1.5+i0.5.

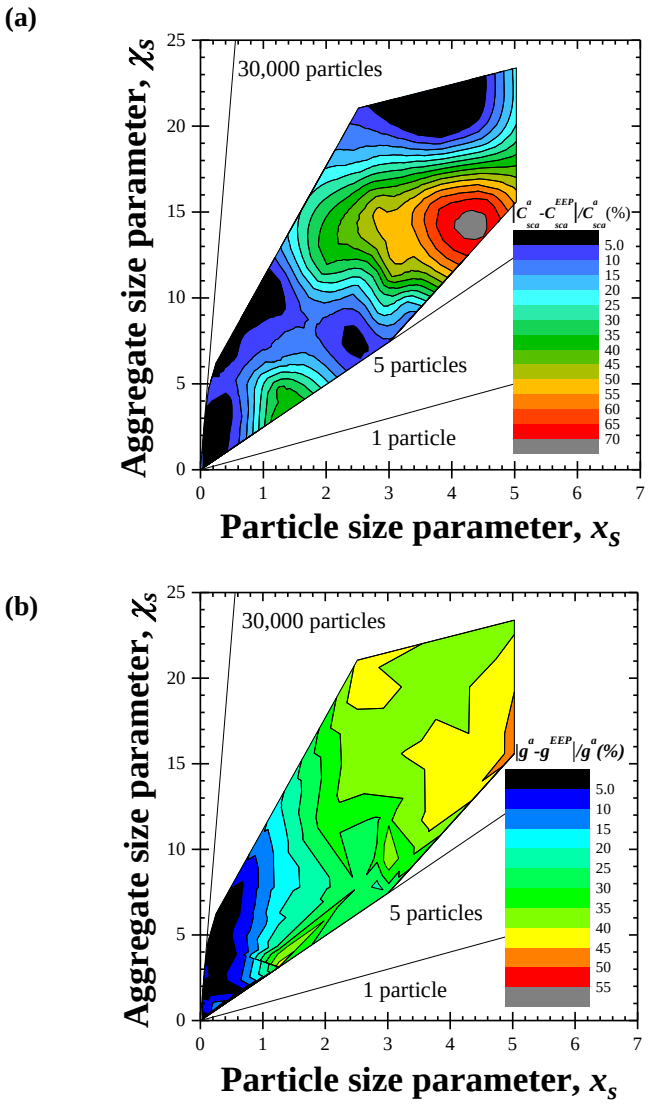

Figure C.2: Relative errors (a) $|C^a_{sca}\text{-}C^{EEP}_{sca}|/C^a_{sca}$ and (b) $|g^a - g^{EEP}|/g^a$ between numerical simulations and EEP approximation predictions for aggregates with particle volume fraction $f_v = 33\pm2\%$ and with point-contact particles with $m = 1.5$ as functions of the particle size parameter x_s and aggregate size parameter χ_s.

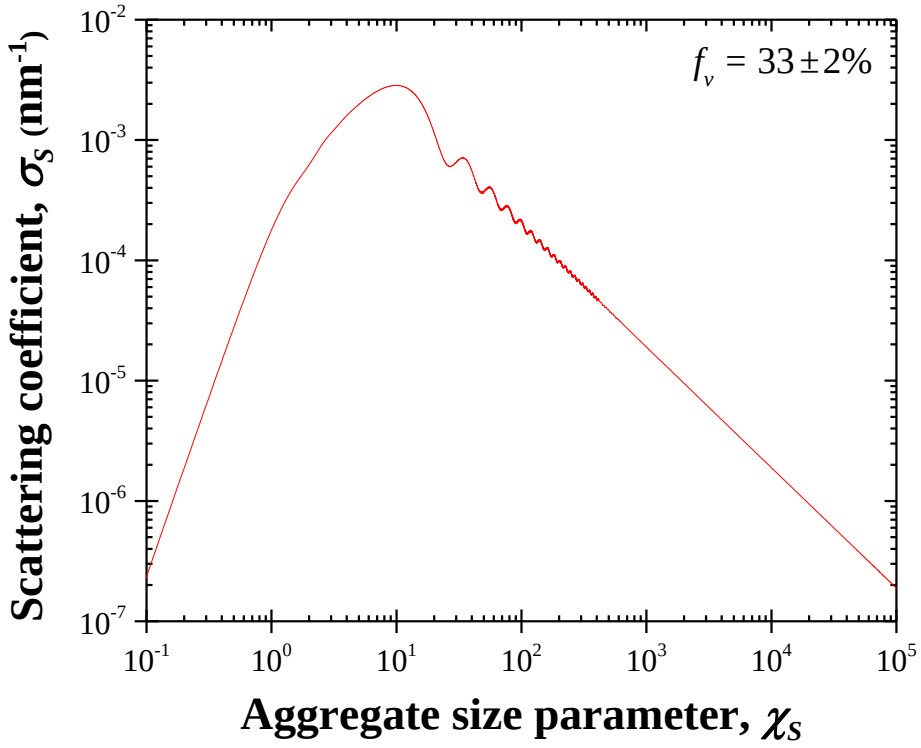

Figure C.3: Scattering coefficient σ_s predicted by the EEP approximation for aggregates with $f_v = 33\pm2\%$ and $m = 1.5$ as a function the aggregate size parameter χ_s.

APPENDIX D

Supplementary Materials for Chapter 5

D.1 Analytical expression of $\bar{V}_D$ (5.11)

$$\bar{V}_D = \int_0^{+\infty} \frac{4\pi}{3} r_D^3 \frac{e^{-\frac{1}{2}\left[\frac{r_D - \bar{r}_D(x_w)}{S}\right]^2}}{S\sqrt{2\pi}} \mathrm{d}r_D \quad \text{(Equation(5.11))}. \tag{D.1}$$

Let us define

$$q = \int_0^{+\infty} r_D^3 e^{-\frac{1}{2}\left[\frac{r_D - \bar{r}_D(x_w)}{S}\right]^2} \mathrm{d}r_D. \tag{D.2}$$

By performing the following change of variable r=(r_D-$\bar{r}_D$)/σ, q can be rewritten as

$$q = \sigma \int_{-\bar{r}_D/\sigma}^{+\infty} e^{\frac{-x^2}{2}} (\sigma r + \bar{r}_D)^3 \mathrm{d}r_D. \tag{D.3}$$

By integrating the integral in the expression of q from $-\bar{r}_D/\sigma$ to 0 and from 0 to $+\infty$, and by expanding $(\sigma r + \bar{r}_D)^3$ such that

$$(\sigma r + \bar{r}_D)^3 = \sigma^3 r^3 + 3\bar{r}_D \sigma^2 r^2 + 3\bar{r}_D^2 \sigma r + \bar{r}_D^3 \tag{D.4}$$

q can then be expressed with 8 integrals that can then be integrated by part. This results in

$$\bar{V}_D = \frac{2}{3}\sqrt{2\pi}\left(\left[\bar{r}_D^2 + 2S^2\right] S \exp\left(-\frac{\bar{r}_D^2}{2S^2}\right) + \sqrt{\frac{\pi}{2}}\left[3\bar{r}_D S^2 + \bar{r}_D^3\right]\left[1 + \mathrm{erf}\left(\frac{\bar{r}_D}{S}\right)\right]\right). \tag{D.5}$$

If $S = 0.1\bar{r}_D$, $\bar{V}_D$ can be further simplified such that $\bar{V}_D = 4.31\bar{r}_D^3$.

D.2 Optical changes in drying nanoparticle-based mesoporous silica monoliths

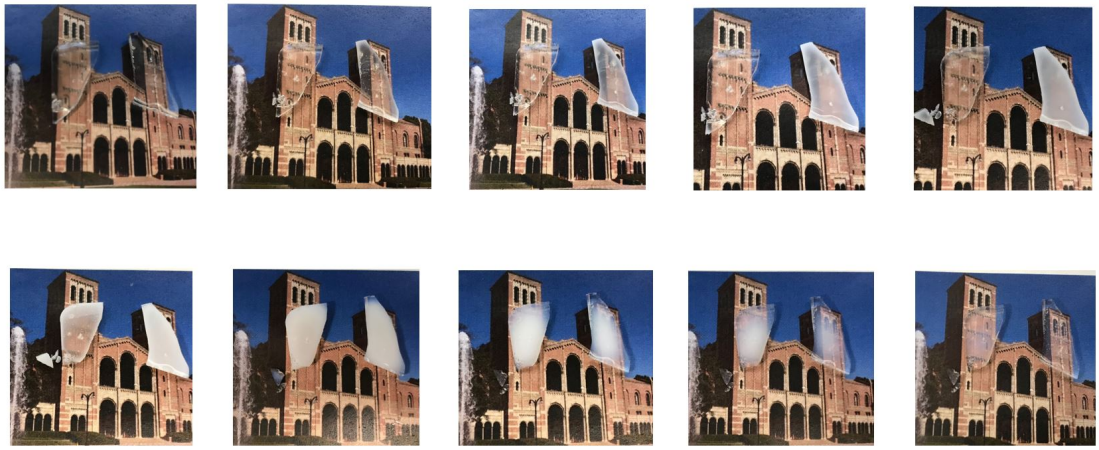

Figure D.1: Photographs of a nanoparticle-based mesoporous silica monolith drying from water in ambient conditions. The monolith was photographed on an image of UCLA Royce Hall [22] (modified and redistributed with permission from Ref. [23] Copyright Prayitno.

Figure D.2: Photographs of a nanoparticle-based mesoporous silica monolith drying from water in a covered dish. The monolith was photographed on an image of UCLA Royce Hall [22] (modified and redistributed with permission from Ref. [23] Copyright Prayitno).

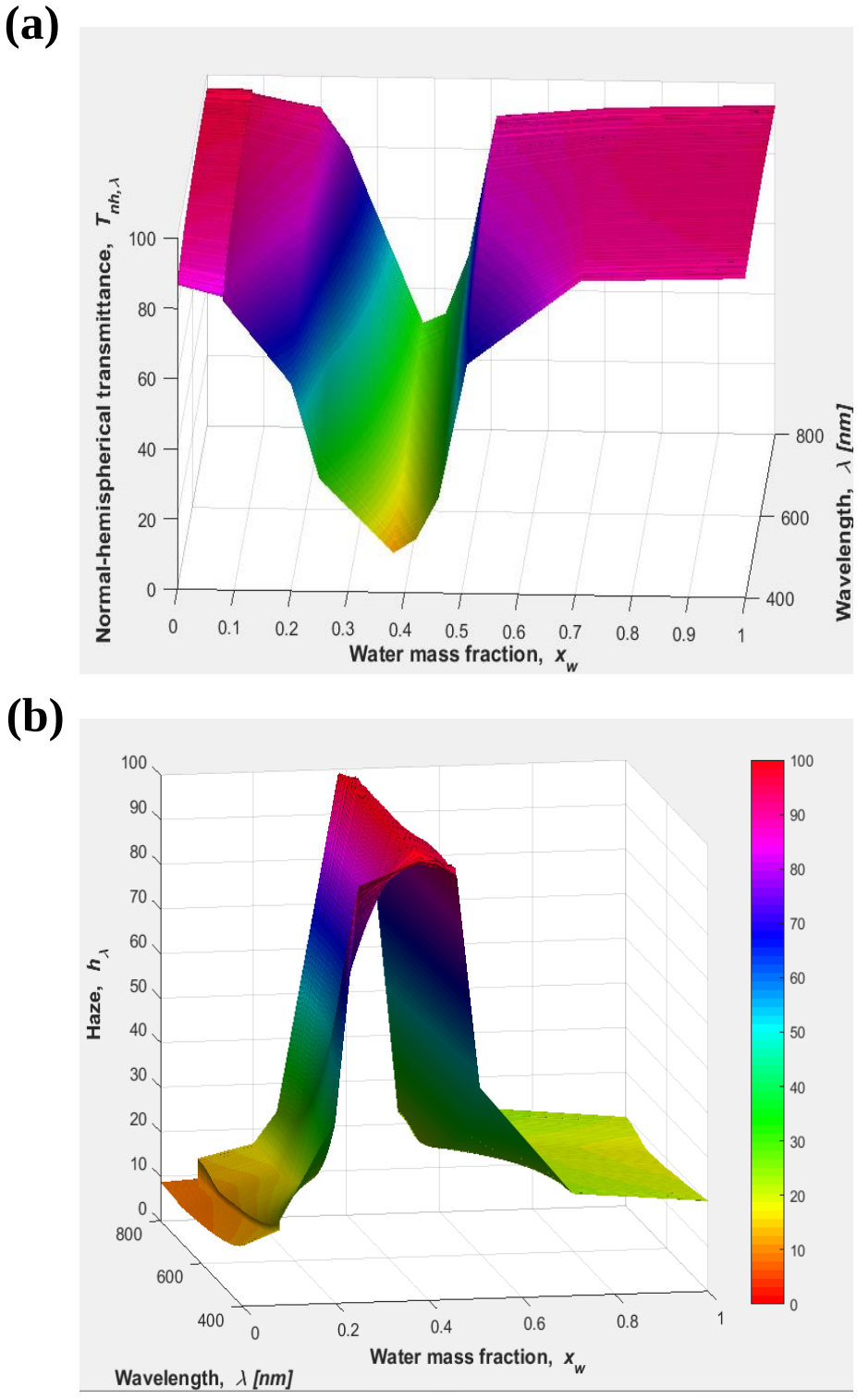

Figure D.3: 3D plots of the spectral (a) normal-hemispherical transmittance and (b) haze of a nanoparticle-based mesoporous monolith (pictures in Figure 1) as a function of the water mass fraction x_w.

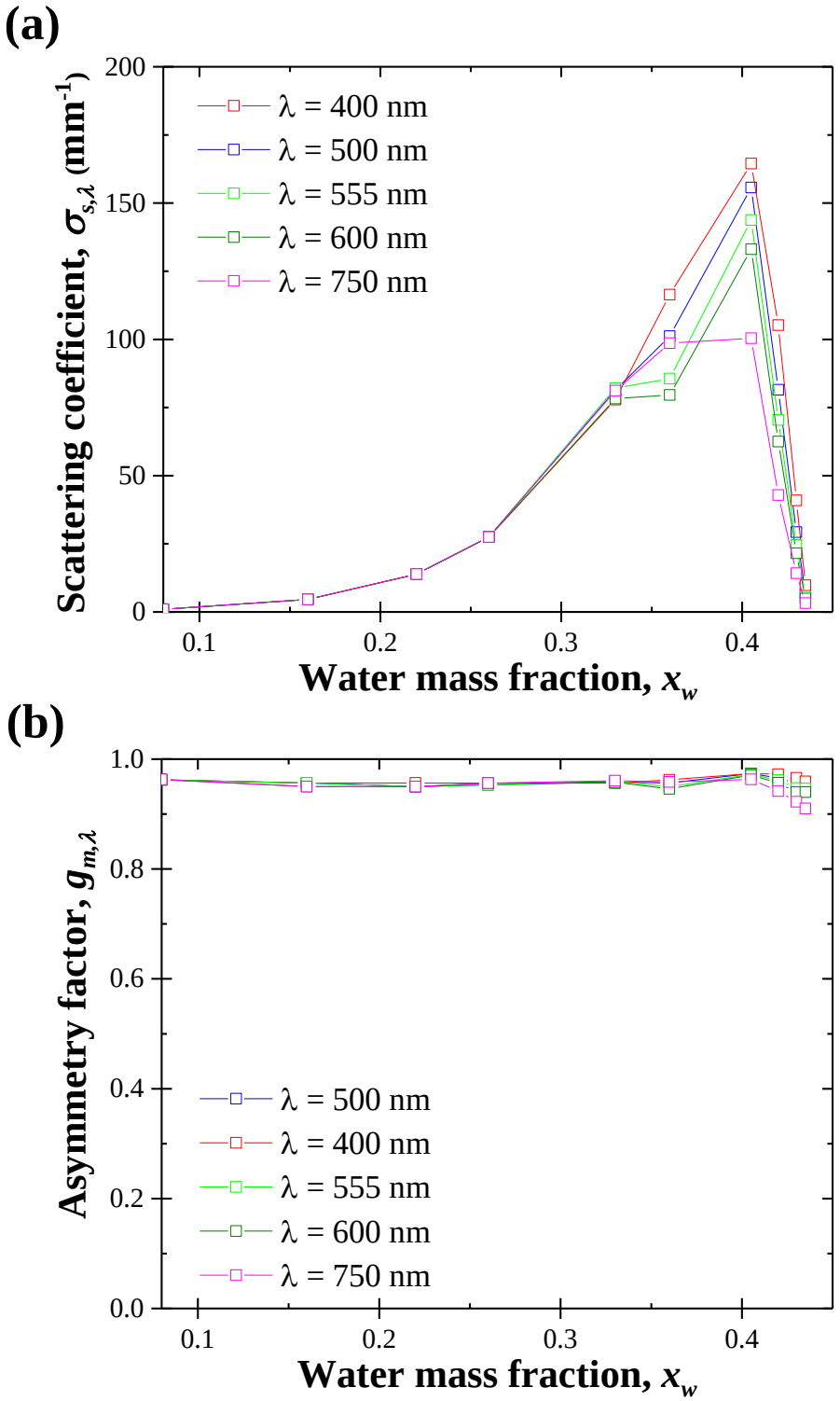

Figure D.4: Modeled (a) scattering coefficient $\sigma_{s,\lambda}$ and (b) asymmetry factor $g_{m,\lambda}$ of a nanoparticle-based mesoporous monolith with porosity $\phi_F = 49\%$ and thickness $L = 2$ mm as a function of the water mass fraction x_w.

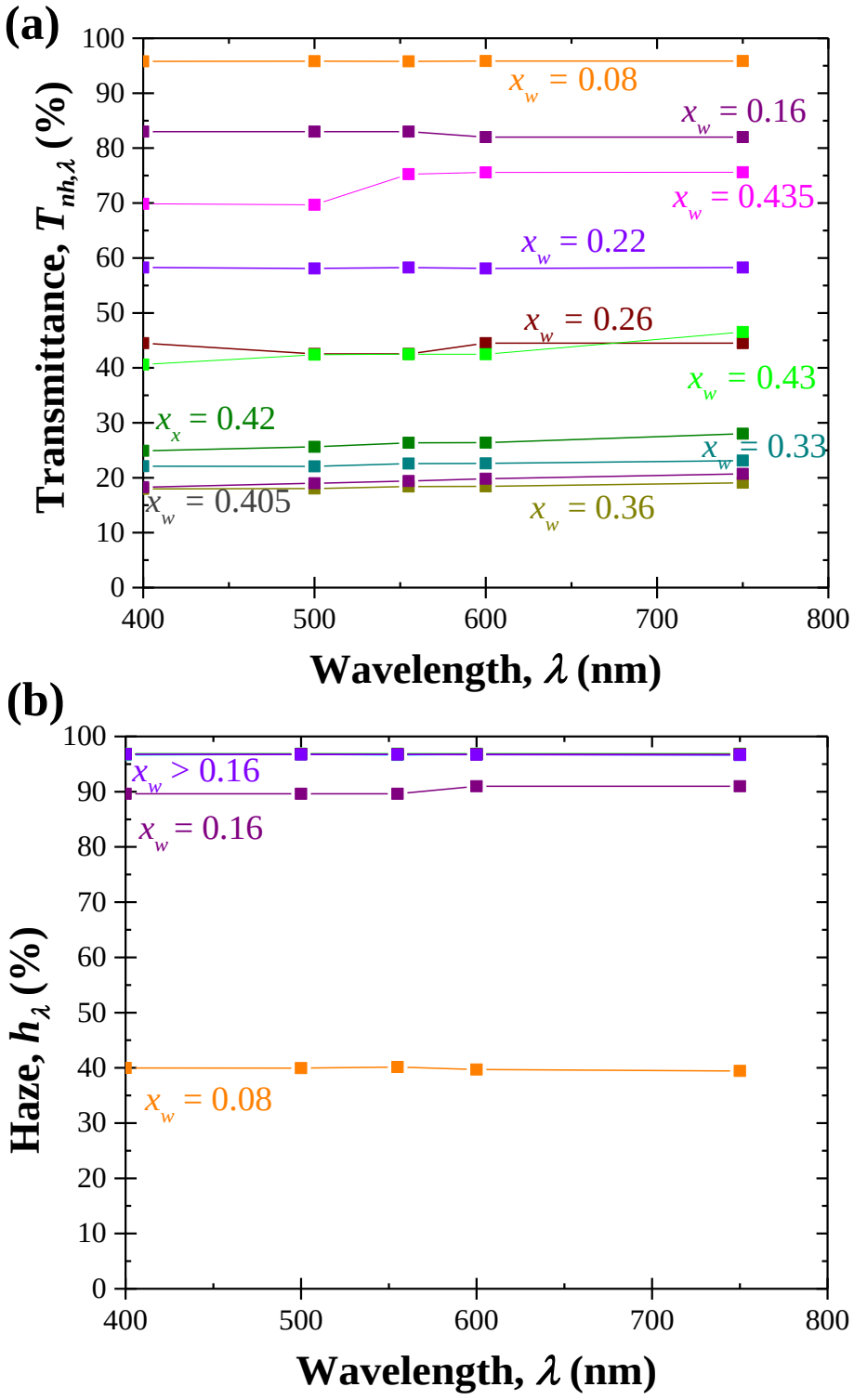

Figure D.5: Modeled spectral (a) normal-hemispherical transmittance $T_{nh,\lambda}$ and (b) haze h_λ of a nanoparticle-based mesoporous monolith with porosity $\phi_F = 49\%$ and thickness $L = 2$ mm as a function of the water mass fraction x_w.

APPENDIX E

Supplementary Materials for Chapter 6

A, B, C	coefficients in Cauchy dispersion law, Equation (S3)
a, b, c, d	coefficients in the expressions of $n_{0,\lambda}$ and γ_λ, Equations (S6)
B_λ	reference intensity, %
C_{N_2}	cross-sectional area of a nitrogen molecule, m^2
D_λ	dark signal, %
d_p	peak pore diameter, nm
L	mesoporous film thickness, nm
M	mass ratio of polymer to inorganic components, g/g
m_λ	complex index of refraction, $m_\lambda = n_\lambda - \mathrm{i}k_\lambda$
N	number of measured data points
$n_{0,\lambda}$	variable in the expression of $n_{3,\lambda}$, Equation (S5)
n_λ	refractive index
$k_{0,\lambda}$	variable in the expression of $k_{3,\lambda}$, Equation (S7)
k_λ	absorption index
P_0	adsorbate saturation pressure, Pa
$R_{pred,\lambda}$	predicted reflectance of the film, %
R_λ	measured reflectance, %
S_a	specific surface area, m^2/g
S_λ	measured reflected intensity, %
T_0	ambient temperature, $T_0 = 20°C$
$v_{p,tot}$	total pore volume, cm^3/g
u_λ, w_λ	variables in the expression of $R_{3,pred,\lambda}$, Equation (S4)
v	volume fraction

Greek symbols

Δ	refers to uncertainty
δR	relative error between experimental and theoretical reflectances
ε	offset, %
γ_λ	variable in the expression of $n_{3,\lambda}$, Equation (S5)
λ	wavelength of radiation, nm
ϕ	total porosity, %
ϕ_o	open porosity, %
ρ	density of the solid phase, g/cm^3
σ_λ	standard deviation of the white noise, %
θ	angle of incidence or transmission, rad

Subscripts

1	refers to the surrounding medium of the sample, i.e., air
2	refers to the thin film
3	refers to the silicon substrate
c	refers to the continuous phase of the porous structure
d	refers to the dispersed phase of the porous structure
eff	refers to effective properties
nn	refers to normal-normal measurement
nh	refers to normal-hemispherical measurement
s	refers to silica
t	refers to titania
std	refers to the high reflecting standard
$\perp$	refers to the perpendicular polarization
$\parallel$	refers to the parallel polarization

E.1 Characterization

E.1.1 Scanning Electron Microscopy

Scanning Electron Microscopy (SEM) images were obtained using a model JSM-6700F (JEOL, Tokyo, Japan) field emission electron microscope with 5 kV accelerating voltage and secondary electron detector configuration.

E.1.2 Contact profilometry

The thickness L of the mesoporous silica and silica-titania films was measured using a surface profiler (Dektak 6, 8, or 150 Veeco, Plainview, USA). The reported thickness was the average of three measurements at different locations. The error bars represented one standard deviation or 68% confidence interval.

E.1.3 Interferometry

Normal-hemispherical reflectance spectra $R_{nh,\lambda}$ were measured using a double-beam UV-Vis spectrophotometer (3101-PC Shimadzu, Kyoto, Japan) equipped with an integrating sphere of internal diameter of 60 mm (ISR 3100, Shimadzu). The sample slit width was 2 mm x 16 mm and the angle of incidence of the light beam into the integrating sphere was $\theta_1 = 8°$. Normal-normal spectral reflectance $R_{nn,\lambda}$ was also measured using a UV-Vis-NIR spectrometer (HR4000 UV-NIR Ocean Optics, Largo, USA) equipped with a bifurcated reflectance probe (R400-7-SR, Ocean Optics) and a UV-Vis-NIR light source (DH2000-BAL, Ocean Optics). A probe holder (RPH-1, Ocean Optics) was used to ensure normal incidence ($\theta_1 = 0°$) and constant distance between the probe and the samples for all measurements. Normal-hemispherical $R_{nh,\lambda}$ and normal-normal $R_{nn,\lambda}$ reflectances were measured in the visible range between 400 and 800 nm with spectral resolution of 1 nm or less. The reflection signals $S_{nh,\lambda}$ and $S_{nn,\lambda}$ for normal-hemispherical and normal-normal measurements were normalized by a corresponding baseline $B_{nh,\lambda}$ and

$B_{nn,\lambda}$ measured using a high specular reflection standard mirror (NIST certified STAN-SSH, Ocean Optics). Then, the experimental spectral reflectances $R_{nh,\lambda}$ and $R_{nn,\lambda}$ were calculated as

$$R_{nh,\lambda} = \frac{S_{nh,\lambda} - D_{nh,\lambda}}{B_{nh,\lambda} - D_{nh,\lambda}} R_{std,\lambda} \quad \text{and} \quad R_{nn,\lambda} = \frac{S_{nn,\lambda} - D_{nn,\lambda}}{B_{nn,\lambda} - D_{nn,\lambda}} R_{std,\lambda} \tag{S1}$$

where $D_{nh,\lambda}$ and $D_{nn,\lambda}$ are the dark signals measured by obstructing the detector window or turning the light source off and $R_{std,\lambda}$ is the normal-normal reflectance of the standard mirror provided by the supplier. The reflectance $R_{nh,\lambda}$ of the different mesoporous films was measured with the spectrometer and the integrating sphere. The reflectance $R_{nn,\lambda}$ of films whose thickness and refractive index could not be retrieved from their reflectance spectrum $R_{nh,\lambda}$ was measured in multiple spots with the reflectance probe that had much smaller sample slit. In fact, thickness non-uniformity altered the reflectance spectrum and focusing the measurement on a smaller surface enabled to minimize the effects of thickness variation. Note that all mesoporous films were degassed at 150°C for at least two hours in air before any reflectance measurement.

Figure 6.2(a) shows a block diagram of the procedure used to retrieve thickness L, effective refractive index $n_{eff,\lambda}$, and total porosity ϕ of mesoporous thin films from their reflectance spectra. All fittings were performed using the generalized reduced gradient (GRG) algorithm implemented in the Microsoft Excel Solver. Thickness L and effective refractive index $n_{eff,\lambda}$ of mesoporous silica and silica-titania thin films were retrieved by minimizing the relative error δR^2 between the predicted $R_{pred,\lambda}(L,n_{eff,\lambda})$ [Equation (6)] and experimentally measured $R_{nh,\lambda}$ or $R_{nn,\lambda}$ [Equation (S1)] reflectances defined as

$$\delta R^2 = \frac{1}{N} \sum_{i=1}^{N} \left(\frac{R_{pred,\lambda_i} - R_{nh,\lambda_i}}{R_{nh,\lambda_i}} \right)^2 \tag{S2}$$

where N is the number of measured wavelengths between 400 and 800 nm. The effective refractive index of mesoporous silica films was assumed to be constant

while the effective refractive index of mesoporous silica-titania films was assumed to obey Cauchy dispersion law given by

$$n_{eff,\lambda} = A + \frac{B}{\lambda^2} + \frac{C}{\lambda^4} \tag{S3}$$

where A, B (in μm^2), and C (in μm^4) are fitting coefficients constrained such that $A \geq 1$, $0 < B < 1$, and $0 < C < 1$ and λ is expressed in μm. In fact, assuming that the effective refractive index of silica-titania films was constant lead to poor fittings indicating that this assumption was not valid for such films.

The complex refractive index of the silicon substrate $m_{3,\lambda} = n_{3,\lambda} - \mathrm{i}k_{3,\lambda}$ used in the calculation of $R_{pred,\lambda}$ [Equations (6)-(8)] was retrieved by minimizing the relative error between the experimentally measured $R_{3,nh,\lambda}$ and the theoretically predicted reflectance spectra $R_{3,pred,\lambda}$ of the silicon substrate treated as a semi-infinite slab and was expressed as [132]

$$\begin{aligned}
R_{3,pred,\lambda} &= \frac{R_{3,\perp,\lambda} + R_{3,\parallel,\lambda}}{2} \\
\text{with} \quad R_{3,\perp,\lambda} &= \frac{(n_{1,\lambda}\cos\theta_1 - u_\lambda)^2 + w_\lambda^2}{(n_{1,\lambda}\cos\theta_1 + u_\lambda)^2 + w_\lambda^2}, \\
R_{3,\parallel} &= \frac{((n_{3,\lambda}^2 - k_{3,\lambda}^2)\cos\theta_1 - n_{1,\lambda}u_\lambda)^2 + (2n_{3,\lambda}k_{3\lambda}\cos\theta_1 - n_{1,\lambda}w_\lambda)^2}{((n_{3,\lambda}^2 - k_{3,\lambda}^2)\cos\theta_1 + n_{1,\lambda}u_\lambda)^2 + (2n_3k_3\cos\theta_1 + n_{1,\lambda}w_\lambda)^2}, \\
\text{and} \quad u_\lambda - iw_\lambda &= \sqrt{m_{3,\lambda} - n_{1,\lambda}\sin\theta_1}.
\end{aligned} \tag{S4}$$

In Equation (S4), the spectral refractive index $n_{3,\lambda}$ of silicon was expressed using the empirical equation of Jellison and Modine [171] given by

$$n_{3,\lambda} = n_{0,\lambda} + \gamma_\lambda T_0 \tag{S5}$$

where $T_0 = 20°$C is the ambient temperature (in °C). The coefficients $n_{0,\lambda}$ and γ_λ were expressed as [171]

$$n_{0,\lambda} = \left(a + \frac{b}{3.648^2 - (1.24/\lambda)^2}\right)^{1/2} \quad \text{and} \quad \gamma_\lambda = c + \frac{d}{3.648^2 - (1.24/\lambda)^2} \tag{S6}$$

where λ is the wavelength (in μm). The absorption index $k_{3,\lambda}$ was expressed as [171]

$$k_{3,\lambda} = k_{0,\lambda}\exp\left(\frac{T_0}{369.9 - \exp(-12.92 + 6.831/\lambda)}\right)$$
$$\text{with} \quad k_{0,\lambda} = \left(-0.0805 + \exp(-3.189 + \frac{7.946}{3.648^2 - (1.24/\lambda)^2})\right). \tag{S7}$$

The fitting parameters a, b, c, and d were fitted from the experimental normal-hemispherical reflectance $R_{3,nh,\lambda}$ of the bare Si substrate used in the present study and found to be $a = 4.463$, $b = 96.99$ eV^{-2}, c = -2x10^{-6} °C^{-1}, and d = 6.6x10^{-5} eV^{-2}.°C^{-1}.

Moreover, the total porosity ϕ of the mesoporous films was calculated based on the Maxwell-Garnett model [Equation (2)] using the effective refractive index $n_{eff,\lambda}$ retrieved from reflectance measurements and the refractive index $n_{d,\lambda} = 1$ of air. For mesoporous silica thin films, the refractive index of the continuous phase $n_{c,\lambda}$ and the effective refractive index $n_{eff,\lambda}$ of the mesoporous films were assumed to be independent of wavelength λ and $n_{c,\lambda}$ was taken as the average refractive index of silica given by the Sellmeier formula derived by Malitson [24] over the 400-800 nm wavelength range, i.e., as $n_{c,\lambda} = 1.459$. In this spectral range, the refractive index of silica does not vary by more than 0.017 [24]. Then, only one value of porosity ϕ was retrieved. On the other hand, for mesoporous silica-titania thin films, the refractive index $n_{c,\lambda}$ of the matrix was expressed using the Cauchy dispersion law [Equation (S3)] and the parameters A and B were fitted based on Equations (6)-(8) from the experimental normal-hemispherical reflectance of dense silica-titania thin films with the same composition as the mesoporous silica-titania films. Note that the coefficient C was fitted only if good fittings could not be obtained by fitting A and B only. At least two dense silica-titania thin films were measured for each composition and the calculated $n_{c,\lambda}$ were averaged at each wavelength. Here, the refractive indices $n_{c,\lambda}$ and $n_{eff,\lambda}$ were functions of wavelength and the retrieval procedure yielded a value of porosity ϕ

for each wavelength. In this case, the reported porosity was taken as the average of all porosities and the error bars were within the estimated uncertainty $\Delta\phi$ (see below).

The method was validated by comparing the retrieved thickness L and refractive index $n_{2,\lambda}$ of a thermal oxide (amorphous silica) thin film on undoped silicon wafer against the thickness and refractive index measured using a NanoSpec 210 film analysis system (Nanometrics, Milpitas, CA). The instrument measured reflectance over the 480-800 nm wavelength range at ambient conditions and calculated average thickness and refractive index of the film. Before measuring each sample, the instrument was calibrated against a bare silicon substrate. The normal-normal reflectance was measured at five spots uniformly spaced across the sample. The thickness and refractive index retrieved from our fitting method fell within 3% of those measured with the Nanospec instrument.

To estimate the uncertainties associated with the film thickness L and effective refractive index $n_{eff,\lambda}$, more than 40 ideal normal-hemispherical spectral reflectance $R_{nh,\lambda}$ were generated using [Equation (1)] for film thickness L ranging from 30 nm to 1 μm and effective refractive index $n_{eff,\lambda}$ ranging from 1 to 1.7. The effective refractive index $n_{eff,\lambda}$ of mesoporous silica films was assumed to be constant and taken between 1 to 1.45. On the other hand, the effective refractive index $n_{eff,\lambda}$ of mesoporous silica-titania films followed the Cauchy dispersion law [Equation (S3)] and varied from 1 to 1.7. In addition, white noise ΔR_λ and an arbitrary offset ε were added to the spectral reflectance $R_{nh,\lambda}$ resulting in a modified reflectance $R_{nh,\lambda}+\Delta R_\lambda+\varepsilon$. The noise ΔR_λ was introduced at each wavelength by adding Gaussian-distributed random values with a mean of 0% and a standard deviation of σ_λ. The standard deviation σ_λ was estimated from actual experimental measurements and based on the expression of $R_{nh,\lambda}$ given by Equation (S1) so

that

$$\sigma_\lambda = \sqrt{\left(\frac{\partial R_{nh,\lambda}}{\partial S_{nh,\lambda}}\Delta S_{nh,\lambda}\right)^2 + \left(\frac{\partial R_{nh,\lambda}}{\partial D_{nh,\lambda}}\Delta D_{nh,\lambda}\right)^2 + \left(\frac{\partial R_{nh,\lambda}}{\partial B_{nh,\lambda}}\Delta B_{nh,\lambda}\right)^2} \quad \text{(S8)}$$

where $\Delta B_{nh,\lambda}$, $\Delta D_{nh,\lambda}$, and $\Delta S_{nh,\lambda}$ are the uncertainties associated with the reference intensity $B_{nh,\lambda}$, the dark signal $D_{nh,\lambda}$, and the reflected signal $S_{nh,\lambda}$, respectively. Note that the uncertainty related to the reflectance $R_{std,\lambda}$ of the NIST-certified mirror was assumed to be zero. The uncertainty of the reference intensity $\Delta B_{nh,\lambda}$ was estimated by calculating the standard deviation and was averaged over 10 experimental measurements of the baseline signal $B_{nh,\lambda}$. The uncertainties of the dark signal $\Delta D_{nh,\lambda}$ and of the measured reflected signal $\Delta S_{nh,\lambda}$ were set as $\Delta D_{nh,\lambda} = \Delta S_{nh,\lambda} = \Delta B_{nh,\lambda}$. In addition, the offset ε was introduced randomly for each modified reflectance spectrum. It was estimated to be $\varepsilon = \pm$ 0.13% corresponding to the mean of the difference ($B_{nh,\lambda}$ - $D_{nh,\lambda}$) over 10 experimental measurements. Finally, the thickness L and effective refractive index $n_{eff,\lambda}$ from the noisy spectral reflectance data, i.e., from $R_{nh,\lambda}+\Delta R_\lambda+\varepsilon$, were determined using the aforementioned fitting procedure.

The uncertainty $\Delta n_{eff,\lambda}$ associated with the retrieved $n_{eff,\lambda}$ was defined as the average absolute difference between the refractive index used to predict the ideal spectral normal-hemispherical reflectance $R_{nh,\lambda}$ and that retrieved from the noisy normal-hemispherical reflectance $R_{nh,\lambda}+\Delta R_\lambda+\varepsilon$. It was found to be (i) $\Delta n_{eff,\lambda}$ = 0.003 for mesoporous silica films with $1 \leq n_{eff,\lambda} \leq 1.45$ and (ii) $\Delta n_{eff,\lambda}$ = 0.005 for mesoporous silica-titania films with $1 \leq n_{eff,\lambda} \leq 1.7$. Similarly, the uncertainty ΔL associated with the film thickness L was defined as the average relative difference between the exact thickness and that retrieved from fitting. It was found to be $\Delta L/L$ = 0.41% for mesoporous silica films and $\Delta L/L$ = 0.31% for mesoporous silica-titania films.

The uncertainty $\Delta\phi$ associated with the retrieved total porosity ϕ was calcu-

lated according to

$$\Delta\phi = \sqrt{\left(\frac{\partial\phi}{\partial n_{eff,\lambda}}\Delta n_{eff,\lambda}\right)^2 + \left(\frac{\partial\phi}{\partial n_{c,\lambda}}\Delta n_{c,\lambda}\right)^2} \tag{S9}$$

where the expression of ϕ can be taken from any EMA [Equations (4)-(8)]. Here, ϕ was expressed according to the Maxwell-Garnett model [Equation (2)]. The uncertainty $\Delta n_{c,\lambda}$ of the refractive index of silica was calculated as twice the standard deviation of $n_{c,\lambda}$ given by the Sellmeier formula (Ref. [24]) over the 400-800 nm wavelength range. It was found to be $\Delta n_{c,\lambda} = 0.009$ while that of the silica-titania matrix was taken as $\Delta n_{eff,\lambda} = 0.005$. Finally, the uncertainty of the total porosity $\Delta\phi$ calculated by error propagation of $\Delta n_{eff,\lambda}$ and expressed by Equation (S9) was estimated as $\Delta\phi = 2\%$ for mesoporous silica films and as $\Delta\phi = 1.5\%$ for mesoporous silica-titania films. Note that the estimated uncertainties were related to the optical measurements and fittings only and do not account for film defects or EMAs uncertainty. In addition, the uncertainty related to the choice of the EMAs affects ellipsometric porosimetry results in the same way as the present method. Note that the uncertainty associated with the reference intensity from normal-normal reflectance measurement $\Delta B_{nn,\lambda}$ was equivalent to $\Delta B_{nh,\lambda}$. Therefore, the uncertainties ΔL, $\Delta n_{eff,\lambda}$, and $\Delta\phi$ for normal-normal reflectance measurements were identical to those calculated for normal-hemispherical reflectance measurements.

E.1.4 Ellipsometry and ellipsometric porosimetry

Ellipsometric porosimetry measurements were performed using a spectroscopic ellipsometer equipped with a porosimetry accessory (PS -1100 Semilab, Budapest, Hungary). Ellipsometry measurements were performed first, under vacuum and at room temperature, and were followed by porosimetry measurements using toluene as adsorbate. All mesoporous films were degassed in air above 100°C for at least 12 hours prior to each measurement to remove adsorbed water. Data analysis

was performed using the associated Spectroscopic Ellipsometry Analyzer software. The procedure is summarized in the block diagram of Figure 6.2(b).

The thickness L and effective refractive index $n_{eff,\lambda}$ of the mesoporous films were retrieved by fitting the ellipsometric spectra using the Cauchy dispersion law [Equation (E.1)] between wavelengths 250 and 1000 nm and assuming the films were non-absorbing. The total porosity ϕ was then calculated using the retrieved effective refractive index $n_{eff,\lambda}$ and the Maxwell-Garnett EMA [Equation (2)]. The open porosity ϕ_o was obtained from the toluene adsorption-desorption isotherms. The isotherms were measured by progressively introducing or pumping out toluene vapor into the sample chamber. The open porosity ϕ_o of the films was estimated based on the Lorentz-Lorenz model [Equation (4)] and calculated from Equation (11) for $\lambda = 632.8$ nm and $n_{d,\lambda}(P_0) = 1.4961$ [155].

The pore size distribution was calculated from the toluene adsorption isotherm based on the Kelvin equation and statistical film thickness of toluene on a reference non-porous adsorbent and assuming the pores were cylindrical. The peak pore diameter d_p was defined as the pore diameter for which the pore size distribution reached its maximum.

E.1.5 Nitrogen porosimetry

Low-temperature nitrogen adsorption-desorption isotherms of sol-gel and nanoparticle-based mesoporous silica powders and sol-gel mesoporous silica-titania powders were measured at -196°C using a surface area and porosity analyzers TriStar II 3020 (Micromeritics Instrument Corp., Norcross, GA, USA). Each sample was degassed in vacuum at 150°C for 20-24 h prior to each measurement. The specific surface area S_a was calculated using the Brunauer-Emmett-Teller (BET) method [82] based on the low-temperature nitrogen adsorption data in the relative pressure P/P_0 range 0.05-0.2, assuming that $C_{N_2} = 0.162$ nm^2 [156]. The total pore volume $v_{p,tot}$ was calculated from the number of moles of nitrogen adsorbed

at a relative pressure $P/P_0 = 0.98$. The open porosity ϕ_o was then calculated using Equation (13). The density of silica-titania was estimated as $\rho_{st} = \rho_s v_s + \rho_t v_{p,tot}$ where v_s and $v_{p,tot}$ are the volume fractions of silica and titania, respectively. The density of silica and titania (anatase) were taken as $\rho_s = 2.2$ g/cm^3 [68] and $\rho_t = 3.8$ g/cm^3 [172]. The pore size distribution was determined using the Kruk-Jaroniec-Sayari (KJS) [173] method based on the Barrett-Joyner-Halenda (BJH) method [83] using (i) the adsorption branch of the isotherm, (ii) the modified Kelvin equation [173] calibrated for cylindrical pores, and (iii) the statistical film thickness curve derived from the nitrogen adsorption isotherm measured for a macroporous silica LiChrospher Si-1000 [85]. In addition, the peak pore diameter d_p was estimated as the pore diameter for which the pore size distribution reached its maximum.

The relative uncertainty of the specific surface area S_a was estimated as $\Delta S_a/S_a = 10\%$ and the uncertainty ΔV_t was taken as 0.03 cm^3/g. The latter was propagated to ϕ using Equation (13) to calculate the experimental uncertainty $\Delta\phi$ from nitrogen adsorption.

Table E.1: Cauchy coefficients [Equation (E.1)] of dense silica-titania samples measured by ellipsometry. The refractive indices $n_{c,\lambda}$ plotted on Figure 3 are those of D91-1, D82-1, and D73-1.

Sample	**Silica:titania molar ratio**	**Cauchy coefficients**		
		A	**B** (in μm^2)	**C** (in μm^4)
D91-1	90:10	1.49	1x10^{-5}	1.1x10^{-3}
D91-2	90:10	1.51	9.1x10^{-3}	8x10^{-5}
D82-1	80:20	1.56	7.7x10^{-3}	0
D82-2	80:20	1.56	8.8x10^{-3}	0
D73-1	70:30	1.65	8x10^{-3}	8.9x10^{-4}
D73-2	70:30	1.68	1x10^{-7}	2x10^{-3}

Table E.2: Thickness L and refractive index $n_{c,\lambda}$ of dense silica-titania films measured by interferometry and ellipsometry.

Sample	**Silica:titania molar ratio**	**Film thickness L**		**Refractive index $n_{c,\lambda}$**	
		Interferometry (nm)	**Ellipsometry** (nm)	**Interferometry** (400-800 nm)	**Ellipsometry** (400-800 nm)
D91-1	90:10	294±1	302	1.51-1.55	1.49-1.53
D91-2	90:10	383±1	347	1.51-1.54	1.53-1.57
D82-1	80:20	149±0.5	149	1.56-1.60	1.57-1.61
D82-2	80:20	133±0.5	130	1.55-1.57	1.58-1.61
D73-1	70:30	137±0.5	137	1.65-1.70	1.66-1.73
D73-2	70:30	307±1	290	1.60-1.65	1.68-1.75

Table E.3: Thickness, effective refractive index, and porosity measurements of sol-gel mesoporous silica thin films.

Sample	**Polymer**	**Mass**	**Film thickness L**			**Effective refractive index $n_{eff,\lambda}$**		**Porosity ϕ**				**Peak pore diameter d_p**	
		ratio M	**Profilometry**	**Interferometry**	**Ellipsometry**	**Interferometry**	**Ellipsometry**	**Interferometry** [a]	**Ellipsometry** [a]	**EP** [b]	**N_2 adsorption** [b]	**EP**	**N_2 adsorption**
		(g/g)	(nm)	(nm)	(nm)		(λ = 400 -800 nm)	(%)	(%)	(%)	(%)	(nm)	(nm)
SGF-2.5	F127	2.5	660±66	701±3	628	1.15	1.11	67±2	76	58	64±1	15.2	7.7 and 21.7
SGF-2	F127	2	380±38	406±2	374	1.19	1.17-1.18	59±2	63	65	61±1	11.5	1.9 and 12.3
SGF-1.7	F127	1.7		241±1	235	1.25	1.22	45±2	52	45	58±1	8.1	8 and 30.3
SGF-1.4	F127	1.4	238±24	256±1	255	1.26	1.22	43±2	52	46	58±1	8.1	1.9 and 7.6
SGF-1.2	F127	1.2		213±1	198	1.27	1.25-1.26	41±2	44	41	50±1.5	8.7	6.8
SGF-1.2-2	F127	1.2	307±31	357±1.5	337	1.22	1.20-1.21	52±2	55	54	50±1.5	15.0	6.8
SGF-0.6	F127	0.6	143±14	185	156	1.35	1.35	24±2	24	31	28±3.5	7.6	< 1.6
SGF-0.4	F127	0.4	203±20	236±1	231	1.37	1.37-1.39	19±2	17	22	25±4	6	< 1.6
SGP-1.5	P123	1.5	436±44	476±2	460	1.18	1.18-1.19	62±2	59	65	61±1	5.2	8
SGP-0.8	P123	0.8	275±28	296±1	297	1.25	1.23-1.24	46±2	49	47	39±2.5	8.0	1.9 and 5.8
SGP-0.2	P123	0.2		80.3±0.3	80.5	1.42	1.41	8±2	10	8	22±4	2.5	< 1.6

[a] Total porosity ϕ

[b] Open porosity ϕ_o

Table E.4: Thickness, effective refractive index, and porosity measurements of nanoparticle-based mesoporous silica thin films.

Sample	**Polymer**	**Mass ratio** M (g/g)	**Film thickness** L **Profilometry** (nm)	**Interferometry** (nm)	**Ellipsometry** (nm)	**Effective refractive index** $n_{eff,\lambda}$ **Interferometry**	**Ellipsometry** (λ = 400 -800 nm)	**Porosity** ϕ **Interferometry** [a] (%)	**Ellipsometry** [a] (%)	**EP** [b] (%)	**N_2 adsorption** [b] (%)	**Peak pore diameter** d_p **EP** (nm)	**N_2 adsorption** (nm)
NPF-1.7	F127	1.7	530±53	566±2	526	1.14	1.15-1.16	70±2	66	59	65±1	16.4	8 and 32.7
NPF-1.5	F127	1.5	500±50	528±2	524	1.15	1.15-1.16	67±2	66	40	65±1	13.9	8.1 and 27.5
NPF-1.2	F127	1.2	380±38	430±2	401	1.17	1.21-1.22	62±2	54	53	56±1.5	13.3	8.7 and 28.5
NPF-1.2-2	F127	1.2	617±62	687±3	530	1.18	1.21-1.22	60±2	54	61	56±1.5	12.7	8.7 and 28.5
NPF-1	F127	1	350±35	372±2	368	1.19	1.19-1.20	57±2	58	55	57±1.5	10.8	8.5
NPF-0.5	F127	0.5	400±40	385±2	406	1.30	1.29	35±2	36	33	47±2	5.8	6.4
NPF-0.3	F127	0.3	433±43	417±2	399	1.28	1.29-1.30	39±2	36	34	49±2	2.8	5
NPP-2	P123	2	495±50	492±2	456	1.18	1.19	60±2	60	56	56±1.5	12.3	8.7
NPP-1.5	P123	1.5	594±59	549±2	461	1.17	1.17-1.18	63±2	62	68	62±1	13.2	11.3
NPP-0.5	P123	0.5	375±35	403±40	396	1.26	1.25-1.26	43±2	43	40	50±1.5	6.4	6
NPP-0.2	P123	0.2	375±38	445±2	438	1.29	1.27-1.28	36±2	40	36	50±1.5	4.4	5.8

[a] Total porosity ϕ

[b] Open porosity ϕ_o

Table E.5: Thickness, effective refractive index, and porosity measurements of sol-gel mesoporous silica-titania thin films.

Sample	**Silica:titania ratio**	**Polymer**	**Mass ratio M**	**Film thickness L**			**Effective refractive index $n_{eff,\lambda}$**		**Porosity ϕ**				**Peak pore diameter d_p**	
				Profilometry	**Interferometry**	**Ellipsometry**	**Interferometry**	**Ellipsometry**	**Interferometry** [a]	**Ellipsometry** [a]	**EP** [b]	**N_2 adsorption** [b]	**N_2 adsorption**	
			(g/g)	(nm)	(nm)	(nm)	(λ = 400 -800 nm)	(λ = 400 -800 nm)	(%)	(%)	(%)	(%)	(nm)	(nm)
STF91-1	90:10	F127	1	246±18	256±1	242	1.35-1.36	1.33-1.35	33±1.5	36	36	15±5.5	4.1	2.6
STF82-2.2	80:20	F127	2.2	583±12	604±2	571	1.28-1.29	1.27	51±1.5	53	58	61±1	4.5	2.3 and 6.4
STF82-2	80:20	F127	2	493±12	540±1.5	508	1.28-1.31	1.28	50±1.5	51	53	60±1.5	4.9	1.9 and 6.0
STF82-1.7	80:20	F127	1.7	400±10	456±1.5	445	1.34-1.35	1.29-1.31	41±1.5	48	42	56±1.5	4	1.2 and 5.8
STF82-1.5	80:20	F127	1.5	410±10	453±1.5	424	1.34-1.37	1.32-1.34	39±1.5	43	41	48±2	4	2 and 5.9
STF82-1	80:20	F127	1	312±10	332±1	321	1.38-1.43	1.32-1.37	30±1.5	41	39	50±2	3.7	2.1
STF73-1.5	70:30	F127	1.5	483±29	481±1.5	452	1.32-1.37	1.33-1.35	49±1.5	48	48	57±1.5	4	2.1 and 5.5
STF73-1	70:30	F127	1	393±6	382±1	369	1.41-1.46	1.40-1.43	35±1.5	38	32	55±2	4	2.1

[a] Total porosity ϕ

[b] Open porosity ϕ_o

Table E.6: Structural characteristics of sol-gel and nanoparticle-based mesoporous silica powders measured by nitrogen porosimetry.

Powder	**Structure**	**Polymer**	**Mass ratio M (g/g)**	**Specific surface area S_a (m^2/g)**	**Total pore volume $v_{p,tot}$ (cm^3/g)**	**Open porosity ϕ_o (%)**	**Peak pore diameter d_p (nm)**
P-SGF-2.5	Sol-gel silica	F127	2.5	730±73	0.817±0.03	64±1	7.7 and 21.7
P-SGF-2	Sol-gel silica	F127	2	790±79	0.720±0.03	61±1	1.9 and 12.3
P-SGF-1.7	Sol-gel silica	F127	1.7	290±29	0.639±0.03	58±1	8 and 30.3
P-SGF-1.4	Sol-gel silica	F127	1.4	740±74	0.617±0.03	58±1	1.9 and 7.6
P-SGF-1.2	Sol-gel silica	F127	1.2	650±65	0.452±0.03	50±1.5	6.8
P-SGF-0.6	Sol-gel silica	F127	0.6	380±38	0.177±0.03	28±3.5	< 1.6
P-SGF-0.4	Sol-gel silica	F127	0.4	310±31	0.148±0.03	25±4	< 1.6
P-SGP-1.5	Sol-gel silica	P123	1.5	500±50	0.700±0.03	61±1	8
P-SGP-0.8	Sol-gel silica	P123	0.8	580±58	0.290±0.03	39±2.5	8
P-SGP-0.2	Sol-gel silica	P123	0.2	300±30	0.130±0.03	22±4	< 1.6
P-NPF-1.7	NP silica	F127	1.7	270±27	0.834±0.03	65±1	8 and 32.7
P-NPF-1.5	NP silica	F127	1.5	310±31	0.839±0.03	65±1	8.1 and 27.5
P-NPF-1.2	NP silica	F127	1.2	310±31	0.576±0.03	56±1.5	8.7 and 28.5
P-NPF-1	NP silica	F127	1	420±42	0.600±0.03	57±1.5	8.5
P-NPF-0.5	NP silica	F127	0.5	400±40	0.406±0.03	47±2	6.4
P-NPF-0.3	NP silica	F127	0.3	420±42	0.435±0.03	49±2	5
P-NPP-2	NP silica	P123	2	390±39	0.573±0.03	56±1.5	8.7
P-NPP-1.5	NP silica	P123	1.5	280±28	0.753±0.03	62±1	11.3
P-NPP-0.5	NP silica	P123	0.5	420±42	0.460±0.03	50±1.5	6.0
P-NPP-0.2	NP silica	P123	0.2	380±38	0.462±0.03	50±1.5	5.8

Table E.7: Structural characteristics of sol-gel mesoporous silica-titania powders measured by nitrogen porosimetry.

Powder	**Silica-to-titania molar ratio**	**Polymer**	**Mass ratio M (g/g)**	**Specific surface area S_a (m^2/g)**	**Total pore volume $v_{p,tot}$ (cm^3/g)**	**Open porosity ϕ_o (%)**	**Peak pore diameter d_p (nm)**
P-STF91-1	90:10	F127	1	97±10	0.069±0.03	15±5.5	2.6
P-STF82-2.2	80:20	F127	2.2	720±72	0.623±0.03	61±1	2.3 and 6.4
P-STF82-2	80:20	F127	2	740±74	0.553±0.03	60±1	1.9 and 6.0
P-STF82-1.7	80:20	F127	1.7	640±64	0.473±0.03	56±1.5	1.2 and 5.8
P-STF82-1.5	80:20	F127	1.45	500±50	0.348±0.03	48±2	2.0 and 5.9
P-STF82-1	80:20	F127	1	630±63	0.363±0.03	50±2	2.1
P-STF73-1.5	70:30	F127	1.5	680±68	0.456±0.03	57±1.5	2.1 and 5.5
P-STF73-1	70:30	F127	1	660±66	0.429±0.03	55±2	2.1

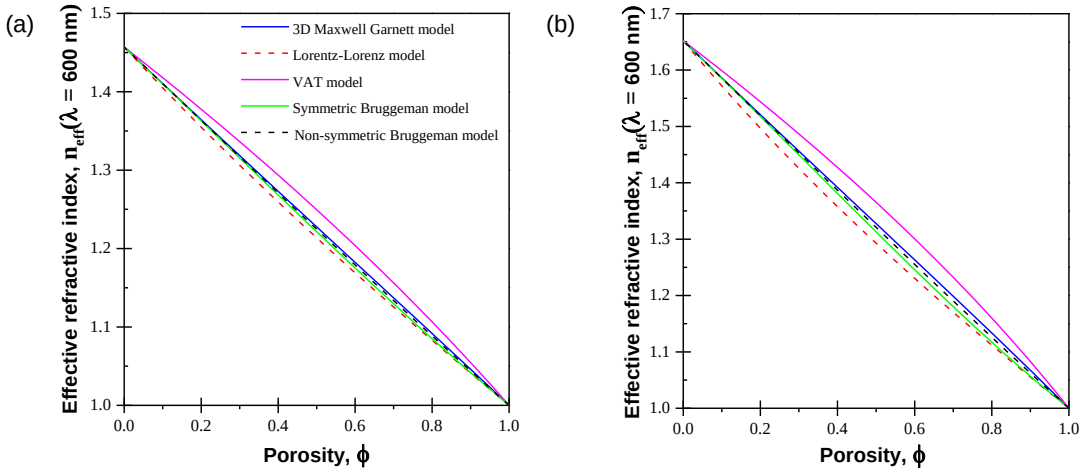

Figure E.1: Effective refractive index $n_{eff}(\lambda = 600$ nm) of (a) a mesoporous silica film with $n_c(\lambda = 600$ nm) = 1.457 and (b) a mesoporous silica-titania thin film with a silica:titania molar ratio of 70:30 and with $n_c(\lambda = 600$ nm) = 1.652 as a function of the total porosity ϕ calculated from various EMAs [Equations (4)-(8)]. It shows that the maximum absolute difference in porosity between all models was at most 8% for the mesoporous silica film and at most 11.3% for the silica-titania film corresponding to the difference between the Lorentz-Lorenz and VAT models for $n_{eff}(\lambda = 600$ nm) = 1.25 and $n_{eff}(\lambda = 600$ nm) = 1.33, respectively. It indicates that differences between the EMAs increases with increasing refractive index mismatch between the dispersed and continuous phases. However, these relative differences in porosity calculated from effective refractive index and using EMAs for mesoporous silica and silica-titania films are similar to those found between different porosimetry methods [25, 26].

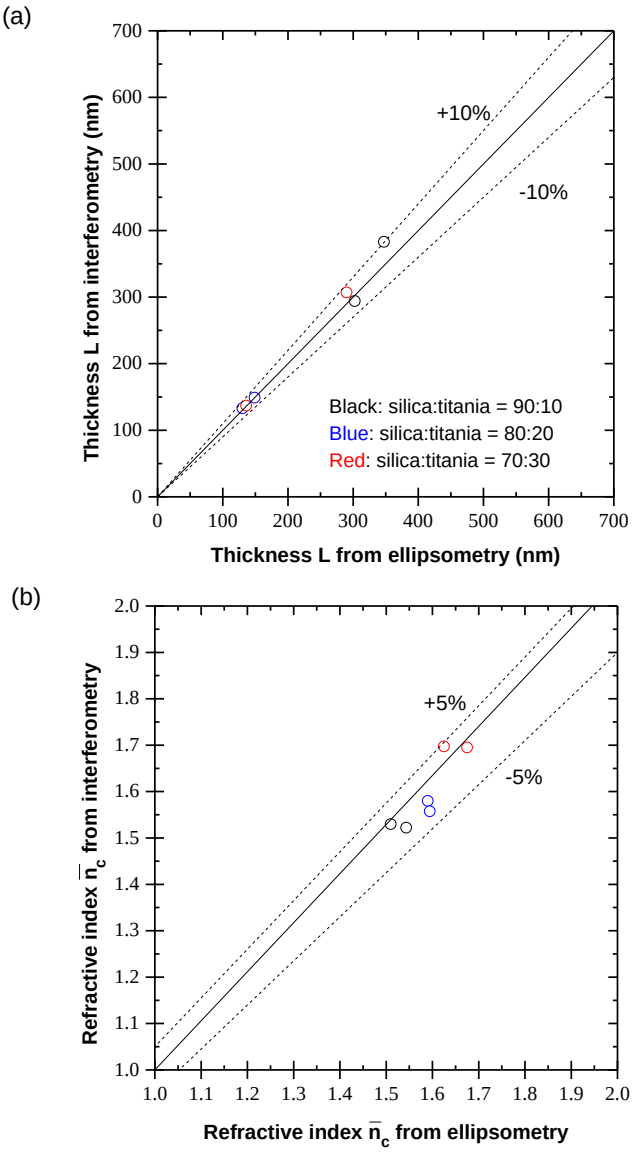

Figure E.2: (a) Thickness L and (b) refractive index of dense silica-titania films $\bar{n}_c$ averaged over the visible range (λ = 400-800 nm) with silica:titania molar ratio of 90:10, 80:20, and 70:30 measured by interferometry and ellipsometry. Results for two films are presented for each silica:titania molar ratio. It shows that the two methods were in very good agreement. Note here that thickness of dense silica-titania films could not be measured using contact profilometry since the dense films could not be scratched.